

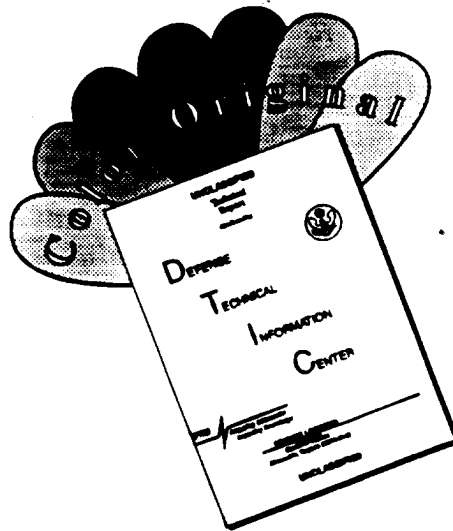


**19951002 000**

**THERE IS NO PAGE 78 OR FIGURE 14  
BECAUSE THEY WERE MISNUMBERED  
PER DEBRA TYRELL (202) 767-8001 AT  
AF OFFICE OF SCIENTIFIC RESEARCH,  
BOLLING AFB, D.C.**

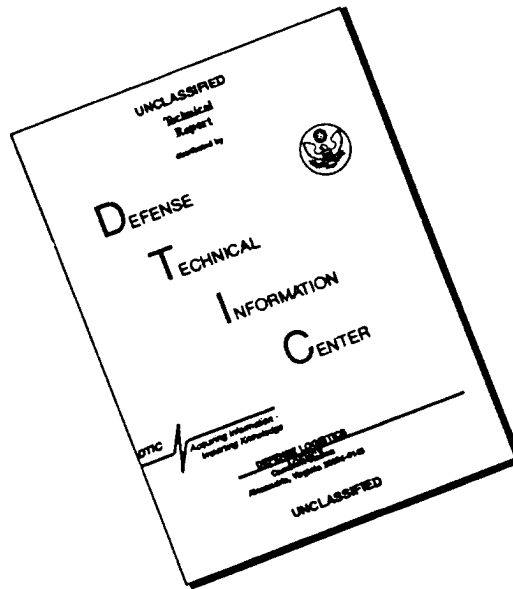
**JUNE 26, 1996**

# DISCLAIMER NOTICE



THIS DOCUMENT IS BEST QUALITY AVAILABLE. THE COPY FURNISHED TO DTIC CONTAINED A SIGNIFICANT NUMBER OF COLOR PAGES WHICH DO NOT REPRODUCE LEGIBLY ON BLACK AND WHITE MICROFICHE.

# DISCLAIMER NOTICE



THIS DOCUMENT IS BEST QUALITY AVAILABLE. THE COPY FURNISHED TO DTIC CONTAINED A SIGNIFICANT NUMBER OF PAGES WHICH DO NOT REPRODUCE LEGIBLY.

# REPORT DOCUMENTATION PAGE

Form Approved  
OMB NO. 0704-0188

1. AGENCY USE ONLY (Leave blank)		2. REPORT DATE January 25 1995		3. REPORT TYPE AND DATES COVERED Final, 1 Oct 91 - 31 Dec 94	
4. TITLE AND SUBTITLE High Resolution Measurements of Mixing and Reaction Processes in Turbulent Flows (U)				5. FUNDING NUMBERS  PE - 61102F PR - 2308 SA - BS G - AFOSR 89-0541	
6. AUTHOR(S)  W.J.A. Dahm					
7. PERFORMING ORGANIZATION(S) AND ADDRESS(ES)  Gas Dynamics Laboratories Department of Aerospace Engineering The University of Michigan Ann Arbor, MI 48109-2118				8. PERFORMING ORGANIZATION REPORT NUMBER  Report No. 026779-12	
9. SPONSORING ORGANIZATION NAME(S) AND ADDRESS(ES)  AFOSR/NA 110 Duncan Avenue, Suite B115 Bolling AFB, DC 20332-0001				10. SPONSORING ORGANIZATION REPORT NUMBER	
11. SUPPLEMENTARY NOTES					
12a. DISTRIBUTION / AVAILABILITY STATEMENT  Approved for public release; distribution is unlimited				12b. DISTRIBUTION CODE	
13. ABSTRACT (Maximum: 200 words)  Fully-resolved, two-, three-, and four-dimensional, spatio-temporal imaging measurements of the fine structure of conserved scalar mixing in turbulent flows are being used to identify new insights into molecular mixing and develop practical models for turbulent combustion. During the past year, the high wavenumber part of the scalar mixing spectrum has been measured and appears to confirm the Batchelor model. However the cutoff wavenumber is found to lie significantly lower than classical theory suggests. We have also obtained the first measurements of the distribution of dissipation layer separations in turbulent flows. These results show a surprisingly simple and potentially insightful -3 power law scaling for scalar mixing that has not yet been explained. A new strained dissipation and reaction layer (SDRL) model has been developed that relates the chemical state of nonequilibrium reaction chemistry to the mixing state of one or more conserved scalar fields. We have coupled this model with our high resolution Rayleigh imaging measurements to predict combustion species concentration and reaction rate fields in turbulent reacting flows. Results from this model show striking agreement with direct species imaging measurements in turbulent combustion, and allow access to species that cannot be measured directly. This new physically-based formulation appears to unify the previous "flamelet" and "distributed" reaction models within a single model capable of treating even deep nonequilibrium combustion.					
14. SUBJECT TERMS  Turbulent Flows; Turbulent Mixing; Turbulent Reacting Flows; Combustion				15. NUMBER OF PAGES  172	
				16. PRICE CODE	
17. SECURITY CLASSIFICATION OF REPORT  Unclassified	18. SECURITY CLASSIFICATION OF THIS PAGE  Unclassified	19. SECURITY CLASSIFICATION OF ABSTRACT  Unclassified	20. LIMITATION OF ABSTRACT  UL		

## 1. Summary of Major Technical Results

This section summarizes some of the most significant technical results found from the work under this grant on the understanding and practical modeling of combustion in turbulent flows.

- A new measurement technique was developed for experimental investigation of the universal, four-dimensional, spatio-temporal, small-scale structure of large Schmidt number conserved scalar mixing in turbulent flows. Measurements were obtained via laser induced fluorescence imaging in conjunction with continuous high-speed acquisition of gigabyte-sized data sets, yielding fully-resolved three- and four-dimensional data for the space- and time-varying conserved scalar field  $\zeta(\mathbf{x}, t)$  and the associated scalar energy dissipation rate field  $\nabla\zeta \cdot \nabla\zeta(\mathbf{x}, t)$  at the small scales of a turbulent flow.
- Measurements were obtained at local outer-scale Reynolds numbers  $Re_\delta$  between 2,600 and 5,000, and local Taylor-scale Reynolds numbers  $Re_\lambda$  ranging from 38 to 52. The resolution achieved reaches below the local strain-limited molecular diffusion scale  $\lambda_D$  in all three spatial dimensions as well as in time.
- The resulting four-dimensional data sets, each comprised of over 3 billion individual point measurements, are simultaneously space- and time-differentiable. Data are in the form of three-dimensional ( $256^3$ ) spatial data volumes which clearly reveal that the entire scalar dissipation field is composed of locally one-dimensional layer-like structures formed into complex patterns by the repeated stretching and folding action of the underlying turbulent flow.
- Numerous structural and statistical features of this small-scale mixing process were investigated, including probability density functions and spectra, which show evidence for weak anisotropy even at the small scales.
- The three-dimensional spatial nature of the data allows the first determination of the three-dimensional scalar energy spectrum  $E_\zeta(\mathbf{k})$ . One-dimensional spatial spectra obtained from these permit comparisons with Batchelor's theory for the high-wavenumber form of the spectrum, and the simultaneous availability of temporal information allows comparisons of temporal and spatial spectra.
- Wavelet analyses motivated by the high degree of internal small-scale intermittency that results from localization of scalar gradients in the layer-like structures yields wavelet spectra and gradient length scale distributions. The latter determines the molecular diffusion layer thickness scaling  $\lambda_D = \Lambda \cdot \delta \cdot Re_\delta^{-3/4} \cdot Sc^{-1/2}$ , with the median value found to be  $\langle \Lambda \rangle \approx 12$  and with the

thickest layers being approximately three times this size.

- The distribution of scalar dissipation layer separations shows lognormal scaling at small separations and a  $-3$  power-law scaling at large separations.
- Results from these detailed imaging studies of passive scalar mixing in turbulent flows have led to a physically-based formulation relating the mixing of conserved scalar fields by the underlying turbulent flow field to the local chemical state. The basis underlying this Strained Dissipation and Reaction Layer (SDRL) formulation is the observation that locally one-dimensional layer-like structures dominate the scalar energy dissipation fields in turbulent reacting flows regardless of the degree of chemical nonequilibrium.
- Results obtained when this strained dissipation and reaction layer formulation is applied to imaging measurements of conserved scalar fields in turbulent flows for conditions ranging from near equilibrium to deep nonequilibrium demonstrate remarkable resemblances with direct PLIF imaging measurements of chemical species under similar combustion conditions. The SDRL formulation inherently produces a predominance of thin (flamelet) mass fraction and reaction rate fields under conditions of relatively weak chemical nonequilibrium, and the natural emergence and dominance of broad (distributed) species concentration and reaction rate fields for increasing equilibrium departures, providing a physical and theoretical framework that reconciles these two widely disparate views of turbulent combustion within a single model.
- A detailed examination of the validity of the SDRL model compared chemical species concentration fields predicted by the SDRL formulation, together with those from the equilibrium and flamelet models, with results from direct numerical simulations (DNS) for Damköhler numbers ranging from near equilibrium to deep nonequilibrium. Results showed substantial improvements by the SDRL model over both the equilibrium and flamelet models, especially under conditions of greatest chemical nonequilibrium.

## 1.1 Introduction and Overview

Work under this AFOSR grant in the Gas Dynamics Laboratories at The University of Michigan involves a combination of experimental, theoretical, and numerical efforts with the following three major objectives:

- (i) to develop and implement new, high-resolution, multi-dimensional, quantitative, imaging capabilities for obtaining direct experimental measurements of the molecular mixing and chemical reaction processes in turbulent flows,

- (ii) to use these new measurement techniques to experimentally investigate the essential physical characteristics of molecular mixing and chemical reactions in turbulent flows, and
- (iii) to incorporate results from these new experimental measurements into practical models of the molecular mixing, chemical reaction, and local extinction processes in reacting turbulent flows of interest for air-breathing propulsion systems.

This Final Report summarizes new insights into the structure and modeling of reacting turbulent flows at the molecular diffusion and chemical reaction scales of the flow obtained during the course of this work. These results have been based on two primary parallel lines of investigation.

The first has involved development and application of a new technique for obtaining fully-resolved four-dimensional spatio-temporal imaging measurements of the small scale structure of conserved scalar mixing in turbulent shear flows. The resulting data characterize the universal high-Reynolds number structure and dynamics of mixing, yielding detailed results for  $Sc \gg 1$ , and comparing with lower-dimensional measurements obtained for  $Sc \approx 1$ . This part of our work has shown that essentially all of the molecular mixing in turbulent shear flows is concentrated on thin, sheet-like, strained laminar diffusion layers having a locally self-similar and universal internal structure. We have also shown why the underlying vorticity field is more complex, consisting of both line-like and sheet-like structures, as well as structures undergoing a transition between these two asymptotic states, whereas the scalar dissipation rate field can sustain only sheet-like structures. This comparative simplicity in the scalar dissipation field allows for relatively simple models of the mixing at the molecular scales in turbulent shear flows, and for a new approach for relating the progress of complex chemical reactions to the molecular mixing process. Results from this part of our work are summarized in §2 of this Final Report.

The second line of investigation has resulted directly from the observation of this structural simplicity at the fine scales of scalar mixing in turbulent shear flows. This has led to the development of a new formulation that relates the local state of nonequilibrium chemistry to the local state of molecular mixing in the underlying conserved scalar field. Termed the "strained dissipation and reaction layer" (SDRL) formulation, this approach is more widely applicable than the "flamelet" model. Results obtained to date show that the SDRL formulation produces thin "flamelet-like" chemical species fields under

a For	
NAI	<input checked="" type="checkbox"/>
cod	<input type="checkbox"/>
ation	<input type="checkbox"/>

Availability Codes	
Dist	Avail and/or Special
A-1	



conditions of relatively low nonequilibrium, as well as the natural emergence and eventual dominance of broad "distributed reaction zones" under conditions of deeper nonequilibrium. OH mass fraction fields produced via the SDRL formulation from experimental conserved scalar fields show remarkable resemblances to OH PLIF measurements under similar conditions. Furthermore, DNS test cases also show that the SDRL formulation is more accurate than the flamelet model, especially under conditions of deep nonequilibrium. This new formulation appears to allow accurate predictions of turbulent combustion chemistry under conditions ranging from near equilibrium to deep nonequilibrium.

In addition to this Final Report and our previous Annual Reports, results have also been described in several technical articles in the refereed archival literature<sup>1</sup>, in several monograph articles, and conference proceedings and presentations<sup>2</sup>.

- 
- <sup>1</sup> Dahm, Southerland & Buch (1991) *Physics of Fluids A* **3**, 1115-1127.  
Tryggvason & Dahm (1990) *Combustion & Flame* **83**, 207-220.  
Chang, Dahm & Tryggvason (1991) *Physics of Fluids A* **3**, 1300-1311.  
Southerland, Porter, Dahm & Buch (1991) *Physics of Fluids A* **3**, 1385-1392.  
Dahm, Su & Southerland (1992) *Physics of Fluids A* **4**, 2191-2206.  
Buch, Dahm, Dibble & Barlow (1992) *Proc. 24th Int'l. Symp. Comb.* 295-301.  
Dahm & Bish (1993) *Turbulence and Molecular Processes in Combustion*, Elsevier Publ.  
Everett, Driscoll, Dahm & Feikema (1993) *Combustion & Flame*, accepted for publ..  
Dahm, Tryggvason & Zhuang (1993) *SIAM J. Appl. Math.*, in review.  
Southerland, Dahm & Dowling (1994) AIAA Paper No. 94-0820, AIAA, Washington, D.C..  
Bish & Dahm (1994) AIAA Paper No. 94-0100, AIAA, Washington, D.C..  
Southerland, Frederiksen, Dahm & Dowling (1994) *Chaos, Solitons & Fractals* **4**, 1057-1089.  
Bish & Dahm (1994) *Proc. 25th Int'l. Symposium on Combustion*, in press.  
Bish & Dahm (1995) AIAA Paper No. 95-0803, AIAA, Washington, D.C..  
Buch & Dahm (1995) *Journal of Fluid Mechanics* in review.
- <sup>2</sup> Dahm, Southerland & Buch (1991) Applications of Laser Techniques to Fluid Mechanics, R. Adrian, Ed., Springer Verlag, Berlin.  
Dahm & Buch (1991) Chemical Reactions and Physical Processes in Turbulent Flows, J. Hunt, Ed., Cambridge University Press.  
Buch & Dahm (1992) Fine Scale Structure of Conserved Scalar Mixing in Turbulent Shear Flows. Sc = 1, Sc ≈ 1, and Implication for Reacting Flows, University of Michigan Report No. 026779-5.  
Dahm (1992) Proceedings of the 13th Symposium on Turbulence, University of Missouri-Rolla, Rolla, MO.  
Dahm (1992) Turbulence and Molecular Processes in Combustion, T. Takeno, Ed., Elsevier.  
Bish, Dahm & Dowling (1993) Proceedings of the 1993 Fall Meeting of the Western States Section of the Combustion Institute, The Combustion Institute, Pittsburgh.  
Southerland & Dahm (1994) A Four-Dimensional Experimental Study of Conserved Scalar Mixing in Turbulent Flows, University of Michigan Report No. 026779-12.

## **2. Structure of Conserved Scalar Mixing in Turbulent Flows**

### *1. Introduction*

The mixing of two or more fluids in turbulent shear flows represents one of the most widely encountered and technically important classes of problems in the fluid sciences. Applications range from the development of new aeropropulsion systems to the reduction of trace species pollutant emissions from industrial combustion processes. Despite the importance of this class of problems, no broadly applicable theory for treating flows involving turbulent mixing currently exists. Often the turbulent mixing process is of primary interest for chemically reacting systems, as in the examples above, where the outcome of a potentially complex set of multi-step chemical reaction kinetics can depend crucially on details of the mixing process at the molecular scales. This is certainly true for systems with high mixing rates that operate far from chemical equilibrium, where the coupling between the reaction chemistry and the mixing state of the flow can be very complex. Development of accurate predictive techniques for dealing with turbulent reacting flow problems of this type requires a physical understanding of the molecular mixing process at the small scales of turbulent shear flows.

It is believed that the quasi-deterministic large scale structures in turbulent shear flows control the entrainment properties of the flow, and that these large structures differ from one flow to another. In contrast, the structure and dynamics of the small scales are believed to be at least quasi-universal, satisfying Reynolds number asymptotics and displaying certain universal scaling properties. Studies of the large scale structure and entrainment properties of turbulent shear flows are thus necessarily flow-dependent, while the mixing at small scales can be investigated in a largely generic context. However, the small scale structure of fully-developed turbulent flows and the mixing processes occurring within them are notoriously difficult to resolve. From the point of view of experimental studies, the microscopically fine lengthscales on which fully three-dimensional spatial variations occur, combined with the exceedingly short time scales on which temporal variations are found, typically frustrate attempts to access the small scales directly. Moreover, a lack of laboratory diagnostic techniques capable of yielding three-dimensional spatial measurements, not to mention simultaneous temporal measurements, has precluded any examination of the gradient fields that are of key interest at the small scales. Such experimental studies have instead been largely confined to single-point time series measurements, from which it can be difficult to infer spatial structure or dynamics.

In recent years, new experimental techniques have evolved that are beginning to permit far more detailed experimental investigations of the small scale structure and dynamics of mixing in turbulent shear flows than have previously been possible. The dense spatial and temporal information that results from these measurement techniques offers a level of resolution and detail that in many ways approaches those achievable in direct numerical simulation (DNS) studies. Moreover, these laboratory measurements allow investigations at certain parameter ranges that exceed those achievable by numerical simulations. The present study belongs to this class of experimental investigations. It is based on fully-resolved, four-dimensional, spatio-temporal imaging measurements of the universal small scale structure of  $Sc \gg 1$  conserved scalar mixing in turbulent shear flows. The goal of this study is to provide insights into the three-dimensional physical structure and dynamics of the scalar mixing process at the small scales in turbulent flows.

### 1.1 Background

In any dynamically passive conserved scalar field  $\zeta(\mathbf{x}, t)$ , the local scalar value can change only through advection of the scalar quantity with the fluid and diffusion relative to the fluid. For a constant scalar diffusivity, the scalar field then satisfies the conservative advection-diffusion equation

$$\left[ \frac{\partial}{\partial t} + \mathbf{u} \cdot \nabla - \frac{1}{ReSc} \nabla^2 \right] \zeta(\mathbf{x}, t) = 0 \quad (1)$$

The mixing process in the resulting conserved scalar field  $\zeta(\mathbf{x}, t)$  can be formulated in terms of the associated scalar energy per unit mass  $1/2 \zeta^2(\mathbf{x}, t)$ , analogous to the kinetic energy per unit mass  $1/2 u^2(\mathbf{x}, t)$ . From (1) the scalar energy follows

$$\left[ \frac{\partial}{\partial t} + \mathbf{u} \cdot \nabla - \frac{1}{ReSc} \nabla^2 \right] \frac{1}{2} \zeta^2(\mathbf{x}, t) = - \frac{1}{ReSc} \nabla \zeta \cdot \nabla \zeta(\mathbf{x}, t) \quad , \quad (2)$$

where the right side gives the local instantaneous rate (per unit mass of fluid) at which scalar energy is irreversibly dissipated by molecular diffusion, and accordingly is termed the "scalar energy dissipation rate." The scalar energy dissipation rate field  $(ReSc)^{-1} \nabla \zeta \cdot \nabla \zeta(\mathbf{x}, t)$  thus gives the local instantaneous rate of molecular mixing at every point in the flow.

The normalization in (1) and (2) is with reference length and velocity scales,  $l^*$  and  $u^*$ , and an arbitrary scalar reference value  $\zeta^*$ . The only resulting dynamical parameter appearing explicitly is the dimensionless scalar diffusivity  $(1/ReSc)$ , where the Péclet number  $ReSc$  is the product of the Reynolds number  $Re \equiv (u^* l^* / \nu)$  and the Schmidt number  $Sc \equiv (\nu/D)$ , with  $\nu$  and  $D$  the vorticity and scalar diffusivities, respectively. However, the velocity field  $\mathbf{u}(\mathbf{x}, t)$  appearing in

these equations introduces a separate Reynolds number dependence through its own transport equation (the Navier-Stokes equation). As a consequence, the scalar field structure in general depends on both  $Re$  and  $Sc$  independently. In turbulent shear flows, if (1) and (2) are normalized with the local outer scales  $l^* \equiv \delta$  and  $u^* \equiv U$  characterizing the local mean shear in the flow, then the resulting local outer-scale Reynolds number is  $Re_\delta \equiv (U\delta/\nu)$  and, when the flow is viewed on these outer scales, the scalar field structure  $z(\mathbf{x}, t)$  will depend on both  $Re_\delta$  and  $Sc$ . However, when the normalization is based on the local inner scales  $l^* \equiv \lambda_v$  and  $u^* \equiv (v/\lambda_v)$ , where for (equilibrium) turbulent shear flows  $\lambda_v \sim \delta \cdot Re_\delta^{-3/4}$  is the local strain-limited vorticity diffusion lengthscale, the resulting inner-scale Reynolds number is unity. In that case, when viewed on the inner scales, the mixing process becomes independent of the outer-scale Reynolds number and depends only on the Schmidt number. This will be true provided the scale separation between the local inner and outer flow scales is sufficiently wide, namely that the local outer-scale Reynolds number  $Re_\delta$  is sufficiently large. Moreover, since the outer variables appear in the governing equations only through  $Re_\delta$ , the mixing process at the small scales will therefore be independent of the outer scale variables, and thus will also be independent of the particular shear flow. In this sense, the fine scale structure of conserved scalar mixing, when viewed on the inner scales of high Reynolds number turbulent flows, is believed to be largely universal, namely independent of the Reynolds number and of the particular shear flow, and depends only on the Schmidt number  $Sc$ .

Of particular relevance to laboratory measurements, the inner (small) scales of turbulent flows at Reynolds numbers sufficiently high for the scale separation to allow this presumed universal structure to form must be compared with the resolution capabilities achievable. Ultimately, the finest experimental resolution attainable places a limit on the highest Reynolds number at which such fine structure measurements can be meaningfully made. In the experimental investigation undertaken here, the objective is to obtain fully resolved measurements of the fine structure scales of the molecular mixing process in turbulent flows at Reynolds numbers that are believed to be high enough for this universality to be approached. In this sense, the overall nature of the fine structure seen here, as well as its detailed features documented in these measurements, are believed to be largely generic to high Reynolds number conserved scalar mixing in turbulent flows, and not specific simply to the particular Reynolds numbers or the particular flows in which the measurements were obtained.

Most previous measurements of the structure of scalar mixing in turbulent shear flows have been based on single-point time series

measurements of the scalar field  $\zeta(t)$ . From these, a mean flow Taylor hypothesis is typically invoked to allow the resulting time derivatives  $\partial\zeta/\partial t$  to be used to estimate the spatial derivative along the mean flow direction. From the resulting approximation for this one component of the scalar gradient vector field, the scalar dissipation is then typically estimated on the basis of a mean isotropy approximation. While it is known that this approximation, and its analog in the kinetic energy dissipation field, can lead to significant inaccuracies, limitations of traditional measurement techniques have dictated this as a basis for analyses of the dissipation field structure. For example, Sreenivasan & Meneveau (1986) and Sreenivasan, Ramshankar & Meneveau (1989) have used this approximation to argue for fractal scaling of the geometric support set on which the resulting dissipation fields are concentrated. Similarly, Sreenivasan (1991) and Meneveau & Sreenivasan (1991) have used the same approach to conclude that multifractal scaling applies to the dissipation fields in turbulent shear flows, and Dowling (1991) and Antonia & Mi (1993) have used this approximation to estimate properties of the scalar dissipation field in a turbulent jet.

In contrast to such time series measurements, multi-dimensional spatial measurements based on the development of new optical techniques over the past decade have led to a number of experimental studies of the structure of conserved scalar mixing. Most of these investigations have examined the topologically simpler large scale features of transitional flows, but have not had the spatial and temporal resolution necessary to resolve the fine scale structure of the conserved scalar fields typical of fully-developed turbulent flows. As a consequence, while such studies have produced useful information on larger flow scales, they have not been designed to allow accurate determination of the true scalar gradient field in fully-developed turbulent flows. There have, however, been a few investigations directed specifically at the small scale structure of mixing in turbulent flows. Yip & Long (1986) have used measurements based on two-dimensional planar laser imaging to yield three-dimensional scalar gradient information by imaging from two parallel and closely spaced laser sheets. However, both the sheet spacing and the pixel separation were significantly larger than the local diffusion scale in the flow. Following a somewhat different approach, Yip, Lam, Winter & Long (1987) and Yip, Schmitt & Long (1988) have swept a laser sheet at very high speed through a turbulent flow, in conjunction with very high speed image acquisition over a short duration, to obtain measurements in up to 16 closely spaced parallel planes. Essentially the same approach has been used by Prasad & Sreenivasan (1990). However, in these measurements the resolution was sufficient only to yield data at comparatively coarse scales of the flow, and the signal quality did not permit accurate differentiation of the resulting data to determine the true scalar dissipation rate fields. Buch (1991) has used very highly resolved imaging

measurements specifically designed to produce high signal quality suitable for direct differentiation to yield the scalar dissipation rate fields at the small scales in  $Sc \gg 1$  and  $Sc \approx 1$  scalar mixing in turbulent shear flows. Those measurements, while spanning only two spatial dimensions, indicated that the scalar dissipation rate fields in both cases consisted entirely of thin, strained, laminar diffusion layers having a locally one-dimensional structure. Results obtained suggested that the thickness of the dissipation layers was a factor of six larger than the classical Batchelor scale.

### 1.2 *Present work*

The present study is aimed at providing the first fully-resolved, four-dimensional, spatio-temporal measurements of the universal small-scale structure of conserved scalar mixing in turbulent flows. It is based on a new technique for measuring the conserved scalar field  $\zeta(\mathbf{x}, t)$  at the small scales of a turbulent shear flow with full spatial and temporal resolution, simultaneously spanning all three spatial dimensions and time, and with sufficiently high signal quality to determine the true scalar gradient vector field  $\nabla\zeta(\mathbf{x}, t)$ . Owing to the fact that the measurements extend simultaneously over all three spatial directions as well as time, there is no need to invoke any Taylor hypothesis or isotropy arguments to determine the scalar energy dissipation rate field  $\nabla\zeta \cdot \nabla\zeta(\mathbf{x}, t)$ .

The scalar field was determined by high-speed imaging measurements of the laser induced fluorescence intensity emitted by the concentration field of a passive water-soluble dye having  $Sc \approx 2075$ , which mixes with undyed fluid in a turbulent shear flow. The measurements were made at a fixed location in the self-similar far field of an axisymmetric turbulent jet at outer-scale Reynolds numbers  $Re_\delta$  in the range 2,600 – 5,000 and with Taylor-scale Reynolds numbers  $Re_\lambda$  ranging from 38 to 52. The Reynolds numbers accessible to these measurements are necessarily limited by the extreme resolution constraints placed on the experiments. Nevertheless, as will be noted later, these values appear to be high enough that the basic structure of the scalar field on the inner flow scale  $\lambda_v$  will have attained its asymptotic high Reynolds number form. As a consequence, the results obtained here are believed to be largely representative of the universal small-scale structure of  $Sc \gg 1$  conserved scalar mixing in all high Reynolds number turbulent shear flows.

Results are presented in the form of individual three-dimensional ( $256^3$ ) spatial data volumes, which clearly show the physical structure of the scalar dissipation field at the small scales, as well as in probability density functions and spectra which quantify various key structural and statistical features of this small-scale mixing process. The nature of these measurements provides detailed

spatio-temporal data of a type that in many ways resembles more the data from direct numerical simulations (DNS) than from traditional experimental measurement techniques. However, unlike DNS studies, the present experiments are capable of addressing the small scale structure of large Schmidt number mixing in turbulent flows. Each experiment produces over 3 billion individual, fully-resolved, point measurements of the scalar field values throughout a four-dimensional space-time domain. Yet owing to the very high resolution of these points, they typically span over only about 3 local outer flow time scales ( $\delta/U$ ). As a consequence, while these measurements provide highly detailed information on the spatial structure and temporal dynamics of the flow, long time statistics are inherently more difficult to obtain. In this sense, these measurements are viewed as complementing traditional single-point time series data, from which spatial structure and gradient information are difficult to obtain, but which provide long time records suitable for statistics of other types of quantities. Similarly, while the present measurements provide very dense and highly resolved three-dimensional spatial information in data volumes as large as  $256^3$ , the need to resolve the smallest scalar gradients within these volumes restricts their physical size to just a few inner flow scales  $\lambda_v$  in each direction. As a consequence, highly detailed spatial information at the dissipative scales of the flow is available, but no access to the inertial range of scales is currently possible. In this sense as well, these measurements are viewed as complementing traditional time series measurements, which have no access to the three-dimensional spatial spectrum, but which can access inertial scales in temporal spectra. These experiments thus provide a unique type of information well suited to the present study, which when viewed in conjunction with results from more traditional laboratory measurements and DNS studies allows a previously inaccessible level of resolution and detail on the structure and dynamics of the  $Sc \gg 1$  scalar mixing process at the small scales of turbulent flows.

## 2. *Experimental technique*

The results reported here were based on a new technique for obtaining fully-resolved, four-dimensional, spatio-temporal laser induced fluorescence measurements of the structure and dynamics of the conserved scalar field at the small scales of turbulent shear flows. All measurements were conducted in the fully-developed self-similar far-field of an axisymmetric turbulent jet at the conditions listed in Table 1. The conserved scalar field  $\zeta(\mathbf{x}, t)$  was determined from the concentration of an inert, water-soluble, passive, laser fluorescent dye (disodium fluorescein) introduced with the jet fluid, which subsequently mixes with ambient fluid in the resulting turbulent flow. For weak aqueous solutions of this dye, the Wilke-Chang method indicates a Schmidt number of 2075. Laser

induced fluorescence from the dye concentration field within a small x-y-z volume in the flow was measured using high-speed, high-resolution, successive planar laser induced fluorescence imaging from a swept laser beam.

## 2.1 Facility

A steady axisymmetric turbulent jet was formed by issuing a weak aqueous disodium fluorescein solution through a 4.9 mm axisymmetric nozzle into de-ionized water in a tank. The nozzle contraction ratio exceeded 300:1 leading to an essentially uniform nozzle exit velocity profile that allows the jet momentum flux  $J$  to be inferred directly from its measured mass flow rate. In the self-similar far field, the local flow width  $\delta$  and mean centerline velocity  $U$  scale with the momentum flux  $J$ , ambient fluid density  $\rho$ , and the downstream location  $x$  as

$$\delta(x) \approx 0.44 \cdot x \quad (3a)$$

$$U(x) \approx 7.2 \cdot (J/\rho)^{1/2} x^{-1} \quad (3b)$$

where the constants are from measurements in the literature (Chen & Rodi 1980). Here  $\delta$  is the full width at which the mean scalar profile drops to 5% of its centerline value. From (3a,b) the local outer-scale Reynolds number  $Re_\delta \equiv (U\delta/\nu)$  that drives the flow remains invariant with  $x$  in the far field. All measurements were made 235 diameters downstream of the jet exit ( $x = 1.15$  m), for which the resulting  $\delta(x) \approx 50$  cm. For comparison, the three-dimensional measurement volume was typically 2.5 cm on each side.

Measurements by Ricou & Spalding (1961) give the total mass flux scaling in the jet far field as

$$m(x) \approx 0.282 \cdot (\rho J)^{1/2} x \quad (4)$$

A small coflow, between 0.6 and 1.2 mm/s depending on the value of  $J$ , was established in the tank to match  $m(x)$  in (4) just downstream of the measurement location, thus preventing recirculation of dyed fluid into the jet. The effect of this coflow is given by the similarity coordinate  $(x/\vartheta)$  for axisymmetric coflowing turbulent jets, where  $\vartheta^2 \equiv J/(\pi \rho_\infty U_\infty^2)$  with  $U_\infty$  the coflow velocity. As  $(x/\vartheta) \rightarrow \infty$  the scaling becomes that of a wake, while  $(x/\vartheta) \rightarrow 0$  recovers the non-coflowing jet scaling. All cases considered here correspond to  $(x/\vartheta) = 0.77$ . Measurements by Biringen (1975) show this to be within the jet-like limit (e.g. Dahm & Dibble 1988). The effect of the coflow is thus negligible and the scaling laws in (3a,b) for the classical axisymmetric turbulent jet apply.

The temperature profile in the tank was measured to insure that stratification effects were negligible (within the 0.1 K resolution of the



thermocouple). Similarly, the temperature difference between the jet and ambient fluids was maintained below 0.1 K. In terms of the Morton length scale this places the measurement location at  $(x/l_M) < 1.7$  for all cases considered, and thus within the momentum-driven jet limit (Papanicolaou & List 1988). To remove any effect of pH variations on the laser induced fluorescence from the dye, the jet and ambient fluids were fixed to  $\text{pH} \approx 11$ .

## 2.2 *Laser induced fluorescence imaging*

A 5W argon-ion laser was operated in multi-line emission mode (see Table 2) to excite the fluorescence. An orange filter [HOYA O(G)] was used to block the Mie scattered light from any particles in the flow. This filter effectively blocks 92% of the light at the longest wavelength (514.5 nm) of the laser, and virtually all of the light at the shorter wavelengths of the remaining laser lines. Near the peak of the dye emission spectrum (at 520 nm) the filter transmits only 19% of the incoming light, but by 540 nm, where the emission is still strong, 78% of the incoming fluorescence intensity is transmitted.

Fluorescence intensity from dye-containing fluid along the path of a swept laser beam was measured with a  $256 \times 256$ -element photodiode array (EG&G Reticon MC9256/MB9000). Fluorescence transmitted through the orange filter was collected by a Vivatar 100mm f-2.8 macro lens operated at full aperture. Figure 1 shows key elements of the data acquisition system assembled to convert and store the serial output from the photodiode array in 8-bit digital format. The array formatter provided a non-interlaced, sampled-and-held output train to the A/D converter. An external clock signal drove the array at pixel rates up to 11 MHz, corresponding to a framing rates up to 120 frames per second. A dual-ported image processor effectively acted as a high speed 16 MB buffer in which segments of the array output data stream were temporarily stored en route to four 823.9 MB capacity disk drives. The 3.1 GB capacity of the disks allowed continuous interleaved acquisition of nearly 200 individual  $256^3$  spatial data volumes, or over 50,000 individual  $256^2$  data planes at the sustained throughput rate of 9.3 MB/sec.

## 2.3 *Beam scanning electronics*

A collimated laser beam was rapidly swept through the measurement volume in a pattern of fast vertical scans and slower horizontal scans synchronized to the imaging array electronics. Beam scanning was accomplished with two fast, low-inertia, galvanometric mirror scanners. For each vertical sweep, the  $256 \times 256$  imaging array captured the fluorescence intensity field emitted from the two-dimensional x-y plane swept by the beam.

A concurrent horizontal sweep effectively stepped this x-y measurement plane through a set of up to 256 increments in the third (z) direction to produce a discrete set of parallel data planes. These planes collectively produced a single three-dimensional spatial data volume containing up to  $256^3$  individual measurement points, as indicated in figure 2. The separations  $\Delta x$  and  $\Delta y$  between points in each plane were set by photodiode array element size and the magnification of the optical system, while the effective separation  $\Delta z$  between parallel planes was set by the interplane spacing and the laser beam diameter.

Once the desired number ( $N_z$ ) of parallel planar beam sweeps had been completed, the beam returned to the original position and the pattern was repeated. A rapid temporal sequence of such three-dimensional spatial data volumes could thus be acquired to produce a four-dimensional spatio-temporal data space. The laser beam diameter and beam sweep rate set the time  $\Delta \tau$  during which each element in the photodiode array was illuminated, effectively determining the temporal resolution of each individual data point. As shown in §2.7, the  $\Delta \tau$  values were typically three orders of magnitude shorter than any relevant fluid dynamical time scale. The elapsed time  $\Delta t$  between acquisition of adjacent parallel spatial data planes was set by the framing rate of the imaging array, and determined the degree to which any measurement was capable of "freezing" the dye concentration field, and thereby determined (in part) the z-differentiability within each three-dimensional spatial data volume. As shown in §2.7,  $\Delta t$  was typically an order of magnitude smaller than the shortest time scale in the dye concentration field. Lastly, the time  $\Delta T$  between acquisition of the same spatial data point in temporally successive three-dimensional spatial data volumes was set by the number of planes  $N_z$  per three-dimensional volume, and effectively determined the time differentiability of the data. For sufficiently small  $N_z$  the resulting data were time-differentiable as well as space-differentiable, producing a genuinely four-dimensional spatio-temporal data space.

#### *2.4 Signal levels*

Accurate differentiability of the resulting experimental data requires sufficiently high signal quality in the original fluorescence intensity measurements. To maximize the overall signal-to-noise ratio, the fluorescence intensity was maximized by operating the laser in multi-line mode. Table 2 gives the relative strengths of each of the laser excitation lines. The resulting multi-spectral excitation, however, complicates the conversion from the measured fluorescence intensity field to the dye concentration field. For any single wavelength  $\lambda_p$ , absorption of beam power by the dye is given by the classical Beer's Law. In multi-line mode, the combined effects of all excitation

wavelengths leads to a modified Beer's Law relating the fluorescence intensity field  $F(\mathbf{x}, t)$  to the dye concentration field  $c(\mathbf{x}, t)$  as

$$F(\xi) = \sum_i P_0 \phi c(\xi) \alpha(\lambda_i) \epsilon(\lambda_i) \cdot \exp \left[ -\epsilon(\lambda_i) \int_0^\xi c(\eta) d\eta \right] . \quad (5)$$

Here  $\xi$  is a coordinate along the beam propagation path,  $c$  is the local molar dye concentration, and  $\epsilon$  is the molar extinction coefficient for each excitation wavelength, with  $\alpha$  the relative laser line strengths in Table 2,  $\phi$  the overall quantum efficiency, and  $P_0$  the reference beam power. The molar extinction coefficients  $\epsilon(\lambda_i)$  in (5) measured for each individual wavelength are given in Table 2. For constant beam power, the fluorescence intensity, even when operating with multiple wavelengths, is linearly related to the dye concentration. In addition the extinction function, a product of the molar extinction coefficient  $\epsilon$  and the concentration  $c$ , is linearly related to the dye concentration for each wavelength. Figure 3a shows this result for the two principle wavelengths (488.0 nm and 514.5 nm), where the slope of each curve gives the molar extinction for that wavelength. Figure 3b gives the result if a single net extinction function is defined for the entire beam. Shown with good agreement is the theoretical result based on the measured line strengths and molar extinction coefficients for the individual wavelengths, demonstrating that the full beam transmission can be accurately determined from the characteristics of its individual components in Table 2. This is essential when accounting for beam attenuation effects in converting the measured fluorescence intensities to the dye concentration field.

The laser beam power and dye concentration combine to set the fluorescence intensity, however (5) shows that increasing the dye concentration  $c$  also increases the beam absorption integral along the propagation path, and thus reduces the local power at the measurement location. The radial location in the jet at which the fluorescence intensity is maximized can range from the centerline to the outer edge of the flow depending on the mean dye concentration, and the resulting peak fluorescence intensity increases as this maximum moves increasingly outward along the jet radius. The center of the measurement volume was thus chosen halfway along the jet radius ( $r/x = 0.11$ ), near the location of maximum mean shear based on the mean velocity profile. For this radial and axial position of the measurement volume, there is a single dye concentration at the jet exit that maximizes the mean fluorescence intensity. From (5), for low dye concentrations the attenuation becomes negligible and the fluorescence intensity becomes proportional to the dye concentration, but the fluorescence signal is weak. Conversely, for high concentrations the dye medium absorbs most of the laser power, again producing a weak net fluorescence intensity. These two competing influences lead to an optimal dye concentration that maximizes the fluorescence intensity, found by maximizing

$F(\xi)$  in (5) for the mean radial dye concentration profile  $c(\xi)$ .

### 2.5 Signal-to-noise ratio

Noise sources in the photodiode array include those that depend on the incident light intensity and those that do not. The latter, dominated by the "dark" current from thermal (Johnson) noise in the photodetector and associated electronics, is independent of the signal level  $S$ . When this noise source is dominant, the absolute noise level  $N$  is constant and thus the resulting signal-to-noise ratio ( $S/N$ ) increases linearly with the measured signal level. In contrast, photon shot noise increases with the illumination level, producing an rms noise level proportional to the square root of the signal level. Noise levels in the imaging array were determined by acquiring data from a nominally uniform illumination source at eight different lens aperture settings. Figure 4a gives the resulting distributions of 8-bit digital signal values obtained for each illumination level, with the corresponding noise distributions shown in figure 4b. The noise distributions at the four lowest signal levels in figure 4a collapse well to a single curve, for which the width in figure 4b (the rms noise level) is constant. The remaining curves in figure 4b, corresponding to higher average signal levels, increasingly deviate by broadening and becoming asymmetric. The broadening of these distributions reflects the increasing noise level. Note, however, that even in the worst case the rms noise level is less than 1.25 digital signal levels out of the 256 levels discernible with 8-bit measurements. The rms noise level (width) from each of the distributions in figure 4b is shown in figure 5, giving the scaling of the signal-to-noise ratio ( $S/N$ ) with the mean digital signal level. The result clearly shows the transition from dark noise-limited measurements below digital signal levels of about 50, identifiable by the characteristic  $(S/N) \sim S^1$  scaling, to the shot noise-limited regime with the characteristic  $(S/N) \sim S^{1/2}$  scaling for signal levels above about 150. The actual fluorescence intensity measurements typically span the full 256 digital signal levels under the same operating conditions, and thus range from camera noise-limited to shot noise-limited. However, the result in figure 5 shows that when the signal level is maximized, the  $S/N$  ratio is slightly over 200, and even at the mean digital signal level of 50 the resulting signal-to-noise ratio is still above 65.

### 2.6 Resolution requirements

The smallest spatial and temporal scales ( $\Delta x$ ,  $\Delta y$ ,  $\Delta z$ ,  $\Delta t$ , and  $\Delta T$  in §2.3) resolved by these measurements must be compared with the finest local spatial and temporal scales on which gradients can exist in the turbulent conserved scalar field. The smallest gradient lengthscales in the underlying turbulent flow are set by a local competition between the thinning effect of the most

compressive principal strain rate  $\epsilon$  and the broadening by the diffusivity  $\nu$  (see §6). These establish an equilibrium strain-limited vorticity diffusion length scale (the inner scale)  $\lambda_\nu \sim (\nu/\epsilon)^{1/2}$ , closely related to the Kolmogorov scale, giving the finest length scale on which spatial gradients in the vorticity can be locally sustained in the flow (e.g. Burgers 1948, Townsend 1951). A similar competition between the effects of strain and molecular diffusion of the scalar establishes a local strain-limited molecular diffusion scale  $\lambda_D \sim (D/\epsilon)^{1/2}$ , related to the Batchelor scale and giving the smallest length scale on which spatial gradients in the conserved scalar field can be sustained (e.g. Carrier, Fendell and Marble 1975). The ratio of vorticity and scalar diffusivities establishes the relation between these two strain-limited diffusion length scales as  $\lambda_D = \lambda_\nu \cdot Sc^{-1/2}$ .

Classical inertial range arguments give the highest local strain rates in terms of the local outer-scale Reynolds number as  $\epsilon \sim (U/\delta) \cdot Re_\delta^{1/2}$ . The smallest strain-limited diffusion length scale in the conserved scalar field is then related to the local outer scale  $\delta$  as

$$\lambda_D \sim \delta \cdot Re_\delta^{-3/4} \cdot Sc^{-1/2}, \quad (6)$$

with the accompanying small-scale time

$$(\lambda_D/u) \sim (\delta/u) \cdot Sc^{-1/2} Re_\delta^{-3/4}. \quad (7)$$

where the constant in (6) and (7) will be referred to as  $\Lambda$ . The precise definition for the scalar gradient lengthscale  $\lambda_D$  in (6) is from the scalar dissipation profile across the layers seen in §3 to dominate the small scale mixing process, as the distance along the local layer normal between the points where the dissipation drops to 20% of the profile maximum value. Some indirect estimates suggest  $\langle \Lambda \rangle$  values as high as 25 (e.g. Dowling & Dimotakis 1990) and  $\langle \Lambda \rangle \approx 15$  can be obtained from measurements by Dowling (1991). More recent direct measurements by Buch (1991) suggest a value of  $\langle \Lambda \rangle \approx 11.2$ . For conservatism the latter estimate will be used here, though one of the goals of this study is to obtain an independent assessment of this constant.

## 2.7 Spatial and temporal resolution

The resolution requirements  $(\Delta x, \Delta y, \Delta z) \ll \lambda_D$  and  $\Delta t \ll (\lambda_D/u)$  must be satisfied to allow meaningful differentiation in all three directions within each three-dimensional spatial data volume to determine the scalar gradient vector field  $\nabla \zeta(\mathbf{x}, t)$ . Furthermore, if the resulting data are to be time-differentiated as well between successive three-dimensional spatial data volumes, then the additional temporal resolution requirement that  $\Delta T \ll (\lambda_D/u)$  must also be met. These requirements ultimately limit the highest  $Re_\delta$  values at which such fully-

resolved measurements are possible. While the demands on  $\Delta x$  and  $\Delta y$  can in principle be satisfied by reducing the image ratio, the resolution  $\Delta z$  is determined by the laser beam thickness and the interplane spacing. The laser beam thickness was larger than the desired spatial separation between planes, however since the time  $\Delta t$  between planes was small enough that the scalar field was effectively frozen, the overlap in the measured scalar field between adjacent planes represents a convolution of the true scalar field with the laser beam profile. The measured scalar field was thus deconvolved with the measured beam profile shape to produce an effective resolution  $\Delta z$  comparable to the spatial separation between adjacent data planes. Note that this overlap extends only to the next adjacent data plane on either side, so that the effect of this deconvolution is relatively small.

For the conditions in Table 1 and the outer flow scalings in (3a,b), (6) gives the local strain-limited molecular diffusion lengthscale estimates  $\lambda_v$  and  $\lambda_D$  in Table 3. These  $\lambda_D$  values must be compared with the corresponding  $\Delta x$ ,  $\Delta y$ , and  $\Delta z$  values given to assess the relative spatial resolution. Note that  $(\Delta x/\lambda_D)$  and  $(\Delta y/\lambda_D)$  range from 0.51 to 0.30, and the interplane spacing  $(\Delta z/\lambda_D)$  varies from 0.47 to 0.24. The characteristic pixel image volume dimension  $(\Delta x \cdot \Delta y \cdot \Delta z)^{1/3}$  is thus typically about 3 times smaller than  $\lambda_D$ , with its maximum dimension ( $\Delta z$ ) typically 2 times smaller than  $\lambda_D$ , indicating that all cases considered here are fully resolved in all three spatial dimensions. Additionally, the measured  $1/e$  laser beam diameter is in all cases less than  $0.74\lambda_D$ , though as noted above the effect of this is largely removed by deconvolving the measured data with the beam profile. Depth-of-field measurements show that the resolution is typically degraded by only a factor of 1.6 at the front and back planes of the  $256^3$  three-dimensional spatial data volumes.

As a test of these spatial resolution estimates, figure 6 presents a "grid refinement" procedure based on the actual measured scalar field values, and compares the results with various models for the dissipation field. Specifically, the abscissa gives the resolution in terms of the number of pixels per diffusion scale, namely  $(\Delta x/\lambda_D)$ , while the ordinate is the fraction of the total scalar dissipation that results from differentiation of data at that resolution scale. The solid curve is the theoretical result for a single, isolated, one-dimensional, scalar dissipation layer with scalar endpoints  $(\zeta^+, \zeta^-) = (0, 1)$  having the classical strain-limited error function profile (see §6.1). The long-dashed curve incorporates variations in the scalar endpoints  $(\zeta^+, \zeta^-)$  using the measured distributions from §6.2. The short-dashed curve further reflects the effects of the varying layer thicknesses from the measured distribution in §5.4. The latter provides a one-dimensional model that best represents the actual three-dimensional turbulent scalar fields. The symbols in figure 6 show the effects of successive resolution

degradations applied to two of the measured scalar field data volumes shown in §3. The scalar field data were averaged over the scale indicated and used to compute the scalar dissipation fields. To interpret figure 6, note first that there is relatively good agreement between the short-dashed model and the experimental data over the entire range of grid refinements. Since the horizontal locations of the data points are set entirely by the resolution estimates in Table 3, this agreement suggests that the  $\lambda_D$  values are quite accurate. Additionally, these results allow the experimental resolution requirements to be more precisely understood. Note that, irrespective of the model chosen, the results indicate that an experimental measurement capable of detecting 98% of the total scalar dissipation would require at least 10 pixels per diffusion scale. On the other hand, a measurement with only two pixels per  $\lambda_D$  would still recover over 75% of the total dissipation, but a measurement with resolution ten times coarser than the local diffusion scale would detect less than 1% of the dissipation. At the actual resolution level of the measurements shown, these experiments detect roughly 80% of the total dissipation.

Table 4 gives the time scale estimates ( $\lambda_D/u$ ) for each of the cases considered, together with the  $\Delta\tau$ ,  $\Delta t$ , and  $\Delta T$  values of the measurements. In all cases, the pixel illumination time  $\Delta\tau$  is never larger than 0.004 ( $\lambda_D/u$ ). Moreover, the interplane time  $\Delta t$  is typically 0.07 ( $\lambda_D/u$ ), and even in the worst case  $\Delta t$  is never larger than 0.14 ( $\lambda_D/u$ ), indicating that the scalar field between parallel planes is effectively "frozen". For cases R0420, R0628, and R0811, the smaller number of z-planes per volume insures that the intervolumetric time  $\Delta T < (\lambda_D/u)$ , so in these cases the measured scalar field is time-differentiable as well.

## 2.8 Data reduction

The measured fluorescence intensity data  $F(\mathbf{x},t)$  is converted to the true dye concentration field  $c(\mathbf{x},t)$ , and then to the conserved scalar field  $\zeta(\mathbf{x},t)$ . Non-uniformities in the imaging array and optical system are first removed by dividing the fluorescence intensity data by a measured transfer function  $h(\mathbf{x},y)$ , obtained from the fluorescence in a uniform dye concentration field. The convolution noted in §2.3 between adjacent spatial data planes can be written as a linear system in which the radial power profile of the beam is represented by a diagonal matrix. In practice the interplane spacing  $\Delta z$  was set relative to the beam diameter, so the resulting convolution matrix was essentially tri-diagonal; i.e. all off-diagonal terms except for the first are virtually zero due to the gaussian rolloff of the beam profile. This reduces the convolution to a tridiagonal matrix equation, which was inverted to obtain the deconvolved fluorescence intensities at all but the front and back planes in each volume.

Conversion of the deconvolved fluorescence intensity field to the

underlying dye concentration field requires correcting for the laser beam attenuation via (5). If the instantaneous dye concentration and beam power were known at some point in each row of every plane, then the integral correction could be precisely implemented. However since the attenuation is an integral effect and the path length is long relative to the scale  $\lambda_D$ , the integrated attenuation is roughly constant. On this basis it is assumed that the beam power entering the measurement volume is constant, and that the dye there is at the local mean dye concentration, establishing reference values from which the attenuation within the measurement volume could be corrected. As a test of this procedure, figure 7a shows the mean measured fluorescence intensity profile across the image volume for two typical cases. Figure 7b gives the corresponding fully-corrected mean dye concentration profiles, with the dotted line showing the theoretical mean profile across the measurement volume. The two corrected profiles follow this mean profile well, with remaining variations presumably due to a lack of complete statistical convergence of the mean profiles.

### 3. *Small scale structure*

Detailed measurements of the small scale structure of conserved scalar mixing in turbulent flows were obtained as outlined in the previous section for each of the cases listed in Table 1. Together these comprise over 20 billion individual point measurements. The results presented here are from analyses of typically one-fifth of the data in each case considered.

#### 3.1 *Two-dimensional intersections*

Figures 8a-c show the measured scalar field data  $\zeta(\mathbf{x}, t)$  in three adjacent, parallel, two-dimensional conserved scalar data planes, separated by a distance  $\Delta z$ , from a single three-dimensional spatial data volume. A total of 256 such individual spatial data planes are stacked as indicated in figure 1 to create each of the three-dimensional  $(256^3)$  spatial data volumes. Nearly 200 such three-dimensional spatial data volumes are acquired in each such case. The axes indicate the orientation and size of these data planes in terms of the local strain-limited vorticity diffusion lengthscale  $\lambda_v$ . As noted in §2.1, the measurement volume was more than 20 times smaller than the local outer scale  $\delta$ . The 256 different color levels give the scalar field value  $\zeta$  at each data point, with pure blue beginning at  $\zeta = 0$  corresponding to pure ambient fluid, and with pure red denoting the highest 0.1% of scalar values seen in that particular data volume.

The nearly imperceptible change in the scalar field structure from one plane to the next in figures 8a-c is a result of the very high spatial resolution. The



three-dimensional spatial nature of these data thus allows differentiation within each plane and between adjacent planes to determine the true scalar gradient vector field  $\nabla\zeta(\mathbf{x},t)$ . Note that all derivative fields presented here were obtained by direct linear central differencing of the measured scalar field data, with no explicit smoothing or filtering applied to any of the results. The resulting scalar energy dissipation rate field  $\nabla\zeta \cdot \nabla\zeta(\mathbf{x},t)$  in the central plane in figures 8a-c is shown in figure 8d. Since the range of scalar dissipation rates in the flow is very wide, the logarithm of the dissipation rate is shown. In this case, the colors denote logarithmically increasing dissipation rates, with the lowest level colored black and denoting zero and very low dissipation rates, with the remaining 255 colors ranging from pure blue through pure red denoting logarithmically increasing dissipation rates. Although effects of noise can be seen in the resultant scalar dissipation field in figure 8d, the relatively smooth fields obtained reflect the high resolution and signal quality attained in the original scalar field measurements.

While the structure of the scalar dissipation rate field at the small scales of turbulent flows is considered in detail below, the basic nature of this structure is evident even in figure 8d. Since this plane shows a two-dimensional intersection through the true three-dimensional scalar dissipation field, the layer-like dissipation features seen represent intersections with a highly convoluted surface around which essentially all of the dissipation is concentrated. Note that variations in the dissipation field along the local normal to this surface far exceed those along the local tangential directions.

The individual scalar gradient vector component fields that form the dissipation rate field in figure 8 are shown in figures 9a-c. Since these component fields can take on both positive and negative values, a pure yellow coloring is used to denote zero values, with colors from yellow through blue denoting negative values, and yellow through red denoting positive values. Note that the individual derivative fields are relatively noise-free, with most of the noise present in the y-derivatives in figure 9b, presumably from imperfections in the laser beam sweep. Figure 9d gives the resulting linear scalar dissipation rate field in the same intersection plane for comparison with figure 8d. This linear representation does not allow the underlying structure in the dissipation field to be as readily discerned as the logarithmic form in figure 8d, but allows the highly intermittent nature of the dissipation field to be more readily seen. In particular, note that high values of the scalar dissipation, corresponding to yellow and red colorings in figure 9d, are relatively rare, while blue colorings denoting low dissipation rates are very common. The distribution of dissipation rates is determined from these measurements in §5.

While figures 8*d* and 9*d* show the magnitude of the scalar gradient vector field, the respective gradient vector component fields in figures 9*a-c* allow the scalar gradient vector orientation field to be determined in terms of the spherical orientation angles  $\vartheta$  and  $\phi$ . The former represents the angle between the positive x-axis and the projection of the scalar gradient vector into the x-y plane, while the latter gives the angle between the scalar gradient vector and the positive z-axis, namely

$$\vartheta \equiv \tan^{-1} \left( \frac{\partial \zeta / \partial y}{\partial \zeta / \partial x} \right) \quad (8a)$$

$$\phi \equiv \cos^{-1} \left( \frac{\partial \zeta / \partial z}{|\nabla \zeta|} \right) \quad (8b)$$

Figure 10 shows the orientation fields  $\vartheta(\mathbf{x}, t)$  and  $\phi(\mathbf{x}, t)$  for the same intersection plane in figures 8 and 9. The color assignments for  $\vartheta$  in figure 10*a* use yellow to denote zero, with values from zero to  $+\pi$  ranging from yellow through red, and with yellow through blue corresponding to zero to  $-\pi$ . The apparent blue-red discontinuities in the  $\vartheta$  field occur where the scalar gradient vector orientation switches from  $+\pi$  to  $-\pi$ , though the orientation field remains continuous. Black denotes points where the magnitude of the gradient is too small to accurately determine the vector orientation. The  $\phi$ -field is shown in figure 10*b*, where the color map begins at blue representing zero, for which the gradient vector points outward normal to the intersecting plane, and increases uniformly to red representing  $\phi = \pi$ , for which the gradient vector points directly into the intersecting plane.

Note that with the exception of the jump in color between  $+\pi$  to  $-\pi$  in the  $\vartheta$  field, the scalar gradient vector orientation field in figure 10*a,b* changes over a much larger length scale than does its magnitude seen in the scalar dissipation fields in figures 8*d* and 9*d*, in apparent agreement with the estimates for the vorticity and scalar gradient lengthscales  $\lambda_D$  and  $\lambda_v$  in Table 3 and the figure axes. Owing to the scalar field dynamics, the scalar gradient vector tends to align in the direction of the most compressive principal strain rate axis, which varies on the scale of the vorticity diffusion lengthscale  $\lambda_v$ . This appears to be consistent with the scale of variations in color patterns and the axis scales in figures 10*a,b*. Unlike the orientation field, the scalar gradient magnitude field (the scalar dissipation) should vary on the lengthscale  $\lambda_D$ , and this too appears to be verified by the data in figures 8*d* and 9*d*.

### 3.2 Three-dimensional data volumes

Figures 11 – 13 give examples of experimentally measured three-

dimensional spatial structure in the conserved scalar fields and scalar energy dissipation rate fields at the small scales of the turbulent flow. In each case, part (a) shows the scalar field  $\zeta(\mathbf{x}, t)$ , part (b) shows the corresponding scalar energy dissipation rate fields  $\nabla \zeta \cdot \nabla \zeta(\mathbf{x}, t)$ , and the logarithm of the dissipation rate fields,  $\log_{10} \nabla \zeta \cdot \nabla \zeta(\mathbf{x}, t)$ , are shown in part (c) of each figure. These figures are constructed by assembling 256 parallel planes of the type discussed in §3.1. The color assignments used to denote In each of these figures, the axes indicate both the orientation and spatial extent of the data volumes in terms of the local strain-limited vorticity diffusion lengthscale  $\lambda_v$ , obtained as described in §2.7. Note that no consistent directional preferences are readily apparent in these data, suggesting that the mixing process at these small scales is at least approximately isotropic. Slight anisotropies consistent with the orientation of the principal axes of the mean strain rate field will, however, be revealed by detailed numerical analyses in §5 and §6.

These logarithmic forms reveal that practically all of the scalar dissipation field, even at the very low levels, is confined to thin, strained, laminar, sheet-like diffusion layers. Such layers were originally envisioned by Burgers (1948) and Townsend (1951) as a consequence of the strain-diffusion competition in the spatially uniform local strain rate field that must result in a Lagrangian frame tied to any material point (see §7.1). Buch (1991) used two-dimensional imaging measurements to conclude that all of the scalar dissipation occurs within such sheet-like structures, rather than the line-like structures that result from a locally axisymmetric and compressive principal strain rate field. That conclusion was based on the observation that no circular dissipation structures were seen in the two-dimensional data. The missing scalar gradient component in any two-dimensional measurement would miss dissipation structures resulting from scalar gradients pointing normal to the measurement plane. However, the three-dimensional nature of the present measurements insures that all dissipation structures can be discerned. Notice that, whereas some dissipation layers may not appear sheet-like where they intersect a two-dimensional surface (such as the cube faces), when viewed in three dimensions these can be seen to be sheet-like structures.

The continual stretching and folding of these scalar dissipation sheets by the underlying strain rate and vorticity fields in the turbulent flow maintains both the scale and topology of these structures. These aspects of the small scale structure are analyzed in subsequent sections. For the present purposes, it is important to point out that this same stretching and folding, when viewed on the outer scales of the flow, leads to the entrainment of ambient fluid into the turbulent jet. Subsequent repetitions of this dynamical process leads to a reduction in scale of this entrained ambient fluid, and molecular mixing with the

mixed fluid already in the jet. Note, however, that at this radial location in the jet, the self-similar entrainment mechanism is capable of bringing large regions of ambient fluid into the measurement volume. Examples of this can be seen in many of the data volumes resulting from these measurements (e.g. see figure 17). Within these relatively large regions of ambient fluid, the conserved scalar and scalar gradient (dissipation) values are both zero. Gibson (1968) has postulated that zero gradients are limited to isolated points in turbulent flows, however when entrainment is present then this becomes an additional source for zero gradient regions. The joint statistics of the conserved scalar and scalar dissipation fields will be considered in §5 and §7.

#### 4. *Scalar and dissipation field statistics*

Measurements of scalar field statistics for large Schmidt number scalar mixing are relatively rare. This section presents results for various single-point probability density functions associated with the conserved scalar field and its gradients. These serve to quantify details of the fundamental structure of the scalar mixing process noted in §3.

##### 4.1 *Scalar field statistics*

Single-point scalar field statistics in turbulent jets have been reported from a number of previous investigations (e.g. Antonia, Prabhu & Stephenson 1975; Becker, Hottel & Williams 1967; Birch *et al* 1978; Chevray & Tutu 1978; Lockwood & Moneib 1980). These allow comparisons with, and partial validation of, the present measurements. However the present resolution is higher than in prior investigations, and thus it is equally interesting to look for differences that may be attributable to the higher resolution.

Figure 15 shows the probability density function (pdf) of the conserved scalar field  $\zeta(\mathbf{x}, t)$  at the  $(r/x) = 0.11$  measurement location for two different cases. Note that this radial location in the axisymmetric turbulent jet is at the point where the mean flow strain rate (e.g. Wygnanski & Fiedler 1969) and scalar fluctuation level (e.g. Becker, Hottel & Williams 1967) are highest. The pdf's obtained for the two cases shown agree quite well, though there are some differences apparent. It appears unlikely that these result from the small difference in Reynolds number (see Table 1), but rather are due to incomplete statistical convergence of the scalar field pdfs. Statistics presented for each of these two cases are from analyses of typically 30 complete  $256^3$  spatial data volumes, each spaced  $3 \Delta T$  apart, and comprising nearly 500 million data points. However, these volumes span a time interval slightly less than 3 local outer flow time scales ( $\delta/U$ ), whereas typically ten or more outer time scales are required to

obtain essentially converged statistics.

Putting the small differences in figure 15 aside, both the general shape and width of the pdfs are remarkable. The area under the spike near  $\zeta = 0$  accounts for a significant fraction of the pdf – approximately 15% of the fluid at this location is at concentrations less than one-tenth of the local mean value. Previous measurements of the  $Sc \gg 1$  pdf at this location in turbulent jets (e.g. Dahm & Dimotakis 1990) show a spike that accounts for a significantly smaller fraction of the fluid. Indeed the entire pdf in figure 15 has a different shape than results from previous investigations of large  $Sc$  mixing in jets. These differences appear directly attributable to the lower spatial resolution of earlier investigations. In particular, prior measurements of the pdf show a broad peak centered near the local mean scalar value, with a small spike near the ambient fluid value. The present results show no peak at the mean value, and show more fluid at extremely low and high concentrations. The most highly resolved of prior measurements (Dahm & Dimotakis 1990) give the maximum scalar value as 2.4 times the local mean at this radial location whereas the present results show the highest scalar values in excess of four times the local mean. Consistent with these differences in the maximum scalar values, prior results for the scalar fluctuation levels from  $Sc \gg 1$  mixing in turbulent jets yield a normalized scalar variance at this radial location no higher than 0.68 (Antonia *et al* 1975). By comparison, the pdfs in figure 15 give normalized variances of 1.06 and 1.08. These differences in the pdf shape and its moments are both consistent with the higher level of resolution in the present measurements. However some of the differences may also be attributable to the corrections for laser beam attenuation. It is possible to discern between these explanations by examining measurements of Dahm & Dimotakis (1987) that indirectly determine the peak scalar value.

Specifically, these authors used a fast, reversible chemical reaction based on the pH sensitivity of laser induced fluorescence from disodium fluorescein dye to measure the axial distance required to molecularly mix all the jet fluid with ambient fluid to at least a given level. This corresponds to the distance required for the fluorescence to completely disappear (the “flame length”), which is both an extremely sensitive measure of the maximum scalar value and a relatively simple quantity to measure accurately. Changing the pH in the jet and ambient fluids showed the mean flame length  $L$  to vary with the acid-base stoichiometric mass ratio  $\phi$  as  $L/d^* \approx 10 \phi$ , and that the maximum fluctuating flame length was 1.33 times the mean. Here  $\phi = (1/\zeta_s) - 1$  where  $\zeta_s$  is the stoichiometric conserved scalar value. The maximum flame length for any  $\phi$  gives the largest  $x$  at which  $\zeta_s$  will be found, thus the  $x$  at which  $\zeta_{max} = \zeta_s$  is  $(x/d^*) = 13.3 [(1/\zeta_s) - 1]$ . Measurements (Dahm & Dimotakis 1990) show the maximum scalar values on

the jet centerline at  $(r/x) = 0$  and at all other radial locations to be the same, with  $\langle \zeta \rangle_{(r/x)=0} = 5.7 (x/d^*)^{-1}$ . Thus the maximum to mean conserved scalar ratio on the jet centerline is  $(\zeta_{\max}/\langle \zeta \rangle)_{(r/x)=0} = 2.33$ , and from the radial similarity profile (e.g. Dahm & Dimotakis 1987) the ratio of the mean scalar values on the centerline and at  $(r/x) = 0.11$  is 2.0, giving the ratio of maximum to mean conserved scalar values at the location in figure 15 as  $(\zeta_{\max}/\langle \zeta \rangle)_{(r/x)=0.11} = 4.6$ . This effectively infinitely-resolved value of the maximum scalar value is in good agreement with the results in figure 15. This suggests that differences between previously reported pdfs for  $Sc \gg 1$  conserved scalars and the present result are due primarily to the higher spatial resolution in the present study.

#### 4.2 Scalar gradient and dissipation statistics

In addition to the higher spatial and temporal resolution, the three- and four-dimensional nature of the present measurements allows all components of the scalar gradient vector field  $\nabla \zeta(\mathbf{x}, t)$  to be determined directly. Figure 16a shows the pdf of the true scalar energy dissipation rate field for the same two cases considered above. Note that, as can be seen from the dissipation fields in figures 11-13, most of the dissipation values are concentrated near zero, with high dissipation rates being rare. This intermittent character of dissipation fields in turbulent flows has been known since the earliest measurements of Batchelor & Townsend (1949). Classical theories of turbulence (e.g. Kolmogorov 1962) suggest a lognormal distribution for dissipation variables to account for this intermittency. Figure 16b shows the pdf of  $\log_e \nabla \zeta \cdot \nabla \zeta(\mathbf{x}, t)$  for the same two cases as in figure 16a, and there is some indication of an at least roughly lognormal distribution at large dissipation rates. For this reason, the pdf for case R0703 is compared with a true lognormal distribution having the same first two moments in figure 16c. Owing to the limited digital resolution of the measurements, the range of dissipation rates that can be distinguished does not allow accurate assessment of the distribution at very low values. However, for relatively high values it can be seen that the lognormal distribution gives a relatively good representation of the pdf.

Figures 17a,b show the joint probability density of the resulting joint distributions of conserved scalar and scalar dissipation rate for the same two cases considered above, with the contours increasing logarithmically. The joint densities verify that the scalar and its dissipation rate are nearly statistically independent. These also show that points in the flow with either very high or low scalar values tend to have low dissipation rates, with the highest dissipation rates typically at points with approximately 80% of the mean scalar value, in good agreement with the estimated results of Anselmet & Antonia (1985).

These joint pdfs also allow the conditional statistics of the scalar dissipation field to be determined. Such conditional dissipation statistics are central to conditional moment closure models of reacting turbulent flows (e.g. Bilger 1993, Mell, Nilsen, Kosály, & Riley 1994). Figures 18*a,b* show the resulting conditional mean and variance obtained from these measurements. The two curves for the conditional variance agree quite well, however there are differences in the results obtained for the conditional mean. Both curves in figure 18*a* increase monotonically and roughly linearly with increasing scalar values. At high scalar values the curves become choppy due to the scarcity of points having simultaneously large values of the scalar and dissipation rate. While it is apparent that, at the absolute maximum conserved scalar value, the conditional mean dissipation rate must be zero, this drop in the curve apparently must occur very abruptly in the far tail of the conserved scalar pdf, where the result becomes statistically irrelevant. Putting aside the limiting form of the conditional statistics at these very large scalar values, it is possible to understand the shape of these curves based on the fundamentally layer-like topology of the scalar dissipation field apparent in figures 11-13. This is done in §6, where the joint pdf of the scalar and dissipation rate are formulated in terms of self-similar distributions for the layer endpoints  $\zeta^+$  and  $\zeta^-$ .

#### 4.3 *Scalar derivatives*

Figures 19*a,b* give the probability densities for the individual scalar gradient vector component fields  $\partial\zeta/\partial x_i(\mathbf{x},t)$ . The joint pdfs between each pair of scalar gradient vector components are shown in figures 20*a-c*. One of the features of interest in figures 19*a,b* is the scaling of the tails of these distributions at very large positive and negative derivative values. Unless these tails are exponentially decreasing, moments of the distribution above some order will become divergent. Certain descriptions of the internal intermittency at the small scales of turbulent flows lead to predictions of nondiverging moments only up to finite order, and thus it becomes important to examine the scaling at large gradient magnitudes. Note that exponential tails in these distributions would appear as straight lines for the semi-logarithmic axes shown. There are indications of an approach to exponential scaling in the results figures 19*a,b*, however owing to the rare occurrence of very large gradient magnitudes, the statistics in the tails converge only very slowly. For a perfectly isotropic scalar field, the distributions of all three gradient vector components in figures 19*a,b* would be identical, yet there are small differences discernible (note that the vertical axis is logarithmic). Moments of each of these pdf's, when normalized with the inner scales  $\lambda_D$  and  $\langle\zeta\rangle$ , show the rms gradient in the x, y, and z directions to be, respectively, 0.20, 0.18 and 0.25 for case R0703 in figure 19*a* and 0.19, 0.21 and 0.24 for case R0806 in figure 19*b*. The consistently higher gradient

magnitude in the z-direction appears to result from (i) small motion in the scalar field between successively acquired planes in the three-dimensional data volume, (ii) errors incurred in the deconvolution procedure, which is an inherently noise-amplifying process, and (iii) possible systematic errors that underestimate the interplanar spacing  $\Delta z$ . A mean flow correction is introduced in §4.4 to partly account for the effect in (i) by assuming that the scalar field is frozen and moves with the mean velocity.

#### 4.4 Gradient vector orientations

A different view of anisotropy in the scalar gradients is shown in figures 21a,b, which show the probability densities for the angles  $\vartheta$  and  $\phi$  giving the orientation of the scalar gradient vector field  $\nabla\zeta(\mathbf{x},t)$ , as shown in figure 10. In an isotropic scalar field, owing to the fact that the scalar gradient vector points in all directions with equal probability, the pdf of  $\vartheta$  will be constant at the value  $1/(2\pi)$ , while the spherical geometry requires the pdf of  $\phi$  to vary sinusoidally as  $1/2 \cdot \sin(\phi)$ . These isotropic distributions are compared with the measured  $\vartheta$  and  $\phi$  distributions for the same cases considered in figure 19. The very sharp, narrow peaks located in both the  $\vartheta$  pdf's at  $-\pi, -\pi/2, 0, \pi/2$ , and  $\pi$  are the result of differentiating the discrete scalar field data. Note that case R0703 has broad peaks around  $\vartheta \approx 0$  and  $\pi$ , suggesting slightly more gradient vector content in the x-derivatives than in the y-derivatives. There was some evidence for this in figure 19, as well as in the joint pdf in figure 20a. These peaks, however, account for only slightly more than 5 percent of the total probability, and appear likely to be due to incomplete convergence of these derivative statistics.

Putting aside any differences presumably due to incomplete convergence of the statistics, it is apparent in figure 21a that there are small peaks in both curves near  $\vartheta \approx -\pi/4$  and  $3\pi/4$ , and valleys in both curves near  $\vartheta \approx \pi/4$  and  $-3\pi/4$ . These orientations coincide with the principle strain axes of the mean flow. Taking into account both the mean axial and radial velocities at the measurement location, the mean strain rate field has its most compressional principal strain axis aligned along  $\vartheta \approx -49^\circ$  and  $131^\circ$ , and its most extensional principal strain axis aligned along  $\vartheta \approx 41^\circ$  and  $-139^\circ$ . Owing to the dynamics of the scalar gradient vector, there is a strong tendency for the scalar gradient to align with the most compressive principal strain axis of the instantaneous strain rate field, and an equally strong tendency for the gradient to rotate away from the most extensional instantaneous principal strain axis. While the instantaneous strain rate field varies, on average the principal axes will align with those of the mean flow. Thus the peaks and valleys in figure 21a at these  $\vartheta$  values are due to a weak anisotropy at the small (inner) flow scales imposed directly by the mean (outer) flow scales. This departure from complete small scale isotropy leads to an



overall sinusoidal shape to the  $\vartheta$  pdf's in both cases.

Figure 21*b* compares the distribution of  $\varphi$  values for the same two cases with the isotropic distribution. The measurements in both cases display a dip away from the isotropic form near  $\varphi = \pi/2$ , so that the gradient vector has a disproportionate tendency not to lie in the x-y plane. It appears likely that this is a manifestation of errors in determining the z-component of the scalar gradient, as noted above. The slight motion of the flow between the acquisition of one plane and the next causes an apparent gradient to be produced in the z-direction if the local velocity vector points significantly in the direction of the local scalar gradient vector. A mean flow correction to the z-derivative was introduced to partly account for this by assuming the scalar field to be frozen and moving at the local mean velocity. The resulting  $\varphi$  pdf is shown in figure 22 where it can be seen that this mean flow correction drives the pdf closer to its isotropic form, but that a mean flow correction alone is not sufficient to account for much of this effect.

### 5. *Spectral and wavelet analyses*

The dense spatial content of these data also permit analyses of multi-point statistics that are central to descriptions of turbulent flows based on concepts from classical statistical mechanics. This section uses the highly-resolved spatio-temporal nature of these data to examine the high frequency portion of spatial and temporal scalar energy spectra, and wavelet bases are used to extract length scale distributions from the conserved scalar and dissipation fields.

Classical theory for locally homogeneous, isotropic turbulence at Reynolds numbers sufficiently high for an inertial subrange suggests a  $k^{-5/3}$  power law scaling for the spatial spectrum of the kinetic energy field in the inertial range of scales. Similar arguments can be applied to the scalar energy spectrum, and measurements suggest that this also follows, at least approximately, a  $k^{-5/3}$  form in the inertial range as well (Gibson & Schwartz 1963; Grant, Hughes, Vogel, & Moillet 1968). For yet higher wavenumbers, Batchelor (1959) argued that, when  $Sc \gg 1$ , owing to the disparate dissipative scales  $\lambda_v$  and  $\lambda_D$  in the scalar and kinetic energy fields, the scalar spectrum should follow a  $k^{-1}$  form for wavenumbers  $k_v \ll k \ll k_D$  where  $k_v \equiv 2\pi/\lambda_v$  and  $k_D \equiv 2\pi/\lambda_D$ . For  $k \geq k_D$  Batchelor's theory suggests an exponential roll-off, giving the one-dimensional scalar spectrum at high wavenumbers [in the notation of Williams & Paulson (1977)] as

$$E_{\zeta}(k / k_B) = \frac{4(\pi q^3 D)^{1/2} \langle \chi \rangle}{(\langle \epsilon \rangle / \nu)^{3/4}} \left[ \frac{N(B)}{B} - \int_B^{\infty} N(y) dy \right] \quad (9)$$

Here  $\langle \chi \rangle$  is the mean scalar energy dissipation rate and  $\langle \epsilon \rangle$  is the mean kinetic energy dissipation rate (which for present purposes is estimated from measurements in axisymmetric turbulent jets by Taulbee, Hussain, & Capp (1987).  $N(B)$  is given by  $(2\pi)^{-1/2} \exp(-B^2/2)$  with  $B \equiv (2q)^{1/2} (k/k_B)$ , where  $k_B$  is the characteristic wavenumber of the Batchelor scale and  $q$  is a constant that relates the magnitudes of the maximum compressive and extensional principal strain rates. Batchelor suggested  $q = 2$ , however experimental studies have suggested values as high as six (Williams & Paulson 1977).

The three-dimensional spatial nature of these data (e.g. figures 11-13) allows the three-dimensional spatial scalar spectrum  $E_{\zeta}(\mathbf{k})$  to be determined. Such measurements have not previously been possible. Moreover, the three-dimensional spatial scalar spectrum then allows determination of the spherical spectrum  $E_{\zeta}(|\mathbf{k}|)$ . For homogeneous, isotropic turbulence, the one-dimensional spectrum  $E_{\zeta}(k)$  in (9) and the isotropic spectrum function  $E_{\zeta}(|\mathbf{k}|)$  are related (e.g. Tennekes & Lumley 1972) as

$$E_{\zeta}(|\mathbf{k}|) = k^3 \frac{d}{dk} \left( \frac{1}{k} \frac{dE_{\zeta}(k)}{dk} \right) \quad (10)$$

Integrating  $E_{\zeta}(\mathbf{k})$  into its three one-dimensional spectra  $E_{\zeta}(k_i)$  allows an isotropy test through this equation. Note from (10) that any power law scaling  $E_{\zeta}(k) \sim k^p$  will also appear in  $E_{\zeta}(|\mathbf{k}|)$ .

### 5.1 One-dimensional spatial spectra

Spectra were obtained using the FFT algorithm of Press *et al* (1992), and are typically presented in Kolmogorov-normalized form as

$$E_{\zeta_K}(k_K) \equiv \frac{E_{\zeta}(k_K)}{\Pi_K^2 \lambda_K} \quad (11)$$

Here  $\Pi_K^2 \equiv \langle \chi \rangle (\nu / \langle \epsilon \rangle)^{1/2}$  is the square of the Kolmogorov scalar scale,  $\lambda_K \equiv (\nu^3 / \langle \epsilon \rangle)^{1/4}$  is the Kolmogorov lengthscale, and  $k_K \equiv k \lambda_K$ , with the normalization

$$\langle \zeta'^2 \rangle = \int_0^{\infty} E_{\zeta}(k) dk \quad (12)$$

#### 5.1.1 Spatial spectra

Results are given in figure 23a for the three one-dimensional spectra in

the x, y, and z directions, together with Batchelor's spectrum in (9) for  $q = 5$ . Owing to the nominally  $256^3$  points in each spatial data volume the range of wavenumbers covered necessarily narrow, and owing to the high resolution lies deep in the dissipation range. Nevertheless insights about the possible validity of Batchelor's spectrum are possible. In particular, there is a possible asymptotic approach to a  $k^{-1}$  scaling in figure 23a. The peak in the dissipation spectrum in figure 23b allows the scaling at lower wavenumbers to be more readily discerned, and also supports a possible approach to the  $k^1$  scaling consistent Batchelor's power law regime.

While all three one-dimensional spatial spectra in these figures appear to asymptote to the Batchelor spectrum at the lowest wavenumbers, there are large disparities between them in the dissipation range. The x and y spectra are in relatively good agreement except at the highest wavenumbers where various noise sources dominate. The z-spectrum, however, shows considerably more high-frequency content than the x- or y-spectra. It appears likely that this is due to the slewing and other effects mentioned in §4.3, which will contain a fairly wide range of frequencies, with the slewing effect providing the lowest frequency contributions. While the motion from plane to plane within the cube is small, it becomes significant over the time  $\Delta T$  for a full  $256^3$  spatial data volume is acquired.

The three one-dimensional spatial spectra are compared in figure 24 with temporal scalar spectra obtained by Clay (1973) for  $Sc \approx 7$  and 0.7 using Taylor's hypothesis. Clay's  $Sc \approx 7$  result is from single-point time-series measurements of temperature in the wake of a sphere in water at  $Re = 27,600$ , while the  $Sc \approx 0.7$  results are from temperature measurements in a heated air jet at  $Re = 100,000$ . Note that the shift in wavenumber between the dissipation regions is consistent with the expected  $Sc^{1/2}$  dependence. In the following section, a more direct comparison of temporal spectra is made from the time information in the present four-dimensional measurements.

## 5.2 Temporal spectra

The fully four-dimensional spatio-temporal measurements, such as case R0811, provide temporal record lengths of up to 4096 points, which far exceed the comparatively short 256-point spatial record lengths available within the three-dimensional data volumes. For comparison with spatial spectra, the temporal separation between points is converted to a spatial separation via Taylor's hypothesis as  $\Delta x = u \cdot \Delta T$ . Here  $u$  is the expected mean velocity at the measurement location and  $\Delta T$  is the time between data volumes as given in Table 4. The resulting  $\Delta x$  is comparable to the spacing between points in the

spatial data. These spectra span the range of frequencies  $k_v < k < k_D$ , allowing a closer test of any asymptotic approach to Batchelor's  $k^{-1}$  scaling in this range. The spectra were averaged from 575 such temporal records, spaced 10 pixels apart in both the x and y directions in the three-dimensional spatial data. This yields well-converged spectra at intermediate and high frequencies, but the correlation between the temporal records from neighboring points is significant at low frequencies.

The resulting temporal spectrum is given in figure 25, where the Clay (1973) results for  $Sc \approx 0.7$  and 7.0 are shown for comparison, and in figure 26 where the comparison with Batchelor's prediction is shown. The spectrum in figure 25 is slightly higher than Clay's results, apparently due to differences in the estimated mean scalar dissipation rates. More relevant to the present measurements is the form of the spectrum in the viscous-convective range in both figures. Note that there is no real agreement of the present temporal spectrum with the  $-1$  scaling in Batchelor's spatial theory. If there is any power-law scaling in this range, it appears to be closer to a  $-1.3$  scaling, in apparent agreement with Miller (1991).

Given the spatial character and resolution of these measurements, they appear to give the only data to date capable of extracting the spatial scalar spectrum at high wavenumbers. In this sense, these measurements are uniquely suited to test Batchelor's theory in (9) for the spatial spectrum. Indeed, the results obtained in figure 23 for the high wavenumber spatial spectrum appear to show a possible asymptotic approach to Batchelor's theory at the lowest wavenumbers accessible to these measurements. Perhaps equally important, however, is that these results for the spatial spectrum seem to agree much better with Batchelor's theory than do the temporal spectra in figure 26. The temporal spectrum, of course, involves Taylor hypothesis which might be responsible for at least some of the poorer agreement obtained. In addition, the pockets of ambient fluid resulting from the intermittency of the turbulence within the jet may artificially enhance the energy content in the low frequency portion of the spectrum, and this could account for the steeper slope observed in the temporal spectrum. In any case, it does appear that the roll-off at very high wavenumbers, even in the spatial spectra in figure 23, does not seem to agree well with Batchelor's result. Collectively, these results suggest that the high frequency form of both the spatial and temporal spectra associated with large  $Sc$  scalar mixing in turbulent flows appears to be far from a closed issue, either theoretically or experimentally (see also Miller 1991). Moreover, the inability of direct numerical simulations to address this issue, owing to the extreme resolution demands posed by the  $Sc \gg 1$  requirement, suggests that its resolution will require experiments capable of addressing the high wavenumber

spatial spectrum.

### 5.3 *The three-dimensional spectrum*

The three-dimensional ( $256^3$ ) spatial character of the present data allows the first direct experimental determination of the three-dimensional scalar energy spectrum  $E_\zeta(\mathbf{k})$ . This spectrum was determined from the same three-dimensional spatial data volumes as were the one-dimensional spectra in §5.1. Each  $256^3$  volume was divided into  $8 \times 128^3$  subvolumes, with a separate three-dimensional spectrum computed for each. The ensemble average of these individual three-dimensional spectra is shown figure 27a. Each of the planes shows an intersection through the three-dimensional wavevector space  $\mathbf{k}$  at a constant  $k_z$  value.

Effects of various noise sources appear as three minor peaks in relatively compact frequency ranges. The most prominent is at large  $k_y$  and small values of  $k_x$  and  $k_z$ , the next largest is the ridge near  $(k_y, k_z) = (0, 0)$  leading to a sharp peak at large  $k_x$ , and the third occurs at large values of  $k_z$  and small values of  $k_x$  and  $k_y$ . Harmonics associated with these peaks are also evident, but at much lower energies. Each of these noise signatures can be traced to various aspects of the measurement technique. Noise in the photodiode array has two primary readout components, one that causes the signal to vary from row-to-row, resulting in the peak in  $k_y$  near  $(k_x, k_z) = (0, 0)$ , and one that manifests itself in a column-to-column variation, leading to the peak in  $k_x$  near  $(k_y, k_z) = (0, 0)$ . High frequency noise in the z-direction is introduced by the very small motion of the scalar field between the successively acquired z-planes, resulting in the peak seen where  $k_z$  is large and  $(k_x, k_y) = (0, 0)$ . Consistent with the approach taken throughout this study, the spectrum will be used in this form without any filtering, remaining cognizant of the various noise sources.

In figure 28, the calculated one-dimensional spatial scalar spectrum in the outward radial direction is compared against that resulting from integration of the full three-dimensional spectrum in the other two directions. Good agreement between the two spectra can be seen. In addition it is possible to integrate the three-dimensional spectrum in figure 27 over spherical shells in the wavevector space  $\mathbf{k}$  to obtain the isotropic spectrum function. Since the full three-dimensional spatial spectrum has not been available to any previous measurement, this spherical spectrum has instead traditionally been calculated under the assumption of isotropy using (10). Here however, no such isotropy assumption is necessary and  $E_\zeta(\mathbf{k})$  can be integrated directly. The result is shown in figure 29, where this spectrum is compared to the individual one-dimensional spatial spectra. All four spectra have been normalized with the

measured scalar variance in (12). Slewing effects appear to account for the higher z-spectrum values at large wavenumbers, but at least some of the differences in the x- and y-spectra appear to be genuine departures from isotropy, since as noted in §4.4 there appear to be measurable anisotropies in the scalar gradient field created from the principal strain rate field imposed by the outer scales on the inner scales.

#### 5.4 Wavelet spectra

Fourier spectra of the type in §5.1-5.3 form the basis of much of classical turbulence theory, in which infinitely wide basis functions (sinusoidal frequency components) are used to decompose the subject turbulence fields. However, the resulting conjugate relationship between the representations of these fields in the spectral and physical domains does not appear well suited to the highly localized sheet-like scalar dissipation features that apparently underlie turbulent mixing fields, as is evident in figures 8-14. The more highly localized these features are in the physical domain, the more broadly distributed they become in spectral representations of the type in figures 23-29, rendering lengthscale information difficult to extract from such Fourier spectra. This is common in a wide range of fields dominated by highly intermittent phenomena. Wavelet transforms provide an alternative decomposition that retains localized basis functions in both the physical and spectral domains, and as such are well suited for identifying characteristic lengthscales. Applications of wavelet analysis to turbulent flows have been undertaken by Lewalle, Petagna, Buresti, & Beux (1994), Lewis & Gharib (1992), and Dallard & Browand (1993). Here we examine the use of wavelet decompositions to identify the lengthscale distribution of the scalar dissipation layers seen in §3.

The one-dimensional wavelet bases considered here are

$$g_1(\kappa x) \equiv \kappa x \exp(-\kappa^2 x^2/2) \quad (13a)$$

$$g_2(\kappa x) \equiv (\kappa^2 x^2 - 1) \exp(-\kappa^2 x^2/2) \quad (13b)$$

shown in figure 30, with the latter being widely referred to as the "Mexican hat" wavelet, and with the factor  $1/\kappa$  setting the wavelet scale. Note that the  $g_1$  wavelet tends to pick out gradients, and the  $g_2$  wavelet, on the other hand, tends to find peaks or troughs in the data. The wavelet transform is computed by passing the wavelet basis  $g$  of various sizes over the data  $f$  and evaluating the integral in (14) at all points in the domain for each wavelet scale  $1/\kappa$  as

$$F(\kappa, x) = \int_{-\infty}^{+\infty} \kappa^{1/2} f(\xi) g(\kappa(\xi - x)) d\xi \quad , \quad (14)$$

with the local spectral power density given by

$$E(\kappa, x) = \frac{1}{2\pi} |F(\kappa, x)|^2 \quad (15)$$

The choice of wavelet basis  $g$  determines what types of features are emphasized in the data.

Figure 31a shows an example of the  $g_1$  wavelet spectrum obtained for a one-dimensional intersection along the  $x$ -direction through the conserved scalar field for case R0703. Note that the color scale is logarithmic. The wavelet scale  $1/\kappa$  is shown on the vertical axis; note that this scale is logarithmic as well. This is an inverse measure of the scale transforming factor  $\kappa$ , and indicates the scale of the wavelet in multiples of the inter-point spacings  $\Delta x$ . For example, a wavelet of scale  $(1/\kappa) = 10$  corresponds to the wavelet basis in figure 30, which unscaled extends 4 points in either direction, and when scaled by this factor would extend 40 points in either direction, for a total width of  $80 \Delta x$ . Since the nature of the  $g_1$  wavelet is to pick out gradients, peaks in the wavelet spectrum  $E(\kappa, x)$  coincide well with those spatial locations  $x$  at which transitions in scalar value occur in the one-dimensional scalar profile. In figure 31b, the  $g_1$  wavelet is used to analyze the structure of the scalar dissipation field along the same one-dimensional intersection. Note that the nearly Gaussian shape of the internal structure within the scalar dissipation layers is evident in these profiles. As was the case for the scalar field intersections, the results obtained for the  $g_1$  wavelet are sensitive to the slopes of these profiles. In effect, the spectral energy  $E(\kappa, x)$  measures the correlation at each  $x$ -location between the chosen wavelet basis  $g$ , stretched by the scale  $1/\kappa$ , and the scalar field data.

Analogous results for the  $g_2$  wavelet are shown in figure 32. Notice that, unlike the scalar field spectra in figures 31a,b, the peak magnitudes in the dissipation spectra in figures 32a,b depend on the choice of wavelet basis, and are typically an order of magnitude lower. Since the nature of the scalar energy dissipation field is to peak and return to zero between each layer, the large scale variations in the data are mostly removed. Moreover, at the smallest wavelet scales, there is much finer variation in the wavelet spectra  $E(\kappa, x)$  than was the case for the scalar field data. Note also that the highest peaks in the dissipation field spectra typically occur at lower values of the wavelet scale  $1/\kappa$ , i.e. the dissipation field structures correlate better with wavelets of a smaller size. Thus with proper choice of wavelet basis, depending on the features whose scale information is sought, the distribution of length scales in the turbulent fields can be ascertained from their corresponding wavelet spectra  $E(\kappa, x)$ .

Wavelet spectra for the  $g_2$  basis can be computed for one-dimensional

intersections through the conserved scalar field, and then ensemble-averaged. The resulting average  $E(\kappa, x)$  is shown in figure 33. The red bands near the two edges indicate where the spectrum is affected by wrap-around due to the finite spatial domain. A profile through this average spectrum, taken at the center  $x$ -location (where this wrap-around effect vanishes) is shown at the top of figure 33, where the inverse wavelet scale  $k$  is roughly analogous to the spatial frequency in the Fourier spectra. Due to the purely dimensional grounds on which Batchelor's  $k^{-1}$  scaling in the viscous-convective range can be derived, the same power law scaling should also apply to the average wavelet power spectrum as well. In fact, the scaling at low  $\kappa$  appears to be very nearly  $\kappa^{-1.2}$ .

### 5.5 Dissipation layer thicknesses

The present interest in the wavelet transform is primarily for measuring the distribution of thickness scales of the scalar dissipation layers. For this purpose, the negative of the  $g_2$  wavelet at least grossly resembles the Gaussian internal profile of the dissipation layers, and thus would appear to be a good basis for determining the layer thicknesses. From the sample results in figures 32b, the relative size of the dissipation structures can be identified at each spatial location  $x$  from the variation in wavelet energy  $E(\kappa, x)$  with the scale  $1/\kappa$ . Specifically, at the  $x$ -location of every local maximum in any one-dimensional intersection through the dissipation profile, the wavelet power spectrum  $E(\kappa, x)$  is examined to find the first peak occurring along the  $1/\kappa$  direction. These peaks correspond to the scale at which the wavelet is a local "best-fit" to the dissipation profile. The resulting "best-fit" thicknesses ( $1/\kappa$ ) determined from the wavelet spectrum is then converted to the dissipation layer thickness  $(\lambda_D)_{20\%}$  by "matching" to the corresponding thickness of a Gaussian profile given by  $g(\kappa x) = \exp(-\kappa^2 x^2)$ . Thus the characteristic thickness of the negative of the  $g_2$ -wavelet in (13b) is also determined by the point at which  $g_2$  is 20% of its maximum value, namely  $\kappa x = 0.845$ . Since the wavelet transform as described here operates on one-dimensional data, the apparent thickness of the 'best-fit' wavelet in the one-dimensional intersection through any dissipation layer must be corrected to account for the layer orientation. Since the scalar gradient vector orientation is known at every point (see figure 10) it is a simple matter to convert the one-dimensional best-fit thickness to the true layer-normal thickness. In practice, only dissipation layers oriented within  $45^\circ$  of the intersection line were examined to reduce the sensitivity to errors in the calculation.

The data for case R0806 were analyzed in this manner, and the dissipation layer thickness distribution determined based on this wavelet spectrum approach. The result is given by the solid line in figure 34, where the resulting



thicknesses  $(\lambda_D)_{20\%}$  are shown both in absolute terms (mm) as well as normalized as in (6), where the scaling constant  $\Lambda$  can be inferred directly. Based on the previous estimate of 11.2 for the scaling constant  $\Lambda$ , Table 3 predicted a mean dissipation layer thickness  $(\lambda_D)_{20\%} \approx 0.21$  mm. This appears to be in fairly good agreement with the result in figure 34, where the wavelet-based distribution gives the mean thickness as 0.26 mm, the median thickness as 0.23 mm, and the modal thickness as 0.19 mm, as indicated in Table 5a. Table 5b gives the resulting values for the scaling constant  $\Lambda$  in (6) based upon these measures of the thicknesses. Note that resolution limitations preclude very small values, thus the median and modal thicknesses are probably more representative of the true mean dissipation layer thickness. Note that these values obtained from the wavelet technique are in good agreement with the estimated layer thickness.

While this wavelet approach provides a relatively simple integral technique for estimating the distribution of dissipation layer thicknesses, the thickness obtained can depend on the neighboring dissipation field. In particular, owing to the "wings" in the wavelet bases, the peaks and valleys formed by the neighboring layers combine to produce a 'best-fit' wavelet that is smaller than that for an isolated layer. Such interacting layers are not uncommon in the experimental data, as can be seen in figures 8-14. For this reason, a related approach was developed based on the correlation between the dissipation field and a Gaussian shape, which does not have such "wings". Unlike the  $g_2$  wavelet, the Gaussian shape does not have zero area, and so the correlation will not show a peak at the 'best-fit' scale. Instead, the 'best-fit' scale  $(1/\kappa)$  is obtained when the normalized correlation

$$R = \frac{1}{f(x)} \cdot \frac{\int_{-\infty}^{+\infty} f(\xi) g(\kappa(\xi - x)) d\xi}{\int_{-\infty}^{+\infty} g^2(\kappa\xi) d\xi} \quad (16)$$

crosses unity. Here  $f(x)$  is the field of interest (in this case a one-dimensional intersection through the scalar dissipation field) and  $g(x)$  is a Gaussian basis given by  $g(\kappa x) = \exp(-\kappa^2 x^2)$ . The dissipation layer thicknesses obtained by applying this correlation technique to the same data used above produces the distribution given by the long-dashed line in figure 34. This distribution gives the mean dissipation layer thickness  $(\lambda_D)_{20\%} \approx 0.32$  mm, the median thickness as 0.30 mm, and the modal thickness as 0.25 mm.

Previous measurements of this thickness distribution by Buch (1991), on which the estimate of 11.2 for the scaling constant  $\Lambda$  in (6) was based, used the

local layer-normal profile integral moments to estimate  $(\lambda_D)_{20\%}$ . In that approach, first and second moments of the local one-dimensional layer-normal scalar dissipation profiles are calculated, and the thickness determined by assuming a Gaussian dissipation profile with the same moments. The distribution obtained by applying this approach to the present data are shown by the short-dashed line in figure 34. The peak in this distribution gives the modal thickness for  $(\lambda_D)_{20\%}$  as 0.22 mm, in good agreement with the estimate in Table 3 based on the measurements of Buch (1991).

## 6. Structure of the dissipation layers

The previous sections presented various results from the present highly resolved, four-dimensional, spatio-temporal measurements of the structure of scalar mixing at the small scales of turbulent shear flows. These have shown that essentially all of the scalar energy dissipation field is concentrated in thin sheet-like scalar dissipation layers, and have established certain statistical and structural properties, in both the physical and spectral domains, that result from this layered structure. This section will examine aspects of the internal structure within these scalar dissipation layers. A previous experimental investigation based on two-dimensional measurements by Buch (1991) examined the shapes of the scalar dissipation profiles across these layers for both  $Sc \gg 1$  and  $Sc \approx 1$  mixing in turbulent shear flows. Here a study of the internal structure of the scalar and dissipation profiles within these layers is undertaken with the aim of understanding the effects of the local scalar differences on these layer profiles, and how the scalar differences act to determine the joint pdf's in figure 17 and the resulting conditional dissipation statistics in figure 18. The results obtained, together with the scaling of the distribution of layer separations in §8, give a relatively simple physical model of the small scale structure of conserved scalar mixing in equilibrium turbulent shear flows.

### 6.1 Layer-normal profiles

In a translating and rotating Lagrangian coordinate frame moving with any chosen material point in the flow and remaining aligned with the local instantaneous principal axes of the strain rate tensor, the local velocity field in the vicinity of the origin reduces to a spatially uniform but time-varying pure strain field determined by the three principal strain rates  $\epsilon_{11} \geq \epsilon_{22} \geq \epsilon_{33}$ . As noted by Buch & Dahm (1991), in constant-density flows the local velocity field in this frame can therefore be reduced to a single parameter  $\sigma \equiv \epsilon_{22} / \epsilon_{33}$  describing the structure of the local strain rate tensor, with  $\epsilon_{11}$  simply serving to rescale the time. Two classes of local flows are thus possible, namely  $\sigma < 0$  corresponding to two extensional and one compressional principal strain axes,

and  $\sigma > 0$  corresponding to one extensional and two compressional principal axes. Kinematics dictate that the  $\sigma < 0$  flows will distort any material volume toward a sheet-like topology, while the  $\sigma > 0$  class will form line-like topologies. In both cases, the resulting  $\nabla\zeta(\mathbf{x},t)$  will rotate toward alignment with the most compressive principal strain rate axis. Exact solutions of the Navier-Stokes and conserved scalar transport equations in this local frame are possible for the limiting cases given by  $\sigma = -1/2, 0$ , and  $+1$ . The latter corresponds to a locally axisymmetric compressive strain field that forms line-like structures in the vorticity and scalar gradient fields, while the former two correspond to planar strain rate fields that lead to the formation of sheet-like gradient structures. As shown by Buch & Dahm (1991), the presence of a stretching term in the vorticity transport equation, and the absence of an analogous term in the scalar transport equation, allows the line-like gradient structures to be indefinitely sustained in the vorticity field, but leads to exponential decay of similar line-like structures in the scalar gradient field. On the other hand, both the vorticity and scalar gradient fields can indefinitely sustain sheet-like structures. In the scalar field, this sheet-like solution corresponds to a scalar gradient layer between two otherwise uniform scalar values  $\zeta^+$  and  $\zeta^-$ , for which the average scalar value,  $1/2(\zeta^+ + \zeta^-)$ , and the scalar difference,  $(\zeta^+ - \zeta^-)$ , remain constant in time, and the one-dimensional scalar field has an error function profile along the layer-normal coordinate  $n$  of the form

$$\zeta = \frac{1}{2}(\zeta^+ + \zeta^-) + \frac{1}{2}(\zeta^+ - \zeta^-)\text{erf}\left(\alpha \frac{n}{\lambda_D}\right), \quad (17)$$

where  $n = 0$  is the layer center and the error function is defined as

$$\text{erf}(\xi) = \frac{2}{\sqrt{\pi}} \int_0^\xi \exp(-\eta^2) d\eta \quad (18)$$

Equation (17) leads to a Gaussian profile for the scalar energy dissipation rate across such a layer, given by

$$\nabla\zeta \cdot \nabla\zeta = \frac{\alpha^2}{\pi} \left[ \frac{(\zeta^+ - \zeta^-)}{\lambda_D} \right]^2 \exp \left[ -2 \left( \alpha \frac{n}{\lambda_D} \right)^2 \right] \quad (19)$$

Note that  $\alpha \equiv 1.79$  was introduced in (17) so that  $\lambda_D$  corresponds to the same definition used throughout this study, namely the full width of the dissipation profile where the dissipation rate drops to 20% of the profile peak value. Eliminating the spatial coordinate  $n$  from (17) and (19) gives the mapping

between the scalar dissipation rates and the conserved scalar values for a layer with thickness  $\lambda_D$  and scalar endpoints  $\zeta^+$  and  $\zeta^-$  as

$$\left[ \frac{\nabla \zeta \cdot \nabla \zeta}{[(\zeta^+ - \zeta^-)/\lambda_D]^2} \right] = \frac{\alpha^2}{\pi} \exp \left[ -2 \left( \operatorname{erf}^{-1} \left[ \frac{\zeta - \frac{1}{2}(\zeta^+ + \zeta^-)}{\frac{1}{2}(\zeta^+ - \zeta^-)} \right] \right)^2 \right] \quad (20)$$

Figure 35 shows the relation between the conserved scalar and the scalar dissipation profiles along several representative one-dimensional intersections through the sheet-like dissipation layers in the turbulent flow data from §4. The intersections were taken in the direction of the local layer normal  $n$ , and scalar endpoints determined as described in §6.2. Note that, as suggested by the discussion above, none of these layers have scalar endpoints  $(\zeta^+, \zeta^-) = (1, 0)$ . Instead the scalar endpoints, where the dissipation drops essentially to zero, vary widely among the layers shown. Notice how the peak scalar dissipation rate typically scales with the scalar difference  $(\zeta^+ - \zeta^-)$  across the layer, as suggested by (20). Since the distribution of dissipation layer thicknesses  $\beta(\lambda_D)$  is fairly narrow (see figure 34), the peak values in the layer-normal dissipation profiles are determined chiefly by the scalar difference.

If dissipation layers such as those in figure 35 conform to (20) then, when normalized as this equation indicates, the profiles should all collapse to the functional form given there. It is shown in figure 36 that this is in fact the case, where the solid line is simply the result in (20) for  $\alpha = 1.79$ , and the symbols are the same as in figure 35. Thus, all of the dissipation profiles in figure 35 are merely manifestations of the same strain-diffusion competition that forms the basis for (17) - (20). Accordingly, the mixing process in the fully developed turbulent flow can be thought of as a collection of locally one-dimensional, strained, laminar diffusion layers with varying endpoint characteristics, *i.e.*, having different  $(\zeta^+, \zeta^-)$  values satisfying some presumably universal distribution relative to  $\langle \zeta \rangle$ .

## 6.2 Scalar endpoint statistics

The local scalar endpoints  $(\zeta^+, \zeta^-)$  throughout spatial data volumes of the type in figures 11 - 13 can be readily determined. The procedure for doing this searches along the layer-normal direction from each point on the surface of dissipation layer maxima until the local dissipation rate profile decreases to 5% of the maximum value along the profile. The scalar endpoints can then be computed via (20) from the local combined values  $(\zeta, \nabla \zeta \cdot \nabla \zeta)$  at these two 5% points. As a test of the sensitivity of the endpoint determination to the 5% criterion, a single  $256^3$  spatial data volume was used to extract  $\zeta^+$  and  $\zeta^-$

distributions both 5% and 20% as the selection criterion. Excellent agreement in both the  $\zeta^+$  and  $\zeta^-$  pdf's is seen in figure 37, showing that the algorithm is insensitive to the choice of this criterion.

Figure 38 shows the joint probability density function of the scalar endpoint values for two cases in Table 1. Note that the two distributions agree quite well. Since by definition  $\zeta^+ > \zeta^-$ , the joint pdf occupies only the upper portion of each graph, with the dashed line ( $\zeta^+ = \zeta^-$ ) forming the boundary of possible values. The contours shown are logarithmically spaced, increasing successively by factors of two. The lack of any contours very near the  $\zeta^+ = \zeta^-$  boundary results from the minimum scalar dissipation threshold for which the layer center algorithm can reliably find clean layer center fields. For the results shown, this threshold corresponds to a minimum scalar difference of  $\langle \zeta^+ - \zeta^- \rangle / \langle \zeta \rangle \approx 0.31$ , which can be compared with the range of scalar values in figure 15a. Layers with a scalar difference smaller than this is not included in figure 38.

Note that, based on the shape of these  $\beta(\zeta^+, \zeta^-)$  distributions, it appears that for any value of  $\zeta^+$  there is an equal probability of almost any  $\zeta^-$  value occurring on the opposite side of the layer. If the two scalar endpoint values ( $\zeta^+, \zeta^-$ ) were completely uncorrelated, then the single-point scalar pdf in figure 15 would suggest there should be an increasing likelihood of finding lower  $\zeta^-$  values. Since that is not the case, apparently the scalar correlation over distances typically one  $\lambda_D$  apart offsets the tendency to produce more layers with lower  $\zeta^-$ 's than those with higher ones.

In addition to the joint pdf in figure 38, the two marginal pdf's  $\beta(\zeta^+)$  and  $\beta(\zeta^-)$  are shown in figure 39 for each of the two cases considered. As demanded by the requirement that  $\zeta^+ > \zeta^-$ , the pdf of  $\zeta^+$  shows a peak at an intermediate scalar value, here at about 1.4 times the local mean scalar value, and falls to zero at the tails. Below  $\zeta^+ = 0.5$  this  $\zeta^+$  pdf is most likely artificially low, due to the dissipation threshold in the layer center algorithm discussed above. The low concentration portion of this curve will be affected the most for two reasons: (i) low values of the mixture fraction are more common, and (ii) layers with a low  $\zeta^+$  have a smaller chance of having a large difference between  $\zeta^+$  and  $\zeta^-$ . A direct result of this is that  $1/2 \langle \zeta^+ + \zeta^- \rangle = 1.53 \langle \zeta \rangle$ , and this is clearly too high. Based on the results of figures 38a,b, this average value should be approximately equal to the mean scalar value in the mixed fluid (excluding  $\zeta \approx 0$ ) if all layers were included. By comparison, the mean scalar value obtained from the mixed fluid part of the pdf in figure 15, determined by removing the ambient spike, is 1.15.

### 6.3 A model of the small-scale statistics

On the basis of results from the present four-dimensional spatio-temporal measurements of  $Sc \gg 1$  conserved scalar mixing in turbulent flows (see figures 11 – 13), as well as earlier measurements of both  $Sc \gg 1$  and  $Sc \approx 1$  scalar mixing by Buch (1991), it appears reasonable to represent the scalar mixing process at the small scales of turbulent flows entirely by an ensemble of such locally one-dimensional sheet-like scalar gradient layers, in which all the mixing is taken to occur. If this is a fair representation of the scalar and dissipation rate fields in figures 11 – 13, then (20) provides a basis for predicting the resulting joint distribution  $\beta(\zeta, \nabla\zeta \cdot \nabla\zeta)$  of these fields, provided that the requisite distributions of the layer thicknesses  $\lambda_D$  and scalar endpoints  $\zeta^+$  and  $\zeta^-$  are also known. As was shown here, as well as by the earlier measurements of Buch (1991), the distribution of inner length scales  $\beta(\lambda_D)$  appears to be universally derivable from the local outer length scale  $\delta$  via (3a) and figure 34, with the scaling constant  $\Lambda$  given in Table 5. If, moreover, the distribution of scalar endpoints  $\beta(\zeta^+, \zeta^-)$  were expressible in terms of the local mean scalar value  $\langle\zeta\rangle$ , then the joint distribution  $\beta(\zeta, \nabla\zeta \cdot \nabla\zeta)$  could in fact be determined from this model. At a somewhat greater level of refinement, the distribution of layer separations  $\beta(\lambda/\lambda_D)$  could even be incorporated as well.

Note that Mell, Nilsen, Kosály, & Riley (1994) have used direct numerical simulations (DNS) of conserved scalar mixing in homogeneous, isotropic turbulence during the early stages of mixing, for which  $\zeta^+$  and  $\zeta^-$  are strictly confined to 1 and 0, to show that (20) accurately represents the joint distribution of conserved scalar and scalar dissipation rate values under those conditions. However, in a fully-developed turbulent flow, such as in the far-field of the turbulent jet, or even the long-time evolution in a chaotic mixing flow, the layer-like structures in the scalar dissipation field will no longer remain bounded by their initial scalar endpoint values of 1 and 0. Indeed, in the later stages of mixing the layers necessarily cannot remain bounded by their initial endpoint values. Instead,  $\zeta^+$  and  $\zeta^-$  will take on widely varying values corresponding to differing degrees of mixing. That can be clearly seen in the turbulent jet mixing results, where figure 15 and the mean concentration scaling together show that the peak (absolute) scalar values rarely exceed 0.06 and  $\zeta^+$  values are generally even far lower than this. Similarly, although the jet continually entrains ambient ( $\zeta = 0$ ) fluid, this subsequently mixes to produce  $\zeta^-$  values significantly higher than zero, as can also be seen from figure 15. Accounting for the effects of these nontrivial scalar endpoints requires measuring the distribution  $\beta(\zeta^+, \zeta^-)$  and assessing its universality and scaling relative to  $\langle\zeta\rangle$ .

It should be possible to largely reconstruct the joint pdf  $\beta(\zeta, \nabla\zeta \cdot \nabla\zeta)$ ,

with the above limitations in mind, from (20) and the joint pdf  $\beta(\zeta^+, \zeta^-)$ . The central idea is that the scalar and dissipation rate fields essentially consist of one-dimensional, strained, laminar dissipation layers of the type in (20), with their scalar endpoints  $(\zeta^+, \zeta^-)$  satisfying the distribution in figure 38 and their thicknesses  $\lambda_D$  satisfying the distribution in figure 34. Since the distribution of layer thicknesses is fairly narrow, for the present purposes the layers are all taken to be of the same thickness, though this added refinement could be included. Thus, for each  $(\zeta^+, \zeta^-)$  pair, a layer profile is obtained in which the dissipation and the conserved scalar are known at every point through (20). A histogram follows in which the value at the pairs  $(\zeta, \nabla\zeta \cdot \nabla\zeta)$  are weighted by the probability density of finding a layer with such endpoint values, namely  $\beta(\zeta^+, \zeta^-)$ . The final weighted histogram is a result of all  $(\zeta, \nabla\zeta \cdot \nabla\zeta)$  pairs within the profiles resulting from all  $(\zeta^+, \zeta^-)$  pairs.

Figure 40 shows the joint pdf  $\beta(\zeta, \nabla\zeta \cdot \nabla\zeta)$  constructed in this manner for case R0703. This can be compared with the result obtained in figure 17a by direct measurement. Note that the two distributions are remarkably similar. The model result shown here also incorporates the intermittency by accounting for zero dissipation rates contained within ambient fluid regions, and therefore not contained within layers, and very low dissipation rates that are not included in the layer center finding algorithm. The intermittency aspect of this model inherently cannot be made universal, since it is intimately tied to the large scale structure (outer variables) responsible for the ambient fluid entrainment process.

## 7. Layer separation distributions

One of the objectives of this work is to analyze the structure of the conserved scalar and scalar dissipation fields at the small scales of turbulent flows. This principally involves the three-dimensional ( $256^3$ ) data volumes owing to their larger spatial extent in all three directions. Many of the analyses in the subsequent chapters require first determining the three-dimensional fields marking the loci of dissipation layer centers. When properly identified, these layer maximum fields appear as thin sheet-like representations of the scalar dissipation layer centers. These in turn are used to analyze the scalar and dissipation rate values in the vicinity of the layer centers, as well to determine the layer endpoint characteristics and the layer separation distributions.

### 7.1 Layer center algorithm

An algorithm is used for automatically finding the dissipation layer centers. However, as is often the case in "machine vision" applications, this is

more difficult to do well than it might appear. Extensive tests conducted with various algorithms revealed features necessary for reliably identifying the layer centers in the algorithm that was finally used. This is based principally on the scalar gradient vector field  $\nabla\zeta(\mathbf{x},t)$ . Briefly, the algorithm begins by thresholding the gradient magnitude field (the dissipation rate field) at a chosen level. The threshold used was typically half the mean dissipation rate, which is typically quite low owing to the prevalence of zero and low dissipation rates. Next, the algorithm identifies the edges of the regions in which the dissipation rate is above the threshold value. To do this, for each point the local unit normal vector for the layer is determined based on the local gradient vector information. The edges of the layer are then found by marching in both directions along this unit normal direction until one of two criteria are met: (i) the scalar dissipation at the candidate edge point drops below the chosen threshold level, or (ii) the dot product between the scalar gradient unit vector at the original point and that at the candidate edge point changes sign. The resulting edge locations for the dissipation layers are then used to identify candidate midpoints representing the dissipation layer centers. A further check is made among these candidate dissipation layer center points to insure single pixel thickness for the resulting surface before finally admitting a pixel to the set of layer center points. This method has proven to work quite well for high Schmidt number mixing fields such as these, due to the tendency of the layer structures to be locally parallel, but may not work as well for low Schmidt number flows since then the dissipation layers are often nearly perpendicular to one another [e.g. see Buch (1991)].

Figure 42 shows the resulting layer centers identified with this algorithm for a complete three-dimensional volume. Note that in the three-dimensional representation, the cube is effectively opaque, so only the intersection of the sheet-like structure with the cube faces can be seen. Moreover, figure 42 only shows the layer centers on the faces of the cube, where the algorithm performs the poorest due to the limited scalar field information available on the cube faces.

Tests conducted with synthetically generated surfaces having varying levels of imperfection verify that the resulting distribution of layer separations can be accurately obtained. An example is shown in figure 43. In figure 43a, the dissipation layer centers are shown as obtained by applying the algorithm to a synthetic scalar field specified by  $\zeta(\mathbf{x}) = \sin(x^2)$  over  $0 < x < 3\pi$ . From the associated scalar dissipation field, the resulting ideal cumulative distribution of layer separations can be obtained analytically, and is shown by the solid line in figure 44. When the layer separation algorithm is applied to the discrete data in figure 43a, this gives the result shown by the diamonds in figure 44. Deviations



from the exact result given by the solid line are principally due to the discrete ( $256 \times 256$ ) nature of the original scalar field. To then test the sensitivity of the algorithm to imperfections in the dissipation layer center fields, a random pattern of holes and extraneous layers of various sizes were introduced in figure 43b to qualitatively match similar defects in the layer centers from the turbulent and chaotic flows. The layer separation distribution resulting from this imperfect layer center field is shown by the "+" symbols in figure 44. Note that except for very small separations, where the discrete nature of the data presents the greatest difficulties, the resulting distribution still follows the ideal distribution quite well, even in this intentionally noisy field, suggesting that the algorithms developed here are sufficiently robust to provide reliable results for both the chaotic and turbulent flows.

### *7.2 Dissipation layer separations*

Probability densities of dissipation layer separations were computed for each of 29 individual three-dimensional  $256^3$  spatial data volumes of the type shown in figures 11 – 13 from the turbulent flow measurements. These volumes were equally spaced in time, and spanned slightly more than 2.5 outer scale turn-over times ( $\delta/U$ ) of the flow. Note that the scalar field within any such volume represents the signature of the mixing process at the small scales of the flow. The dissipation layer separation distribution resulting from ensemble statistics over the entire set of spatial data volumes is shown in figure 45. A roughly  $-3$  power law scaling can be seen in the distribution of layer separations over this range of length scales, reminiscent of the power-law scale-similarities typically found in high Reynolds number turbulent flows.

Although the ensemble-averaged distribution exhibits this  $-3$  power law scaling, the individual dissipation layer separation distributions vary considerably from one data volume to the next, as shown in figure 46. The  $-3$  scaling appears to result only from averaging over many such individual uncorrelated volumes, but is not evident in any single volume. However, while the distribution varies significantly at large layer separations, for small separations the results for all volumes are nearly the same. The distributions for small separations are essentially invariant and show a roughly lognormal scaling, while for large separations the distributions are very different. In chaotic flows, the multiplicative processes that lead to rapid generation of small separations with lognormal scaling in regions of high strain (large stretching values) are fairly well understood. Moreover, in chaotic flows the presence of low stretching values leads to locally strong departures from lognormal scaling for large separations. It might be tempting to speculate that similar dynamical processes may control the scaling characteristics of the mixing process at these scales in turbulent

flows. However, there are important differences between closed chaotic flows and open turbulent flows. In particular, closed chaotic flows initially require that repeated iterations must lead to reductions in the separation distances of dissipation layers. In open turbulent flows, however, ambient fluid is continually entrained into the mixing region, creating voids in the dissipation field which are subsequently broken down by the stretching and folding process. The large separations in the turbulent flow result principally from this entrainment process, and the  $-3$  scaling in the ensemble-averaged distribution is merely the result of the distribution of large voids created by the entrainment and their subsequent breakdown ("cascade") process. In the chaotic flow, the breakdown of the initial voids might be expected to occur by a different process, leading to a different scaling of the dissipation layer separations.

## 8. Discussion and Concluding Remarks

This study has provided the first fully-resolved four-dimensional, spatio-temporal measurements of the small-scale structure of scalar mixing in turbulent flows. As noted in §1, the aim has been to obtain experimental data on the generic physical structure associated with large Schmidt number mixing at the small scales of turbulent shear flows. Though the measurements were obtained at a particular fixed location in the self-similar far field of an axisymmetric turbulent jet, the Reynolds numbers are believed to be large enough for the presumed universality of the small scales to be approached. Specifically, as summarized in Table 1, these measurements were obtained at outer scale Reynolds numbers  $Re_\delta$  in the range 2,600 – 5,000, and Taylor scale Reynolds numbers  $Re_\lambda$  in the range 38 – 52. While these values may seem relatively low in comparison with traditional turbulence studies, there is considerable evidence in the literature that the physical structure of the small scales in turbulent flows establishes itself well before many of the traditional hallmarks of high Reynolds number turbulence are reached. These "hallmarks" (such as an extensive  $k^{-5/3}$  inertial range) are then believed to instead be *signatures* of this fundamental physical structure of the flow that manifest themselves once sufficiently high Reynolds numbers are reached, rather than being minimum requirements necessary to achieve this fundamental physical structure in the first place. Indeed, experimental evidence [Dowling, D.R., *Phys. Fluids A* **3**, 2229-2246; see figure 18 therein] shows that the small-scale portion of the Kolmogorov-normalized scalar power spectra collapse for Reynolds numbers from 5,000 to 40,000 even though no  $k^{-5/3}$  range exists for the lower Reynolds numbers. Moreover, recent evidence from direct numerical simulations of turbulent flows appears to support this view. In DNS studies with  $Re_\lambda$  in the range 35-170, Jiménez, Wray, Saffman, and Rogallo [JFM **225**, 65-90] find essentially perfect collapse of small-scale spectra (see their figures 1a and 2a) as well as small-scale

vortical structure (see their figures 11a and 11b) and, regarding the small-scale structure of the flow, these authors state "it is surprising that no obvious increase in complication is detected as  $Re_\lambda$  increases." They conclude that "it is surprising that we are able to find similarity laws spanning the whole range of Reynolds numbers, and that even the lowest- $Re_\lambda$  flow seems to be essentially turbulent." Collectively, these observations suggest that the Taylor-scale Reynolds numbers accessible to these measurements are indeed large enough for the small scale structure to approach its Reynolds number asymptotic state. As a consequence, the results obtained here are believed to be largely representative of the universal small scale structure of  $Sc \gg 1$  conserved scalar mixing in all high Reynolds number turbulent shear flows.

The present measurements are unique both in terms of the four-dimensional spatio-temporal nature of the data and the simultaneous spatial and temporal resolution and signal quality they represent. As regards the first point, in many ways the nature of the data from these measurements is more comparable with data from direct numerical simulation (DNS) studies of turbulence than from traditional experimental studies. Indeed, the Taylor-scale Reynolds numbers achieved in these experiments are only about one-and-a-half to two times lower than in most simulations, and the Schmidt number here far exceeds that accessible to any DNS study. In this sense, experimental measurements of this type are a necessity for investigations of the small scale structure of  $Sc \gg 1$  scalar mixing in turbulent flows. Moreover, the dense four-dimensional spatio-temporal character of the data is fundamentally different from the traditional single-point time series data classically associated with experimental studies of turbulent flows. Similarly, unlike traditional time series data, the fully resolved nature of the present data in all three spatial dimensions as well as in time allows direct simultaneous differentiation in both space and time. Finally, owing to the exceptional signal quality and the high resolution of the measurements, the resulting derivative fields are manifestly smooth without the need to resort to explicit smoothing or filtering such as is commonly employed when differentiating experimental data.

The resulting data have given several new insights into the small scale structure of turbulent shear flows. First, these measurements have verified the locally one-dimensional, thin, strain-limited, laminar diffusion layer as the basic structural element of the scalar energy dissipation rate field, as had been suggested by the earlier lower-dimensional measurements of Buch & Dahm (1991). Indeed as noted, among the line-like and sheet-like topologies that can result from the advection-diffusion competition in §1.1 under differing strain rate tensor structures, only the sheet-like topology can be indefinitely sustained in the scalar gradient field, while the vorticity field can sustain both topologies

owing to the presence of a stretching term. In this sense, the small scale structure of the scalar dissipation field in turbulent shear flows is considerably simpler than that of the underlying flow field, from which turbulence largely draws its reputation for complexity.

Moreover, the three-dimensional spatial nature of these data has allowed a direct examination of the internal structure of these dissipation layers, and also allowed identification of their scalar boundary values  $\zeta^\pm$ . In particular, these scalar boundary values differ significantly from the  $(\zeta^+, \zeta^-) = (0, 1)$  boundary values associated with initial scalar interfaces. The distribution of mixed fluid states which these boundary values take on lead to very different conditional statistics than for the case  $(\zeta^+, \zeta^-) = (0, 1)$  dealt with in the early-time simulations of Mell *et al* (1993). Once these scalar boundary value distributions are taken into account, the fundamentally layer-like structure of the dissipation field leads to the joint statistics in figure 17, as verified by the model result in figure 40.

Moreover, these fundamentally layer-like dissipation field structures, together with the distribution of separations into which these layers are arranged by the underlying flow field, leads to the statistical and spectral signatures of the mixing process documented in §6. In particular, the scalar variance resulting from these structures appears to be much larger than previous lower-resolution measurements have suggested. The present measurements indicate a normalized variance of 1.07, in contrast to the highest values (0.68) reported to date from other investigations. This higher observed variance appears to be consistent with the highest scalar values observed, which also far exceed any previous results. The present results indicate the maximum normalized scalar value to be approximately 4.6, retrospectively consistent with previous molecularly-resolved measurements based on chemically reactive tracers. As far as the spectral characteristics of these layer-like patterns are concerned, figures 23*a,b* show a possible asymptotic approach to the  $k^{-1}$  scaling predicted by Batchelor (1959) for the mixing of  $Sc \gg 1$  scalar quantities in turbulent flows. However, at yet higher wavenumbers no agreement with Batchelor's theory is obtained. Moreover, when temporal spectra are considered (figures 26*a,b*), no approach to Batchelor's  $k^{-1}$  scaling is found, suggesting a fundamental difference between these two types of spectra.

Lastly, analyses of the thickness of these layer-like dissipation structures based on wavelet decompositions yield a distribution of thicknesses in good agreement with the earlier measurements of Buch & Dahm (1991) based on lower-dimensional measurements. For the scaling constant  $\Lambda$ , the present measurements give the median value as 12, with the thickest layers having roughly three times this thickness.

### References

- Anselmet, F. and Antonia, R.A. (1985) Joint statistics between temperature and its dissipation in a turbulent jet. *Phys. Fluids* **28** (4), 1048-1054.
- Antonia, R.A. and Mi, J. (1993) Temperature dissipation in a turbulent round jet. *J. Fluid Mech.* **250**, 531-550.
- Antonia, R.A., Prabhu, A. and Stephenson, S.E. (1975) Conditionally sampled measurements in a heated turbulent jet *J. Fluid Mech.* **72**, 455-480.
- Batchelor, G.K. (1959) Small-scale variation of convected quantities like temperature in a turbulent fluid. Part 1 General discussion and the case of small conductivity. *J. Fluid Mech.* **5**, 113-133.
- Batchelor, G.K. and Townsend, A.A. (1949) The nature of turbulent motion at large wavenumbers. *Proc. Roy. Soc. Lond. A* **199**, 238-255.
- Becker, H.A., Hottel, H.C. and Williams, G.C. (1967) The nozzle fluid concentration field of the round turbulent jet. *J. Fluid Mech.* **30**, 285-303.
- Bilger, R.W. (1988) The structure of turbulent nonpremixed flames. *Proc. 22nd (Int'l.) Symp. Combustion.* 475-488, The Combustion Institute, Pittsburgh.
- Bilger, R.W. (1993) Conditional moment closure for turbulent reacting flow. *Phys. Fluids A* **5** (2), 436-444.
- Birch, A.D., Brown, D.R., Dodson, M.G. and Thomas, J.R. (1978) The turbulent concentration field of a methane jet *J. Fluid Mech.* **88**, 431-449.
- Biringen, S. (1975) An experimental investigation of an axisymmetric jet issuing into a coflowing stream. *VKI Technical Note 110*.
- Buch, K.A. (1991) Fine scale structure of conserved scalar mixing in turbulent shear flows:  $Sc \gg 1$ ,  $Sc \approx 1$  and implications for reacting flows. *Ph.D. Thesis*, The University of Michigan, Ann Arbor, MI.
- Buch, K.A. and Dahm, W.J.A. (1991) Fine scale structure of conserved scalar mixing in turbulent shear flows:  $Sc \gg 1$ ,  $Sc \approx 1$  and implications for reacting flows. Report No. 026779-5, The University of Michigan, Ann Arbor, MI.
- Burgers, J.M. (1948) A mathematical model illustrating the theory of turbulence. *Adv. Appl. Mech.* **1**, 171-199.
- Carrier, G.F., Fendell, F.E. and Marble, F.E. (1975) The effect of strain rate on diffusion flames. *SIAM J. Appl. Math.* **28**, 463-500.
- Chen, C.J. and Rodi, W. (1980) *Vertical turbulent buoyant jets – A review of experimental data*. Pergamon Press, Oxford.

- Chevray, R. and Tutu, N.K. (1978) Intermittency and preferential transport in a round jet. *J. Fluid Mech.* **88**, 133-160.
- Clay, J.P. (1973) Turbulent mixing of temperature in water, air, and mercury, Ph. D. Thesis, University of California San Diego, La Jolla.
- Cook, A.W. and Riley, J.J. (1994) Subgrid-scale modeling of turbulent reacting flows. To appear in *Physics of Fluids*.
- Dahm, W.J.A. and Buch, K.A. (1991) Fine structure characteristics of large schmidt number molecular mixing in turbulent flows. *Proceedings of the ERCOFTAC International Symposium on Chemical Reactions in Turbulent Liquids*, to appear in *Chemical Reactions and Physical Processes in Turbulent Liquids*, Cambridge University Press.
- Dahm, W.J.A. and Dibble, R.W. (1988) Combustion stability limits of coflowing turbulent jet diffusion flames. *AIAA Paper* 88-0538. American Institute of Aeronautics and Astronautics, Washington, D.C.
- Dahm, W.J.A. and Dimotakis, P.E. (1987) Measurements of entrainment and mixing in turbulent jets. *AIAA J.* **25**, 1216-1223.
- Dahm, W.J.A. and Dimotakis, P.E. (1990) Mixing at large Schmidt number in the self-similar far field of turbulent jets. *J. Fluid Mech.* **217**, 299-330.
- Dahm, W.J.A., Southerland, K.B. and Buch, K.A. (1990) Four-dimensional laser induced fluorescence measurements of conserved scalar mixing in turbulent flows. *Applications of Laser Techniques to Fluid Mechanics*. Springer-Verlag, Berlin, pp. 3-18.
- Dahm, W.J.A., Southerland, K.B. and Buch, K.A. (1991) Direct, high-resolution, four-dimensional measurements of the fine scale structure of  $Sc \gg 1$  molecular mixing in turbulent flows. *Phys. Fluids A* **3**, 1115-1127.
- Dahm, W.J.A., Su, L.K. and Southerland, K.B. (1992) A scalar imaging velocimetry technique for fully resolved four-dimensional vector velocity field measurements in turbulent flows. *Phys. Fluids A* **4** (10), 2191-2206.
- Dallard, T. and Browand, F.K. (1993) The growth of large-scales at defect sites in the plane mixing layer. *J. Fluid. Mech.* **247**, 339-368.
- Dowling, D.R. (1991) The estimated scalar dissipation rate in gas-phase turbulent jets. *Phys. Fluids A* **3** (9), 2229-2246.
- Dowling, D.R. and Dimotakis, P.E. (1990) Similarity in the concentration field of gas-phase turbulent jets. *J. Fluid Mech.* **218**, 109-141.
- Drexhage, K.H. (1973) *Dye Lasers*. Springer-Verlag, Berlin.

- Effelsberg, E. and Peters, N. (1988) Scalar dissipation rates in turbulent jets and jet diffusion flames. *Proc. 22nd (Int'l.) Symp. Combustion.* 693-700, The Combustion Institute, Pittsburgh.
- Gibson, C.H. (1968) Fine structure of scalar fields mixed by turbulence. I. Zero-gradient points and minimal gradient surfaces. *Phys. Fluids* **11**, 2305-2315.
- Gibson, C.H. (1968) Fine structure of scalar fields mixed by turbulence. II. Spectral theory. *Phys. Fluids* **11**, 2316-2327.
- Gibson, C.H. and Schwartz, W.H. (1963) The universal equilibrium spectra of turbulent velocity and scalar fields. *J. Fluid Mech.* **16**, 365-384.
- Grant, H.L., Hughes, B.A., Vogel, W.M. and Moilliet, A. (1968) The spectrum of temperature fluctuations in turbulent flow. *J. Fluid. Mech.* **34**, 423-442.
- Jiménez, J., Wray, A.A., Saffman, P.G., and Rogallo, R.S. (1993) The structure of intense vorticity in isotropic turbulence. *J. Fluid Mech.* **255**, 65-90.
- Kolmogorov, A.N. (1962) A refinement of previous hypotheses concerning the local structure of turbulence in viscous incompressible fluid at high Reynolds number. *J. Fluid Mech.* **13**, 82-85.
- Lewalle, J., Petagna, P., Buresti, G. and Beux, F. (1994) Wavelet statistics and the near-field structure of coaxial jets. *AIAA Paper* 94-2323. American Institute of Aeronautics and Astronautics, Washington, D.C.
- Lewis, C.G. and Gharib, M. (1992) An exploration of the wake three-dimensionality caused by a local discontinuity in cylinder diameter. *Phys. Fluids A* **4** (1), 104-117.
- Lockwood, F.C. and Moneib, H.A. (1980) Fluctuating temperature measurements in a heated round jet. *Comb. Sci. Tech.* **22**, 63-81.
- Mell, W.E., Nilsen, V., Kosály, G. and Riley, J.J. (1993) Direct numerical simulation investigation of the conditional moment closure model for nonpremixed turbulent reacting flows. *Phys. of Fluids* **6** (3), 1331-1356.
- Mell, W.E., Nilsen, V., Kosály, G. and Riley, J.J. (1994) Investigation of closure models for nonpremixed turbulent reacting flows. *Comb. Sci. Tech.* **91**, 179-186.
- Meneveau, C. and Sreenivasan, K.R. (1991) The multifractal nature of turbulent energy dissipation. *J. Fluid Mech.* **224**, 429-484.
- Miller, P.L. (1991) Mixing in high Schmidt number turbulent jets. *Ph.D. Thesis*, California Institute of Technology, Pasadena, CA.
- Miller, P.L. and Dimotakis, P.E. (1991) Scalar spectra from turbulent jets. *Bulletin of*

- the Amer. Phys. Soc.* **36** (10), 2699-2700.
- Papanicolaou, P.N. and List, E.J. (1988) Investigations of round vertical turbulent buoyant jets. *J. Fluid Mech.* **195**, 341-391.
- Peters, N. (1986) Laminar flamelet concepts in turbulent combustion. *Proc. 1st (Int'l.) Symp. Combustion.* 1231-1250, The Combustion Institute, Pittsburgh.
- Poinsot, T., Veynante, D. and Candel, S. (1990) Diagrams of premixed turbulent combustion based on direct simulation. *Proc. 23rd (Int'l.) Symp. Combustion.* 613-619, The Combustion Institute, Pittsburgh.
- Pope, S.B. (1990) Computations of turbulent combustion: progress and challenges. *Proc. 23rd (Int'l.) Symp. Combustion.* 591-612, The Combustion Institute, Pittsburgh.
- Prasad, R.H. and Sreenivasan, K.R. (1990) Quantitative three-dimensional imaging and the structure of passive scalar fields in fully turbulent flows. *J. Fluid Mech.* **216**, 1-34.
- Press, W.H., Teukolsky, S.A., Vetterling, W.T. and Flannery, B.P. (1992) *Numerical Recipes, 2nd Edition.* Cambridge University Press, New York, pp. 490-529.
- Redner, S. (1990) Random multiplicative processes: An elementary tutorial. *American Journal of Physics* **58**, 267-273.
- Ricou, F.P. and Spalding, D.B. (1961) Measurement of entrainment by axisymmetrical turbulent jets. *J. Fluid Mech.* **11**, 21-32.
- She, Z. and Jackson, E. (1993) On the universal form of energy spectra in fully developed turbulence. *Phys. Fluids A* **5** (7), 1526-1528.
- Sreenivasan, K.R. (1991) Fractals and multifractals in fluid turbulence. *Annual Reviews of Fluid Mechanics* **23**, 539-600.
- Sreenivasan, K.R. and Meneveau, C. (1986) The fractal facets of turbulence. *J. Fluid Mech.* **173**, 357-386.
- Sreenivasan, K.R., Ramshankar, R. and Meneveau, C. (1989) Mixing, entrainment, and fractal dimension of surfaces in turbulent flow. *Proc. Royal Society of London A* **421**, 79-108.
- Su, L.K. and Dahm, W.J.A. (1994) Scalar imaging velocimetry studies of the dissipative scales of motion in turbulent flows. *AIAA Paper* 94-0403. American Institute of Aeronautics and Astronautics, Washington, D.C.
- Taulbee, D.B., Hussain and Capp (1987) The round jet: Experiment and inferences on turbulence modeling. *Sixth Symposium of Turbulent Shear Flows*, Toulouse, France.



- Tennekes, H. and Lumley, J.L. (1972) *A first course in turbulence*. The Massachusetts Institute of Technology Press, Cambridge, MA.
- Townsend, A.A. (1951) On the fine-scale structure of turbulence. *Proc. Roy. Soc. Lond. A* **208**, 534-542.
- Walker, D. A. (1987) A fluorescence technique for measurement of concentration in mixing liquids. *J. Phys. E: Sci. Instrum.* **20**, 217-224.
- Williams, R. M. and Paulson, C. A. (1977) Microscale temperature and velocity spectra in the atmospheric boundary layer. *J. Fluid Mech.* **83**, 547-567.
- Wynanski, I. and Fiedler, H. (1969) Some measurements in the self-preserving jet. *J. Fluid Mech.* **38**, 577-612.
- Yariv, A. (1976) *Introduction to Optical Electronics*, Holt, Rinehart, and Winston.
- Yip, B., Lam, J.K., Winter, M., and Long, M.B. (1987) Time resolved three-dimensional concentration measurements in a gas jet. *Science* **235**, 1209-1211.
- Yip, B. and Long, M.B. (1986) *Optics Letters* **11**, 64-70.
- Yip, B., Schmitt, R.L. and Long, M.B. (1988) *Optics Letters* **12**, 96-103.

Case #	$Re_{\delta}$	$Re_{\lambda_g}$	$J (N \cdot 10^{-3})$	$x (m)$	$r (m)$	$x/d^*$	$r/x$	$N_z$
R0420	3,000	41	0.902	1.15	0.127	235	0.11	6
R0628	3,200	42	1.03	1.15	0.127	235	0.11	6
R0811	4,200	48	1.77	1.15	0.127	235	0.11	6
R0212	2,600	38	0.677	1.15	0.127	235	0.11	256
R0304	2,900	40	0.842	1.15	0.127	235	0.11	256
R0703	3,700	45	1.37	1.15	0.127	235	0.11	256
R0806	5,000	52	2.50	1.15	0.127	235	0.11	256

Table 1. Experimental conditions for each of the seven cases analyzed with  $Re_{\delta}$  and  $Re_{\lambda_g}$  referring to the local outer-scale Reynolds number and Taylor scale Reynolds number respectively. Each case consists of a total of over three billion individual point measurements of the conserved scalar field. Note that four of these cases are designed to allow detailed three-dimensional spatial structure of the mixing process to be determined. These involve temporal sequences of nominally  $256^3$  three-dimensional spatial data volumes (see figure 2). The remaining three cases are designed to yield fully four-dimensional spatio-temporal data spaces, simultaneously differentiable in all three spatial directions and in time.

Wavelength $\lambda(nm)$	Relative Line Strength $\alpha(\lambda)$	Molar Extinction Coefficient $\epsilon(\lambda) \cdot (10^{-6}/m \cdot M)$
514.5	0.392	1.44
501.7	0.075	8.29
496.5	0.116	9.70
488.0	0.262	8.91
476.5	0.116	6.16
472.7	0.039	6.05

Table 2. Measured line strengths  $\alpha(\lambda)$  in (5) for the 5W Ar<sup>++</sup> laser (Coherent Innova 70-5) in multi-line emission mode. These line strengths are essential for correct conversion from the measured fluorescence intensity field  $F(\mathbf{x},t)$  to the dye concentration field  $c(\mathbf{x},t)$ , and subsequently to the conserved scalar field  $\zeta(\mathbf{x},t)$ . Also shown are the molar extinction coefficients for the individual wavelengths.

Case #	$Re_\delta$	$Re_{\lambda_\delta}$	$\lambda_D (\mu m)$	$\lambda_v (\mu m)$	$\Delta x, \Delta y (\mu m)$	$\Delta z (\mu m)$	Beam ( $\mu m$ )
R0420	3,000	41	303	13,800	108	90	191
R0628	3,200	42	289	13,200	116	120	168
R0811	4,200	48	239	10,900	107	110	154
R0212	2,600	38	331	15,100	100	79	234
R0304	2,900	40	309	14,100	110	88	218
R0703	3,700	45	257	11,700	109	120	181
R0806	5,000	52	209	9,520	107	100	154

Table 3. Spatial resolution characteristics for each of the cases listed in Table 1. The local outer scale Reynolds number is  $Re_\delta \equiv U\delta/\nu$ , where  $U$  and  $\delta$  denote the length and velocity scales characterizing the local mean shear in the flow, namely the local mean centerline velocity and the local flow width.  $Re_{\lambda_\delta}$  is the local Taylor-scale Reynolds number. The local strain-limited molecular diffusion scales for the vorticity and scalar fields are  $\lambda_v \approx 11.2 \cdot \delta \cdot Re_\delta^{-3/4}$  and  $\lambda_D = \lambda_v \cdot Sc^{-1/2}$ , respectively. Deconvolution of the fluorescence intensity data between parallel measurement planes reduces the effective resolution in the  $z$ -direction from the  $1/e$  laser beam thickness to the interplane spacing  $\Delta z$ . The spatial resolution achieved in these scalar field measurements is determined by comparing the interpoint separations ( $\Delta x, \Delta y, \Delta z$ ) to the local strain-limited scalar diffusion scale  $\lambda_D$ . Note that all cases are fully resolved in all three spatial dimensions.

Case #	$Re_\delta$	$Re_{\lambda_g}$	$\lambda_D/u$ (ms)	$\Delta\tau$ (ms)	$\Delta t$ (ms)	$\Delta T$ (ms)
R0420	3,000	41	152	0.0238	8.87	53.2
R0628	3,200	42	136	0.0238	8.87	53.2
R0811	4,200	48	85	0.0238	8.87	53.2
R0212	2,600	38	187	0.0238	8.87	2,270
R0304	2,900	40	158	0.0238	8.87	2,270
R0703	3,700	45	103	0.0238	8.87	2,270
R0806	5,000	52	62	0.0238	8.87	2,270

Table 4. Temporal resolution characteristics for each of the cases listed in Table 1. For each case, the pixel illumination time is given by  $\Delta\tau$ , the time between acquisition of successive parallel planes is given by  $\Delta t$ , and the time between acquisition of the same spatial point in successive volumes is  $\Delta T$ . The characteristic advection time scale for the scalar field is given by  $\lambda_D/u$ , where  $\lambda_D$  is the local strain-limited molecular diffusion scale (see Table 3) and  $u$  is the local mean velocity. The temporal resolution achieved in these scalar field measurements is determined by comparing the measurement time scales ( $\Delta\tau$ ,  $\Delta t$ ,  $\Delta T$ ) to the local diffusion scale advection time  $\lambda_D/u$ . Note that in all cases each of the individual data points are fully resolved in time, since  $(\Delta\tau, \Delta t) \ll \lambda_D/u$ . Additionally, the data in the first three cases are time-differentiable as well, since for them  $\Delta T < \lambda_D/u$ .

Technique	Mean $(\lambda_D)_{20\%}$ (mm)	Median $(\lambda_D)_{20\%}$ (mm)	Modal $(\lambda_D)_{20\%}$ (mm)	(a)
$g_2$ -Wavelet	0.26	0.23	0.19	
Gaussian Correlation	0.32	0.30	0.25	
Moment	0.30	0.28	0.22	

Technique	Mean $\Lambda$	Median $\Lambda$	Modal $\Lambda$	(b)
$g_2$ -Wavelet	14	12	10	
Gaussian Correlation	17	16	13	
Moment	16	15	12	

Table 5

Measures of the layer thicknesses for the turbulent data of Case R0806. Shown are (a) the mean, median, and modal thicknesses determined from the distributions of figure 34 for the three separate layer thickness-finding techniques listed; (b) the resulting mean, median, and modal scaling constant  $\Lambda$  in (6). Compare against the estimated dissipation layer thickness of 0.21 mm given in Table 3 and  $\Lambda \approx 11.2$  from measurements for  $Sc \approx 1$  of Buch (1991).

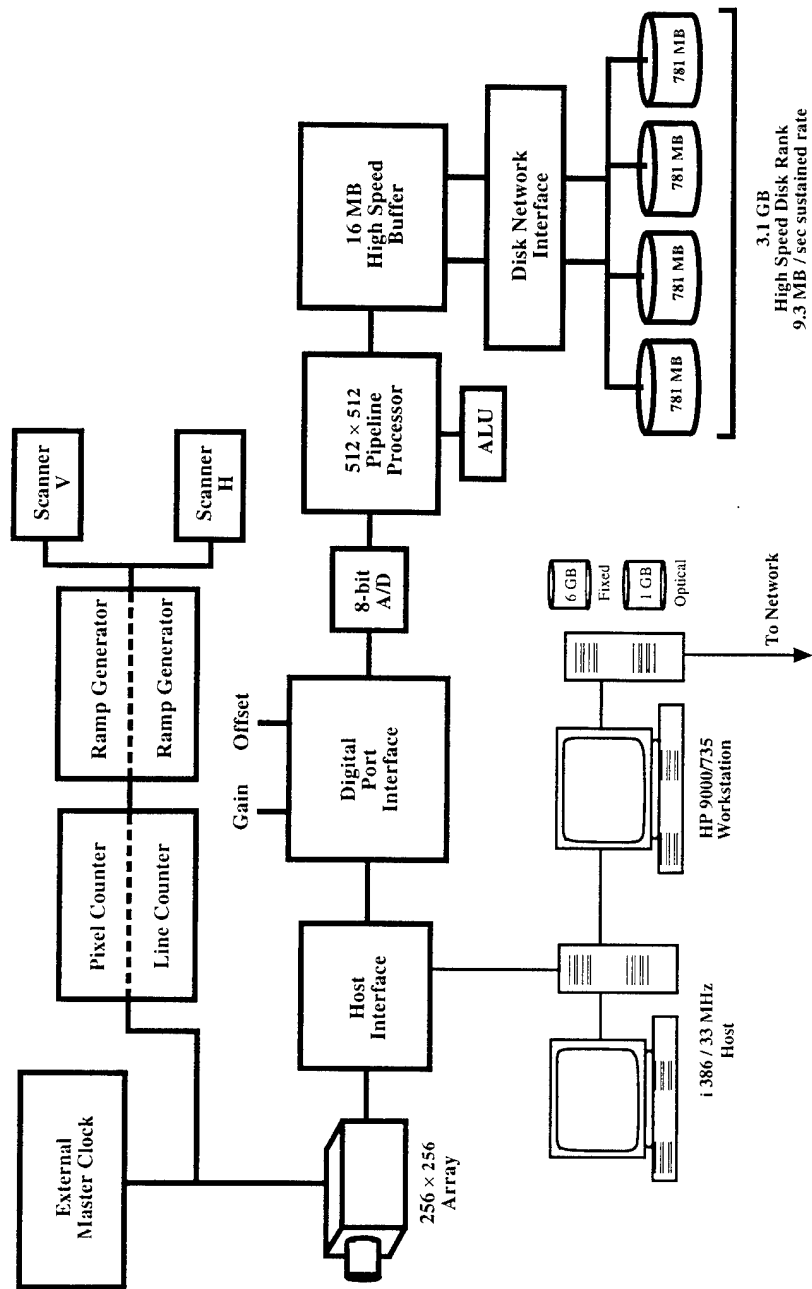


FIGURE 1. Key elements of the high-speed variable rate imaging and data acquisition system assembled for these highly resolved four-dimensional measurements of scalar mixing in turbulent flows. Two low-inertia galvanometric mirror scanners are slaved to the imaging array timing to rapidly sweep the laser beam in a successive raster scan fashion through the scalar field. The data acquisition system can achieve sustained data throughput rates up to 9.3 MB/sec for volumes as large as the full 3.1 GB disk capacity.

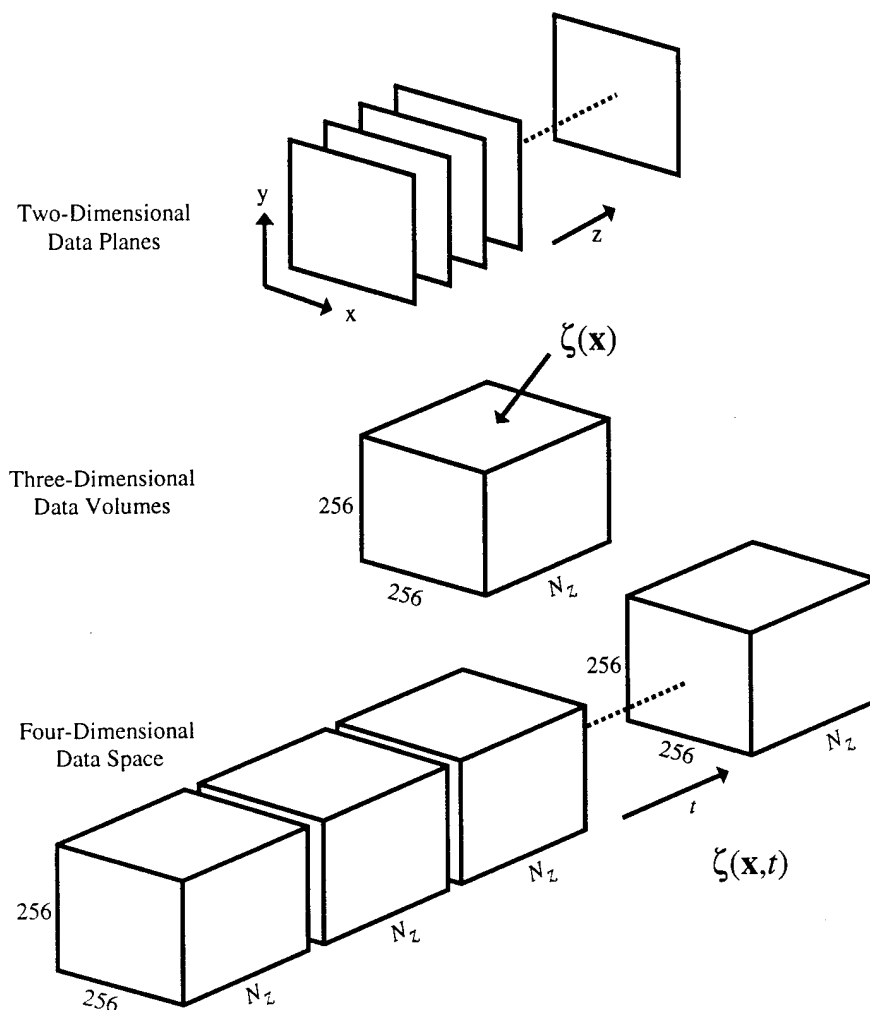


FIGURE 2. Schematic showing the structure of the conserved scalar measurement data. Each measurement produces the scalar field  $\zeta(\mathbf{x}, t)$  at over 3 billion individual points in space and time, arranged as a temporal sequence of individual three-dimensional spatial data volumes. Each of these spatial data volumes are composed of a sequence of two-dimensional spatial data planes, which in turn each consist of an array of  $256 \times 256$  spatial data points. The spatial separation between adjacent points within each data plane, and between adjacent data planes within each data volume, is smaller than the local strain-limited molecular diffusion lengthscale  $\lambda_D$  of the scalar field (see Table 3). Similarly, the temporal separation between successive points in the same data volume, and between the same point in successive data volumes, is given in Table 4.



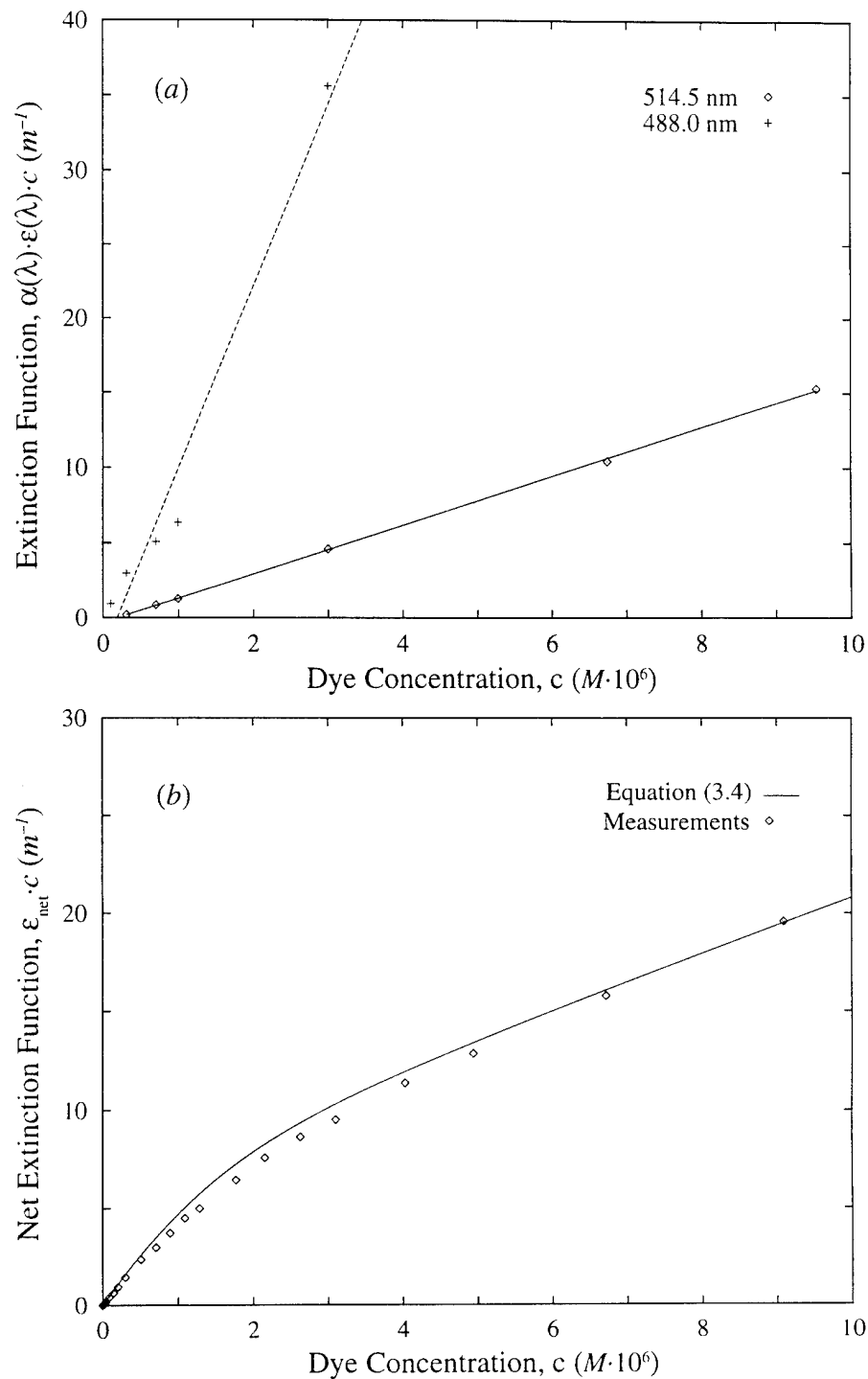


FIGURE 3. The measured extinction function in (5) for disodium fluorescein dye, obtained from absorption measurements for fixed dye concentration  $c$ . Shown are: (a) the single-line extinction function for the primary 488.0 nm and 514.5 nm lines of the  $\text{Ar}^{++}$  laser, where the slopes give the molar extinction coefficient  $\epsilon(\lambda)$  in Table 2, and (b) the net extinction function when the laser is operated in multi-line mode, showing good agreement between the measured net extinction function and the theoretical result in (5) for the initial line strengths and extinction coefficients.

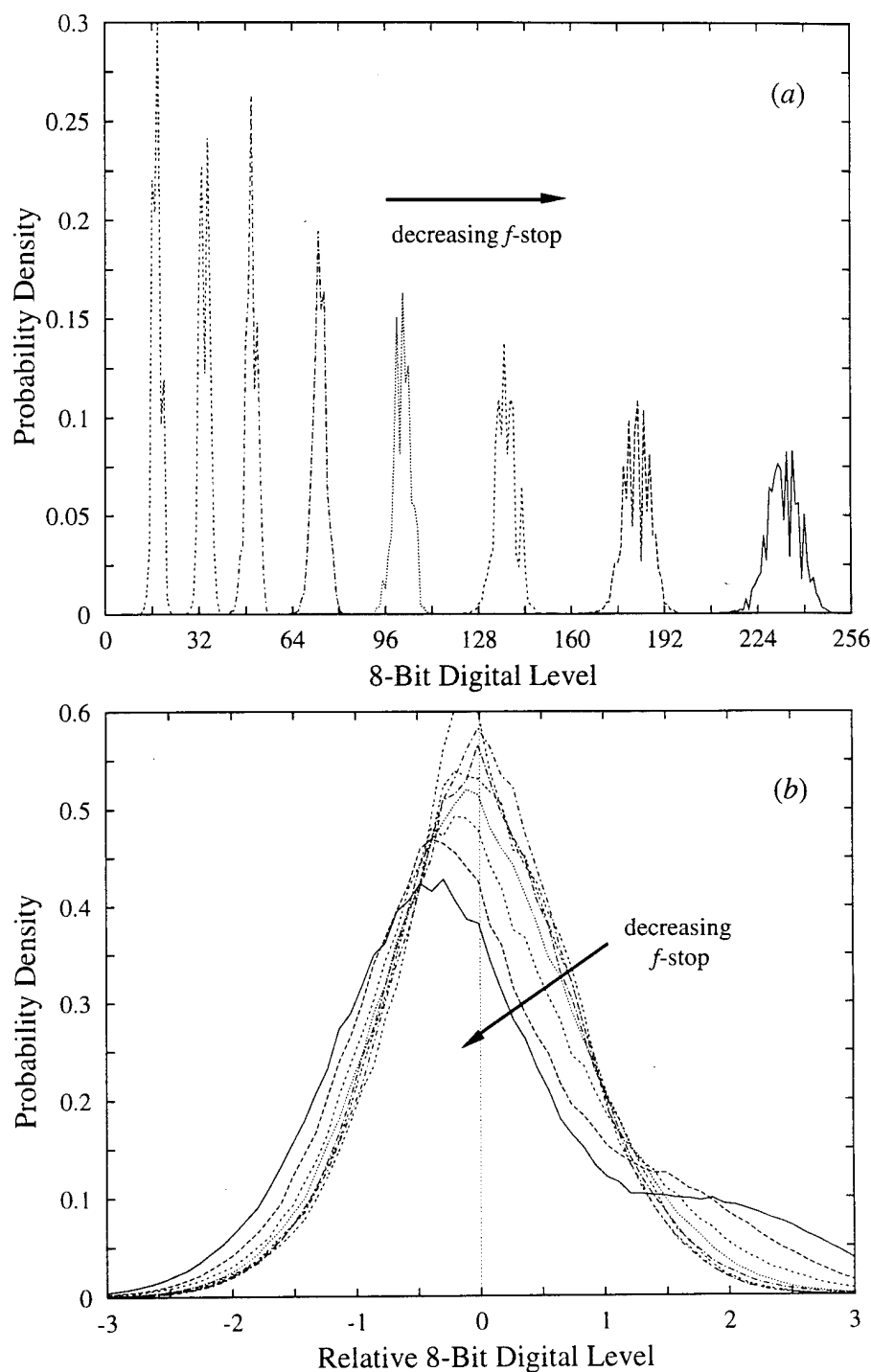


FIGURE 4. Measured variation of the noise level with the signal level for a nearly uniform camera illumination. Shown are: (a) the distribution of absolute digital signal levels for 8 different  $f$ -stop settings of the imaging lens, and (b) the resulting relative digital signal level distributions. Notice that the first four distributions collapse rather well, indicating that the resulting noise is independent of the signal level, typical of a camera noise-limited measurement. The four remaining curves at higher signal levels show a relative noise distribution that widens and becomes asymmetric with increasing signal level, typical of a shot noise-limited measurement. The resulting signal-to-noise ratios are given in figure 5.

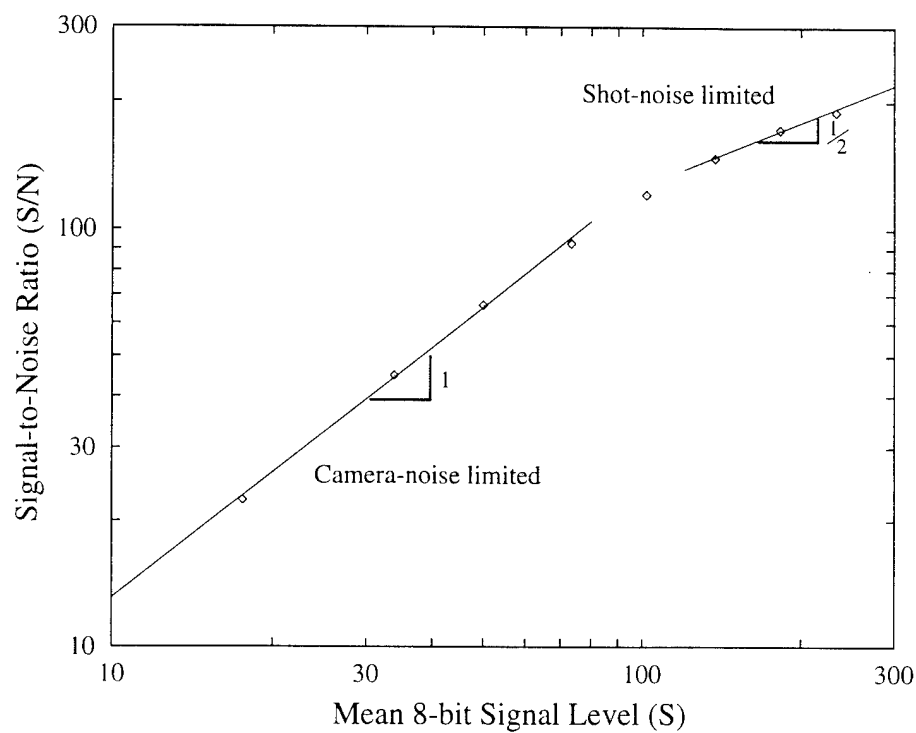


FIGURE 5. Measured dependence of the signal-to-noise ratios ( $S/N$ ) obtained from each of the distributions in figure 6 on the signal strength ( $S$ ), showing the characteristic  $(S/N) \sim S^1$  scaling in the camera noise-limited regime, together with the characteristic  $(S/N) \sim S^{1/2}$  scaling in the shot noise-limited regime. The scalar field measurements typically span across both noise regimes, with the mean signal to noise ratio above 65.

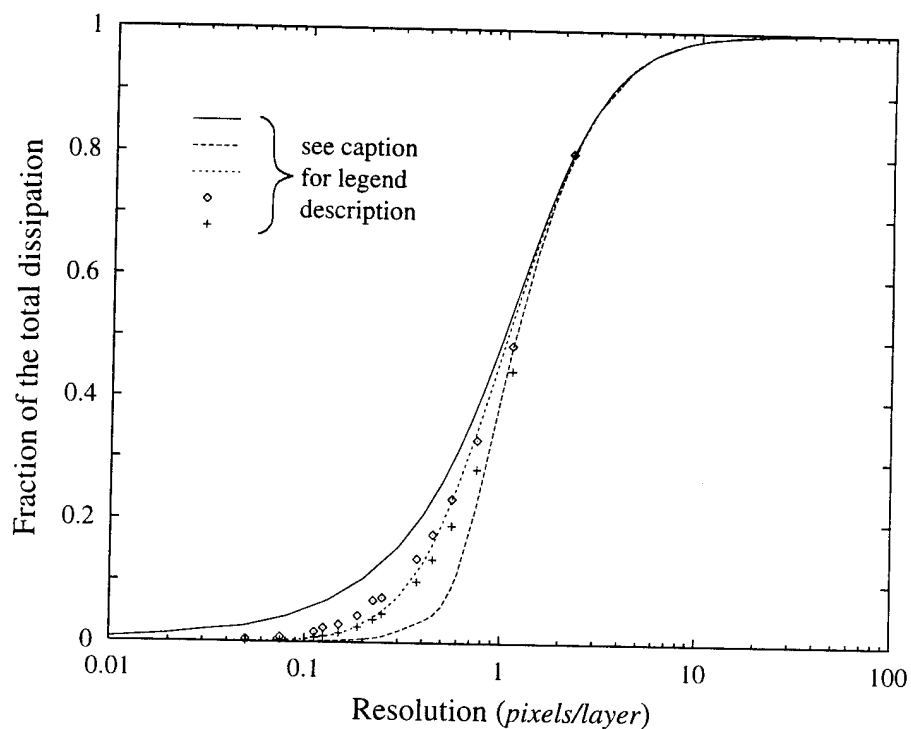


FIGURE 6. Experimental convergence test of the true measurement resolution obtained in these experiments, showing the fraction of the total scalar dissipation obtained from a measurement having a finite number of pixels per strain-limited diffusion layer length scale  $\lambda_D$ . Notice that the experimental results are in excellent agreement with the short dashed theoretical result, indicating that the present measurements are sufficiently resolved to detect about 80% of the true scalar dissipation. Note also that any measurement having spatial resolution coarser by an order of magnitude or more than the present study would miss virtually all of the true scalar dissipation field.

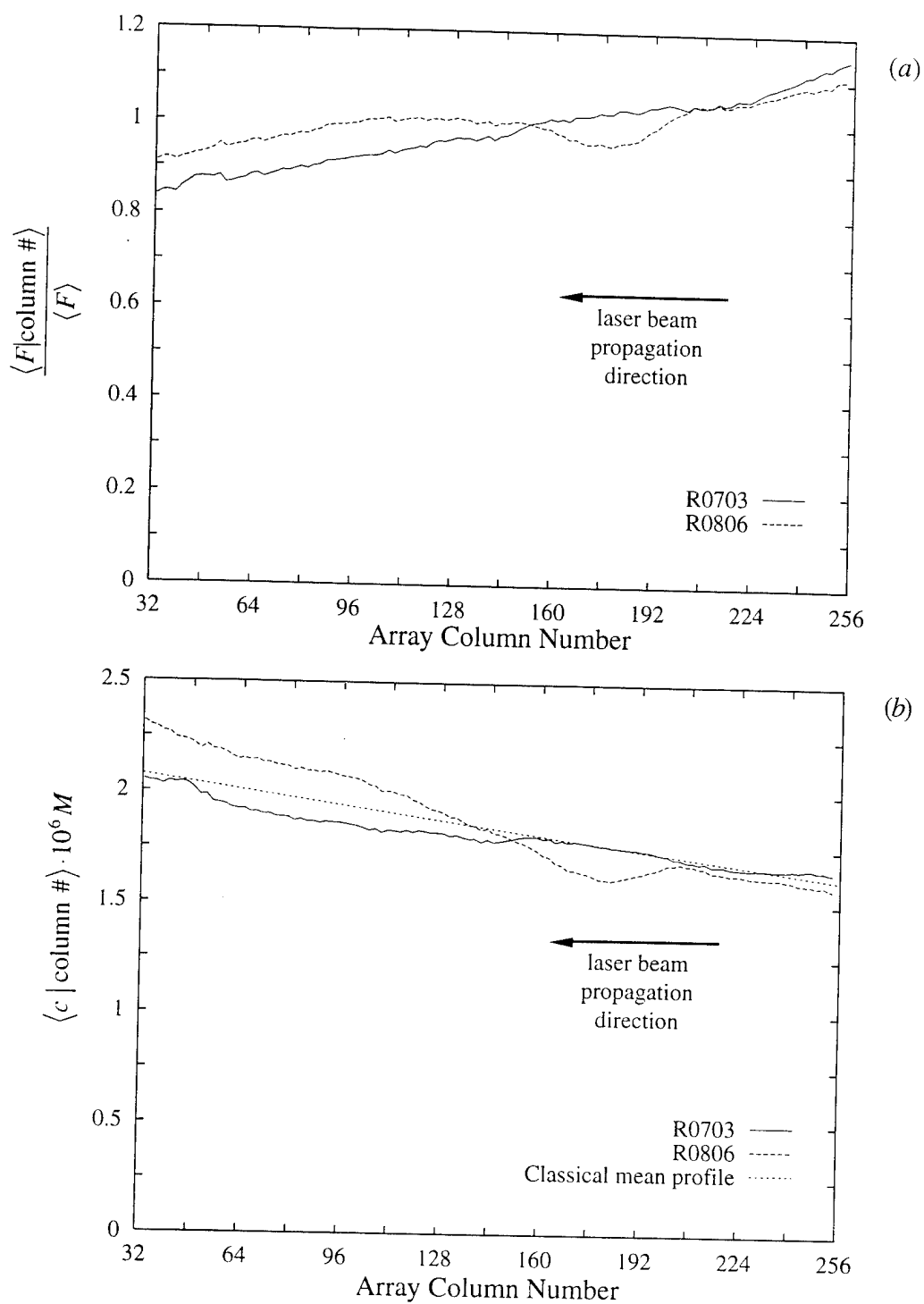


FIGURE 7. Stages in the conversion from the measured fluorescence intensity field to the dye concentration field. Shown are: (a) the average fluorescence intensity obtained in each column of the array, normalized by the time-and-volume-averaged fluorescence intensity; (b) the same result after correction for laser beam attenuation. Note the good short-duration statistical agreement in panel (b) between the measured mean radial variation in the dye concentration field and the classical mean profile over the imaged region in the flow.

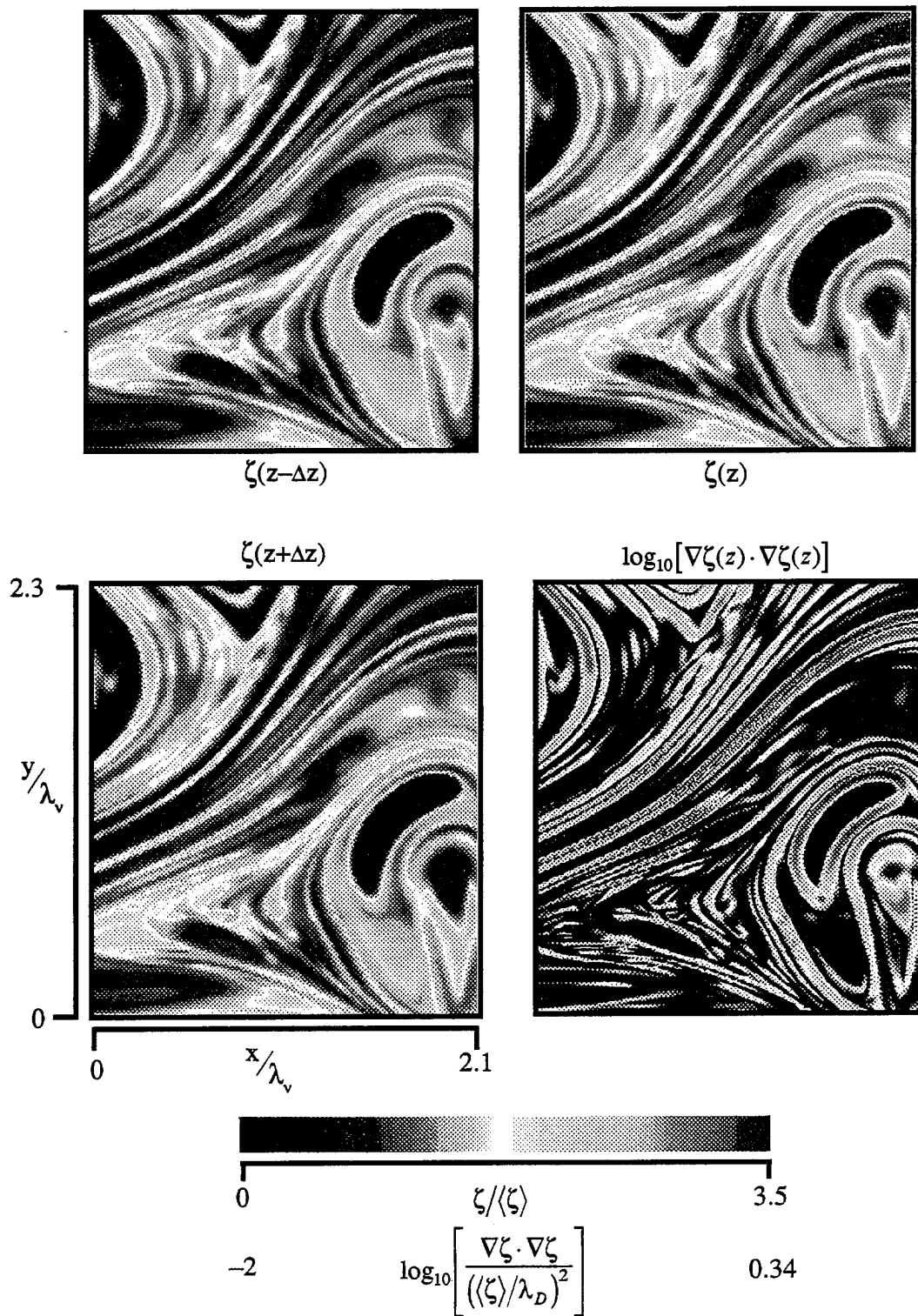


FIGURE 8. The structure of the conserved scalar field  $\zeta(\mathbf{x}, t)$  in three adjacent spatial data planes from a typical  $(256^3)$  data volume. The small changes between these three planes results from the high spatial resolution achieved (see Table 3). Also shown is the scalar dissipation field that results from direct differentiation of the data in these three spatial planes.

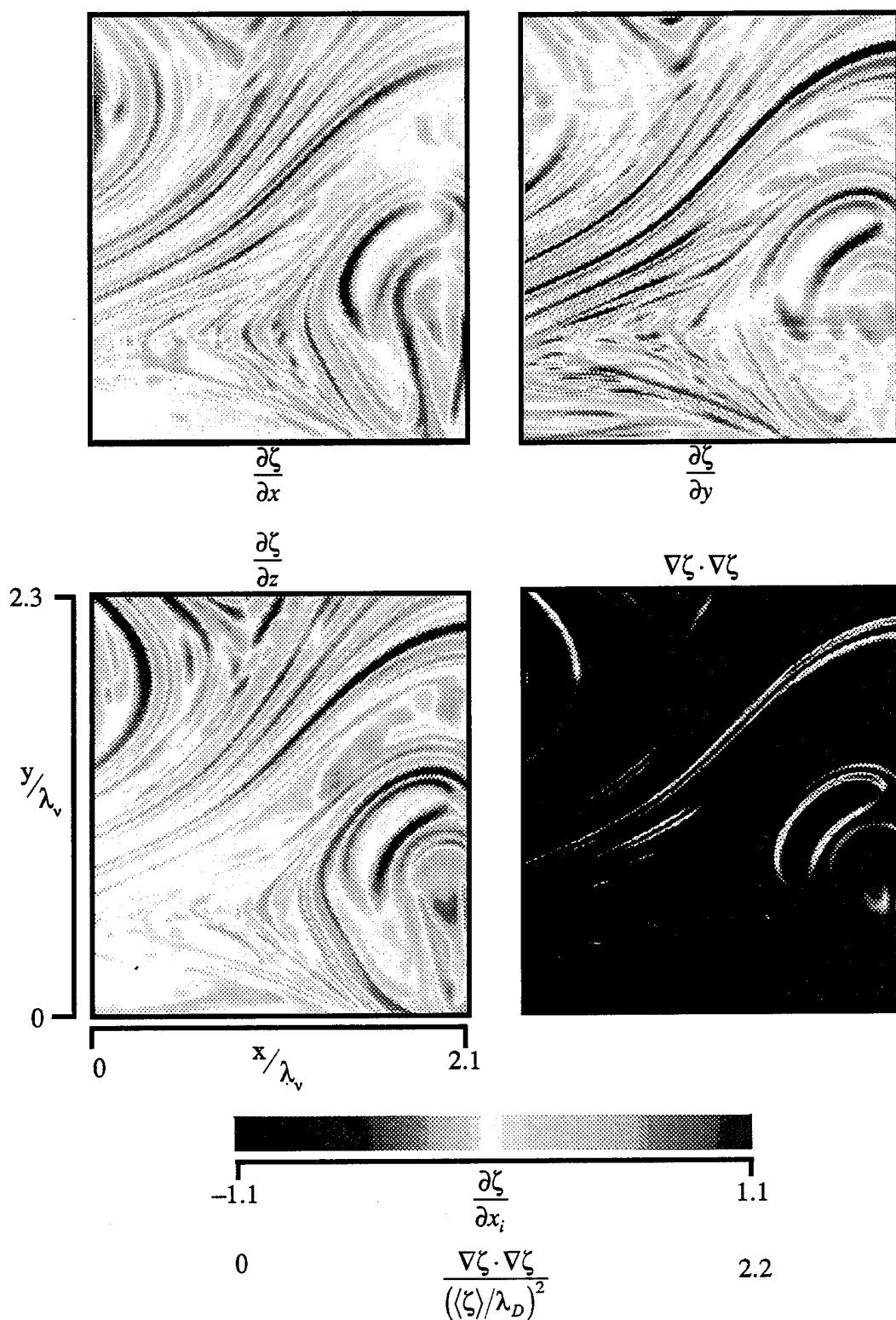


FIGURE 9. Individual scalar gradient vector component fields ( $\partial \zeta / \partial x_i$ ) in the same intersection plane shown in figure 8. Note that positive and negative values are shown with red and blue colorings, respectively. Compare the linear dissipation field with figure 8.

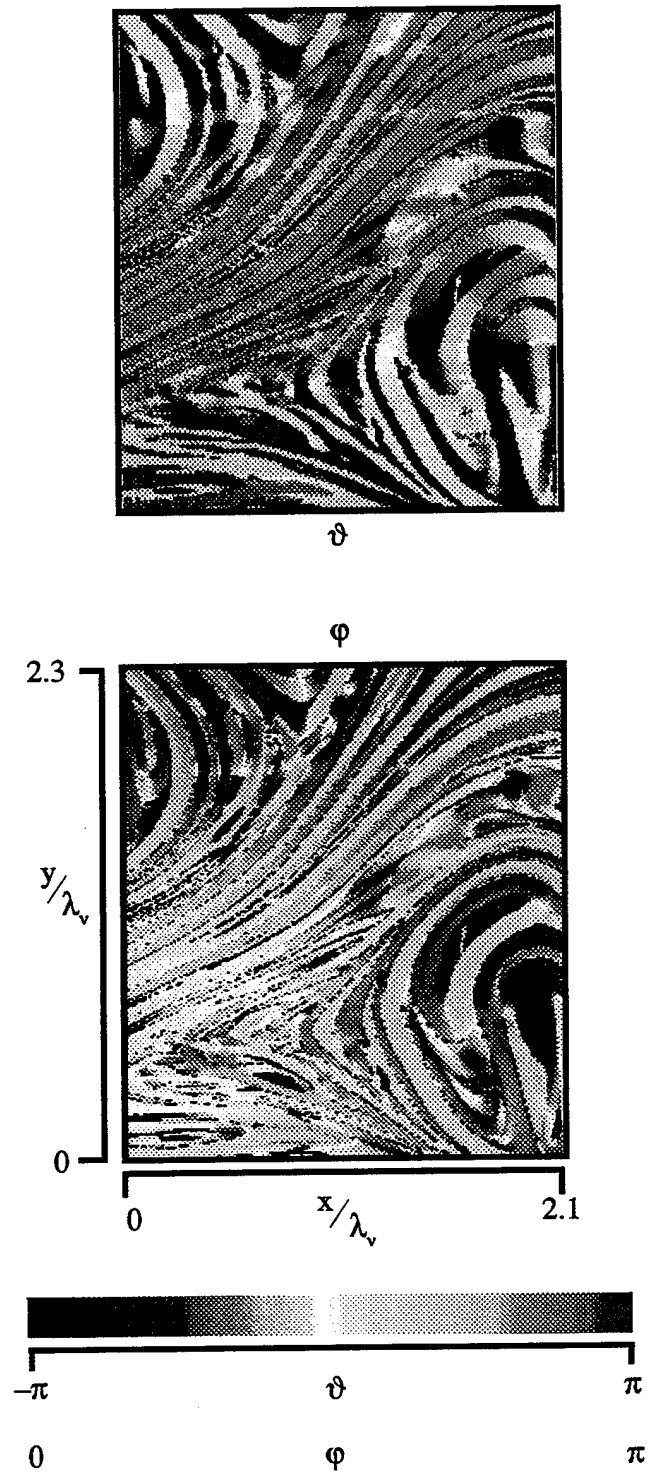


FIGURE 10. The spherical orientation angle fields  $\vartheta(\mathbf{x}, t)$  and  $\varphi(\mathbf{x}, t)$  for the scalar gradient vector field  $\nabla\zeta(\mathbf{x}, t)$  in the same intersection plane shown in figures 8 and 9. Note variations in the scalar gradient orientations occur on the lengthscale  $\lambda_v$  while the vector magnitude varies on the lengthscale  $\lambda_D$ .



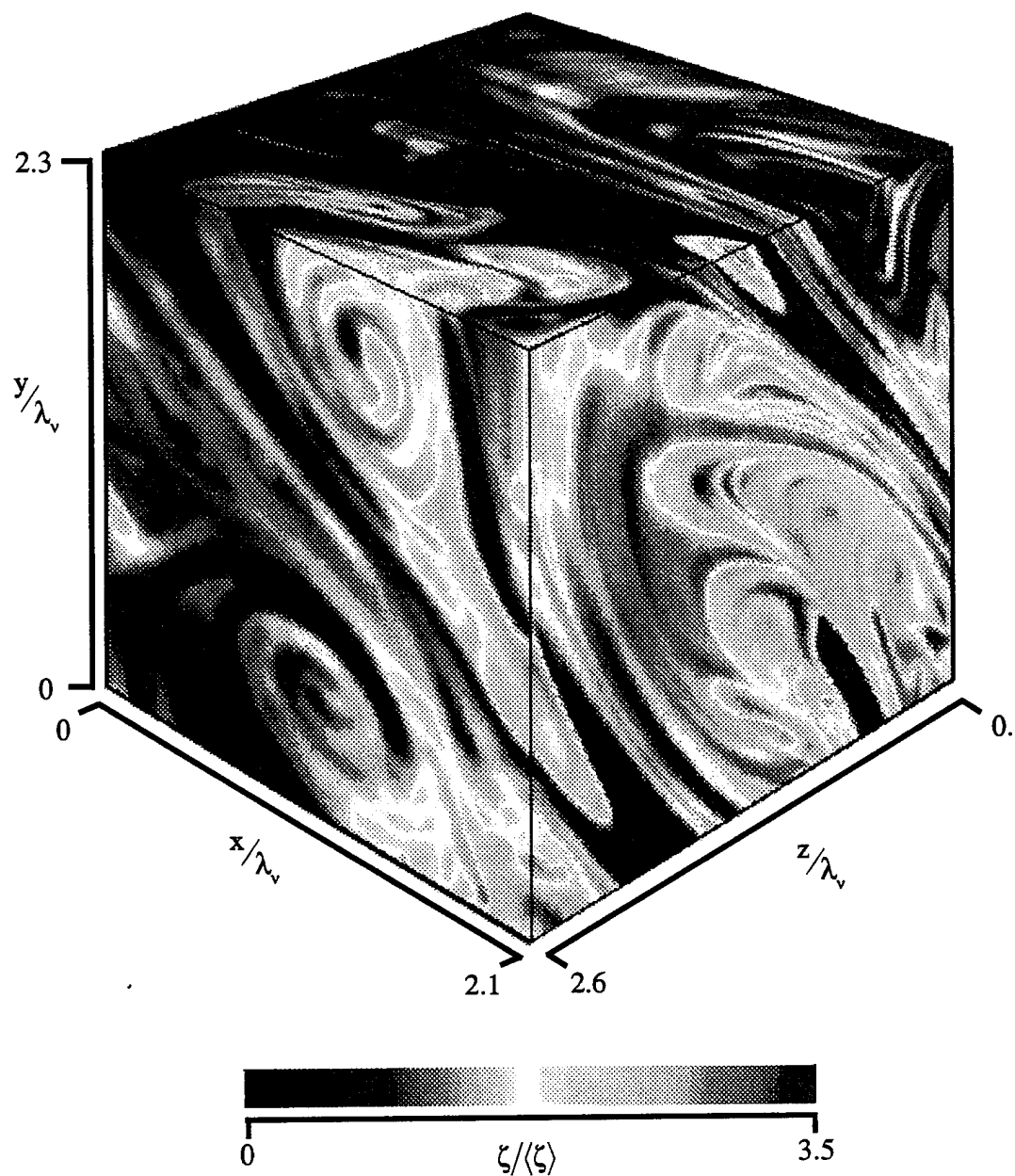


FIGURE 11a. Example of a high-resolution, three-dimensional ( $256^3$ ), spatial data volume (see Fig. 2) from the measured conserved scalar field  $\zeta(\mathbf{x}, t)$  from Case R0703 in Tables 1, 3 and 4. The measurements for each case typically acquire nearly 200 such three-dimensional spatial data volumes, spaced  $\Delta T$  apart in time. Note that each edge of the cubic volume is approximately 20 times smaller than the local outer scale  $\delta(\mathbf{x})$ , and as indicated by the axes is of the order of the local inner scale  $\lambda_v(\mathbf{x})$  of the underlying turbulent flow field.

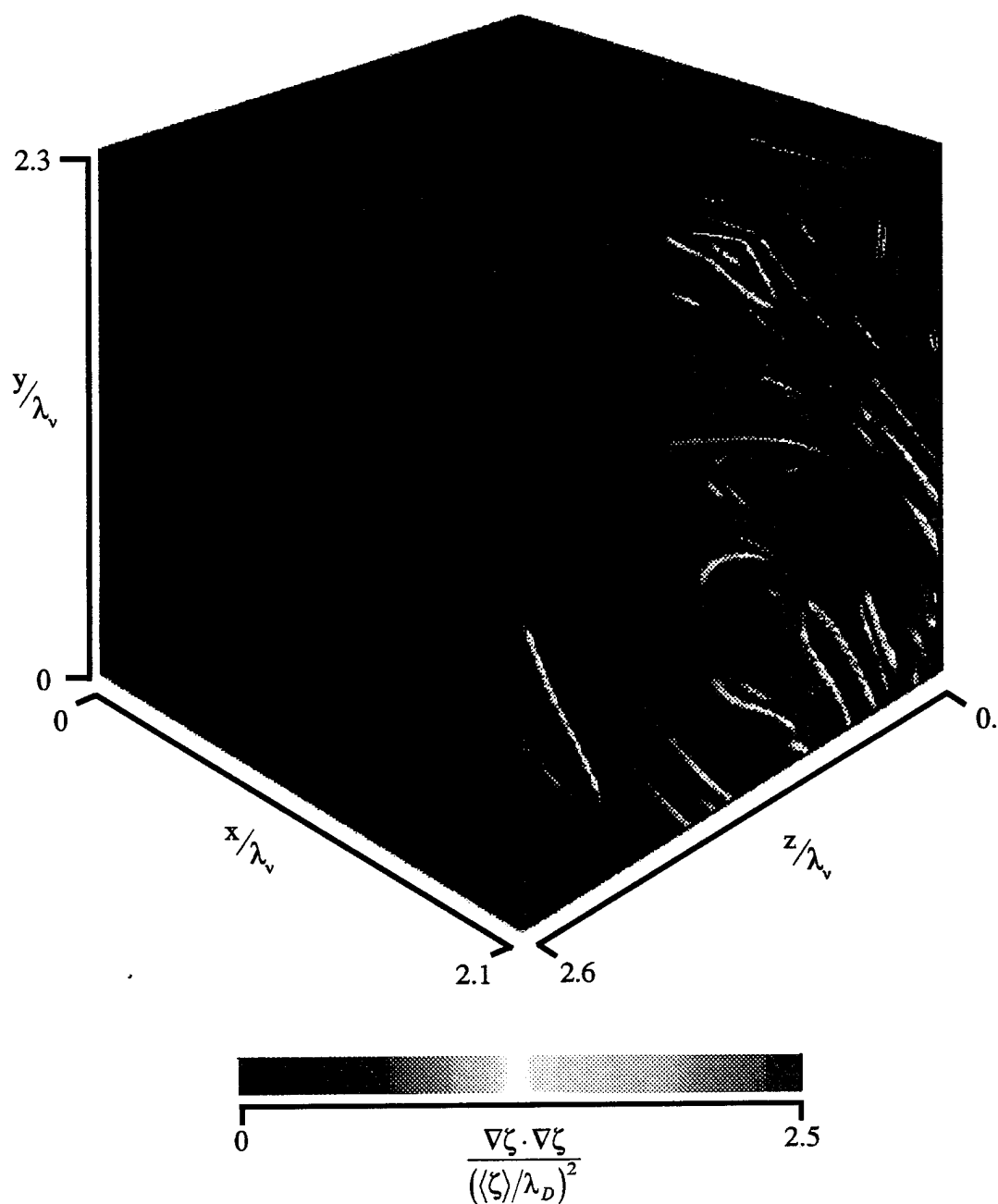


FIGURE 11*b*. The three-dimensional scalar energy dissipation rate field  $\nabla\zeta \cdot \nabla\zeta(\mathbf{x}, t)$  obtained by direct differentiation of the conserved scalar field measurements  $\zeta(\mathbf{x}, t)$  in the same spatial data volume shown in figure 11*a*. No smoothing or filtering has been applied to the resulting derivatives; the smoothness of the dissipation field obtained is a consequence of the high resolution and signal quality attained by the measurements. The dissipation field gives the local instantaneous rate at which the scalar energy per unit mass of fluid,  $\frac{1}{2}\zeta^2(\mathbf{x}, t)$ , is being irreversibly reduced by molecular diffusion in the flow.

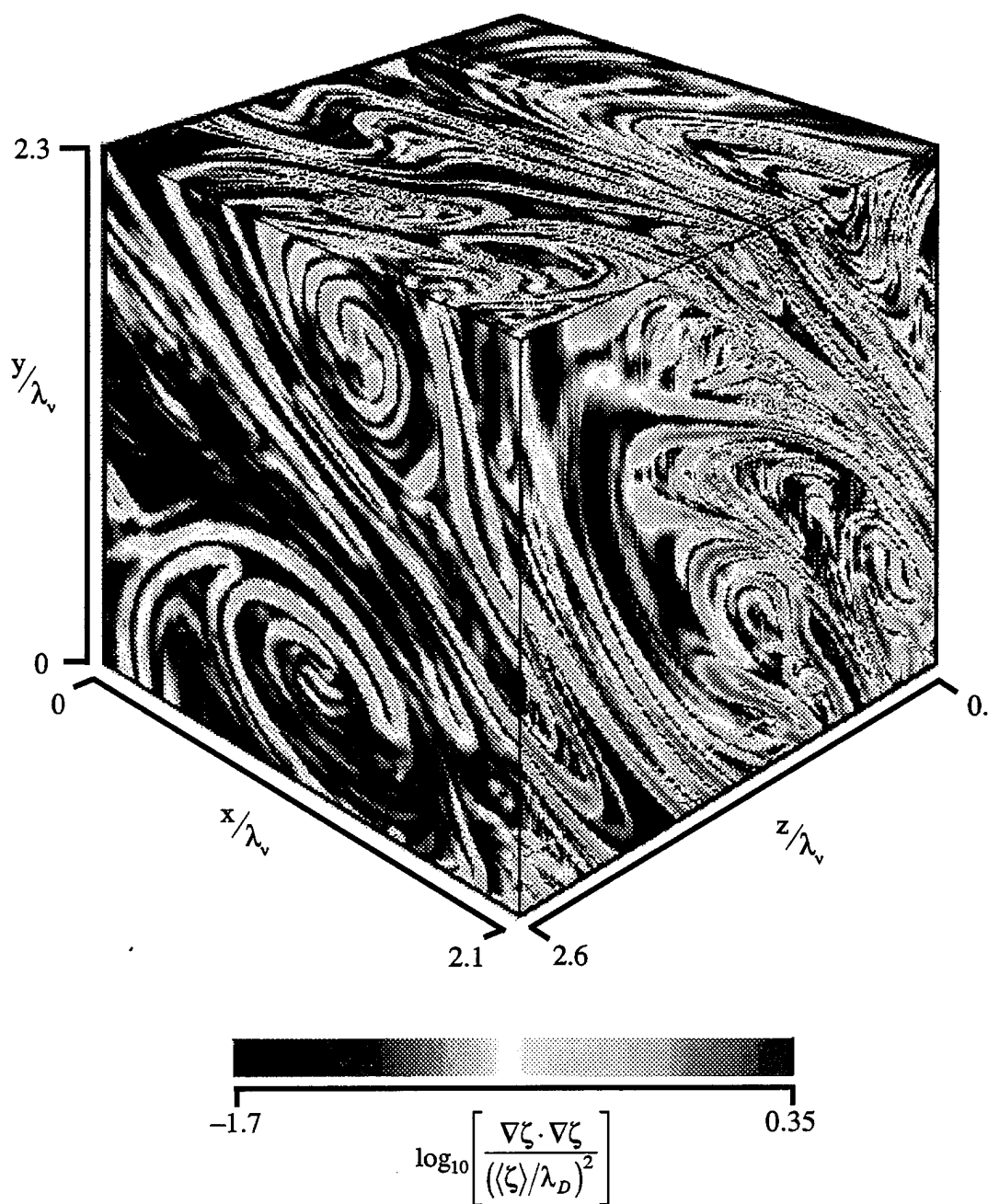


FIGURE 11*c*. The instantaneous scalar energy dissipation rate field  $\log_{10} \nabla \zeta \cdot \nabla \zeta(\mathbf{x}, t)$ , shown in logarithmic form, for the same data volume shown in Figs. 11*a, b*. In this form, it can be readily seen that all the scalar dissipation is confined to thin, sheet-like, strained, laminar diffusion layers, which are stretched and folded by the underlying turbulent strain rate and vorticity fields into a topologically complex surface.

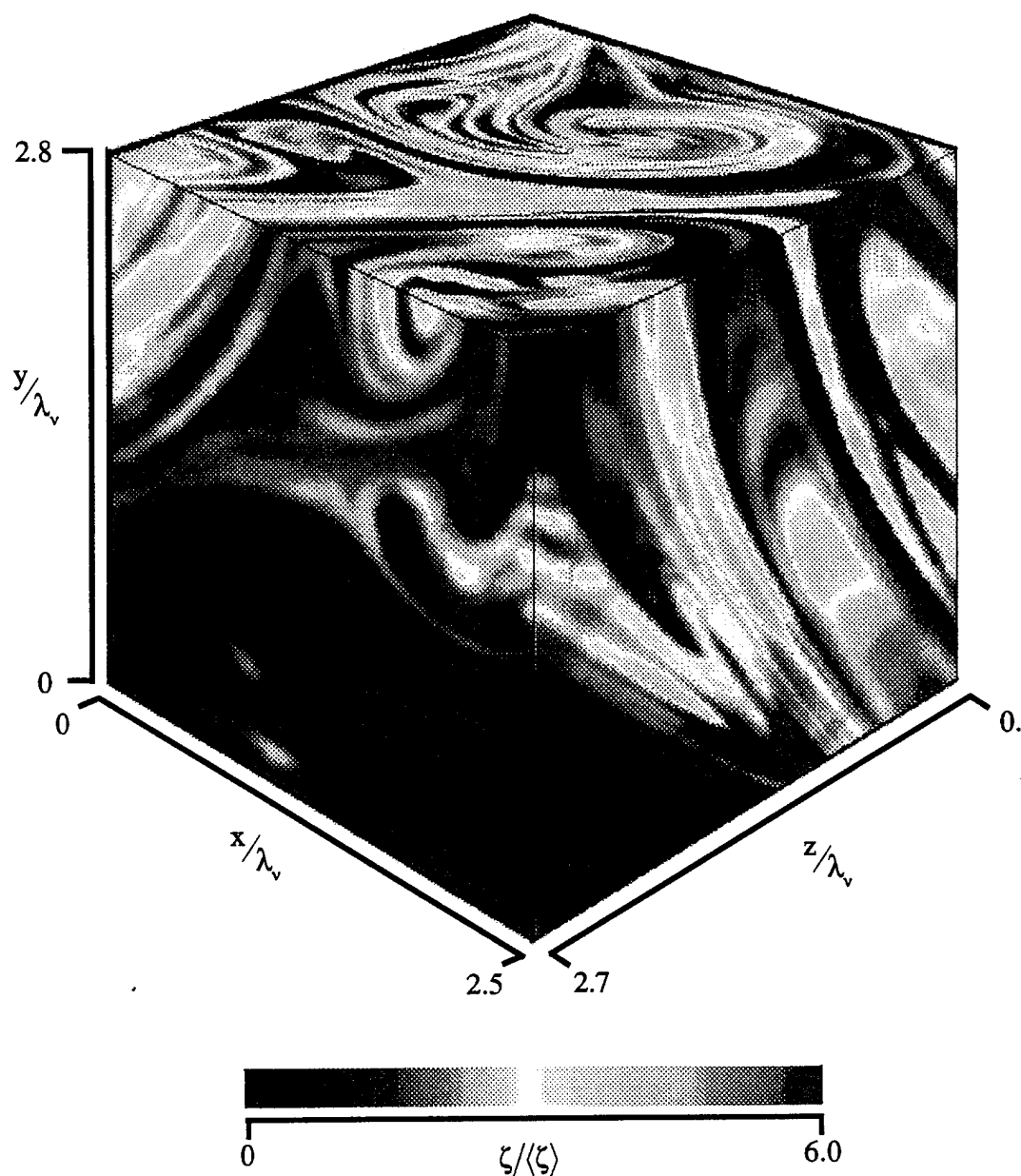


FIGURE 12a. An example of a high-resolution, three-dimensional ( $256^3$ ), spatial data volume from the measured conserved scalar field  $\zeta(\mathbf{x}, t)$  from Case R0806. The axes give the orientation of the cubic volume relative to the flow. Note in comparing among figures 11 through 13 that no preferred orientation is readily apparent in the mixing process at these scales, suggesting near isotropy of the small scales of the flow. Slight anisotropies consistent with the orientation of the principal axes of the mean strain rate field are, however, revealed by detailed numerical analyses of these volumes.

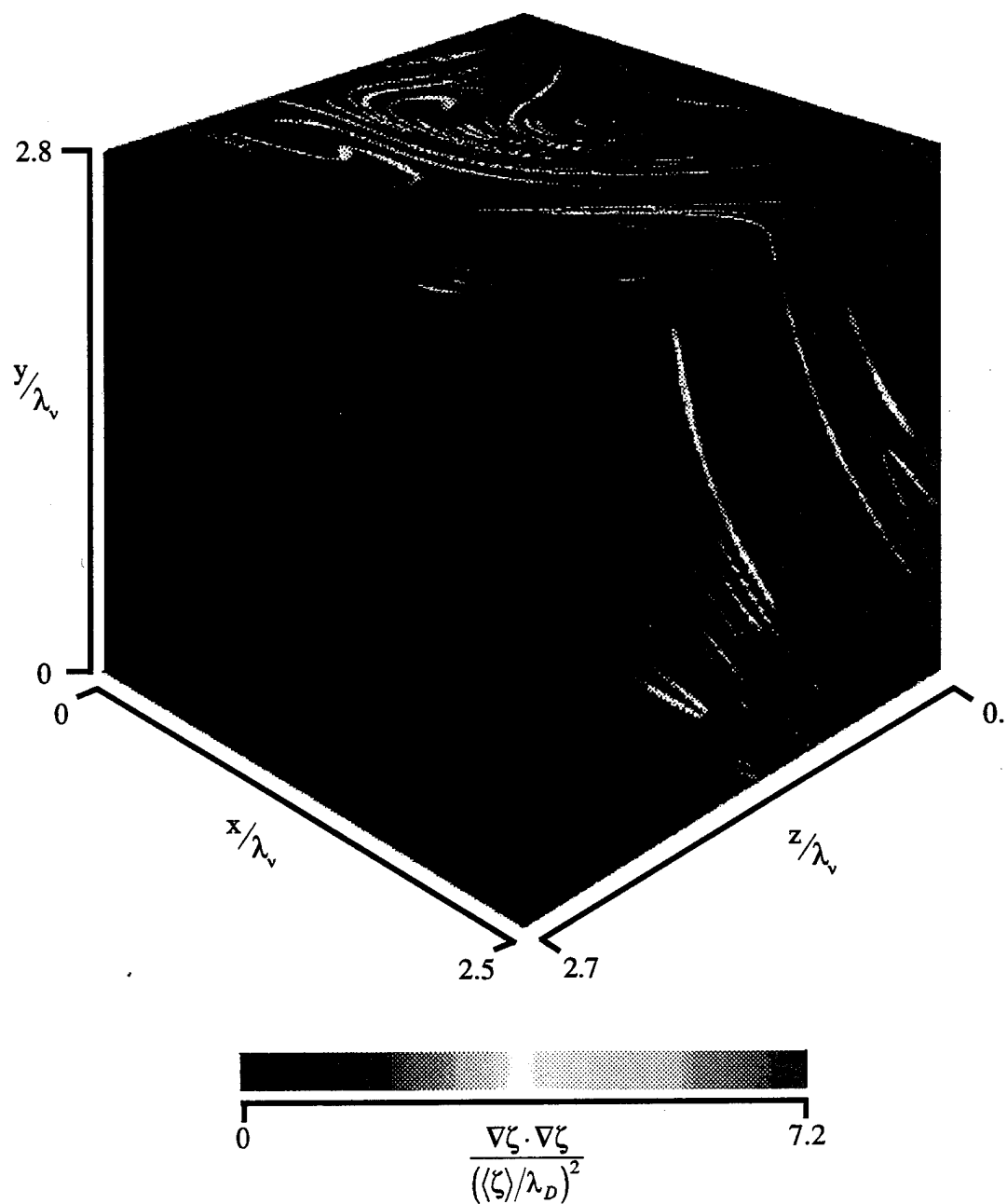


FIGURE 12*b*. The three-dimensional scalar energy dissipation rate field  $\nabla\zeta \cdot \nabla\zeta(\mathbf{x}, t)$  corresponding to the conserved scalar field measurements  $\zeta(\mathbf{x}, t)$  in Fig. 12*a*. Note the high degree of internal intermittency evident in these scalar dissipation fields, where large values of the dissipation rate are seen only very rarely, and most of the data volume contains very low dissipation rates.

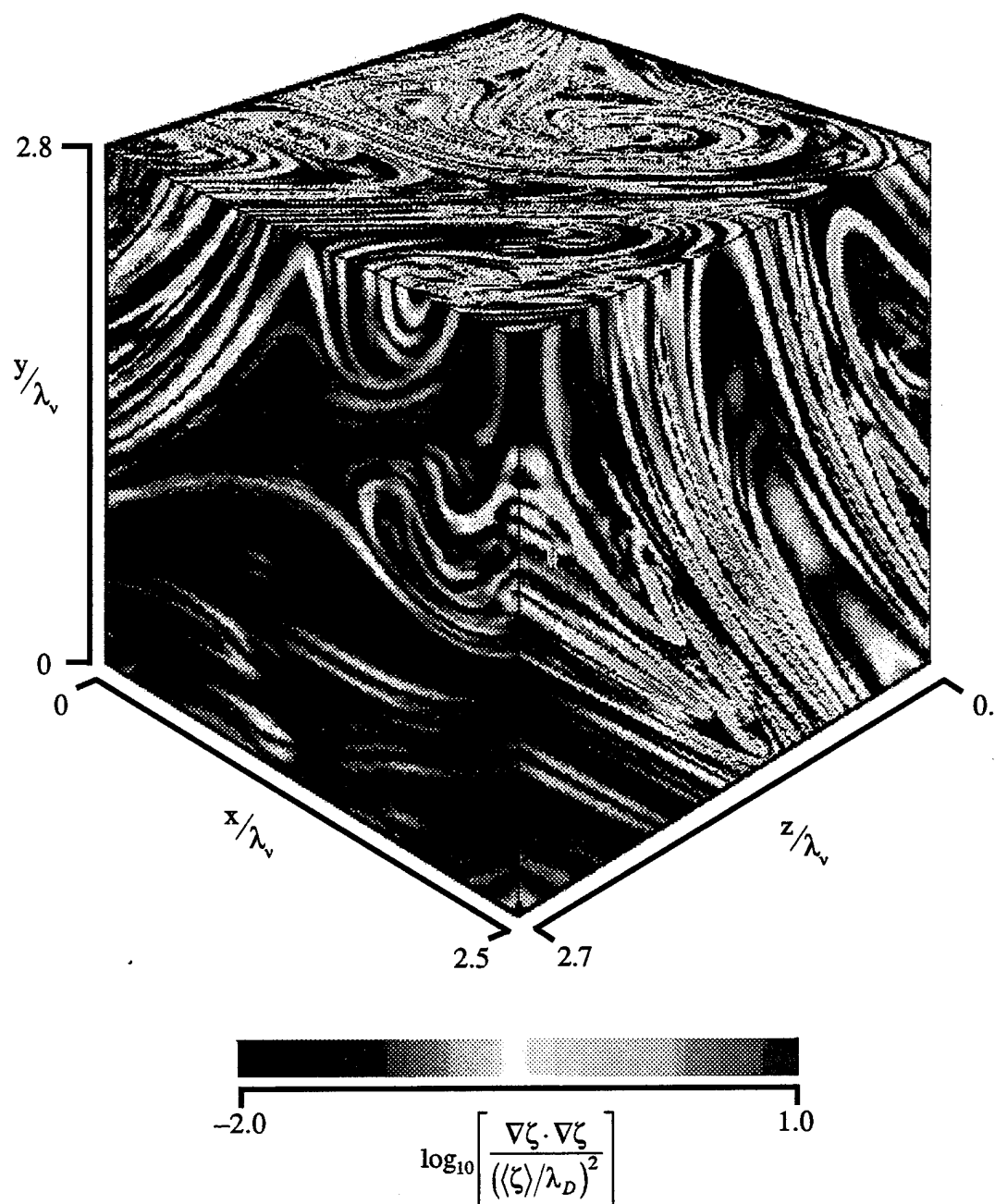


FIGURE 12c. The instantaneous scalar energy dissipation rate field  $\log_{10} \nabla \zeta \cdot \nabla \zeta(\mathbf{x}, t)$  in logarithmic form for the same data volume shown in Figs. 12a,b. The high internal intermittency is evident here as well. In this form it can be seen that this intermittency results from the concentration of scalar gradients in thin, sheet-like layers formed by the competing effects of strain and molecular diffusion in the flow. The stretching and folding of these sheets by the small scale motion in the underlying turbulent flow produces the wide distribution of striation thickness evident in these data.

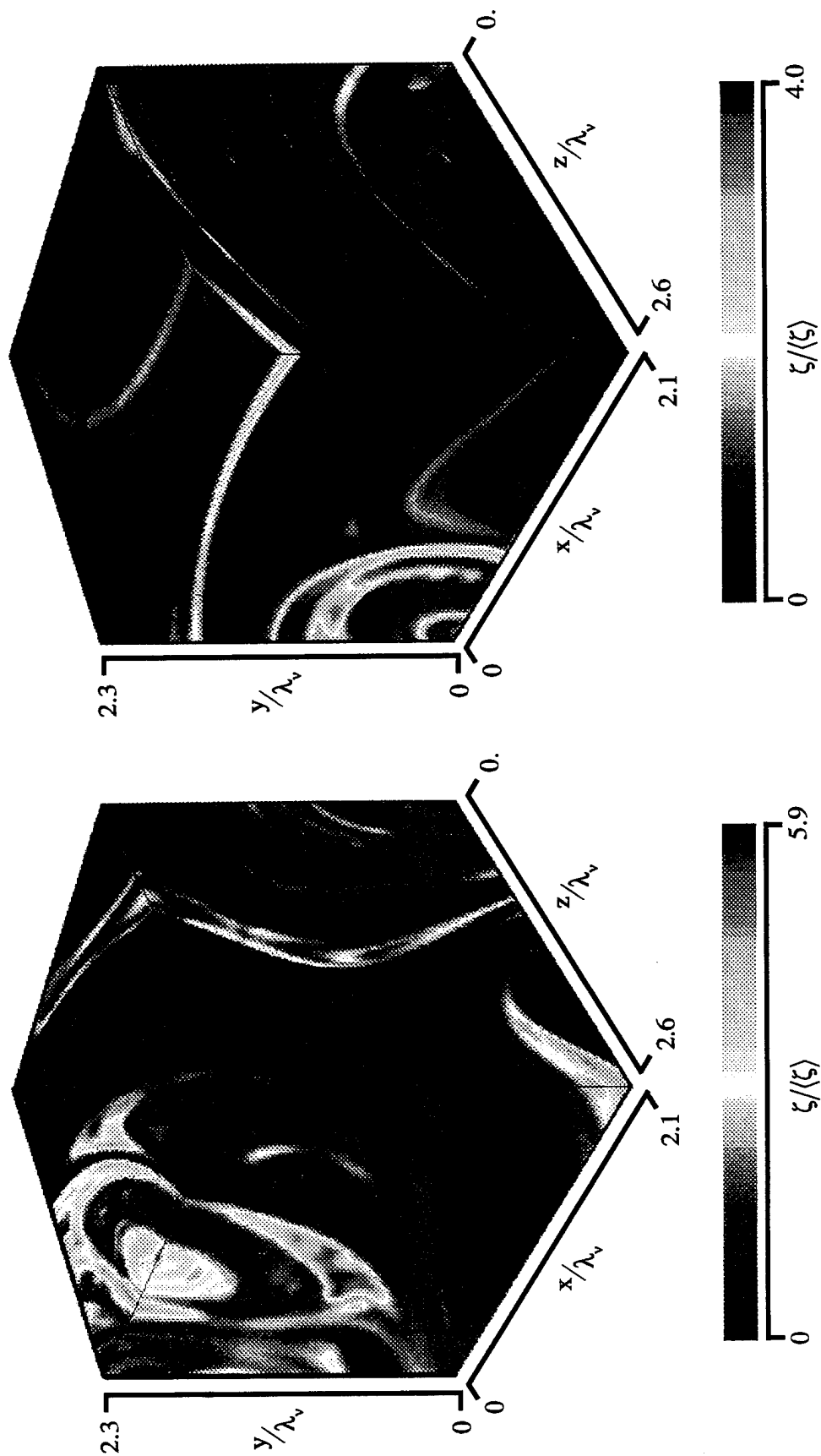


FIGURE 13a. Two further examples of individual, three-dimensional ( $256^3$ ), spatial data volumes from the conserved scalar field measurements in Cases R0703 (left) and R0806 (right).

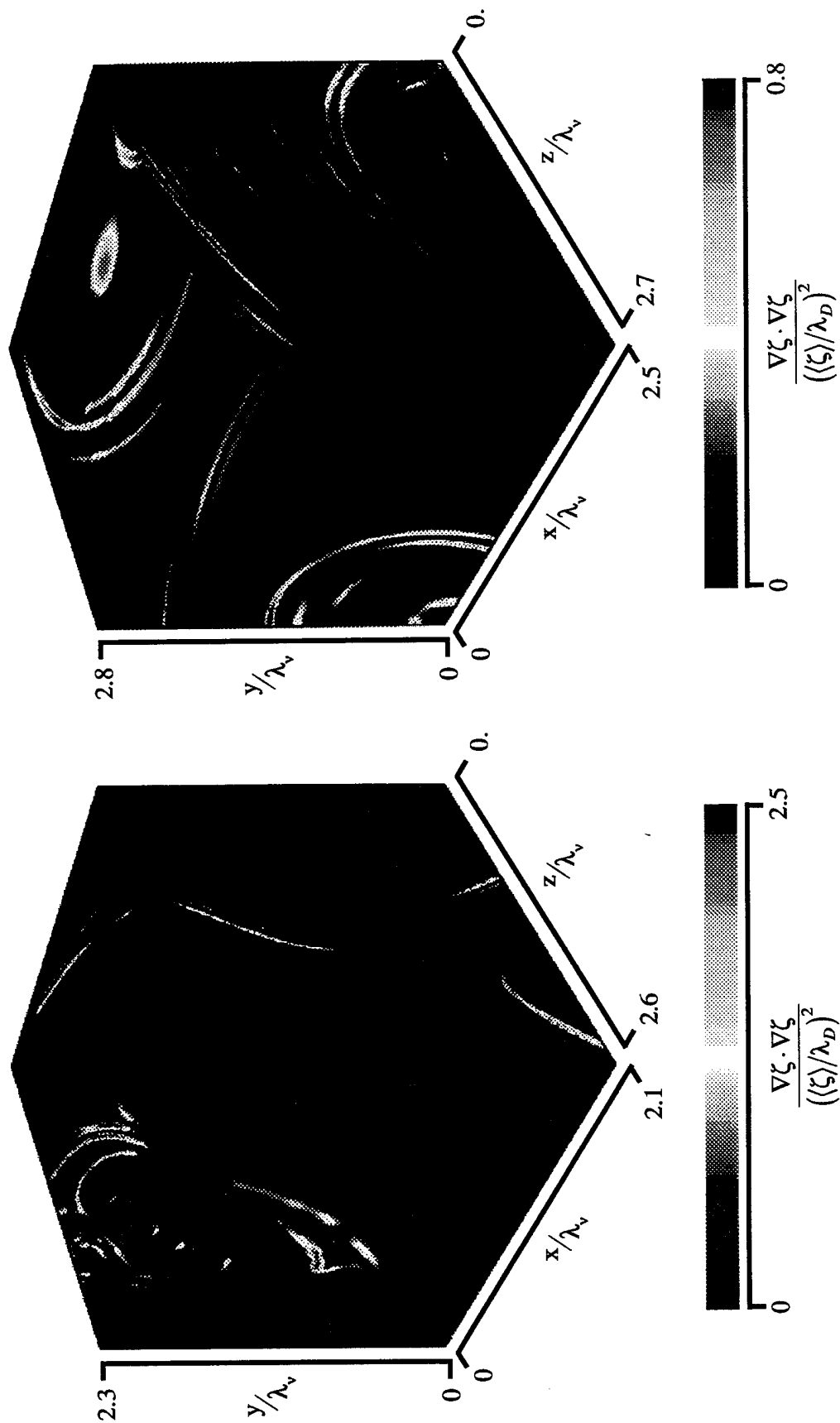


FIGURE 13*b*. The instantaneous three-dimensional scalar energy dissipation rate fields corresponding to the conserved scalar data volumes in Fig. 13*a*. Note the high degree of internal intermittency resulting from the layer-like structure in these dissipation fields.



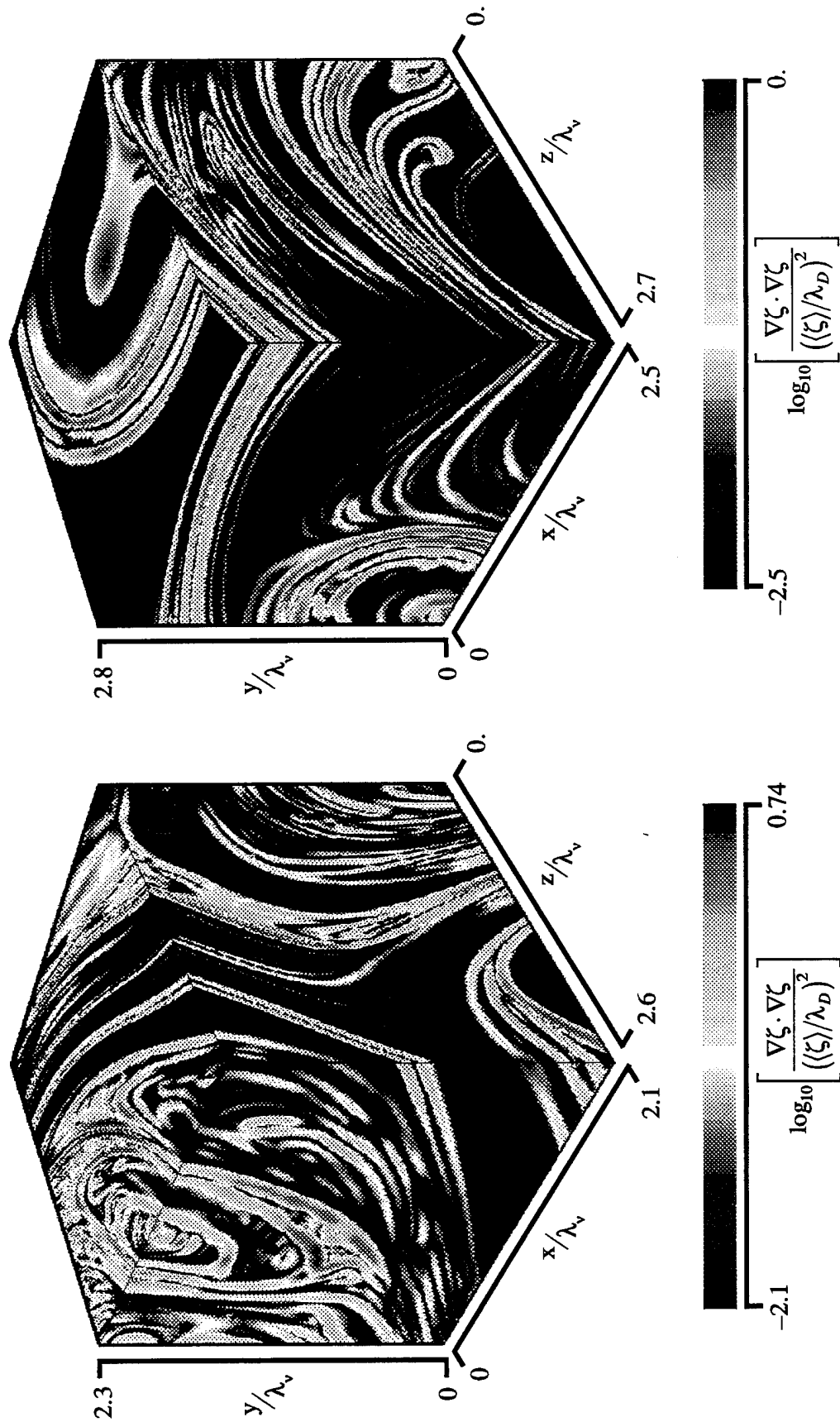


FIGURE 13c. The logarithm of the scalar dissipation fields for the same data volumes shown in figures 13a,b. The striation thickness distribution that results from the layer-like small scale structure of turbulent mixing is analyzed in section 5.

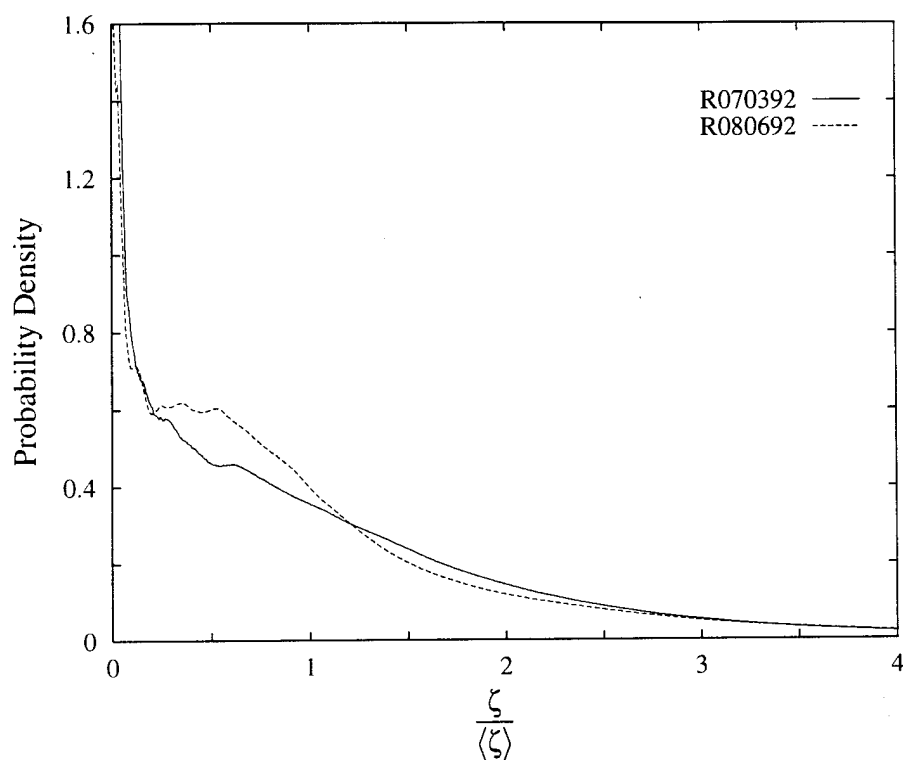


FIGURE 15. The probability density function of the conserved scalar  $\zeta(\mathbf{x},t)$  determined from measurements in two cases, shown normalized with the local mean scalar value. Note that the long tail at large scalar values appears consistent with other measurements of the peak normalized scalar values at this radial location in the turbulent jet.

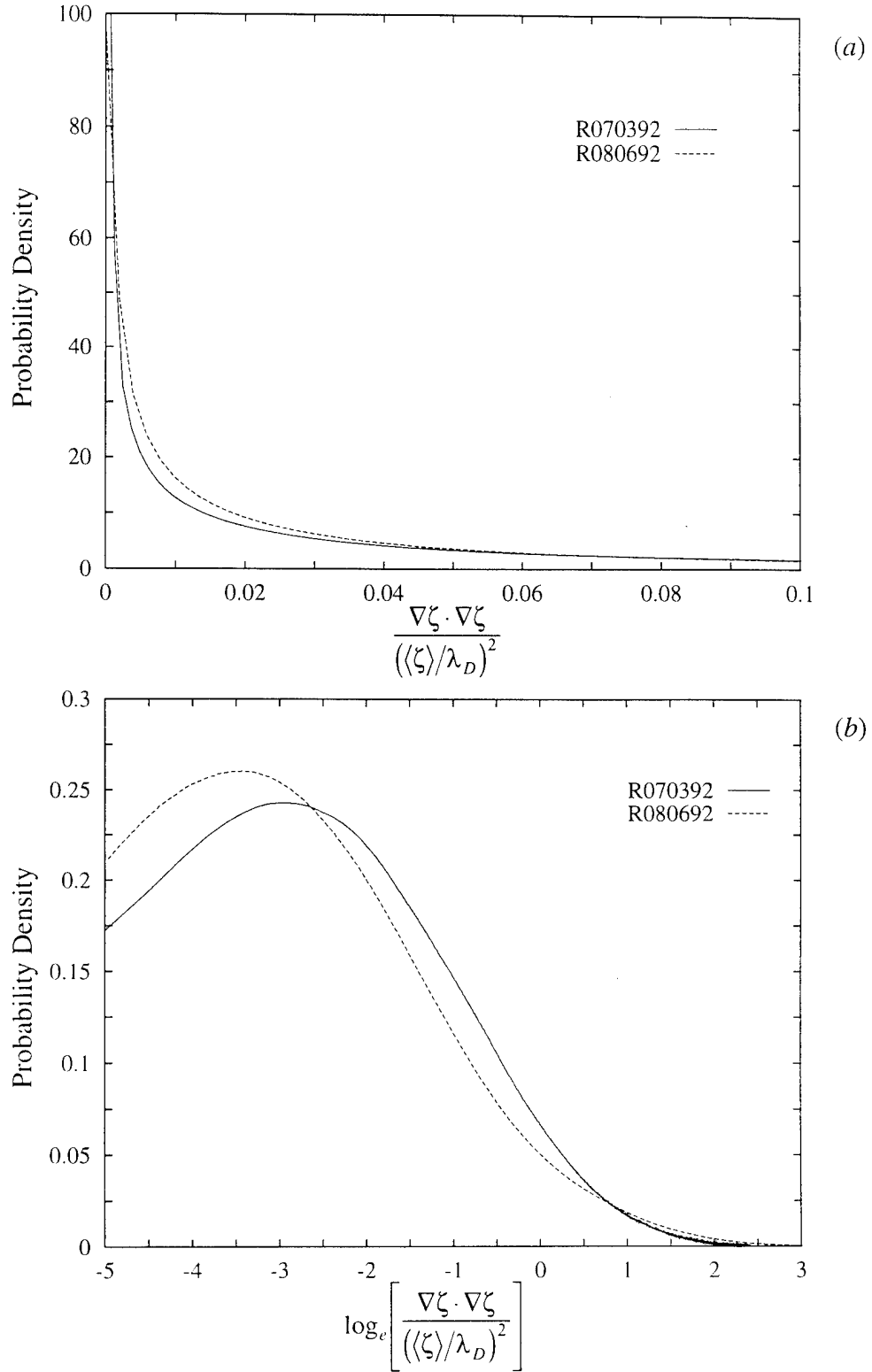


FIGURE 16. Probability densities of the scalar energy dissipation rate  $\nabla \zeta \cdot \nabla \zeta(\mathbf{x}, t)$  determined for the same two cases as in figure 15. Shown are (a) the probability densities of  $\nabla \zeta \cdot \nabla \zeta(\mathbf{x}, t)$  normalized by inner variables; (b) the probability densities of  $\log_e \nabla \zeta \cdot \nabla \zeta(\mathbf{x}, t)$  normalized by inner variables; (c) a comparison of the probability density of  $\log_e \nabla \zeta \cdot \nabla \zeta(\mathbf{x}, t)$  with the lognormal distribution.

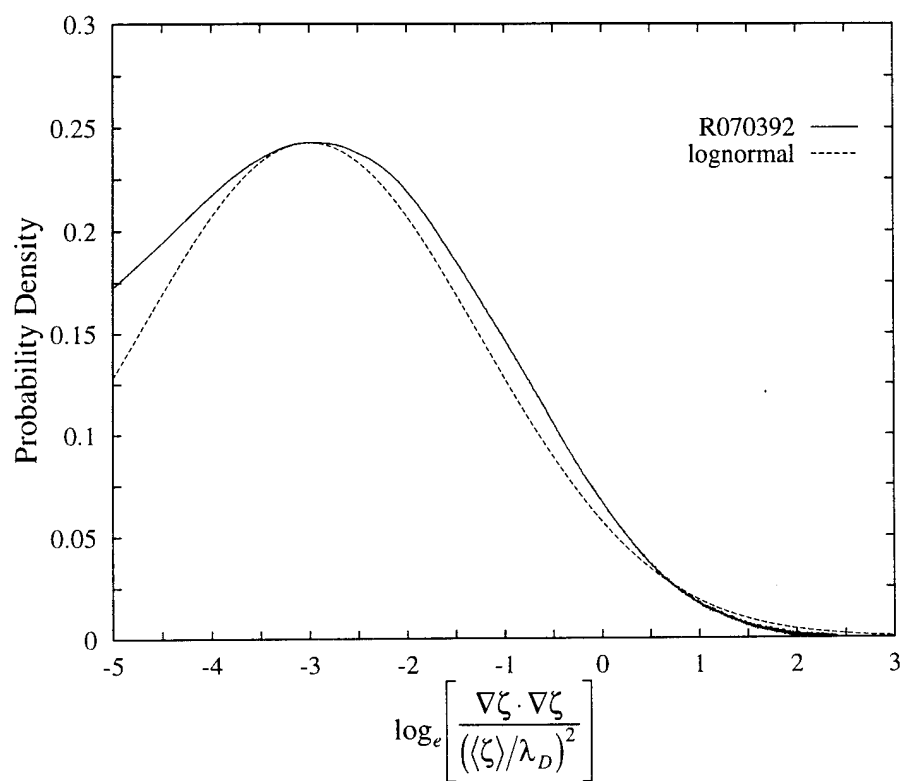


FIGURE 16. (concluded).

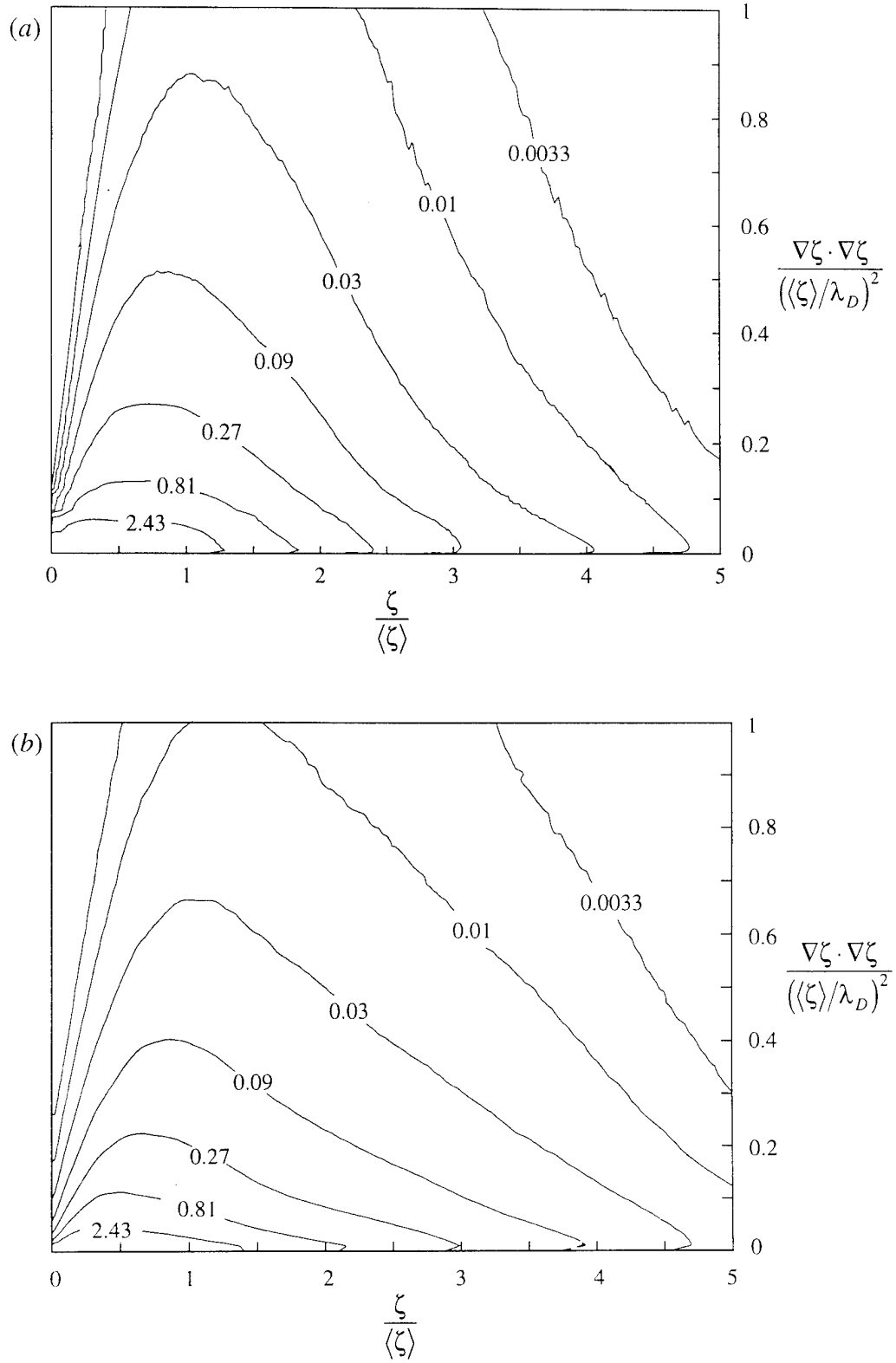


FIGURE 17. The joint probability densities of the conserved scalar field  $\zeta(\mathbf{x}, t)$  and the scalar energy dissipation rate field  $\nabla \zeta \cdot \nabla \zeta(\mathbf{x}, t)$  normalized by inner variables for the same two cases as in figures 15 and 16. Shown are: (a) case R0703; (b) case R0806.

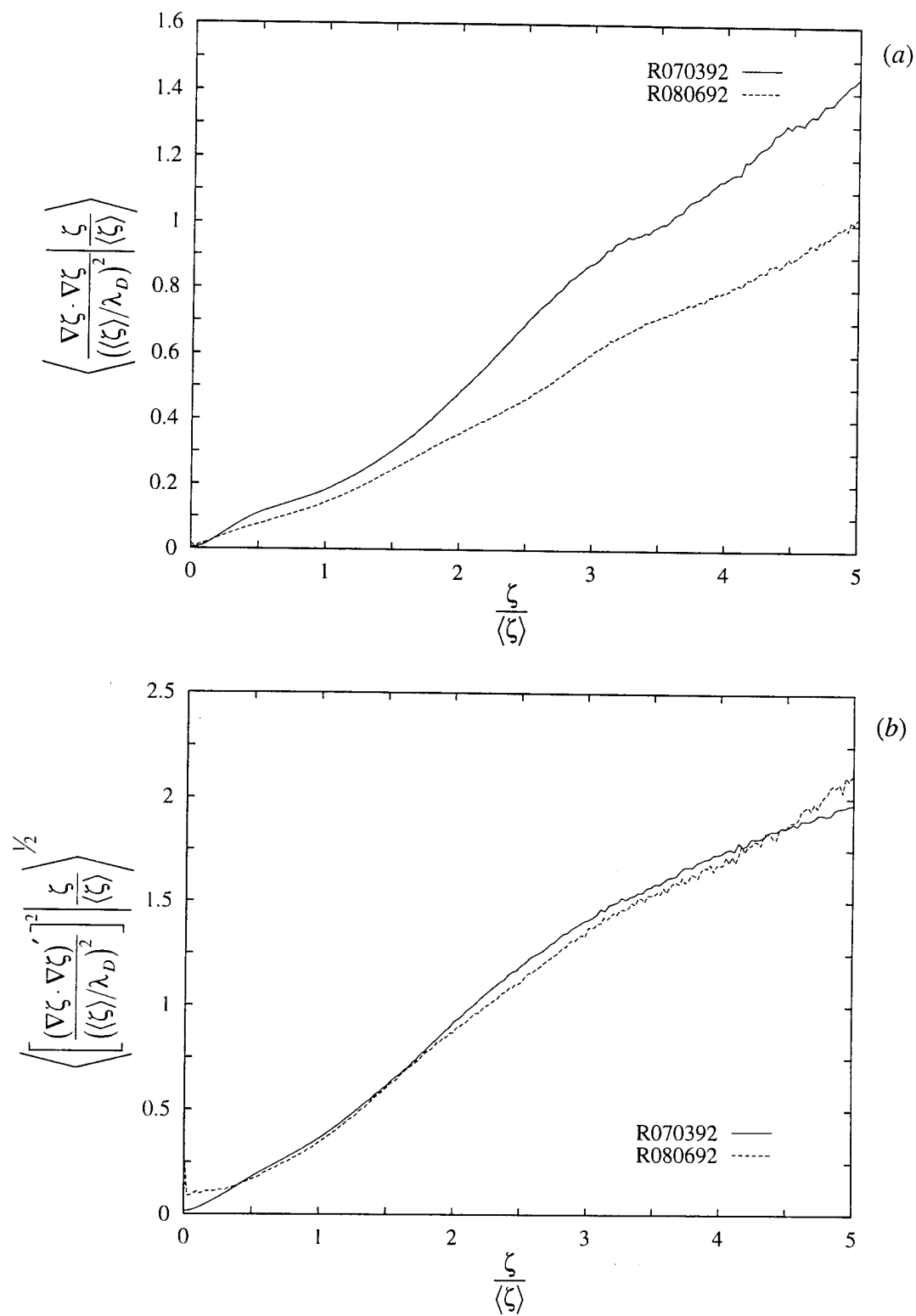


FIGURE 18. Conditional statistics of the scalar dissipation rate field normalized by inner variables for the same two cases. Shown are: (a) the conditional mean dissipation; (b) the conditional variance of the dissipation.

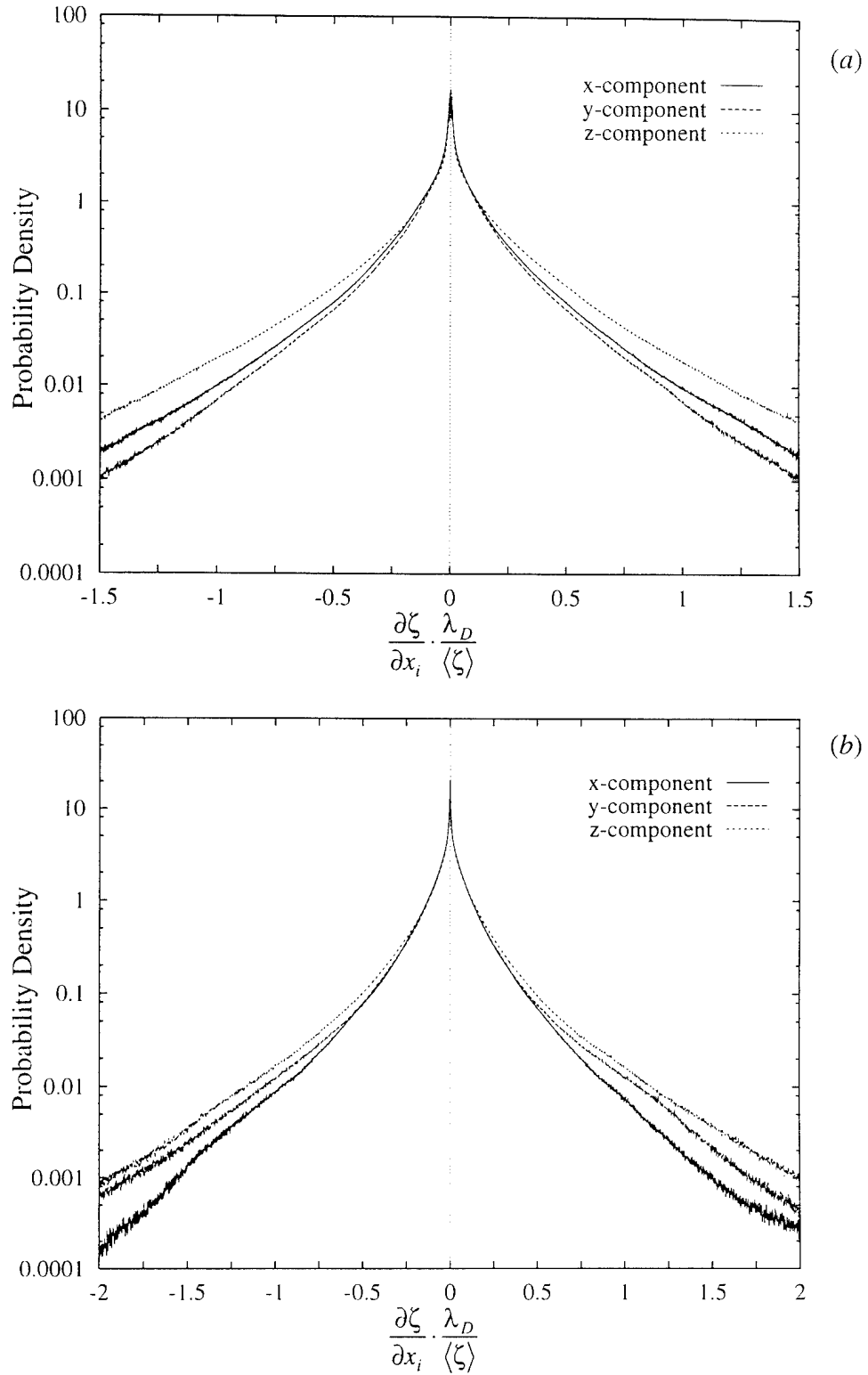


FIGURE 19. Probability densities of the individual scalar gradient vector component fields  $\partial \zeta / \partial x_i(\mathbf{x}, t)$  normalized by inner variables for the same two cases. Shown are: (a) case R0703; (b) case R0806. Note that positive  $x$  represents the radial outward direction, positive  $y$  the upstream direction, and  $z$  the azimuthal direction.

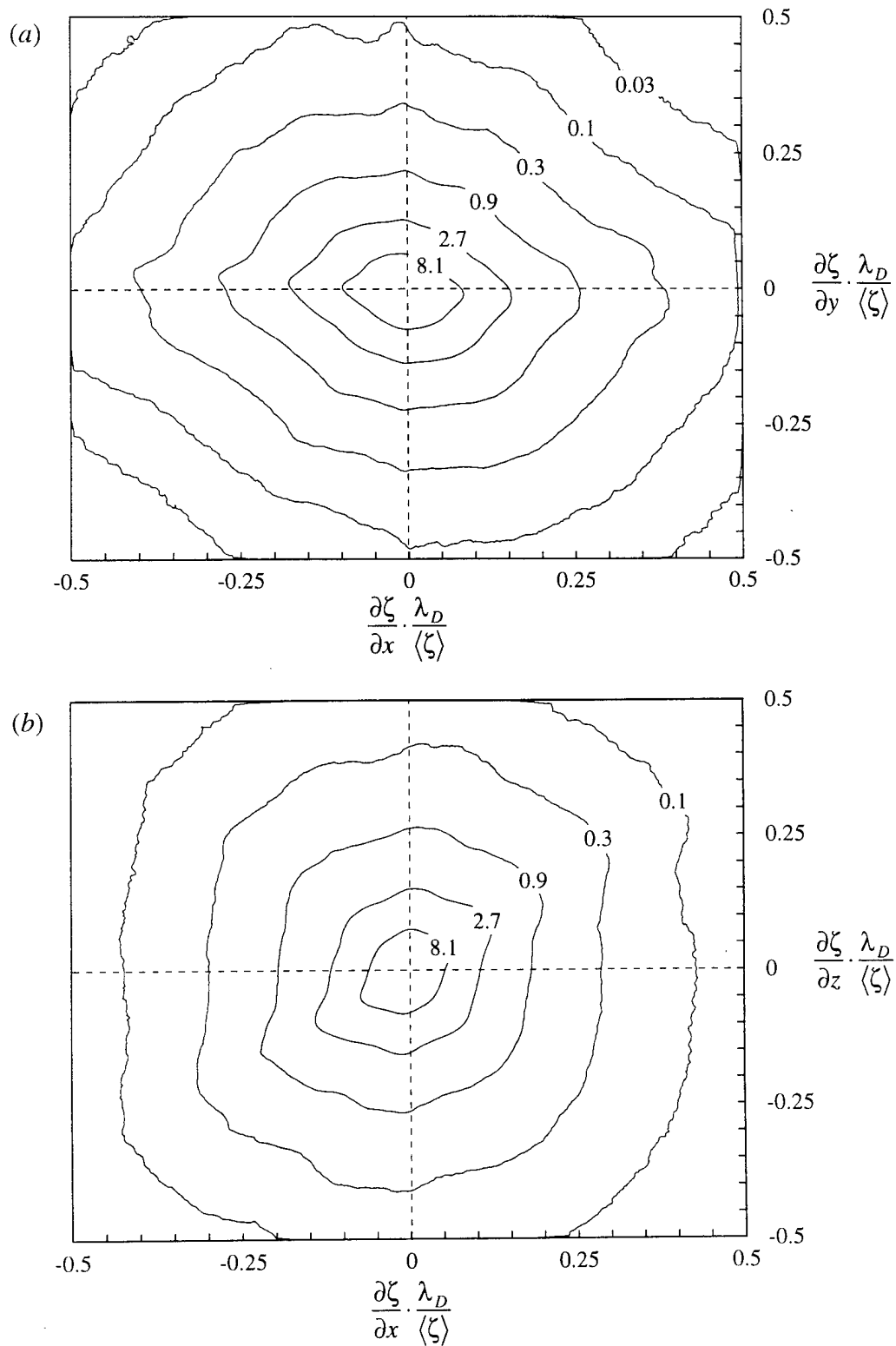


FIGURE 20. Joint probability densities of the individual scalar gradient vector component fields  $\partial \zeta / \partial x_i(\mathbf{x}, t)$  normalized by inner variables. Shown are: (a) the joint pdf between the x- and y-derivatives; (b) the joint pdf between the x- and z-derivatives; (c) the joint pdf between the y- and z-derivatives.



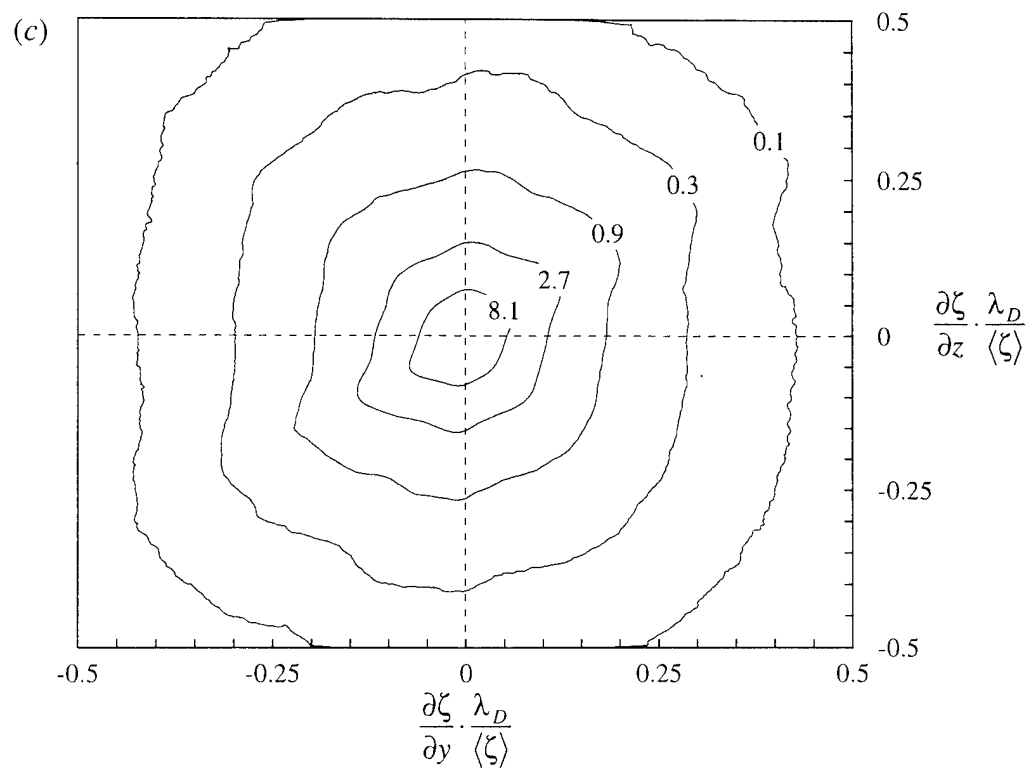


FIGURE 20. (concluded).

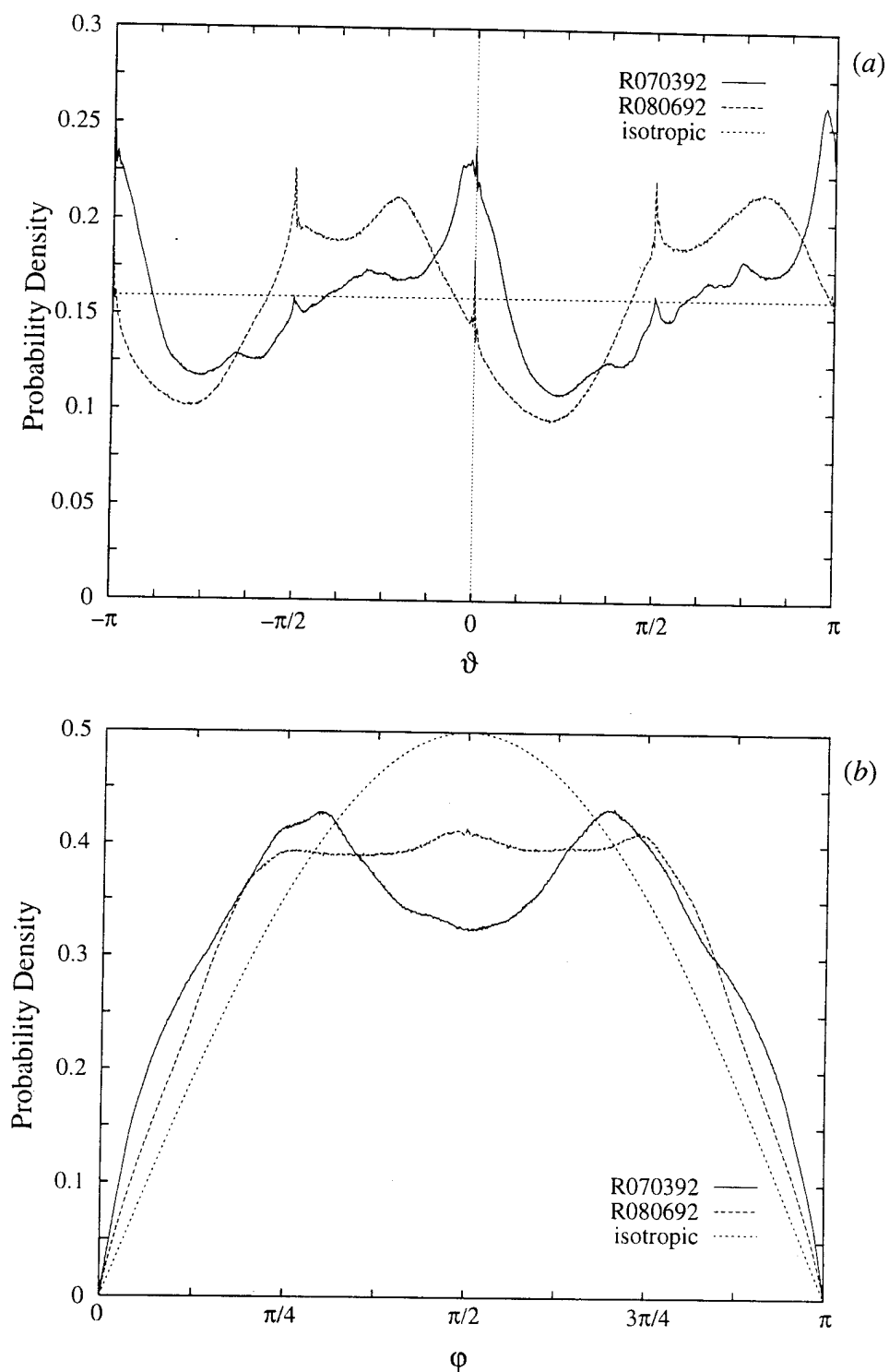


FIGURE 21. Probability densities of the spherical orientation angles ( $\vartheta$ ,  $\varphi$ ) specifying the scalar gradient vector orientation. Shown are: (a) the pdf of  $\vartheta$ , giving the angle between the projection of the scalar gradient vector into the x-y plane and the x-axis; (b) the pdf of  $\varphi$ , giving the angle between the scalar gradient vector and the z-axis. In each case, also shown is the corresponding isotropic distribution.

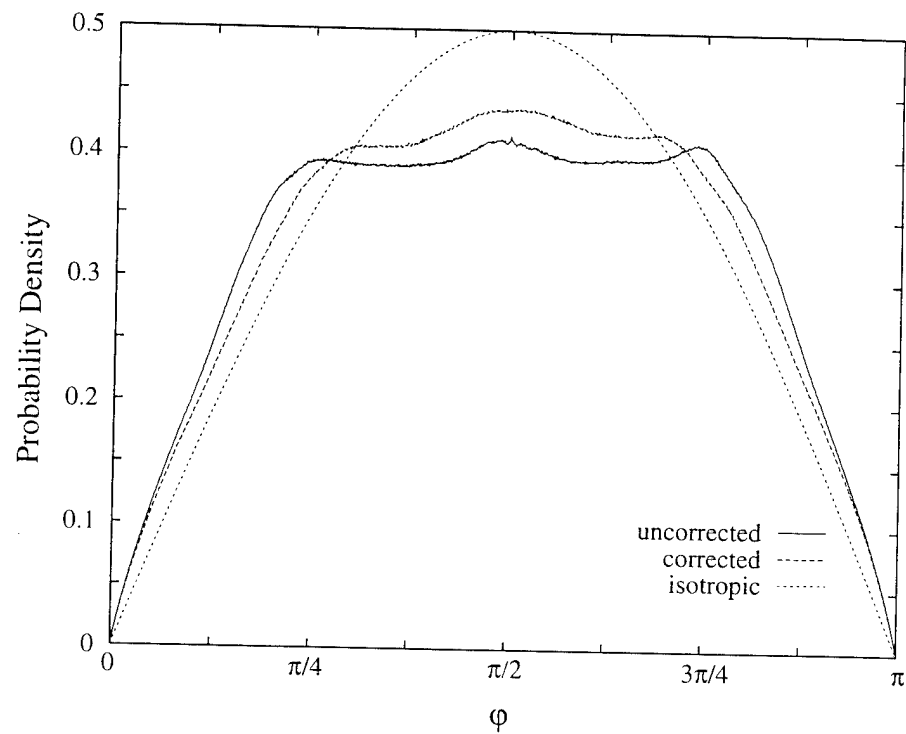


FIGURE 22. The probability density function of the scalar gradient vector orientation angle  $\phi$ , showing the distribution before and after the mean flow slewing correction, together with the corresponding isotropic distribution.

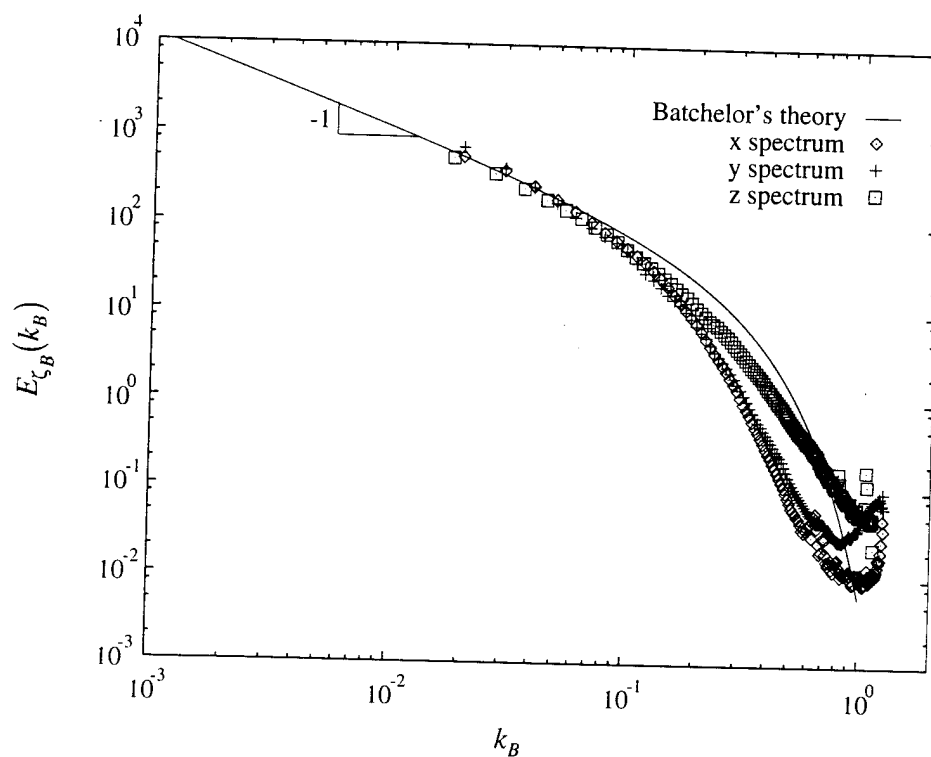


FIGURE 23a. One-dimensional spatial scalar energy spectra determined from each of the three orthogonal directions in three-dimensional ( $256^3$ ) spatial data volumes of the type shown in Figs. 11 through 13, compared with the Batchelor (1959) theory with  $q = 5$  for the high wavenumber spectrum in  $Sc \gg 1$  scalar mixing in turbulent flows. The data are presented in Batchelor-normalized form.

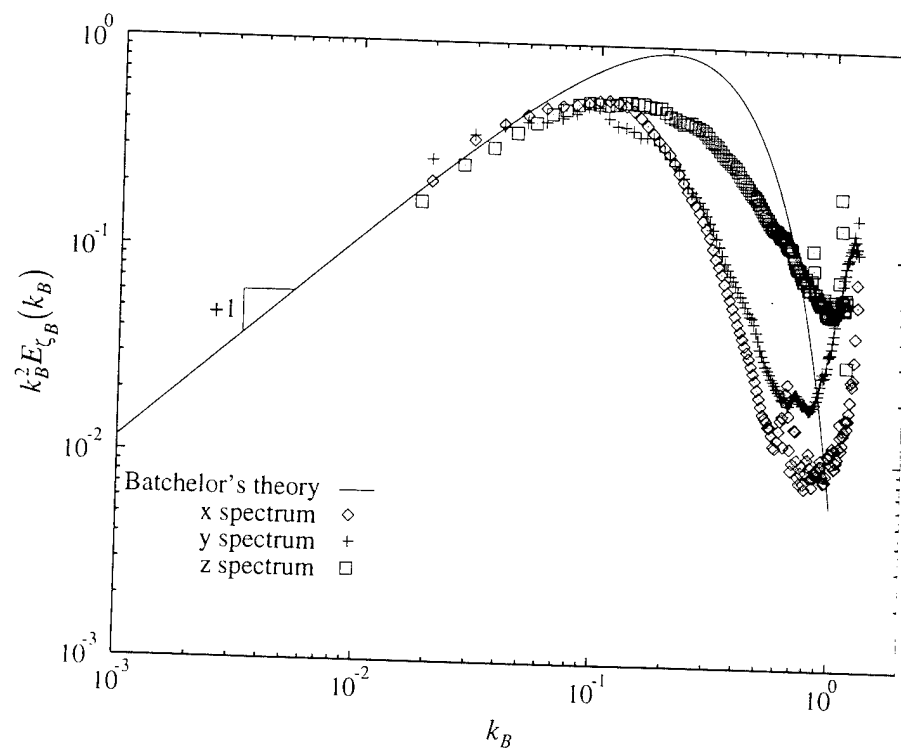


FIGURE 23*b*. The one-dimensional spatial scalar energy spectra from Fig. 23*a* shown plotted in dissipation form, compared with the Batchelor (1959) theory with  $q = 5$ . Note the approximate asymptote to the  $k^{-1}$  scaling in the viscous-convective subrange.

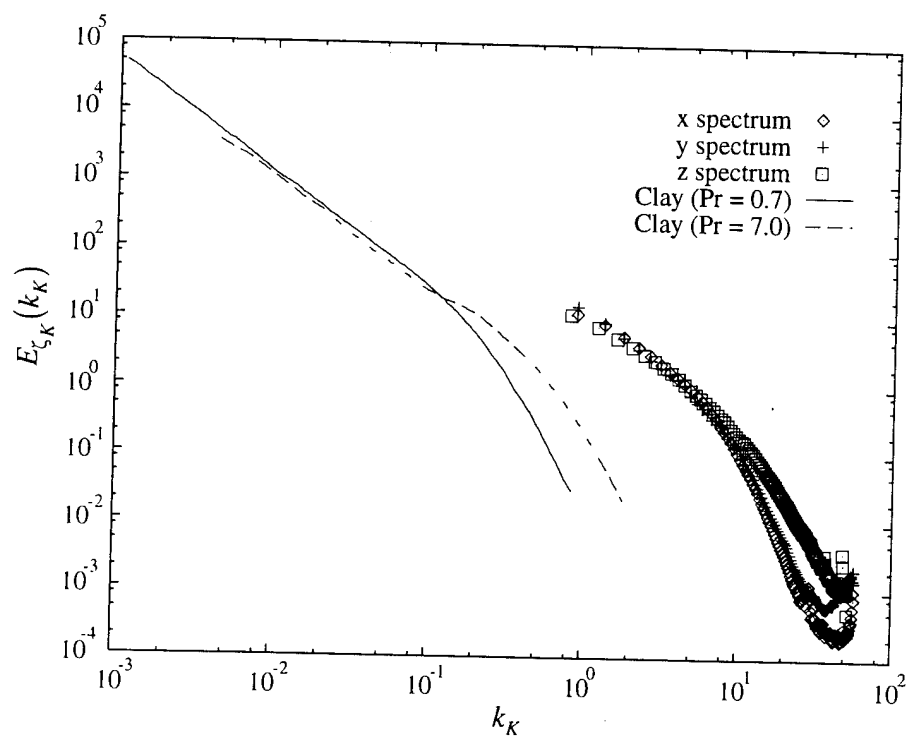


FIGURE 24. Comparison of the present one-dimensional spatial scalar energy spectra obtained for  $Sc = 2075$  with the temporal spectra of Clay (1973) for  $Pr = 0.7$  and  $Pr = 7.0$ . The data are presented in Kolmogorov-normalized form.

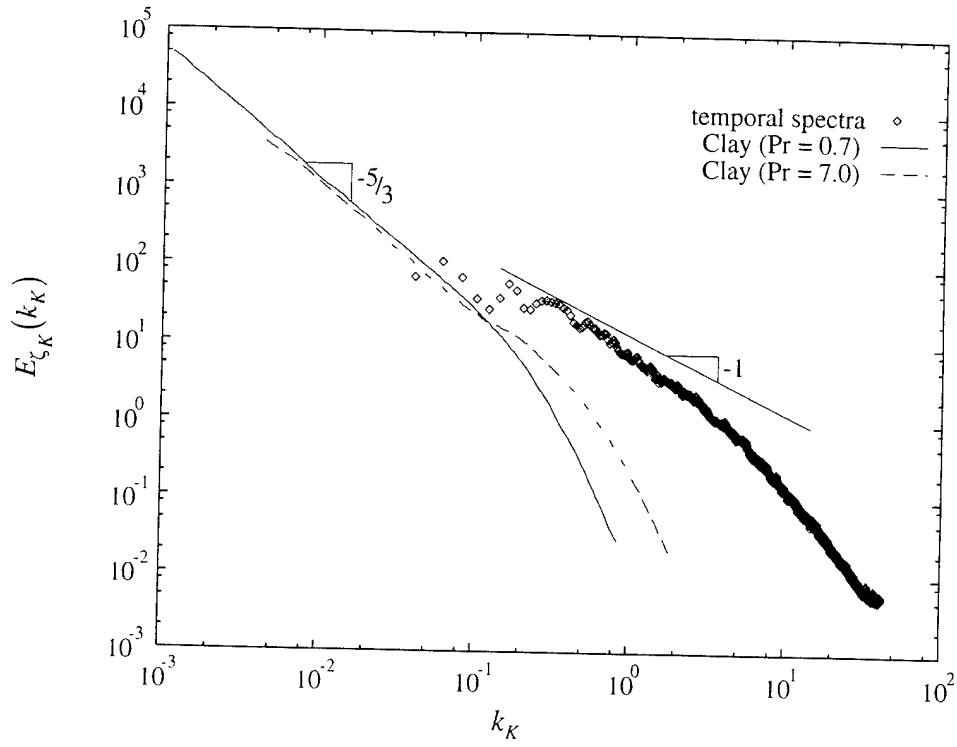


FIGURE 25. Comparison of the present temporal scalar energy spectrum from case R0811 for  $Sc = 2075$  with the temporal spectra of Clay (1973) for  $Pr = 0.7$  and  $Pr = 7.0$ . Also shown for comparison is a  $k^{-1}$  scaling in the viscous-convective subrange for  $Sc \gg 1$  predicted by the Batchelor (1959) theory.

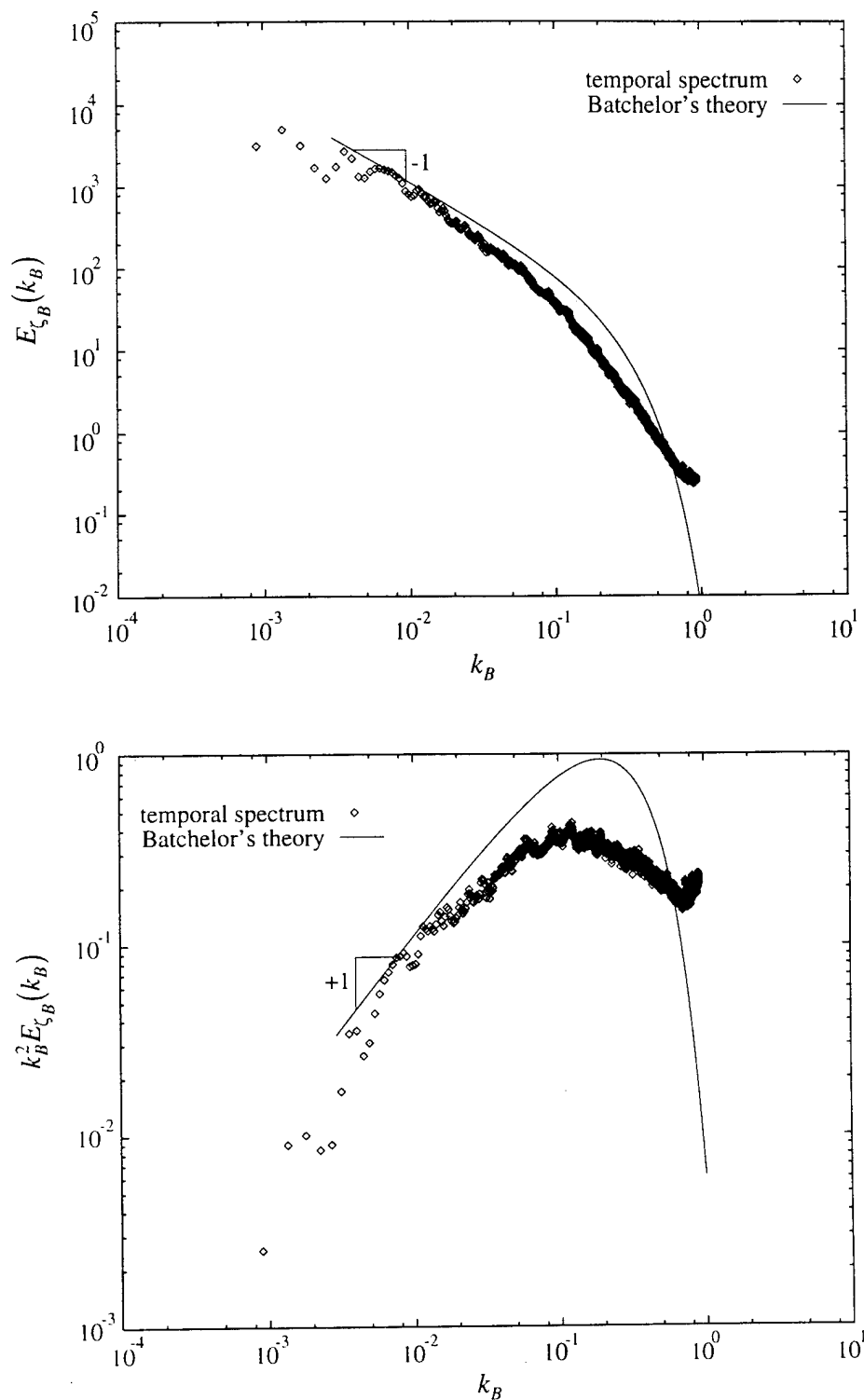


FIGURE 26. Comparison of the present temporal scalar energy spectrum from case R0811 for  $Sc = 2075$  with the Batchelor (1959) theory using  $q = 5$  for the high wavenumber spatial spectrum in  $Sc \gg 1$  scalar mixing in turbulent flows. Shown here are: (a) the scalar energy spectrum; (b) the resulting dissipation spectrum.



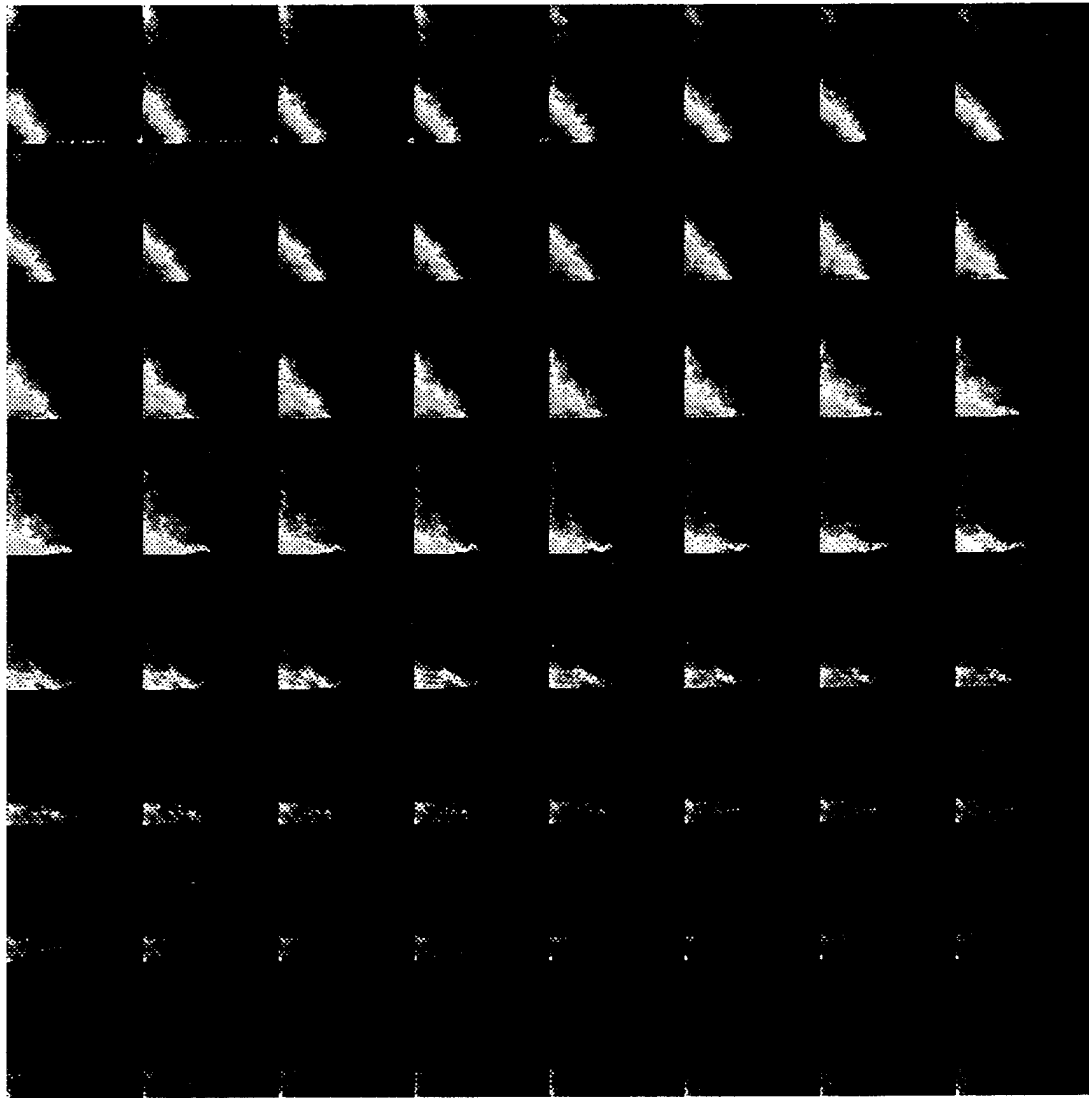


FIGURE 27a. The full three-dimensional spatial scalar energy spectrum  $E_z(\mathbf{k})$  obtained from an ensemble average of spectra from 232 individual data subvolumes of the type shown in figures 11 through 13. Each of the 64 panels shown is an intersection through the three-dimensional  $\mathbf{k}$ -space for a fixed value of  $k_z$ . In each panel,  $(k_x, k_y) = (0, 0)$  is at the lower right corner, with  $k_x$  increasing to the right, and  $k_y$  increasing toward the top of the page. The top left panel corresponds to  $k_z = 0$ , with  $k_z$  increasing from left to right, and then from top to bottom. The colors from blue to red correspond to four decades of logarithmically increasing energy values.

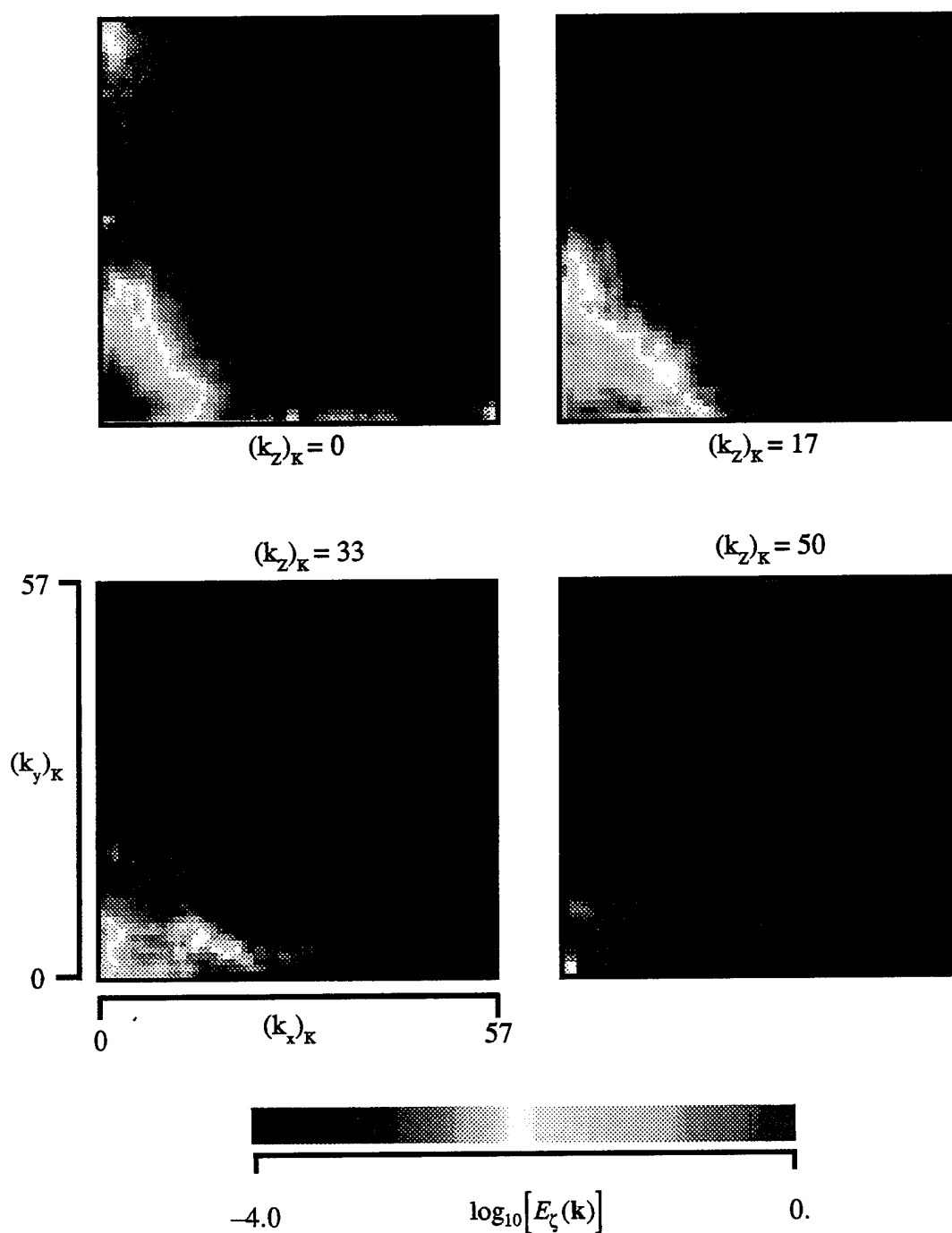


FIGURE 27b. Four intersections for  $k_z = \text{constant}$  through the three-dimensional  $\mathbf{k}$ -space showing the three-dimensional spatial scalar energy spectrum  $E_z(\mathbf{k})$  from figure 27a. In each panel,  $(k_x, k_y) = (0, 0)$  is at the lower right corner, with  $k_x$  increasing to the right, and  $k_y$  increasing toward the top of the page. The top left panel corresponds to  $k_z = 0$ , with  $k_z$  increasing from left to right, and then from top to bottom. The colors from blue to red correspond to four decades of logarithmically increasing energy values.

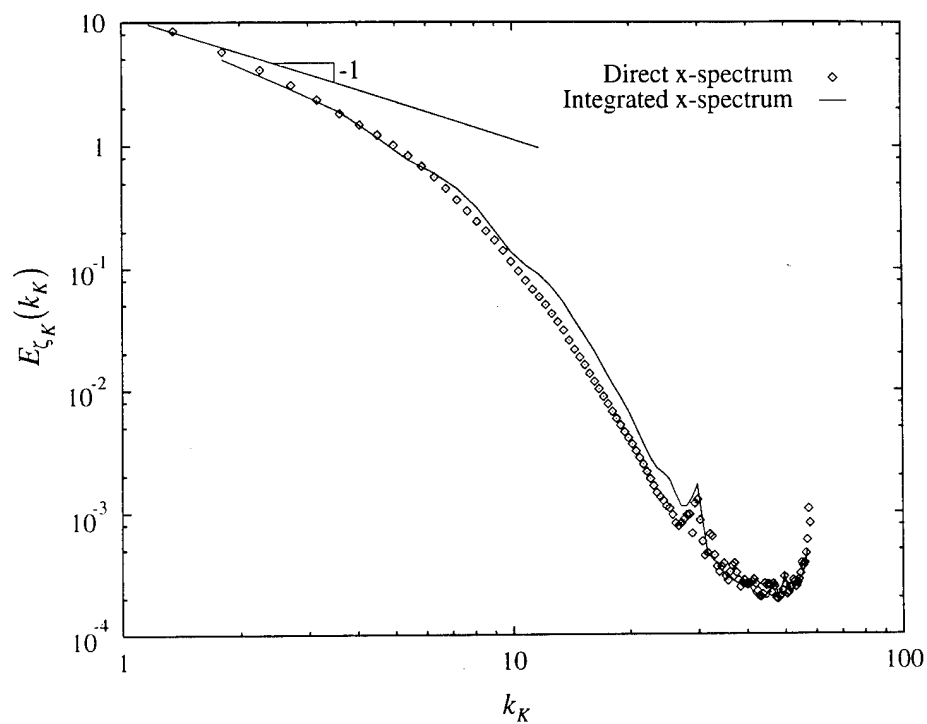


FIGURE 28. The one-dimensional spatial scalar energy spectrum obtained by integrating the three-dimensional spectrum  $E_{\zeta}(\mathbf{k})$  in figure 27 in  $k_y$  and  $k_z$ , compared with the original one-dimensional spatial spectrum in  $k_x$  from figure 23a.

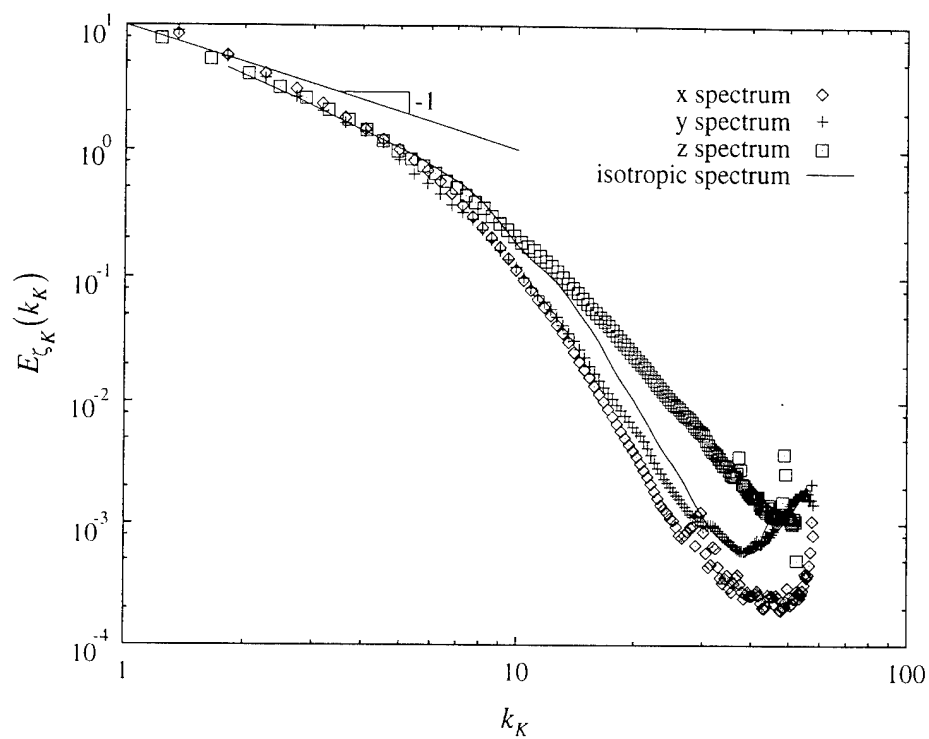


FIGURE 29. The one-dimensional spatial scalar energy spectrum obtained by integrating the three-dimensional spectrum  $E_{\zeta}(\mathbf{k})$  in figure 27 over spherical shells in  $\mathbf{k}$ -space, compared with the three individual one-dimensional spectra from figure 23a.

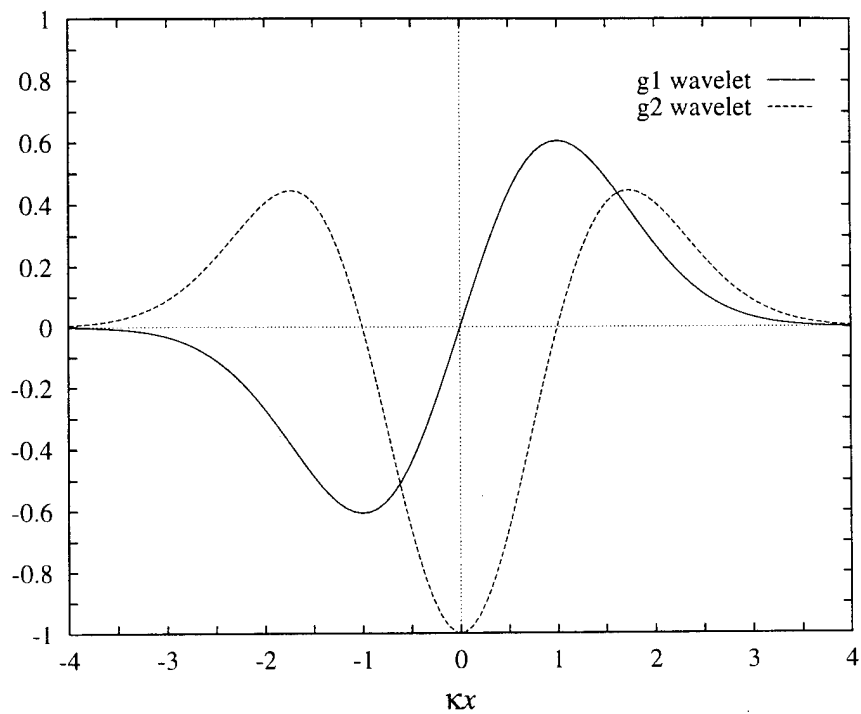


FIGURE 30. The wavelet bases  $g_1(\kappa x)$  and  $g_2(\kappa x)$  used to analyze scale information in the scalar and dissipation fields via the wavelet spectra in figures 31 through 34.

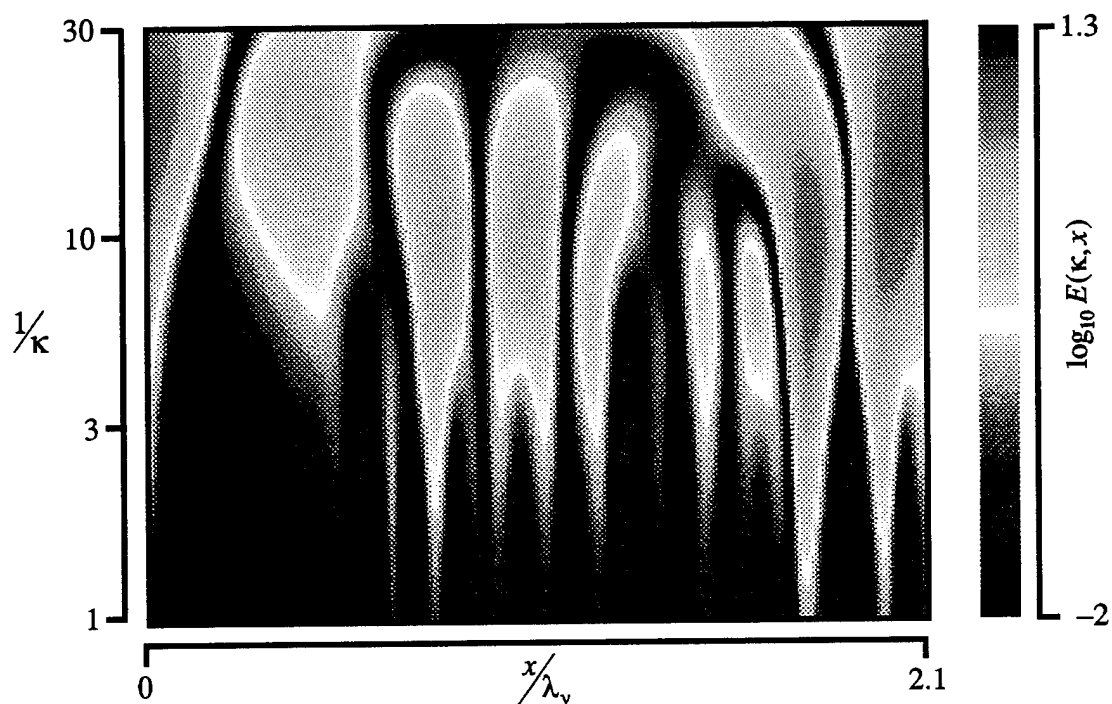
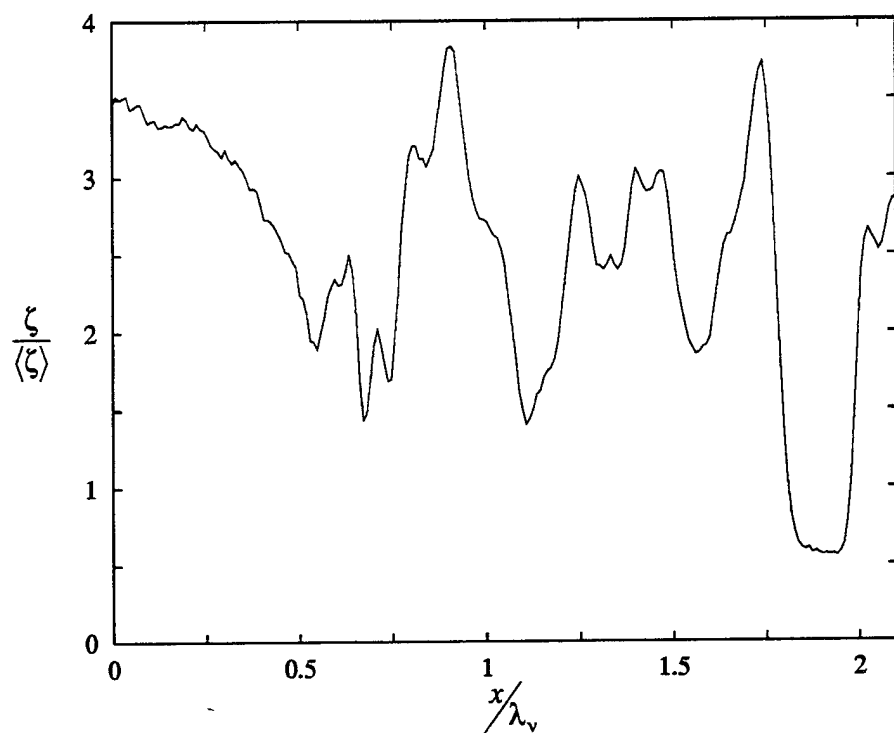


FIGURE 31a The logarithm of the  $g_1$  wavelet power spectrum applied to another one-dimensional cut through the turbulent conserved scalar field shown above.

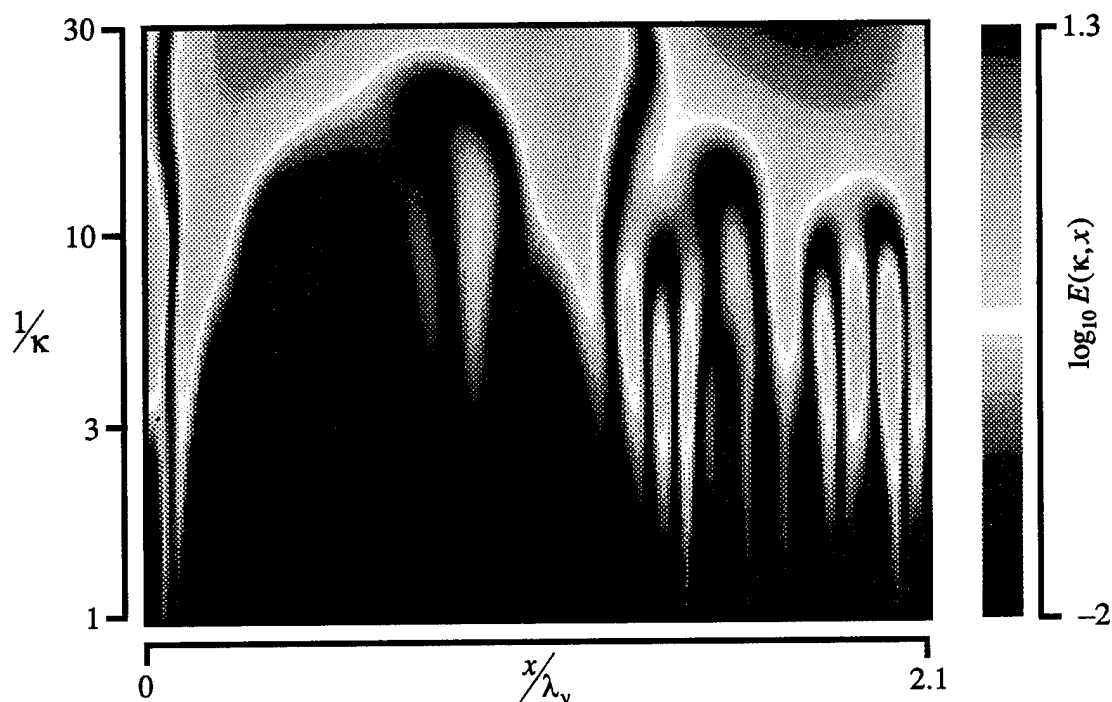
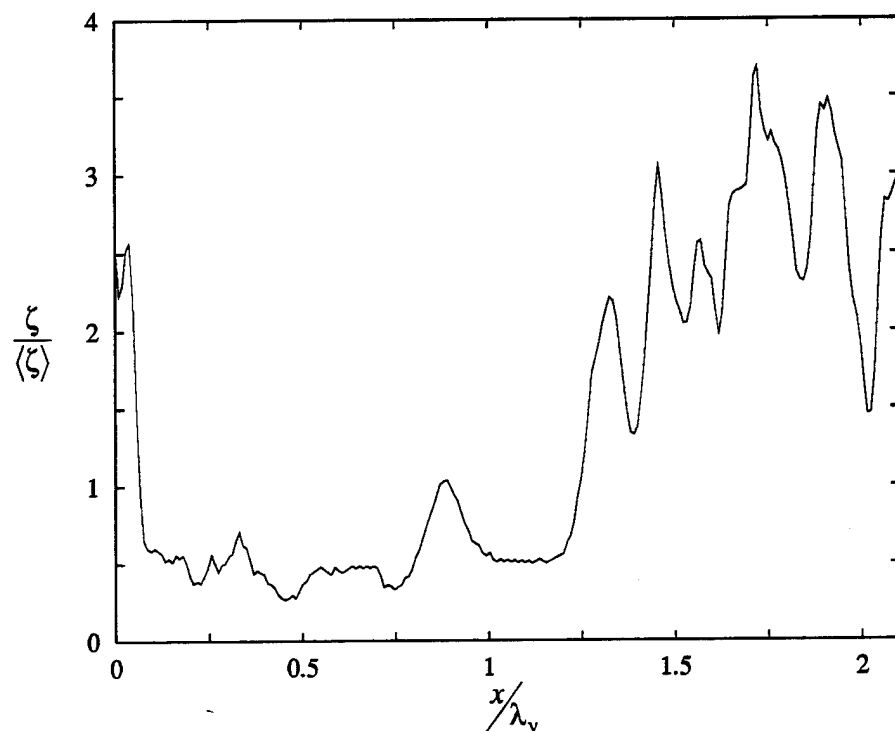


FIGURE 31*b* The logarithm of the  $g_2$  'Mexican hat' wavelet power spectrum applied to the same one-dimensional cut through the turbulent conserved scalar field shown above.

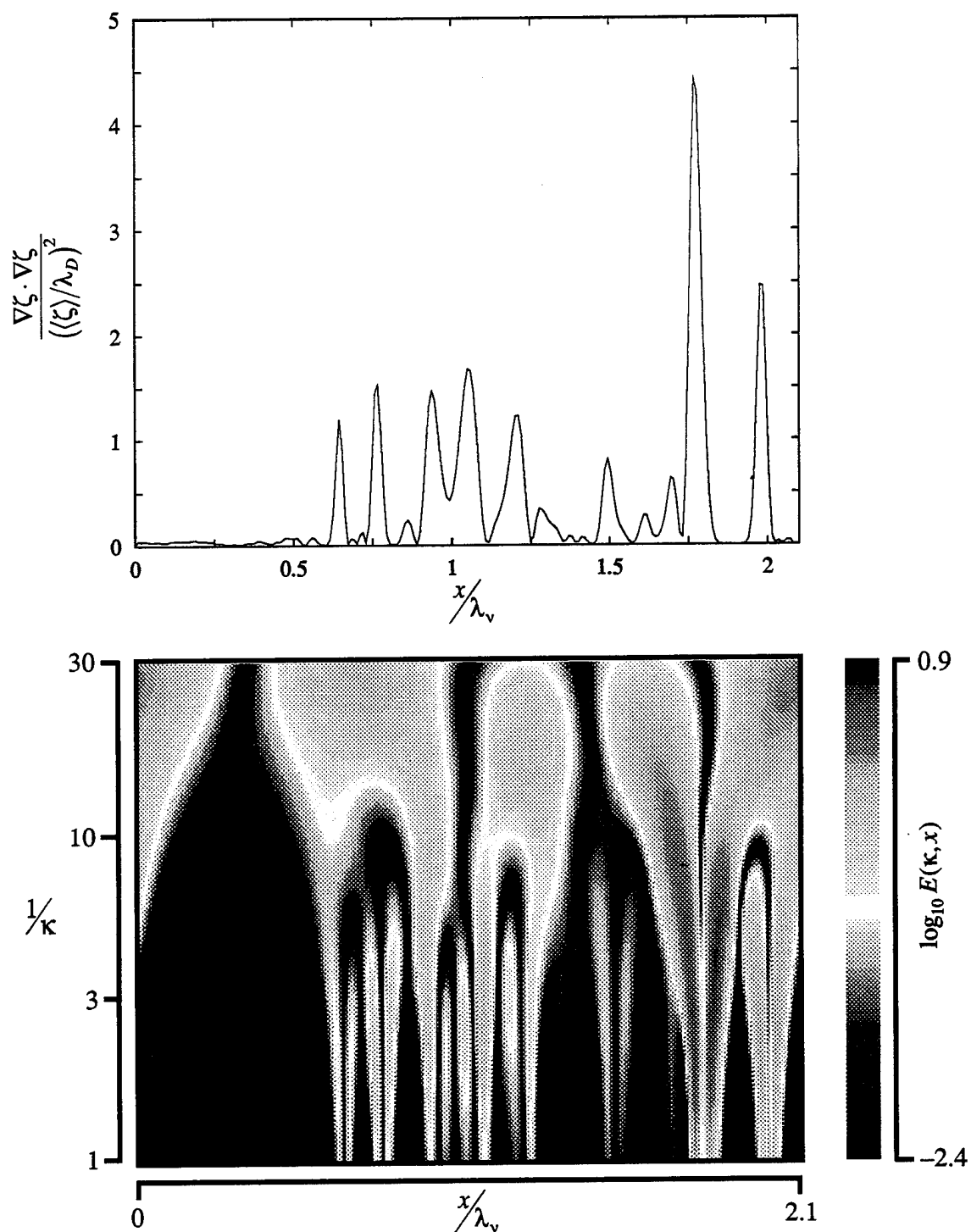


FIGURE 32a The logarithm of the  $g_1$  wavelet power spectrum applied to the one-dimensional cut through the scalar dissipation field shown above. The dissipation shown is the full three-dimensional scalar energy dissipation corresponding to the conserved scalar field of Fig. 31a.



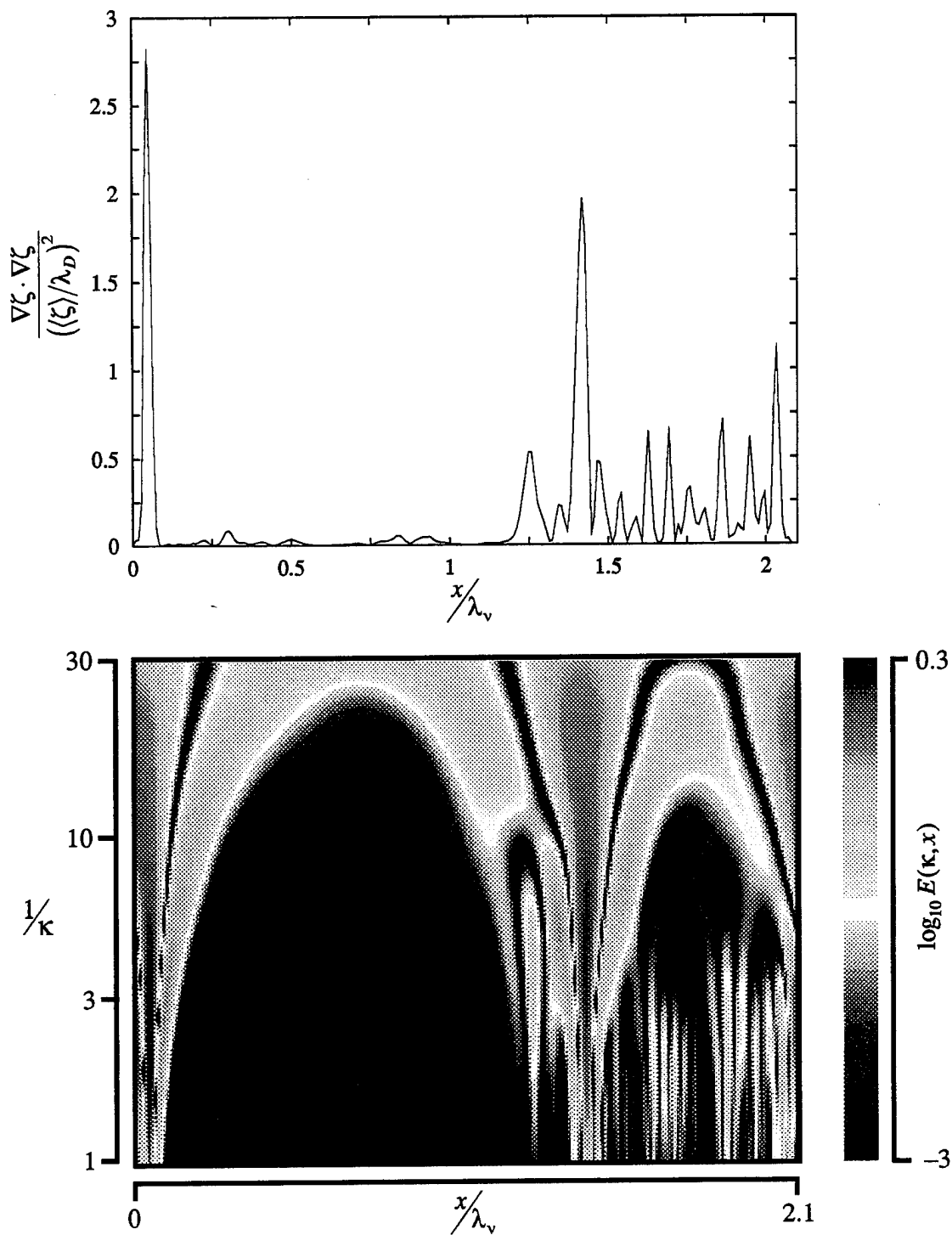


FIGURE 32*b* The logarithm of the  $g_2$  wavelet power spectrum applied to the one-dimensional cut through the scalar dissipation field shown above.

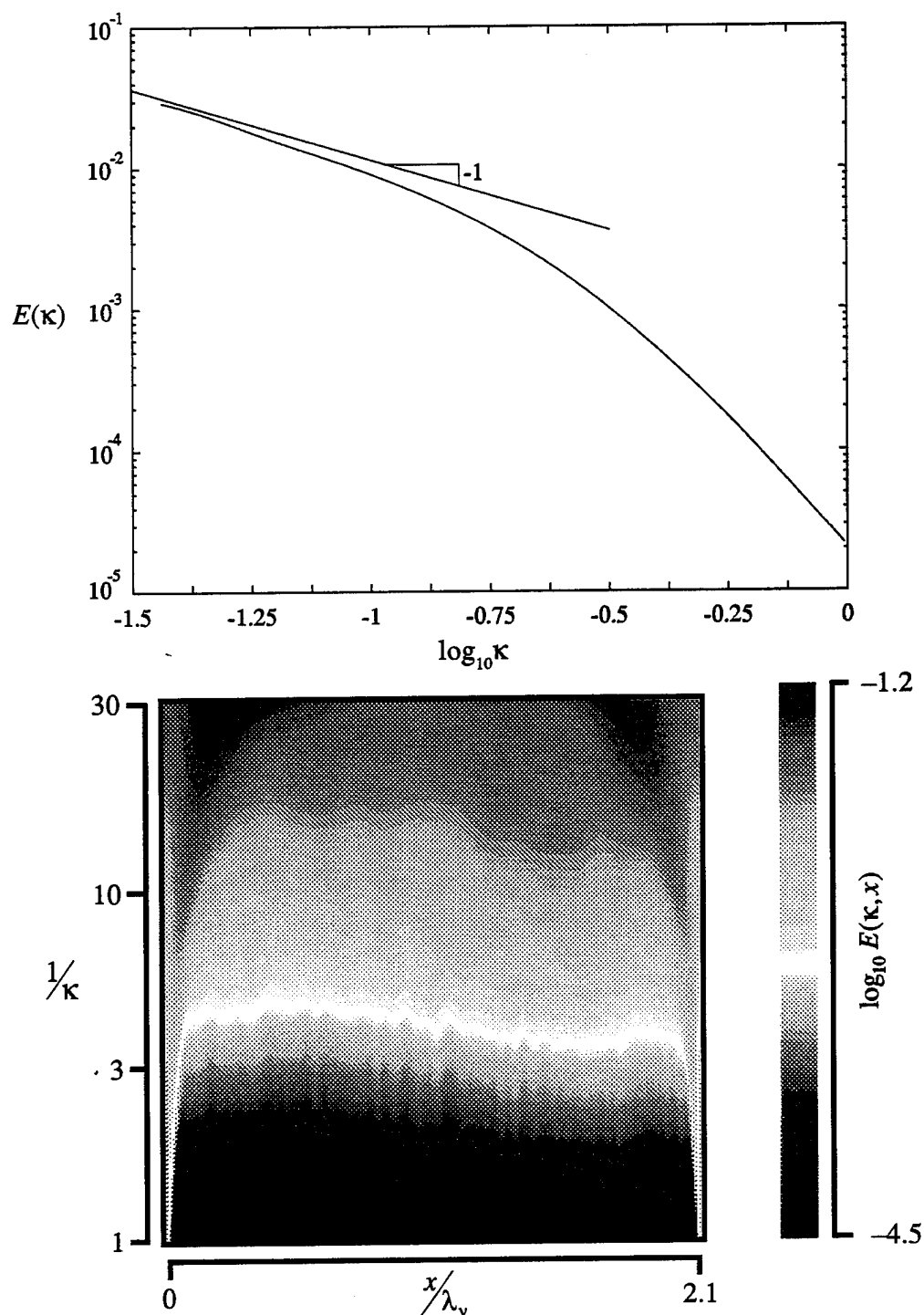


FIGURE 33 The logarithm of the  $g_2$  'Mexican hat' wavelet transform averaged over all the one-dimensional data records available in one arbitrarily chosen  $256^3$  data volume within the turbulent flow. Very little spatial variation remains even after this small ensemble average. The plot above it shows the one-dimensional profile of the wavelet transform at the center  $x$  position, *i.e.*  $x/\lambda_v = 1.05$ .

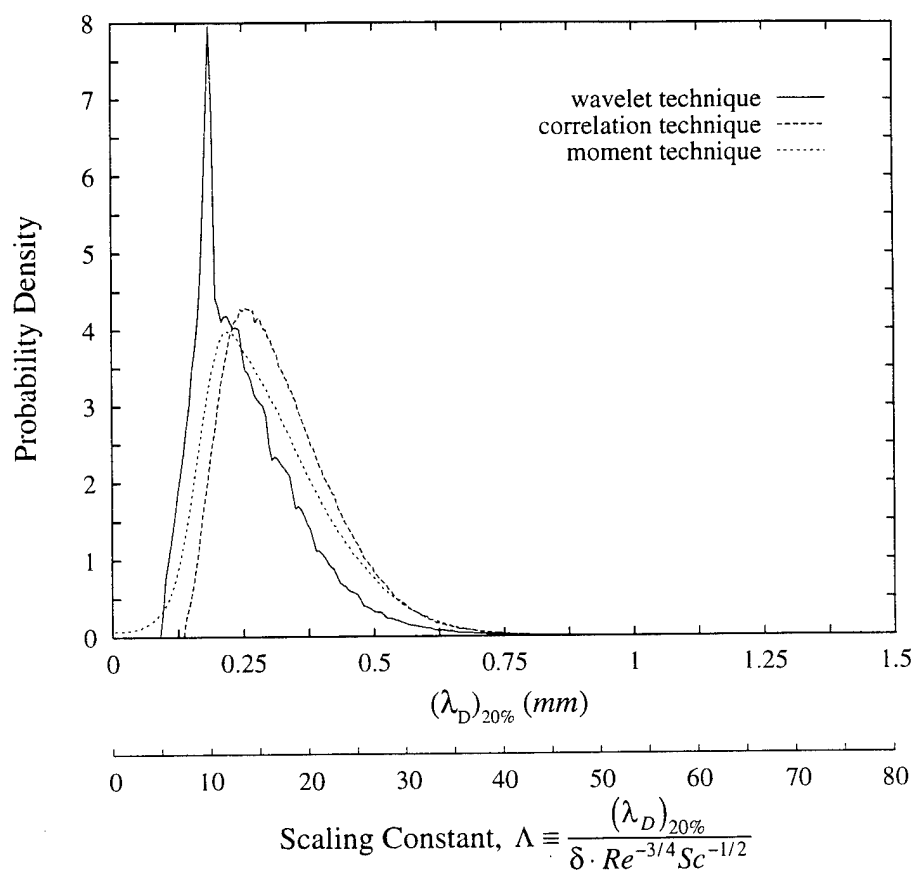


FIGURE 34. Distributions of the dissipation layer thicknesses,  $(\lambda_D)_{20\%}$ , shown in absolute terms and normalized as in Eq. (6) to show the scaling constant, obtained from using the wavelet analysis, the correlation analysis, and the integral moment method. See also Table 5 and compare with  $\langle \Lambda \rangle \approx 11.2$  for  $Sc \approx 1$  from Buch (1991).

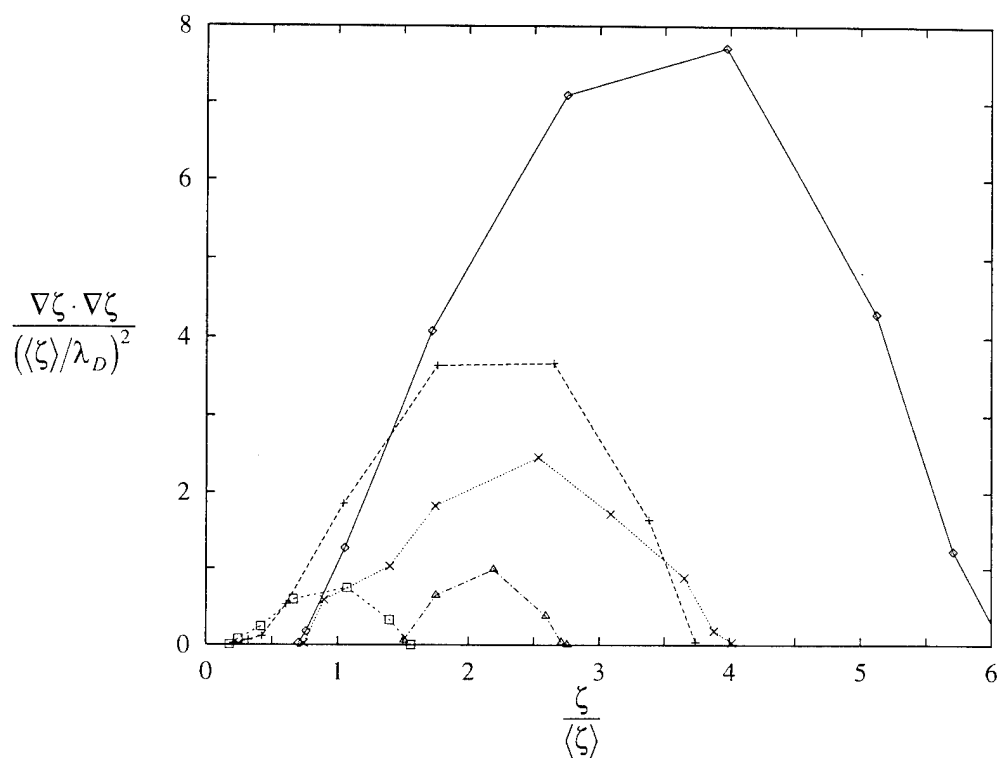


FIGURE 35. The measured scalar dissipation rate profiles for several representative one-dimensional layer-normal intersections through layer-like dissipation structures of the type evident in figures 11 – 13. Shown are the scalar dissipation rates as functions of the conserved scalar values. Note the differing scalar endpoints ( $\zeta^+$ ,  $\zeta^-$ ) for the various layers, and how the peak dissipation rate within each profile typically scales with the scalar difference ( $\zeta^+ - \zeta^-$ ).

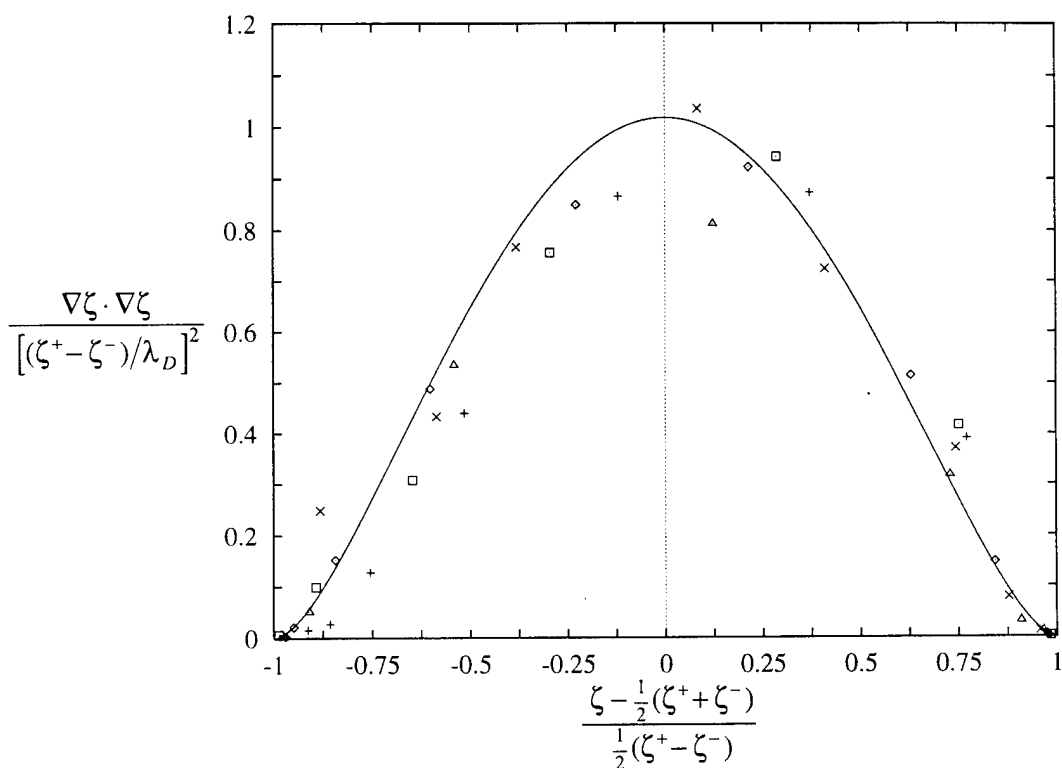


FIGURE 36. The widely differing profiles in figure 35 are shown normalized with their scalar endpoints  $(\zeta^+, \zeta^-)$  for  $\alpha = 1.79$ . Note that when viewed in this form, the internal structure for all the layers can be seen to agree well with the result given by the solid line for a locally one-dimensional, strained, laminar diffusion layer, and take into account the effects of varying scalar endpoints and layer thicknesses. The solid line can be used to model  $\beta(\zeta, \nabla\zeta \cdot \nabla\zeta)$  due to the small scales of turbulent mixing if the presumably universal distributions of layer thicknesses  $\beta(\lambda_D)$  and scalar endpoints  $\beta(\zeta^+, \zeta^-)$ , normalized by the local inner variables, are known.

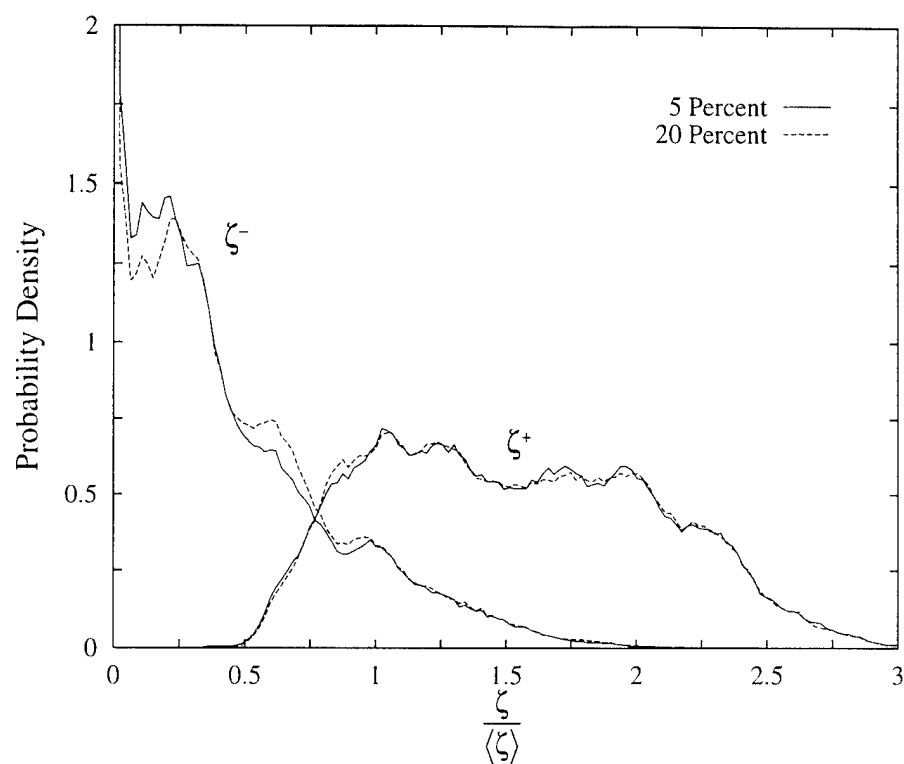


FIGURE 37. Measured marginal distributions of the scalar endpoints,  $\beta(\zeta^+)$  and  $\beta(\zeta^-)$ , obtained as described in §6.2 for a single three-dimensional ( $256^3$ ) spatial data volume. Results obtained show the insensitivity of the algorithm to the threshold criterion. Analogous marginal distributions obtained from a large number of such data volumes are shown in figure 39, and the corresponding joint distributions are shown in figure 38.

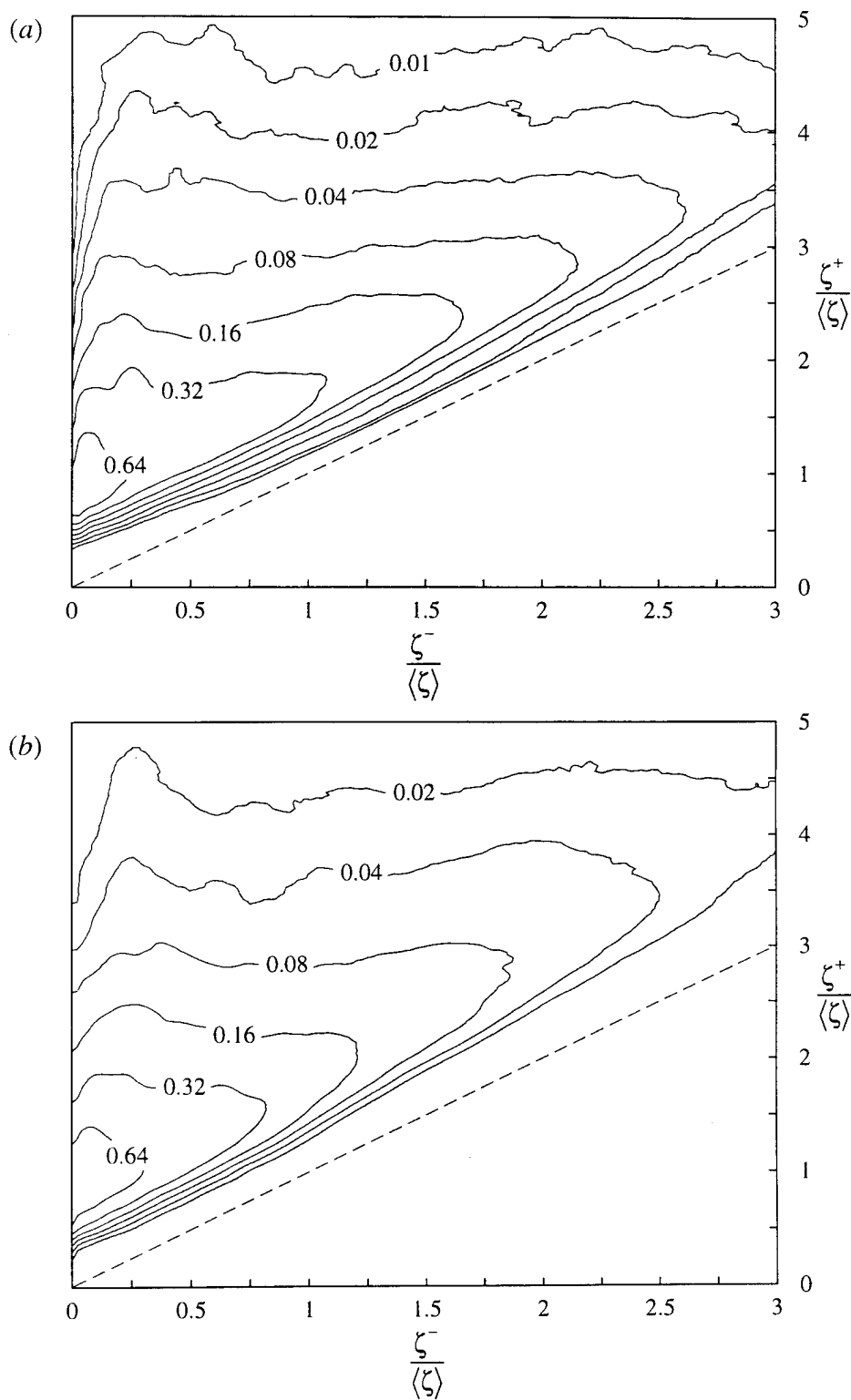


FIGURE 38. The measured joint probability density function (pdf) of scalar endpoint values  $\beta(\zeta^+, \zeta^-)$  for all the layer-like dissipation structures from volumes of the type shown in figures 11 – 13 and figures 41 and 42. Shown are the results obtained for (a) case R0703 and (b) R0806 which can be seen to agree quite well. Note that by definition  $\zeta^+ > \zeta^-$ , with the dashed lines denoting the limit  $\zeta^+ = \zeta^-$ .

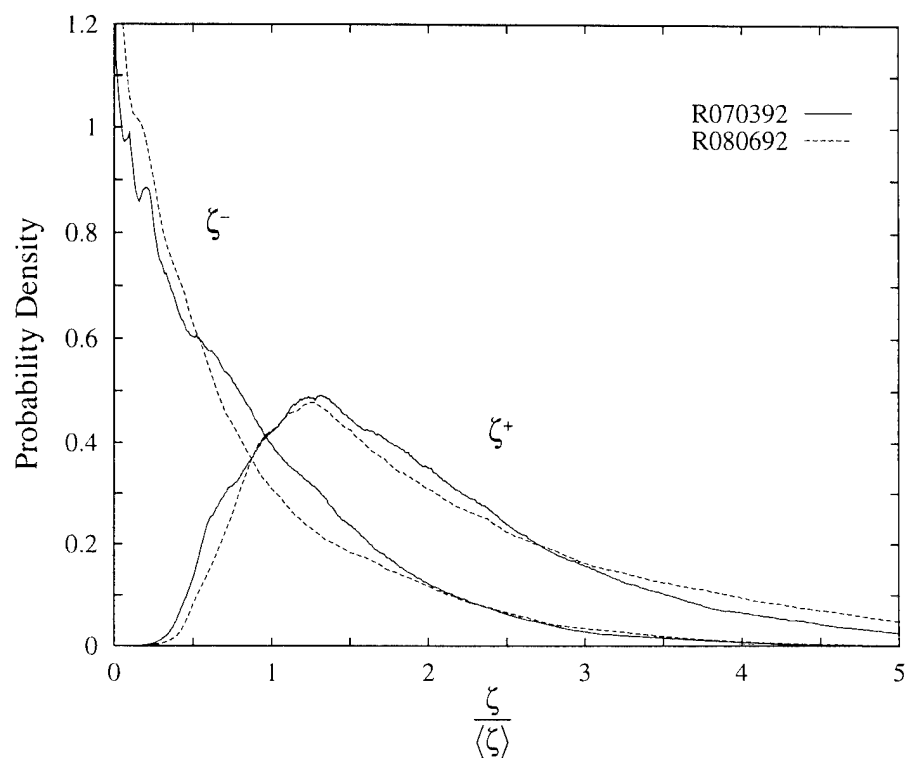


FIGURE 39. The marginal probability density functions  $\beta(\zeta^+)$  and  $\beta(\zeta^-)$  of scalar endpoint values obtained from the joint distributions in figure 38. Note that the requirement that  $\zeta^+ > \zeta^-$  leads to a peak in  $\beta(\zeta^+)$  near the local mean scalar value. Compare with figure 37 showing the results obtained from a single three-dimensional ( $256^3$ ) spatial data volume of the type shown in figure 11 – 13.



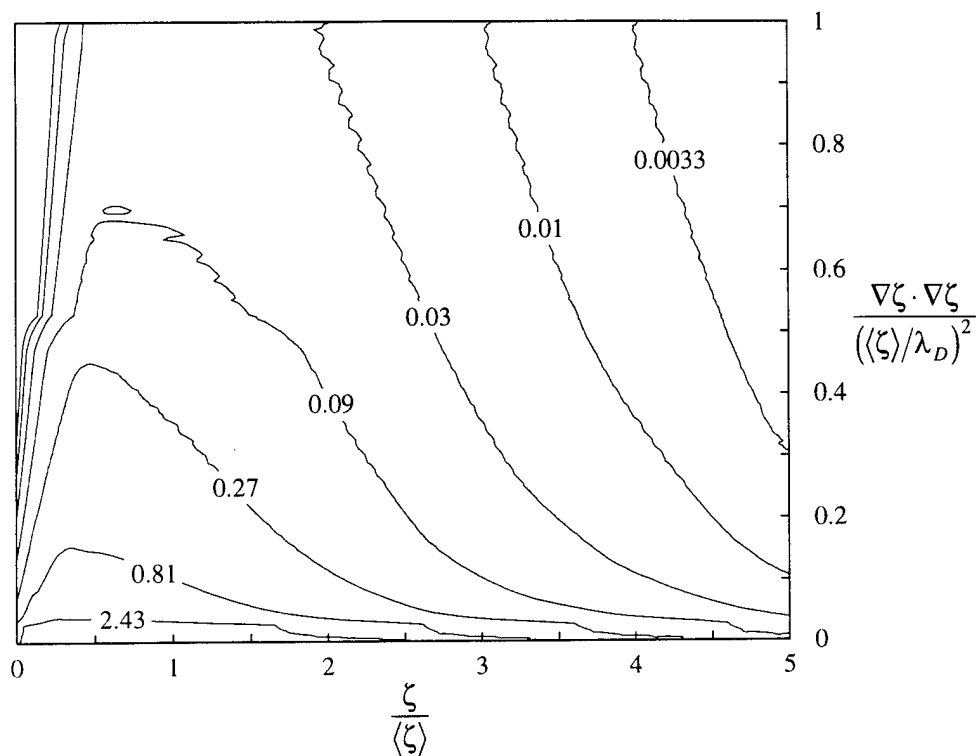


FIGURE 40. The joint probability density function  $\beta(\zeta, \nabla\zeta \cdot \nabla\zeta)$  obtained from the model in §6.3 for the small scales of turbulent mixing. Contour levels shown are logarithmically spaced. The result is obtained via the joint distribution  $\beta(\zeta^+, \zeta^-)$  in figure 38, and can be compared with the direct measurement in figure 17a.

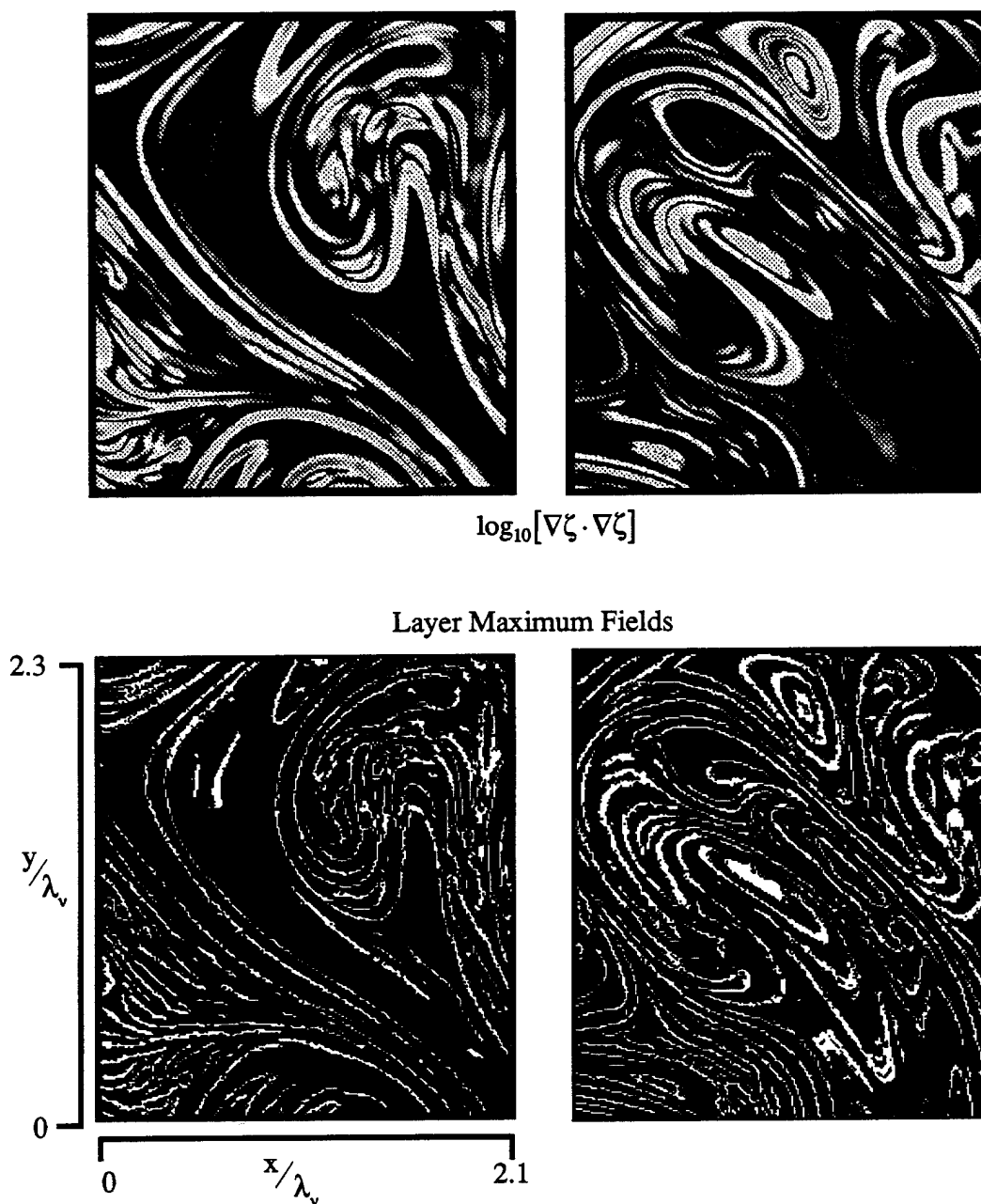


FIGURE 41. Examples of two-dimensional intersections of the instantaneous scalar energy dissipation rate field and the associated dissipation layer center field of the type shown in figure 42. Note that the algorithm appears to successfully find the centers of even very weak dissipation layers.

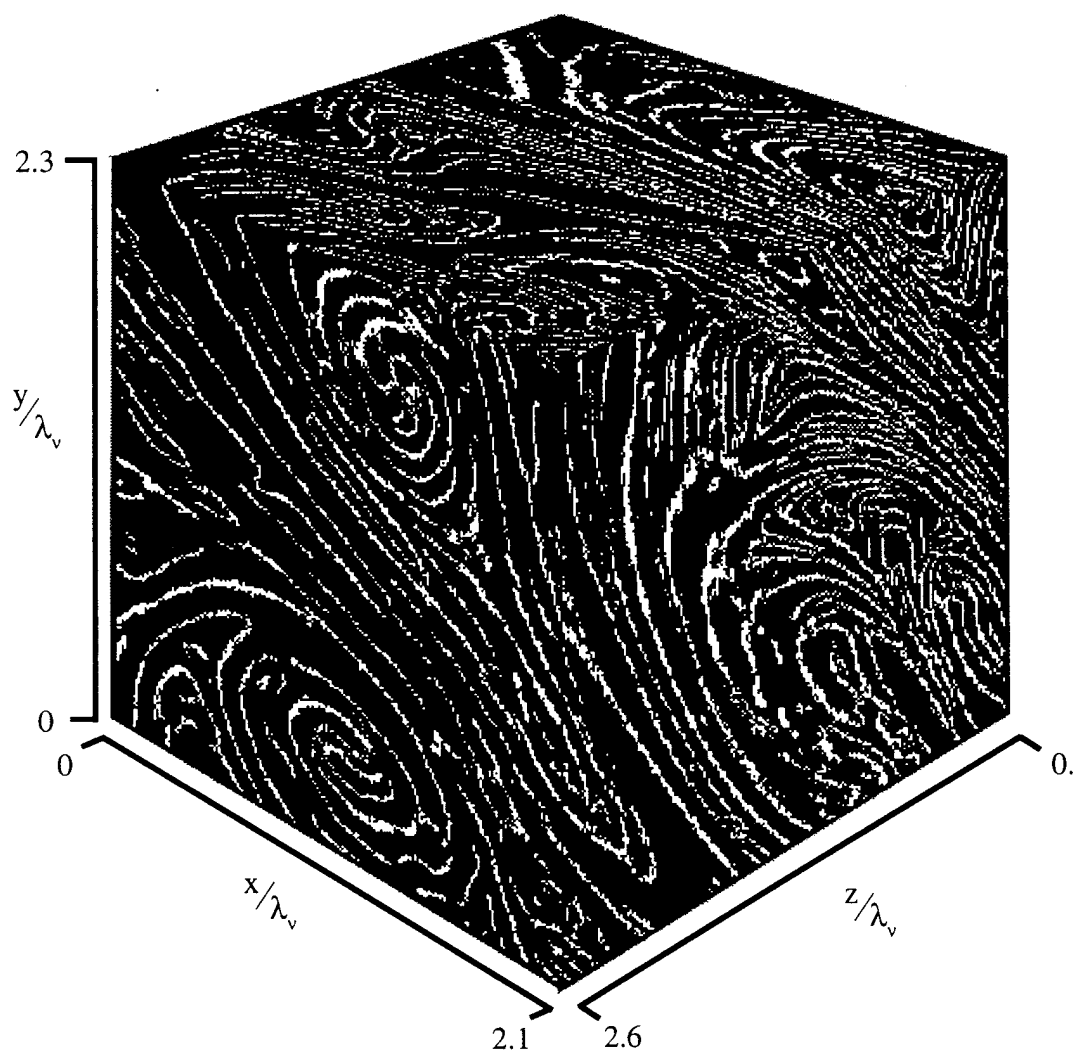


FIGURE 42. The dissipation layer center field computed for the same data shown in figure 11. Compare especially with the dissipation field in figure 11c. The layer center fields are used to analyze the scalar endpoints and thickness properties of the turbulent mixing process.

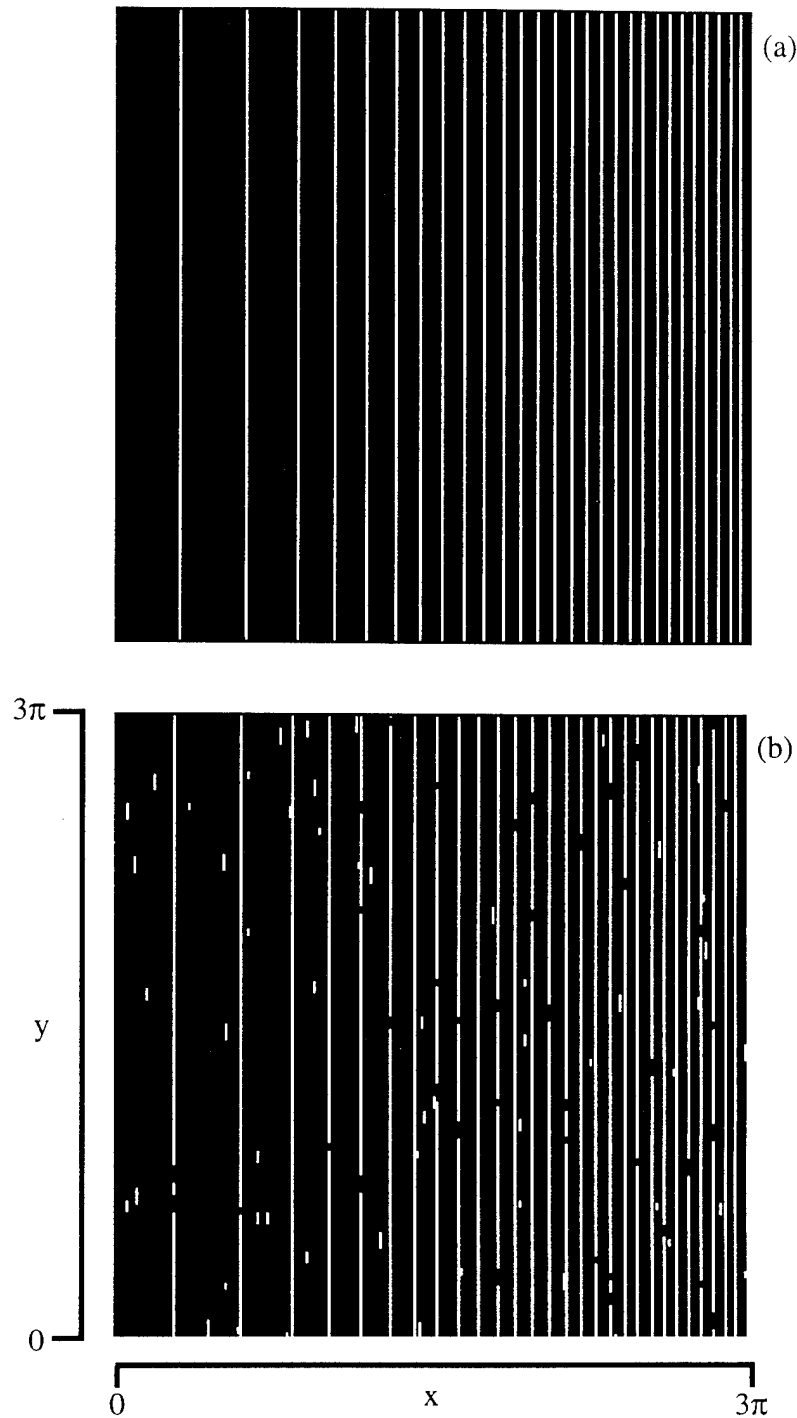


FIGURE 43. Layer center definition fields for a test case that was formulated in terms of a conserved scalar field  $\zeta(\mathbf{x}, t)$  that varied as  $\sin(x^2)$ . The scalar energy dissipation field in this case varies as  $\nabla\zeta \cdot \nabla\zeta(\mathbf{x}, t) = 4x^2\cos(x^2)$  so that the magnitude as well as the frequency of the layers vary with the coordinate  $x$ . Shown in (a) is the clean version of this field resulting from our layer maximum finding algorithm and in (b) is the field in (a) made noisy by the addition of intentional holes and extraneous layers in a random manner. Both were subjected to a comparison measurement of their individual layer separation distance distribution functions which can be seen in figure 44.

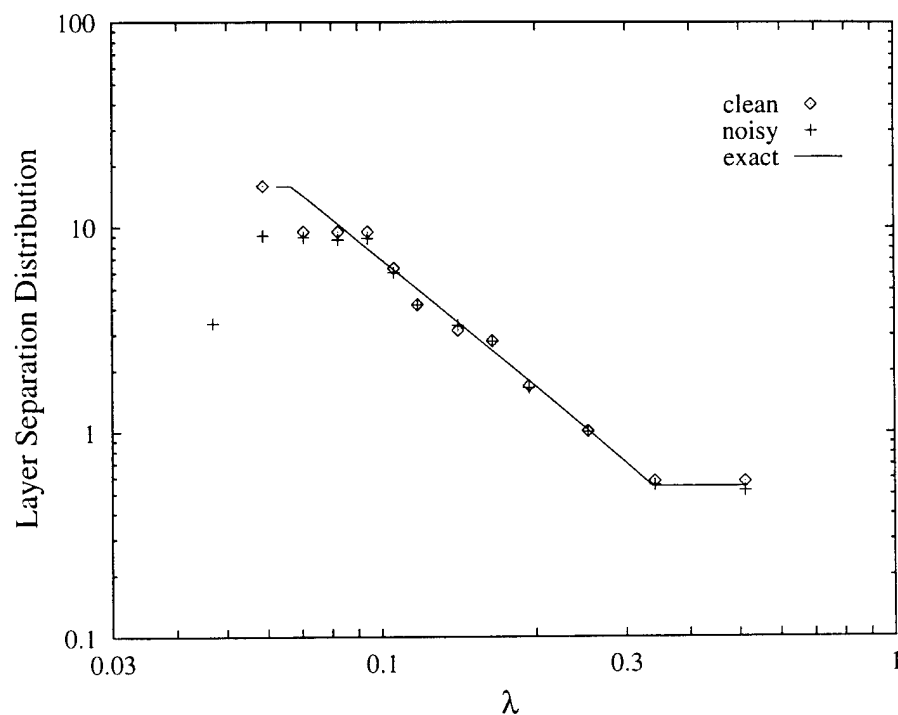


FIGURE 44. The distributions of scalar dissipation layer separations for the test fields in figure 43, compared with the exact analytical result. Note that both the “clean” field in figure 43*a* and the “noisy” field in figure 43*b* produce results that agree with each other except at the very smallest separations. Moreover, both cases agree well with the “exact” result, with the differences discernible being due to the inherently discrete ( $256 \times 256$ ) nature of the “clean” and “noisy” fields.

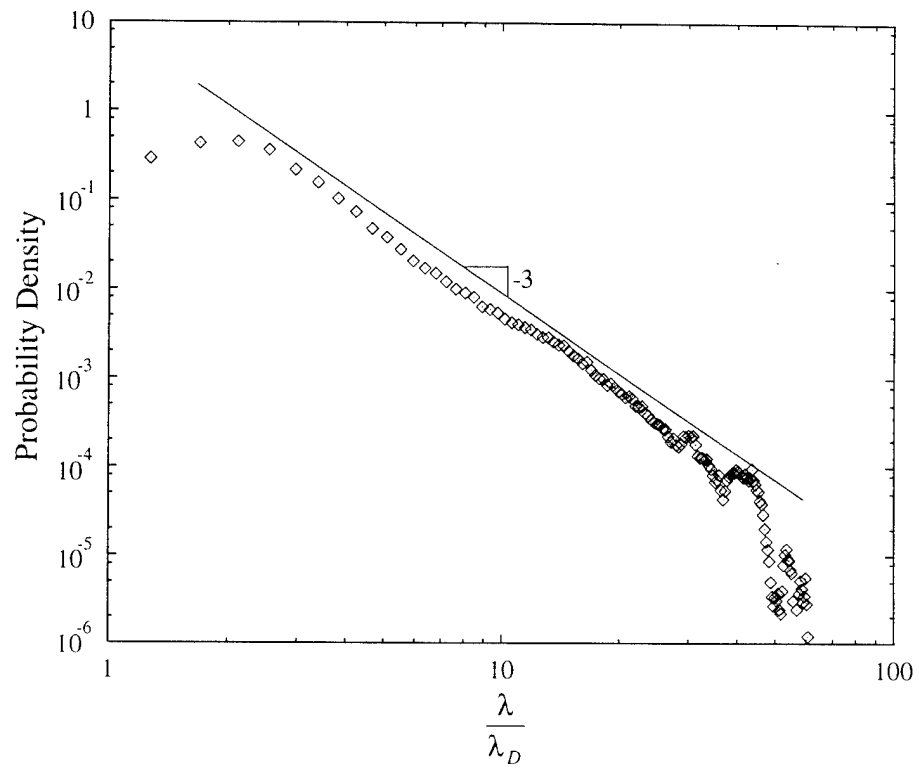


FIGURE 45. The distribution of scalar dissipation layer separation distances obtained by ensemble averaging the results for turbulent flow data of the type shown in figures 11 - 13. Note the  $-3$  power-law scaling in the distribution over nearly the entire range of separation scales.

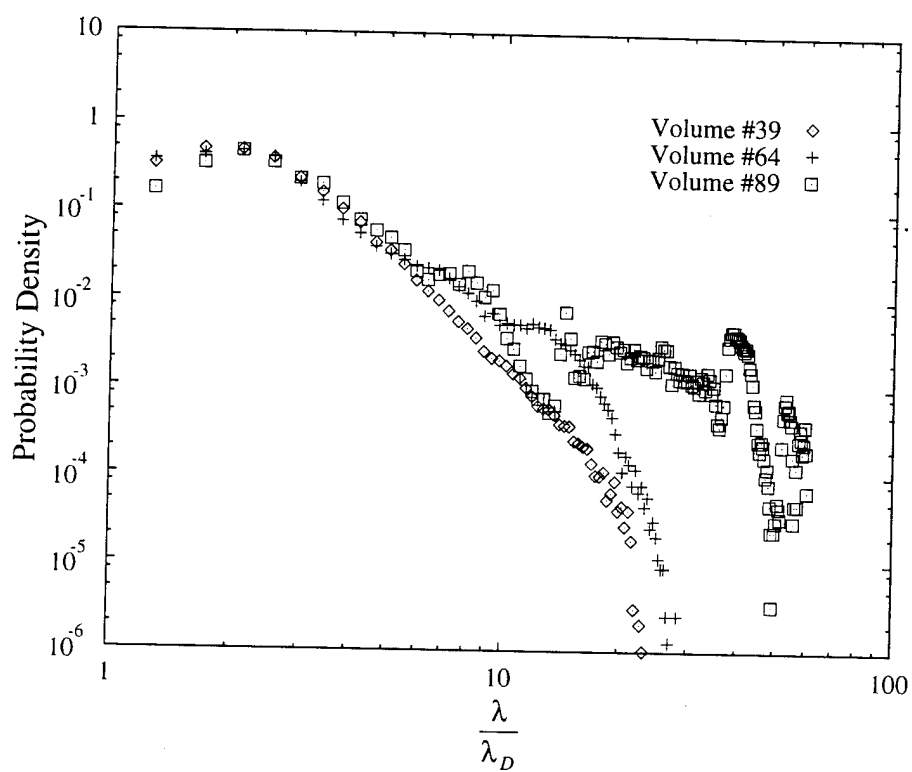


FIGURE 46. The distribution of scalar dissipation layer separation distances obtained by ensemble averaging the results for turbulent flow data in individual three-dimensional spatial data volumes.

### 3. The Strained Dissipation and Reaction Layer Formulation

#### 1. Introduction

Results from detailed conserved scalar imaging measurements in nonreacting turbulent flows such as those in §2 of this Report, and [1-3] as well as direct numerical simulations (DNS) of passive scalar mixing in turbulent flows [4-7], have shown that whereas the underlying hydrodynamics of turbulent flows are quite complex, the structure of scalar mixing in such flows is considerably simpler. In particular, while the instantaneous kinetic energy dissipation rate field is a complex arrangement of line-like, sheet-like, and intermediate structures, for dynamically passive conserved scalar fields  $\zeta(\mathbf{x}, t)$  with Schmidt numbers  $(\nu/D_\zeta)$  of unity or larger, essentially all of the instantaneous scalar energy dissipation rate field  $\chi(\mathbf{x}, t) \equiv (ReSc)^{-1} \nabla \zeta \cdot \nabla \zeta(\mathbf{x}, t)$  is organized into locally one-dimensional layer-like dissipation sheets. Examples of these dissipation layers can be seen in Fig. 1, from Buch & Dahm [3]. The dynamics of the strain-diffusion competition involved in scalar mixing, which leads to the inexorable formation of such layer-like scalar dissipation structures and to the exclusion of the complementary line-like dissipative structures found in the underlying vorticity field, are discussed in detail in Ref. [3]. These layer-like scalar dissipation sheets are simply the three-dimensional analog of the localized dissipation "shocks" that arise naturally from the advection-diffusion balance in high Reynolds number solutions to the diffusive Burgers' equation.

In reacting turbulent flows, the advection-diffusion balance that leads to the formation of these ubiquitous scalar dissipation layers is present as well. In the presence of combustion heat release, the individual chemical species diffusivities  $D_i$  vary with local temperature, however the hydrodynamic viscosity  $\nu$  scales in essentially the same way and thus  $Sc$  remains essentially constant near unity. This leads to a change in the lengthscale characterizing the thickness of these layer-like dissipation structures, but does not alter the basic strain-diffusion competition that establishes these structures. Additionally, the underlying strain rate and vorticity fields are modified by the fluid expansion due to combustion heat release, and the baroclinic vorticity due to the interaction of density gradients with the hydrostatic pressure gradient (buoyancy) and with local hydrodynamic pressure gradients. However for heat release values typical of hydrocarbon combustion, the local velocity gradients leading to formation and preservation of these dissipation sheets remain dominant in turbulent flows with combustion as well. Recent results from scalar imaging measurements by Long [8] as well as DNS computations appear to confirm that these layer-like scalar dissipation structures remain present even in turbulent flows undergoing



highly exothermic combustion reactions.

The implications of this fundamentally layer-like structure of scalar mixing in turbulent flows are substantial, especially for turbulent combustion. As noted above, these dissipation layers result entirely for hydrodynamical reasons. Thus all conserved scalar quantities with  $Sc \geq 1$  must have their scalar energy dissipation concentrated in such locally one-dimensional layer-like structures. This will be true irrespective of whether the scalar is a passive physical quantity (such as an inert dye or gaseous tracer), or a more abstract quantity formed from the concentrations of various chemical species evolving in the flow (such as any of various mixture fraction variables). Thus the dissipation fields associated with all conserved scalar mixture fractions must also remain manifestly layer-like, and since this is a consequence solely of the hydrodynamics of scalar mixing, this must remain true irrespective of the degree of chemical nonequilibrium to which the various constituent chemical species fields are subjected – the presence of locally one-dimensional dissipation layers in mixture fraction fields is entirely independent of the chemical state in the flow. As a consequence, any model relating the combustion chemistry in a turbulent flow to the underlying fluid dynamics must, at a minimum, recover this layer-like dissipation structure once the resulting reactive species concentrations are formed into mixture fraction variables. Conversely, the inherently layer-like structure of the dissipation rate fields associated with mixture fraction variables in turbulent flows provides a rigorous starting point for models of nonequilibrium chemistry in turbulent flows.

## 2. *The Strained Dissipation and Reaction Layer Formulation*

The ubiquitous scalar energy dissipation layers noted above allow for a physically-based formulation that relates the mixing state of one or more conserved scalars by the underlying turbulent flow to the chemical state of nonequilibrium combustion occurring within the flow. This approach begins by noting that any conserved scalar mixture fraction variable  $\zeta_i$  can be written as a linear sum over the chemical species fields  $Y_j(\mathbf{x}, t)$  as

$$\zeta_i(\mathbf{x}, t) = \sum_{j=1}^N a_{i,j} Y_j(\mathbf{x}, t) \quad i = 1, 2, \dots, m \quad (1)$$

where  $N$  is the number of chemical species and  $m$  the number of elements involved in the chemical system. Each of the  $m$  conserved scalars  $\zeta_i$  must satisfy the conservative advection-diffusion equation

$$\frac{\partial \zeta_i}{\partial t} + \mathbf{u} \cdot \nabla \zeta_i - \frac{1}{\rho} \nabla \cdot (\rho D_{\zeta_i} \nabla \zeta_i) = 0. \quad (2)$$

Owing to the locally one-dimensional state of the scalar field within any given dissipation layer, as discussed in §1 (see Fig. 1), derivatives of  $\zeta_i$  along the local layer-normal coordinate  $n$  far exceed those along the layer. Thus (2) above reduces to the locally parabolized form

$$\frac{\partial \zeta_i}{\partial t} - v(n,t) \frac{\partial \zeta_i}{\partial n} - \frac{1}{\rho} \frac{\partial}{\partial n} \cdot \left( \rho D_{\zeta_i} \frac{\partial \zeta_i}{\partial n} \right) = 0 \quad (3)$$

where  $v(n,t)$  is the local velocity component along the layer-normal direction  $n$ . In a Howarth-transformed normal coordinate  $\tilde{n}$ , the layer-normal velocity becomes  $-\varepsilon(t) \cdot \tilde{n}$ , where  $\varepsilon(t)$  is the locally uniform strain rate. Moreover, if the Chapman gas approximation is made, then (3) becomes the classical advection-diffusion equation for a constant diffusivity  $D$ .

As is evident in Fig. 1, in general the scalar dissipation layers in turbulent flows do not involve pure fuel or pure air on either side of the layer. Instead the correct *local* boundary conditions for (3) can be expressed as

$$\zeta_i \rightarrow \zeta_i^\pm \quad \text{as} \quad n \rightarrow \pm\infty \quad (4)$$

where the appropriate  $\zeta_i^\pm$  typically vary slowly along the layer. Practical implementation of these boundary conditions will be dealt with below. We will first examine the implications of this local one-dimensionality in the scalar field for the chemical species fields  $Y_j(\mathbf{x},t)$ .

Replacing  $\zeta_i$  in (3) with its definition in terms of the various chemical species concentration fields in (1), and recalling that the  $a_{ij}$  are constants, gives

$$\begin{pmatrix} a_{1,1} & a_{1,2} & \cdots & a_{1,N} \\ a_{2,1} & a_{2,2} & \cdots & a_{2,N} \\ \vdots & \vdots & \ddots & \vdots \\ a_{m,1} & a_{m,2} & \cdots & a_{m,N} \end{pmatrix} \begin{pmatrix} L[Y_1(\mathbf{x},t)] \\ L[Y_2(\mathbf{x},t)] \\ \vdots \\ L[Y_N(\mathbf{x},t)] \end{pmatrix} = \begin{pmatrix} 0 \\ 0 \\ \vdots \\ 0 \end{pmatrix} \quad (5)$$

where

$$L[Y_j(\mathbf{x},t)] \equiv \left[ \frac{\partial Y_j}{\partial t} - v(n,t) \frac{\partial Y_j}{\partial n} - \frac{1}{\rho} \frac{\partial}{\partial n} \cdot \left( \rho D_{\zeta_i} \frac{\partial Y_j}{\partial n} \right) - \dot{w}_j / \rho \right]. \quad (6)$$

Here we have also introduced the requirement that, since the  $\zeta_i$  are conserved, the weighted chemical species reaction rate terms  $w_j(\mathbf{x},t)$  must sum to zero as

$$\sum_{j=1}^N a_{i,j} \dot{w}_j(\mathbf{x},t) \equiv 0. \quad (7)$$

We now want to consider the implications of (5) - (7) for the structure of the  $Y_j(\mathbf{x},t)$  fields. Briefly, we will argue that these constraints together require

that the only physically realizable solution is the trivial case  $L[Y_j(\mathbf{x},t)] \equiv 0$ , in which case the species conservation equations satisfy locally one-dimensional advection-diffusion-reaction equations within each dissipation layer. In effect, we are arguing from precisely the opposite point of view from that usually taken in deriving the classical "flamelet" model. In deriving the flamelet model, conditions are assumed for which the flamelet is thin, and the species transport equations then formally reduce to locally one-dimensional equations which, in turn, dictate a locally one-dimensional structure in the mixture fraction fields  $\zeta_i(\mathbf{x},t)$ . However, the conditions under which the requisite thin flamelet assumption actually holds are so restrictive as to render the resulting classical flamelet model useful only for small equilibrium departures. Here, we take exactly the opposite point of view. We *begin* with the physical observation from §1 that the mixture fraction fields  $\zeta_i(\mathbf{x},t)$  in turbulent flows must be locally one-dimensional, and argue that this requires the constituent chemical species fields  $Y_j(\mathbf{x},t)$  to also be locally one-dimensional. (It will be seen below that, unlike the flamelet model, the resulting one-dimensionality in this case does not demand thin "flamelet-like"  $Y_j(\mathbf{x},t)$  fields.) That argument for one-dimensionality in the  $Y_j(\mathbf{x},t)$  fields is complete if  $L[Y_j(\mathbf{x},t)] \equiv 0$  is the only physically realizable solution to (5) - (7). There are three key physical requirements that we argue demand this trivial solution in (5).

- (i) Note that all the  $a_{ij} \geq 0$  in (5), since from (1) each mixture fraction  $\zeta_i$  is simply a sum over all the chemical species  $Y_j$  of their contributions to the tally of each element  $i$ . Thus, owing to the fact that all the  $a_{ij}$ 's have the same sign, the zero sums in (5) can only result from either the trivial solution  $L[Y_j(\mathbf{x},t)] \equiv 0$ , or else from a fortuitous cancellation of positive and negative  $L[Y_j(\mathbf{x},t)]$ 's. If the latter is the case, then this cancellation would need to be preserved for each of the  $m$  sums corresponding to the elements  $i = 1, 2, \dots, m$  for the single set of species fields  $Y_j(\mathbf{x},t)$ .
- (ii) Since typically  $N \gg m$ , there are combinations of the  $L[Y_j(\mathbf{x},t)]$ 's that will produce these  $m$  zero sums in (i) above, however each of these combinations imposes specific relations between the various  $Y_j(\mathbf{x},t)$  fields. The restricted  $Y_j(\mathbf{x},t)$  fields necessary to preserve these  $m$  zero sums would, at the same time, need to be consistent with the kinetics associated with the resulting reaction rate terms. In other words, each of the combinations of the  $Y_j(\mathbf{x},t)$  fields that satisfies the required cancellation of  $L[Y_j(\mathbf{x},t)]$ 's corresponds to a set of net elementary reaction rates  $w_j(\mathbf{x},t)$ . However the resulting  $w_j(\mathbf{x},t)$  fields must at the same time preserve the zero sum in (7). This would, at a minimum, greatly reduce the set of  $L[Y_j(\mathbf{x},t)]$ 's simultaneously consistent with both (5) and (7).

(iii) Lastly, the zero sums in (5) and (7) must be preserved for *all* possible chemical systems, not merely any particular reaction set under consideration. No features of the reaction kinetics specific to any one chemical system can be invoked to satisfy the relations among the  $Y_j(\mathbf{x}, t)$  fields necessary to achieve cancellation of positive and negative  $L[Y_j(\mathbf{x}, t)]$ 's in (5), while at the same time preserving the additional zero sum in (7) for the resulting elementary reaction rates. In other words, the layer-like structure in the scalar dissipation field as expressed by (5) - (7) must be recovered for *every conceivable* elementary chemical system that could hypothetically occur.

Each one of these three observations places strong constraints on the  $Y_j(\mathbf{x}, t)$  fields. The fact that all three of these requirements must be simultaneously met by the coupled  $Y_j(\mathbf{x}, t)$  fields suggests a set of constraints collectively so restrictive as to be physically unrealizable. We therefore hypothesize that the set of simultaneous conditions under which (5) can have a non-trivial solution are mutually exclusive, and that the only physically realizable solution is the trivial case  $L[Y_j(\mathbf{x}, t)] \equiv 0$  for each  $j$ , namely

$$\frac{\partial Y_j}{\partial t} - v(n, t) \frac{\partial Y_j}{\partial n} - \frac{1}{\rho} \frac{\partial}{\partial n} \cdot \left( \rho D_{\zeta_i} \frac{\partial Y_j}{\partial n} \right) = \dot{w}_j / \rho. \quad (8)$$

In other words, the one-dimensionality of the local conserved scalar field across each of these strained dissipation layers implies a locally one-dimensional structure for the underlying chemical species fields within the layer. However, owing to the *local* boundary conditions on (8), this does *not* imply that the resulting  $Y_j(\mathbf{x}, t)$  fields must be layer-like, as will be seen from the results in §4.

As noted in (4), these locally one-dimensional strained dissipation and reaction layers are in general not between pure fuel and air. Instead, the appropriate local boundary conditions on (8) are

$$Y_j \rightarrow Y_j^\pm \quad \text{as} \quad n \rightarrow \pm\infty. \quad (9)$$

Solutions  $Y_j(n, t; \epsilon, Y_j^+, Y_j^-)$  to (8) are thus parametrized by the strain rate  $\epsilon(t)$  and the boundary values  $Y_j^\pm$ . In practice, specification of the appropriate *local* boundary conditions for these one-dimensional advection-diffusion-reaction equations within any given dissipation layer is a non-trivial matter. For the moment, it should be noted that the  $(n, \epsilon)$  dependence in (8) can of course be equivalently replaced with  $(\zeta, \chi)$  from the corresponding conserved scalar solution in (3) to yield the classical "flamelet" equations, though the physical assumptions leading to these two equations are quite different, as are the boundary conditions. Specification of the *correct* local boundary conditions for the flamelet equation is equally difficult, though usually pure fuel and air

conditions corresponding to  $\zeta^\pm = (0,1)$  are specified.

Putting the discussion of boundary conditions aside for the moment, it is appropriate first to comment on the similarities and differences between the present strained dissipation and reaction layer (SDRL) model, and the classical flamelet model, since both arrive at the same governing equations. The SDRL formulation above is a consequence of the one-dimensionality of any conserved scalar variable across the locally layer-like structures seen to dominate scalar energy dissipation rate fields in turbulent flows. The formulation, in this sense, is based entirely on hydrodynamical arguments, and makes no statements about thinness of reaction zones, or places any other requirements on the reaction chemistry. The flamelet model [9,10], on the other hand, is derived explicitly on the basis of a presumed one-dimensionality in the chemical species fields under conditions for which the flamelet is "thin" relative to the dissipation scales. This thinness requirement is expressed in various flamelet implementations either as a requirement that variations in the scalar dissipation within the reaction zone must be negligible, or else that these variations can be modeled via some presumed function such as  $\chi \sim \zeta^p$  or the self-similar solution of the scalar transport equation (3) for free stream boundary conditions.

The latter class of flamelet models is most closely related to the present approach, though the thinness requirement to which these are subject is not a constraint here. Moreover the appropriate *local* boundary conditions in (9) for the one-dimensional advection-diffusion-reaction equations within any given dissipation layer differ fundamentally from classical flamelet models. Instead, these correspond to the mass fraction values  $Y_j^\pm$  between neighboring dissipation layers. In practice, the information required to specify the correct  $Y_j^\pm$  will rarely be available. However, the physical nature of the approach developed here allows some insight into how these boundary conditions can be simplified. In particular, we note that the mapping from  $(\zeta, \chi)$  to the strain rate  $\varepsilon$  in the local Howarth-transformed coordinate

$$\varepsilon = 2\pi D \left[ \frac{\nabla \zeta \cdot \nabla \zeta}{(\zeta^+ - \zeta^-)^2} \right] \exp 2 \left\{ \operatorname{erf}^{-1} \left[ \frac{\zeta - \frac{1}{2}(\zeta^+ + \zeta^-)}{\frac{1}{2}(\zeta^+ - \zeta^-)} \right] \right\}^2 \quad (10)$$

is very sensitive to the conserved scalar boundary values  $\zeta^+$  and  $\zeta^-$  in (4). Since the strain rate drives the local molecular mixing rate and thus plays a dominant role in setting the depth of nonequilibrium chemistry, it is of primary importance to account for the scalar boundary values properly. In comparison with  $\zeta^+$  and  $\zeta^-$ , the corresponding precise chemical species boundary values  $Y_j^+$  and  $Y_j^-$  would appear to have less of an effect on the nonequilibrium levels

within the layer, since these influence the reaction progress only indirectly. The local departures from chemical equilibrium in each of the species concentrations will therefore be determined principally by the local scalar value  $\zeta$  and the *correct* local strain rate  $\epsilon(\zeta; \zeta^+, \zeta^-)$ , and less by the precise chemical species boundary values. We therefore assume that for a given layer the local  $Y_j$  may be determined relatively accurately by assigning the species boundary values to  $Y_j^\pm = Y_j(\zeta^\pm, \epsilon^*)$  from the solution for with pure fuel and air boundaries. The local chemical species concentrations are then determined by a mapping, via the quasi-steady solution from the local scalar value  $\zeta$  and the correct local strain rate  $\epsilon(\zeta; \zeta^\pm, \nabla\zeta \cdot \nabla\zeta)$  to the species mass fraction  $Y_j$ .

### 3. Qualitative Comparisons with OH PLIF Imaging Data in Turbulent Jet Flames

We have applied this strained dissipation and reaction layer formulation to examine variations in the structure of chemical species concentration and reaction rate fields for increasing degrees of chemical nonequilibrium in a turbulent jet diffusion flame. The results are obtained by applying the strained dissipation and reaction layer formulation in §3 to imaging measurements of conserved scalar fields obtained in the corresponding nonreacting flow. The experimental technique has been described in detail elsewhere [3,11,12]. Briefly, these conserved scalar imaging measurements were made in the self-similar far field of an axisymmetric coflowing turbulent jet in the Turbulent Diffusion Flame (TDF) wind tunnel at the Combustion Research Facility of Sandia National Laboratories. The flow was established in the 30 cm  $\times$  30 cm  $\times$  200 cm test section of the forced draft vertical tunnel with free stream velocity  $U_\infty$  by issuing a jet of undiluted technical grade propane with momentum flux  $J_0$  through a 7.7 mm diameter nozzle. The beam from a 300 mJ/pulse Nd:YAG laser was doubled to 532 nm and formed into a thin sheet passing through the flow. The  $1/e$  laser sheet thickness was measured as 230  $\mu$ m. Rayleigh scattered light from this sheet was imaged onto a 14-bit, slow-scanned, cooled, nonintensified imaging array. The array was sampled in a 256  $\times$  512  $\times$  8-bit format, with each element measuring 23  $\mu$ m  $\times$  23  $\mu$ m. The imaging optics were arranged to give a 1:1 image ratio, with the array output giving the Rayleigh signal integrated over the 10 ns laser pulse duration. The measurement location was centered 39 nozzle diameters downstream of the jet exit at a local outer-scale Reynolds number  $Re \approx 14,000$ . The spatial and temporal resolution achieved were sufficient to distinguish the smallest spatial and temporal scales in the scalar field. Reference measurements with pure air in the test section gave the laser sheet intensity distribution and allowed the effects of non-uniformities in the laser sheet to be largely removed from the data. The Rayleigh signal at each point was then converted to the instantaneous value of the propane mass fraction, yielding a *generic*  $Sc \approx 1$  conserved scalar field  $\zeta(\mathbf{x}, t)$  in the turbulent

flow. The structure of the scalar energy dissipation rate field  $\nabla\zeta \cdot \nabla\zeta(\mathbf{x},t)$  was obtained from the measured  $\zeta(\mathbf{x},t)$  data using linear central differences on a  $3 \times 3$  template centered on each data point.

Figure 1a shows a typical  $256 \times 512$  data plane of the instantaneous conserved scalar field  $\zeta(\mathbf{x},t)$ . The 256 different colors denote ranges of conserved scalar values as indicated, with pure blue beginning at  $\zeta(\mathbf{x},t) = 0$ , corresponding to pure air, and increasing uniformly to pure red denoting the highest conserved scalar values in the data. The jet centerline runs down the right edge of the plane, and the axes indicate the spatial extent in terms of the local strain-limited scalar gradient lengthscale  $\lambda_D$ . Derivatives of the measured conserved scalar field give the projection of the true three-dimensional scalar gradient vector  $\nabla\zeta(\mathbf{x},t)$  into the plane. Figure 1b shows the logarithm of the corresponding scalar dissipation rate field formed from this projection,  $\log_e \nabla\zeta \cdot \nabla\zeta(\mathbf{x},t)$ . The 256 different colors denote the local scalar dissipation rate, with black beginning at  $\nabla\zeta \cdot \nabla\zeta = 0$ , and pure blue through pure red denoting logarithmically increasing dissipation rates.

The local outer variables  $u(x)$  and  $\delta(x)$ , and the mass fraction-based conserved scalar field  $\zeta(\mathbf{x},t)$ , in the far field of axisymmetric turbulent jets follow self-similar scalings with downstream location  $x$ . Since these scalings produce a Reynolds number that remains constant with increasing downstream distance, measurements such as those in Fig. 1 can be rescaled to map the instantaneous scalar and dissipation rate fields to any  $x$ -location in the self-similar far field of the flow. A given set of chemical reactions occurring in this conserved scalar field would then correspond to a turbulent jet diffusion flame of length  $L$ , where the flame tip is taken to occur at the  $x$ -location for which the maximum conserved scalar value achieves stoichiometry for the fuel and oxidizer combination being considered. The mass fraction and reaction rate fields for any chemical species in this flame can then be constructed from the local values of the scalar and dissipation rate fields using the steady strained dissipation and reaction layer formulation.

Results are presented for the OH mass fraction and reaction rate fields at various downstream locations for three jet flames corresponding to increasing degrees of chemical nonequilibrium. The conditions for each case considered are shown in Fig. 2, where the depth of nonequilibrium is indicated relative to the flame blowout limit for an unpiloted hydrogen-air turbulent jet diffusion flame. The three cases each have the same far field Reynolds number ( $Re = 14,000$ ), but correspond to conditions in the flame ranging from near equilibrium (Case 1) to moderate nonequilibrium (Case 2) to deep nonequilibrium (Case 3). With a characteristic temperature of roughly 1800 K,

and with  $v \sim T^{1.5}$ , a cold-flow Reynolds number of 210,000 in Fig. 2 produces a hot-flow conserved scalar field consistent with the  $Re = 14,000$  measurements in Fig. 1. All results presented below are constructed via the SDRL formulation outlined in §2 using the conserved scalar and scalar dissipation fields in Fig. 1, with a uniform rescaling of these  $\zeta$  and  $\chi$  fields mapping them to any  $x/L$  location for any of the three cases considered. Relative local strain rates for each of the three cases and each of the four downstream locations at which results are presented are given in Table 1.

In Fig. 3 we compare the resulting OH mass fraction fields  $Y_{OH}(\mathbf{x}, t)$  at  $x/L = 0.25$  for each of the three cases. (Color bars identifying quantitative values for each case are given in Figs. 5-7.) Notice that at this location in the flame, the SDRL formulation produces thin layer-like OH fields for the near-equilibrium conditions in Case 1. The OH layer at these conditions is relatively straight and aligned with the downstream direction, and lies well off the jet centerline. Overall, the resulting OH field for Case 1 is strikingly similar to OH PLIF measurements at small  $x/L$  locations in turbulent jet diffusion flames under conditions of relatively weak nonequilibrium [13, 14]. By comparison, in Case 2 the strain rates at this location are significantly higher (see Table 1), and the SDRL formulation produces considerably broader and more diffuse structures in the OH mass fraction field, with little remaining evidence of the thin layer-like OH zones seen for Case 1. This is also consistent with direct OH PLIF imaging measurements in turbulent jet diffusion flames. For Case 3, the strain rates at this  $x/L = 0.25$  location are so high that local extinction of the reactions occurs throughout much of the flow, as evidenced by the zero OH values coincident with the high dissipation rates in Fig. 1. The remaining OH zones evident in Case 3 are completely broad and distributed, and show no remaining evidence of the layer-like structure in the underlying scalar dissipation rate field.

<u>x/L</u>	<u>Case 1</u>	<u>Case 2</u>	<u>Case 3</u>
0.25	10 ( $10^{-5}$ )	1	10
0.50	2.5 ( $10^{-5}$ )	0.25	2.5
0.75	1.1 ( $10^{-5}$ )	0.11	1.1
1.00	0.6 ( $10^{-5}$ )	0.06	0.6

Table 1. Relative strain rates at each of the four downstream locations and each of the three cases identified in Fig. 2 for which results are shown.



Moving to a location further downstream in the flame, Fig. 4 shows the OH mass fraction fields that result from the SDRL formulation at  $x/L = 0.50$  for each of the same three flows. A similar transition from thin, layer-like OH mass fraction fields at conditions near chemical equilibrium to broad, distributed OH zones with increasing depth of nonequilibrium, can be seen in the results obtained. There again is a striking resemblance of the OH fields that result for each of these three cases with the basic features of OH PLIF images obtained from direct measurements in turbulent jet diffusion flames under conditions of increasing chemical nonequilibrium [13, 14]. Notice that the thin layer-like OH field that results near equilibrium in Case 1 becomes more diffuse with increasing chemical nonequilibrium, leading to a broad and distributed OH reaction rate field for Case 3. It is essential to keep in mind that all of these fields were constructed from the *single* conserved scalar and scalar dissipation rate plane in Fig. 1 via the SDRL formulation. The differences evident among the three cases result entirely from the uniform rescaling of the scalar dissipation fields for the three flow conditions. Evidently the SDRL formulation allows the transition from thin "flamelet-like" fields near chemical equilibrium to broad "distributed" fields for large equilibrium departures with no need to explicitly distinguish between these two combustion environments, and without any need for separate models for treating them.

Figures 5-7 compare the OH mass fraction fields obtained from the SDRL formulation throughout the entire length of the flame for each of the three cases in Fig. 2. In each case the fields are shown at four different downstream locations relative to the mean flame length  $L$ , centered at  $x/L = 0.25, 0.50, 0.75$  and  $1.0$ . The size of each panel has been correctly scaled and placed for its downstream location to give a proper indication of the structure of the flame. Differences evident in the OH concentration fields when comparing panels at the same downstream location for the three cases shown are due solely to the differing degrees of nonequilibrium. However, changes in the OH mass fraction fields among panels corresponding to differing  $x/L$  values for the same case reflect changes in both the depth of nonequilibrium as well as changes in the scalar and dissipation rate values with increasing downstream location in the flame. For the jet similarity scalings, the scalar field values decrease with increasing distance from the jet source as  $\zeta \sim x^{-1}$ . Coupled with the linear increase in all length scales in the jet with increasing  $x$ , the resulting scalar dissipation field values decrease with distance from the jet source like  $\nabla\zeta \cdot \nabla\zeta \sim x^{-4}$ . Thus, in examining these results, it must be kept in mind that comparisons made among different cases but at the same  $x/L$  location show the effects of the degree of nonequilibrium only, while comparisons made at different downstream locations within the same case demonstrate the effects of both nonequilibrium level and changes in the scalar field values. Arranging the results

as shown in Figs. 5-7 allows separating the changes resulting solely from the degree of nonequilibrium from those resulting from changes in the conserved scalar and dissipation rate values. Table 1 gives the relative strain rates in each panel.

Note that the features of the resulting OH fields in Figs. 7-9 look very similar to those in direct OH PLIF imaging measurements in turbulent jet flames under varying degrees of chemical nonequilibrium [13, 14]. This is all the more striking in view of the fact that, despite the wide variations in the OH concentration field structure seen in these results with changing downstream position and with increasing depth of nonequilibrium among the three cases considered, all of these fields ultimately resulted from the same conserved scalar data plane shown in Fig. 1. Thus thin "flamelet-like" OH mass fractions and reaction rates at small  $x/L$  in Case 1, and the broad "distributed" regions of high OH concentrations and reaction rates in Case 3, all resulted from a simple layer-like structure in the scalar dissipation rate field in Fig. 1b and all can be reconciled with the single physically-based formulation given in §2 for these strained dissipation and reaction layers.

#### 4. Validation Study using Direct Numerical Simulations (DNS)

A more detailed validation study was done using DNS data from chemically reacting turbulent flow simulations. To do this, we apply the SDRL formulation, the equilibrium assumption, and the laminar flamelet model to conserved scalar fields resulting from direct numerical simulations (DNS) by the U. Washington group of Kosály & Riley [15] of homogeneous, decaying turbulence with chemistry governed by a single step, second-order, irreversible, isothermal reaction. This allows a direct examination of the ability of the SDRL formulation to predict the fuel, oxidizer, and product concentration fields, and evaluation of the relative accuracy of the SDRL formulation as compared to more traditional means of predicting chemical properties within the turbulent reacting flow for a wide range of Damköhler numbers.

##### 4.1 Direct Numerical Simulations

The direct numerical simulations of Mell, Nilsen, Kosály, and Riley [15] refer to a one-step, second-order, irreversible reaction without heat release in homogeneous, decaying turbulence. The equations for the conservation of mass

$$\nabla \cdot \mathbf{u} = 0 \quad (1)$$

and momentum

$$\frac{\partial \mathbf{u}}{\partial t} + \mathbf{u} \cdot \nabla \mathbf{u} - \nu \nabla^2 \mathbf{u} = -\frac{1}{\rho} \nabla p \quad (2)$$

govern the evolution of the velocity field. The global chemical reaction may be written in the form



where  $\phi$ , the stoichiometric coefficient, is the mass of oxidant that is consumed by reaction with a unit mass of fuel. The fuel, oxidizer, and product diffusivities are all equal, and the Schmidt number  $Sc = \nu/D$  is unity. The equations for the species mass fractions may then be written as

$$\frac{\partial Y_j}{\partial t} + \mathbf{u} \cdot \nabla Y_j - D \nabla^2 Y_j = \omega_j \quad (4)$$

$$\omega_j = \begin{cases} Z Y_F Y_O & j=F \\ -\phi Z Y_F Y_O & j=O \\ (\phi+1) Z Y_F Y_O & j=P \end{cases}$$

where  $Z$  is the reaction rate constant. An appropriately defined conserved scalar variable  $\zeta$  given by

$$\zeta = \frac{\phi Y_F - Y_O + 1}{\phi + 1} \quad (5)$$

satisfies the conservative advection-diffusion equation

$$\frac{\partial \zeta}{\partial t} + \mathbf{u} \cdot \nabla \zeta - D \nabla^2 \zeta = 0 \quad (6)$$

with  $\zeta = 0$  and  $\zeta = 1$  corresponding to pure oxidizer and pure fuel conditions, respectively. The numerical domain for which the governing equations are solved consisted of either  $64^3$  or  $128^3$  grid points with periodic boundary conditions on all sides of the computational cube. The numerical simulations thus provide fully three-dimensional species concentration fields  $Y_j(\mathbf{x}, t)$  within the reacting turbulent flow field as well as conserved scalar fields  $\zeta(\mathbf{x}, t)$  sufficiently resolved so that the scalar energy dissipation fields  $\nabla \zeta \cdot \nabla \zeta(\mathbf{x}, t)$  may be extracted. Representative conserved scalar and scalar energy dissipation planes are shown in Figure 8. Notice the predominance of one-dimensional, layer-like dissipation structures. Simulations were chosen so that the conserved scalar fields had become sufficiently developed. Images corresponding to the earliest time are shown at the far left with time increasing from left to right. Fields were generated for differing degrees of chemical nonequilibrium characterized by the global Damköhler number  $Da \equiv Z(L/u)$ , where  $L$  is the velocity integral length scale and  $u$  is the rms velocity. Cases were chosen to

emulate conditions ranging from nearly equilibrium to clearly nonequilibrium in the mean sense.

#### 4.2 Equilibrium Approximation

For a single step, second-order, irreversible chemical reaction of the type shown in (3), the limit of infinite Damköhler number (equilibrium chemistry) requires that fuel and oxidizer not coexist at any location [16]. This limit leads to piece-wise linear relations for the fuel, oxidizer, and product mass fractions in terms of the mixture fraction field  $\zeta(\mathbf{x}, t)$  only. These expressions are given by

$$Y_F^{eq} = \begin{cases} 0 & , \quad \zeta \leq \zeta_{ST} \\ \frac{(\phi + 1)\zeta - 1}{\phi} & , \quad \zeta > \zeta_{ST} \end{cases}$$

$$Y_O^{eq} = \begin{cases} -(\phi + 1)\zeta + 1 & , \quad \zeta \leq \zeta_{ST} \\ 0 & , \quad \zeta > \zeta_{ST} \end{cases}$$

$$Y_P^{eq} = 1 - Y_F^{eq} - Y_O^{eq}$$

The parameter  $\zeta_{ST} \equiv 1/(\phi+1)$  is the stoichiometric conserved scalar value.

#### 4.3 Flamelet Approximation

Unlike the equilibrium approximation which requires infinite Damköhler number, the flamelet model [9, 10] allows for large but finite local Damköhler numbers. The reaction zone is assumed to be asymptotically thin such that its structure may be considered one-dimensional with the reactants mixing within a laminar flow field. The governing equations for the species mass fractions are given by

$$\frac{-\chi}{2} \frac{d^2 Y_j}{d\zeta^2} = \omega_j \quad j = F, O \quad (8)$$

with pure fuel and pure oxidizer boundary conditions

$$Y_F = \begin{cases} 0, & \zeta = 0 \\ 1, & \zeta = 1 \end{cases} ; \quad Y_O = \begin{cases} 1, & \zeta = 0 \\ 0, & \zeta = 1 \end{cases} \quad (9)$$

The introduction of the instantaneous scalar dissipation rate  $\chi \equiv 2D\nabla\zeta \cdot \nabla\zeta(\mathbf{x}, t)$  allows for molecular mixing effects to be considered. As is customary in flamelet analyses the local dissipation rate is found from the self-similar solution of the conserved scalar transport equation for a counter flow configuration with local strain rate  $\epsilon$  and scalar boundaries  $\zeta^\pm = 0, 1$  and is given by

For the global chemical reaction given by (3) with reaction rates given in (4), the fuel, oxidizer, and product mass fractions may be determined in terms of the local Damköhler number  $Da^* \equiv 2Z/\epsilon$ , as  $Y_j = Y_j(\zeta, Da^*)$ . The product mass fraction solution  $Y_p(\zeta, Da^*)$ , found from (8) with pure fuel and air boundary conditions, is shown in Figure 9. For this simple global chemical reaction knowing  $Y_p(\zeta, Da^*)$  is sufficient for determining  $Y_F(\zeta, Da^*)$  and  $Y_O(\zeta, Da^*)$ .

#### 4.4 Results

The three-dimensional conserved scalar  $\zeta(\mathbf{x}, t)$  and corresponding scalar energy dissipation fields  $\nabla \zeta \cdot \nabla \zeta(\mathbf{x}, t)$  generated as part of the reacting flow simulation provide the basis for prediction of species concentrations within the computational domain for each of the three models examined here. Comparisons were made for global Damköhler numbers ranging from near equilibrium ( $Da = 22$ ) to deep nonequilibrium ( $Da = 0.5$ ). The DNS data provide the ability to make direct comparisons of chemical species concentrations with those predicted by the flame sheet approximation (EQLM), the laminar flamelet model (FLMT), and the strained dissipation and reaction layer (SDRL) formulation.

Figure 10 gives product mass fraction fields,  $Y_p(\mathbf{x}, t)$ , for the DNS simulation as well as the equilibrium, flamelet, and SDRL models for conditions of near equilibrium chemistry ( $Da = 22$ ). The corresponding  $\zeta(\mathbf{x}, t)$  and  $\nabla \zeta \cdot \nabla \zeta(\mathbf{x}, t)$  planes are shown at the far left of Figure 8. Figure 11 gives product mass fraction fields for the DNS simulation and these same three models corresponding to conditions of moderate nonequilibrium chemistry ( $Da = 4$ ). The corresponding  $\zeta(\mathbf{x}, t)$  and  $\nabla \zeta \cdot \nabla \zeta(\mathbf{x}, t)$  fields are given by the middle planes shown in Figure 8. Product mass fraction field results for deep nonequilibrium chemistry ( $Da = 0.5$ ) are shown in Figure 12, and the  $\zeta(\mathbf{x}, t)$  and  $\nabla \zeta \cdot \nabla \zeta(\mathbf{x}, t)$  fields corresponding to this case are shown at the far right of Figure 8.

Figure 13 shows a graph of mean product concentration error  $\langle Y_p \rangle_{error}$ , for the three models examined versus global Damköhler number where the percent error is defined as

$$\langle Y_p \rangle_{error} = \frac{|\langle Y_p \rangle - \langle Y_{p_{DNS}} \rangle|}{\langle Y_{p_{DNS}} \rangle} \cdot 100\%$$

Each model predicts mean product concentrations quite accurately for large Damköhler numbers, ie for conditions near chemical equilibrium. The EQLM model errors diverge rather quickly as deeper nonequilibrium conditions are

approached ( $Da \rightarrow 0$ ) and are the worst of the three models over the entire range of global Damköhler numbers examined. The FLMT model shows consistent improvement over the EQLM model for all Damköhler numbers but shares the EQLM model's fate of rapidly decreasing accuracy for increasing degrees of chemical nonequilibrium. The SDRL formulation results are slightly less accurate than those of the EQLM and FLMT models for large Damköhler numbers, but unlike the EQLM and FLMT models the SDRL formulation demonstrates only a small reduction in accuracy for increasingly large equilibrium departures. This results in substantial improvements in the prediction of mean product concentrations by the SDRL formulation for those cases involving the greatest degrees of chemical nonequilibrium.

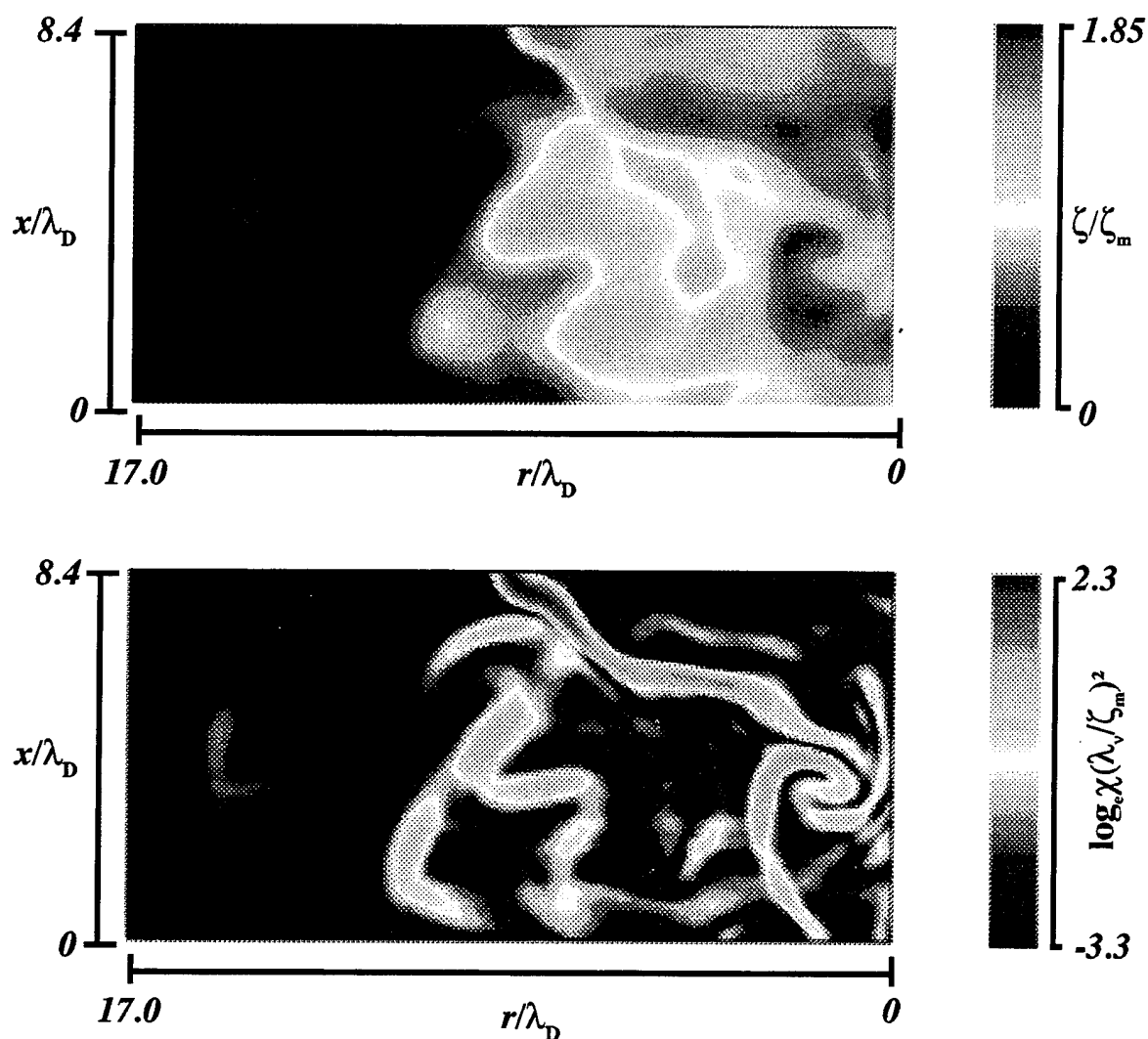
Such DNS validation studies permit direct comparisons of chemical species concentration fields with those predicted by these models for Damköhler numbers corresponding to chemical states ranging from near equilibrium to deep nonequilibrium. Results have shown not only the applicability of the SDRL formulation but also the accuracy with which it predicts species concentrations and their structure in turbulent reacting flows. Substantial improvements by the SDRL formulation are seen in the prediction of mean product concentrations for those cases involving the greatest degrees of chemical nonequilibrium.

### References

- [1] Dahm, W. J. A. & Buch, K. A. (1991) High resolution, three-dimensional (2563), spatio-temporal measurements of the conserved scalar field in turbulent shear flows; Turbulent Shear Flows 7, pp. 17-26, W.C. Reynolds, Ed., Springer Verlag, Berlin.
- [2] Dahm, W. J. A., Southerland, K. B. & Buch, K. A. (1991) Direct, high resolution, four-dimensional measurements of the fine scale structure of  $Sc \gg 1$  molecular mixing in turbulent flows; *Phys. Fluids A* 3, 1115-1127.
- [3] Buch, K. A. & Dahm, W. J. A. (1992) Fine scale structure of conserved scalar mixing in turbulent shear flows:  $Sc \gg 1$ ,  $Sc = 1$  and implications for reacting flows; University of Michigan Report No. 026779-5, The University of Michigan, Ann Arbor, MI.
- [4] Kerr, R. M. (1985) Higher-order derivative correlations and the alignment of small scale structures in isotropic numerical turbulence; *J. Fluid Mech.* 153, 31-58.
- [5] Reutsch, G. R. & Maxey, M. R. (1991) Small-scale features of vorticity and passive scalar fields in homogeneous isotropic turbulence; *Phys. Fluids A* 3,

1587-1597.

- [6] Mell, W. E., Kosály, G. & Riley, J. J. (1993) An investigation of closure models for nonpremixed turbulent reacting flows; AIAA Paper No. 93-0104, AIAA, Washington, D.C.
- [7] Montgomery, C. J., Kosály, G. & Riley, J. J. (1993) Direct numerical simulation of turbulent H<sub>2</sub>-O<sub>2</sub> combustion using reduced chemistry; AIAA Paper No. 93-0248, AIAA, Washington, D.C.
- [8] Long, M. B. (1993) Proceedings of the 1993 AFOSR Contractors Meeting in Propulsion, AFOSR, Washington, D.C.; also private communication.
- [9] Peters, N. (1984) Laminar diffusion flamelet models in nonpremixed turbulent combustion. *Prog. Energy Combust. Sci.* **10**, 319-339.
- [10] Peters, N. (1986) Laminar flamelet concepts in turbulent combustion. Proc. 21st Symp. (Int'l) on Combustion, 1231-1250. The Combustion Institute, Pittsburgh
- [11] Bish, E. S., & Dahm, W. J. A. (1994) Nonequilibrium structure of H<sub>2</sub>-air combustion in turbulent jets; AIAA Paper No. 94-0100, AIAA, Washington, DC.
- [12] Bish, E. S. & Dahm, W. J. A. (1994) Strained dissipation and reaction layer analyses of nonequilibrium chemistry in turbulent reacting flows; Proc. 25th Symp. (Int'l) on Combustion, Irvine, CA.
- [13] Seitzman, J., Paul, P. H., Hanson, R. K. & Ungut, A. (1990) AIAA Paper No. 90-0160, AIAA, Washington, D.C.
- [14] Clemens, N. T., Paul, P. H. & Mungal, M. G. (1992) private communication.
- [15] Mell, W. E., Nilsen, V., Kosály, G. & Riley, J. J. (1994) Investigation of closure models for nonpremixed turbulent reacting flows; *Phys. Fluids* **6**, 1331-1356.
- [16] Burke, S. P., Schumann, T. E. (1928) *Ind. Engng. Chem.* **20**, 998.



Scalar mixing measurements for a  $Sc \approx 1$  conserved scalar field, obtained in the self-similar far field of an axisymmetric turbulent jet at  $Re_\delta \approx 14,000$ . (top) The conserved scalar field  $\zeta(x,t)$ . (bottom) The associated two-dimensional scalar dissipation rate field  $\log \chi(x,t)$ . Note that essentially all of the scalar dissipation field is organized into locally one-dimensional layer-like structures being stretched and folded by the underlying velocity gradient field.



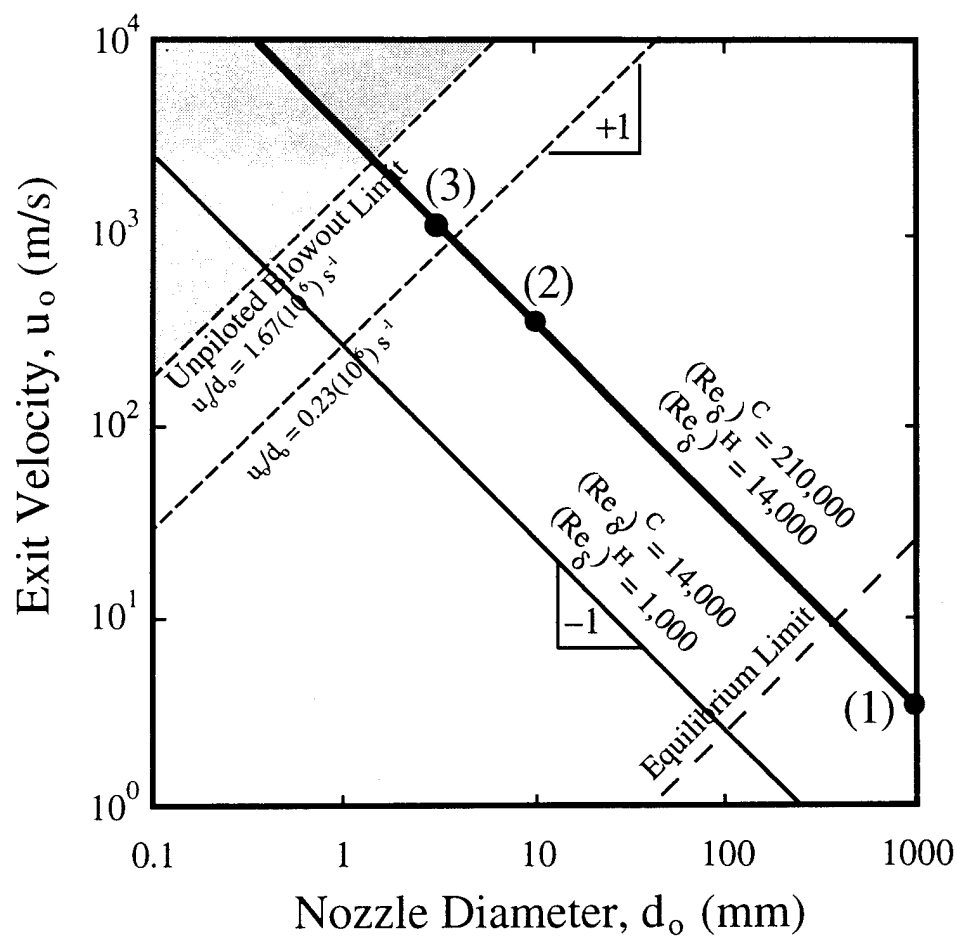
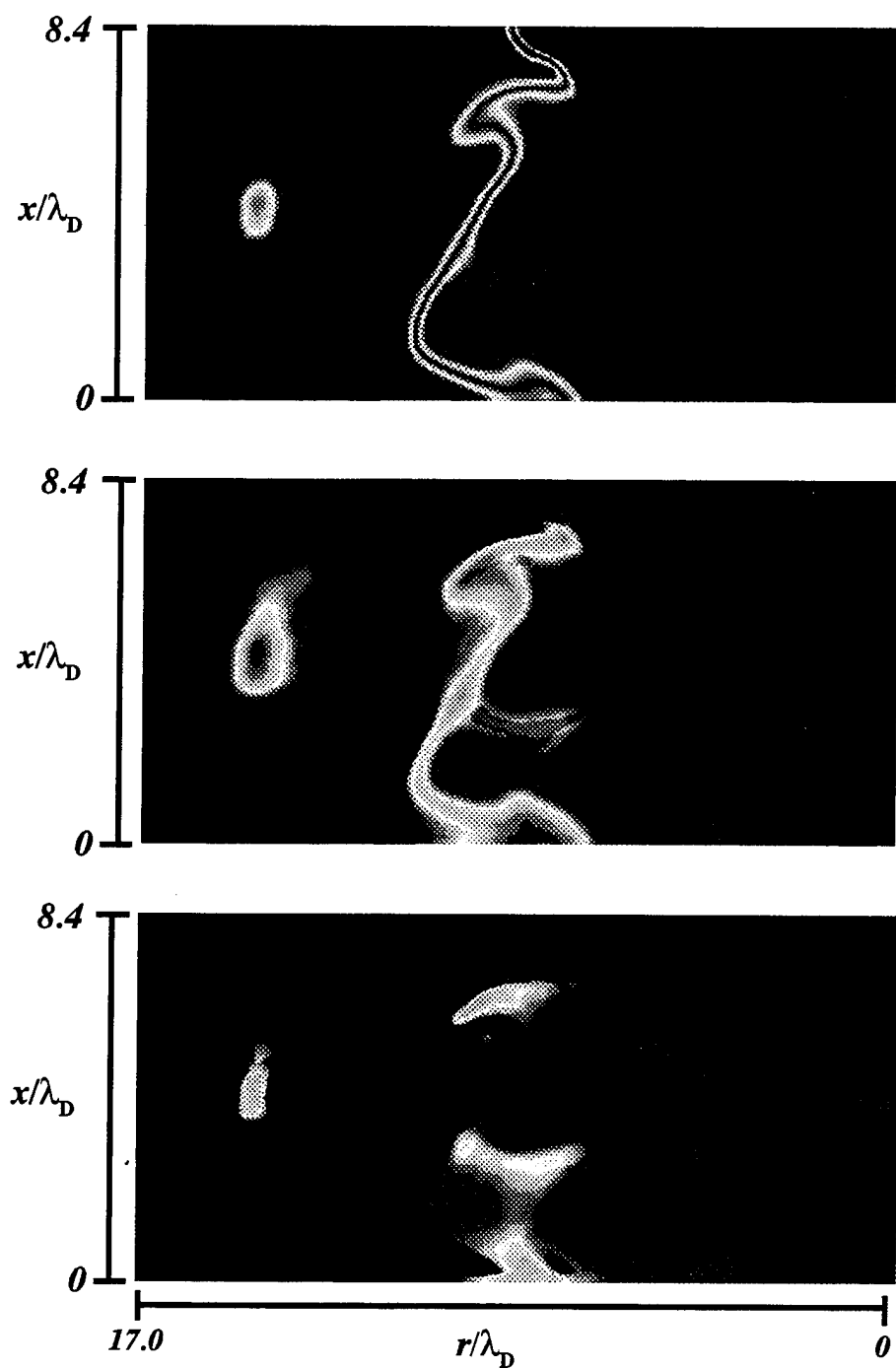
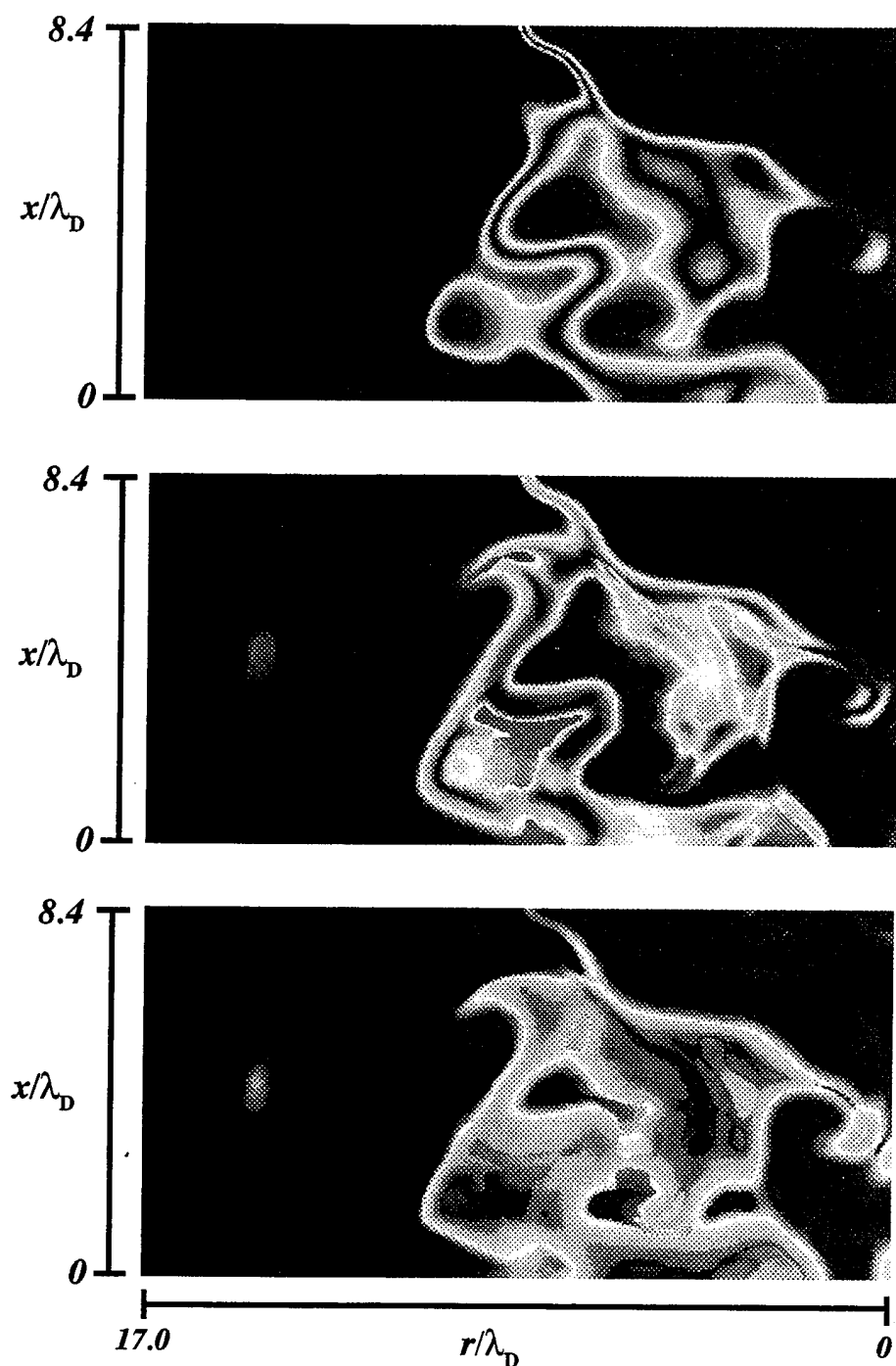


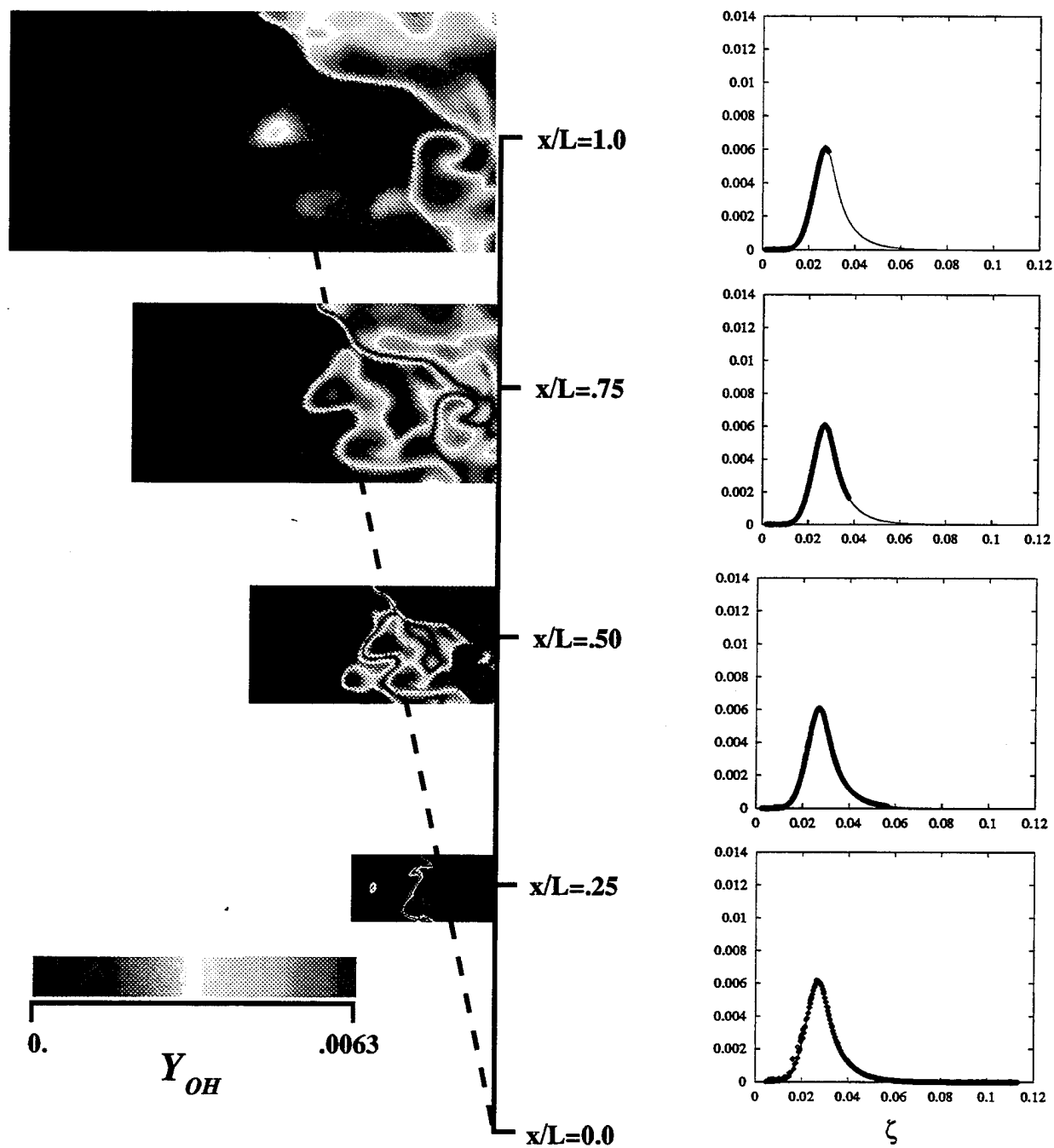
Fig. 2. Source conditions for turbulent hydrogen-air jet diffusion flames, showing depth of chemical nonequilibrium relative to the unpiloted blowout limit, given by  $u_o/d_o = 1.67 \cdot 10^6 s^{-1}$ . Solid line denotes conditions giving far-field hot flow Reynolds number  $Re = 14,000$  corresponding to cold flow  $Re = 210,000$ . Dashed lines denote constant global Damköhler number ( $u_o/d_o = \text{const.}$ ) Shown are the conditions for three cases, giving (Case 1) the equilibrium limit, (Case 2) moderate nonequilibrium, and (Case 3) deep nonequilibrium.



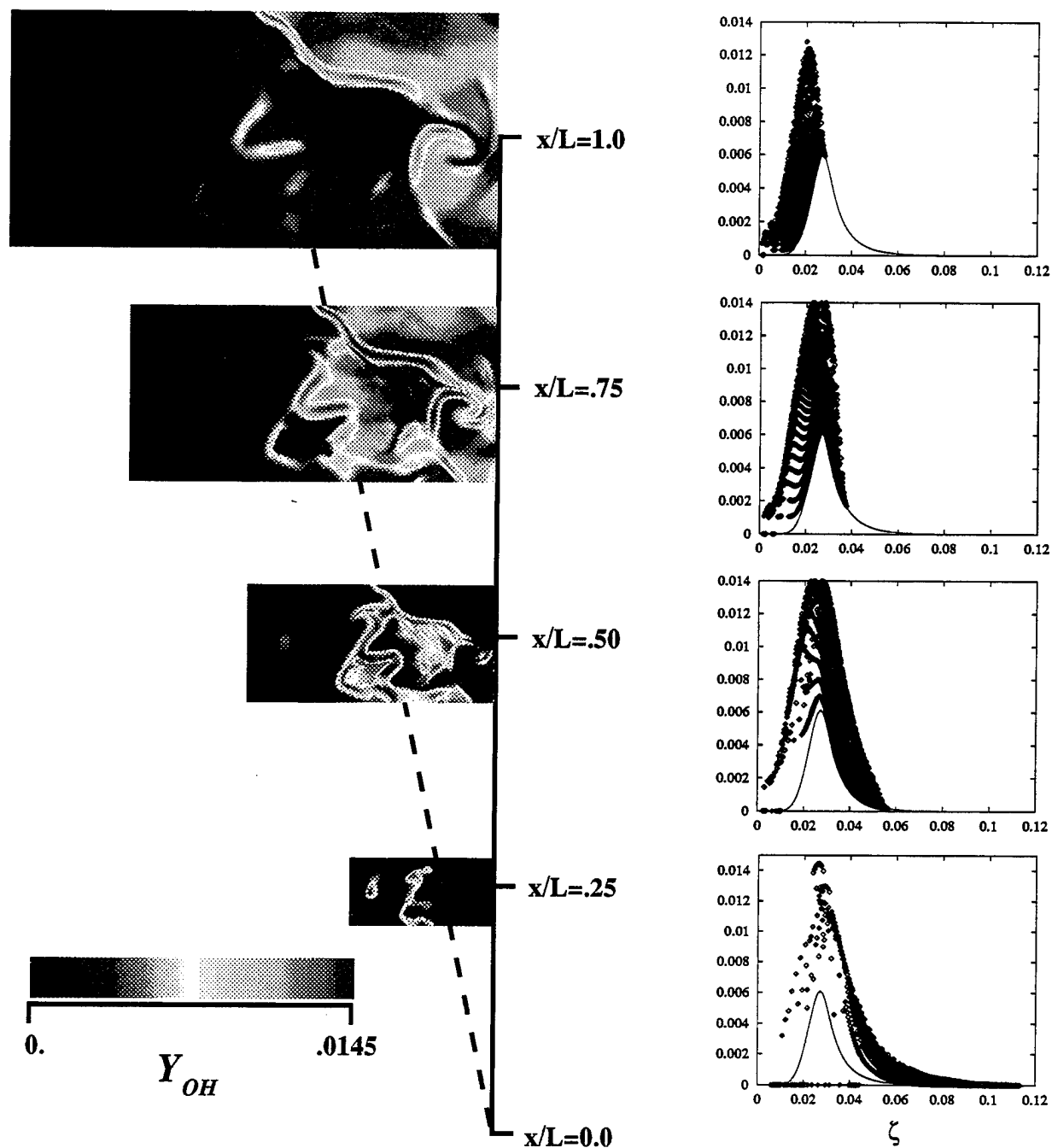
Strained dissipation and reaction layer (SDRL) model results for OH mass fraction field  $Y_{OH}(x,t)$  in a hydrogen-air turbulent diffusion flame at  $x/L = 0.25$  for Case 1 (top), Case 2 (middle), and Case 3 (bottom), from the scalar mixing measurements in Fig. 1. Note the progression from thin "flamelet-like" OH zones near equilibrium (Case 1), to broad "distributed" OH zones with increasing depth of chemical nonequilibrium.



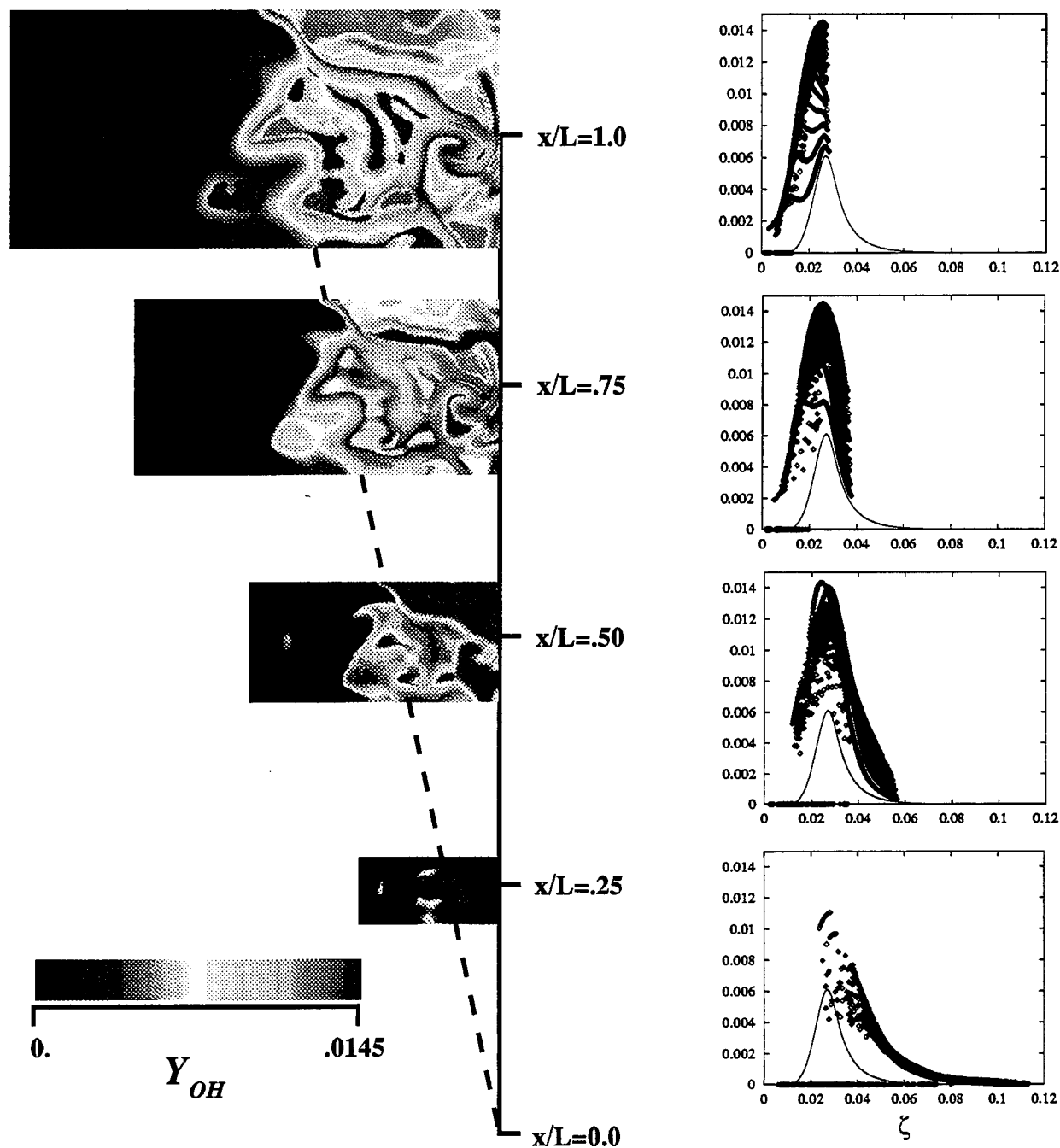
Strained dissipation and reaction layer (SDRL) model results for OH mass fraction field  $Y_{OH}(x,t)$  in a hydrogen-air turbulent diffusion flame at  $x/L = 0.50$  for Case 1 (top), Case 2 (middle), and Case 3 (bottom), from the scalar mixing measurements in Fig. 1. Note the progression from thin "flamelet-like" OH zones near equilibrium (Case 1), to broad "distributed" OH zones with increasing chemical nonequilibrium.



Strained dissipation and reaction layer (SDRL) model results for composite OH mass fraction fields  $Y_{OH}(x,t)$  and the associated scatter plots for a hydrogen-air turbulent jet diffusion flame in the equilibrium limit (Case 1) at four downstream locations:  $x/L = 0.25, 0.50, 0.75$ , and  $1.0$ . The solid curve in each of the scatter plots gives the equilibrium OH mass fraction distribution.



Strained dissipation and reaction layer (SDRL) model results for composite OH mass fraction fields  $Y_{OH}(\mathbf{x}, t)$  and the associated scatter plots for a hydrogen-air turbulent jet diffusion flame at moderate nonequilibrium (Case 2) conditions at four downstream locations:  $x/L = 0.25, 0.50, 0.75$ , and  $1.0$ . The solid curve in each of the scatter plots gives the equilibrium OH mass fraction distribution.



Strained dissipation and reaction layer (SDRL) model results for composite OH mass fraction fields  $Y_{OH}(x,t)$  and the associated scatter plots for a hydrogen-air turbulent jet diffusion flame at deep nonequilibrium (Case 3) conditions at four downstream locations:  $x/L = 0.25, 0.50, 0.75$ , and  $1.0$ . The solid curve in each of the scatter plots gives the equilibrium OH mass fraction distribution.

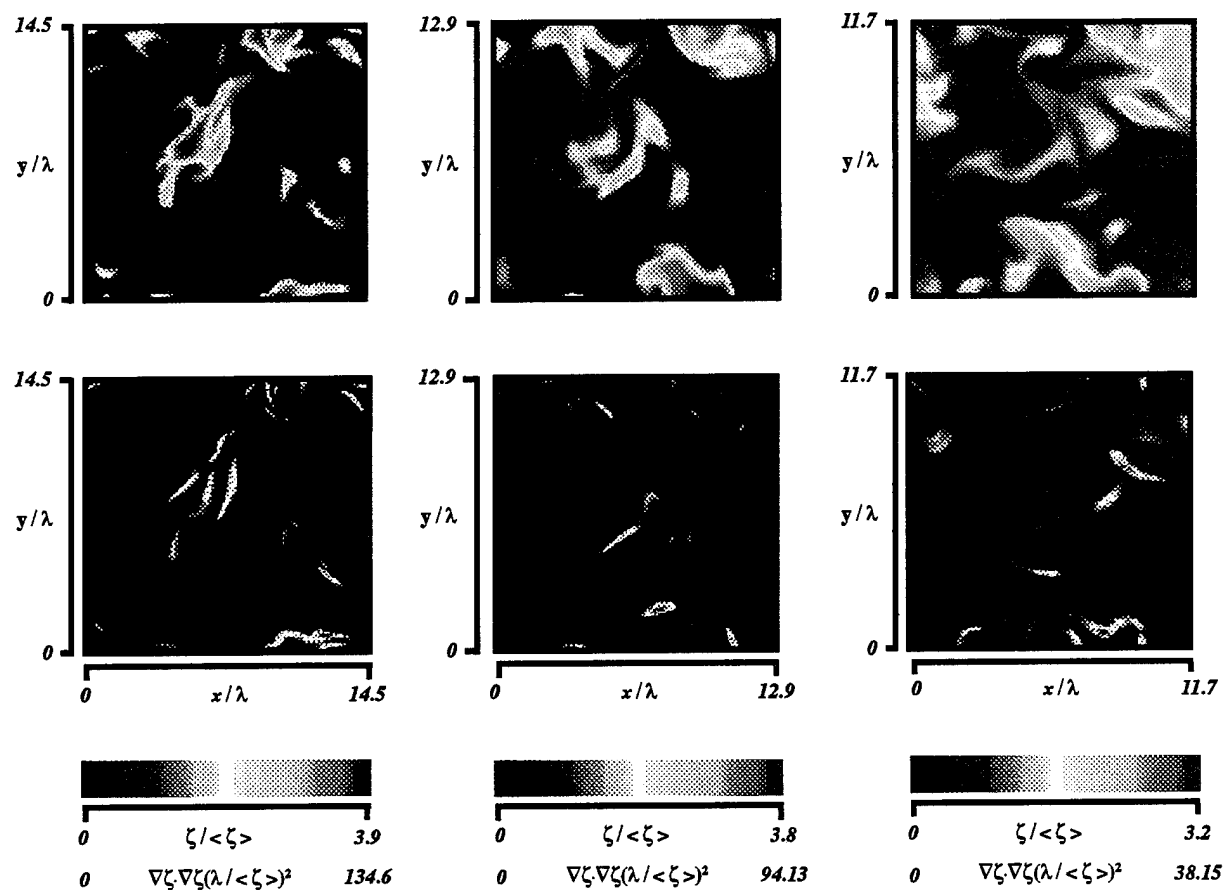


Figure 8. DNS results of Mell *et al* (1994) for  $Sc = 1$ , homogeneous, decaying turbulence. For each case, the conserved scalar field,  $\zeta(\mathbf{x}, t)$ , is shown at the top, and the associated scalar energy dissipation field,  $\nabla \zeta \cdot \nabla \zeta(\mathbf{x}, t)$ , extracted from the full three-dimensional scalar gradient vector field is displayed on the bottom.

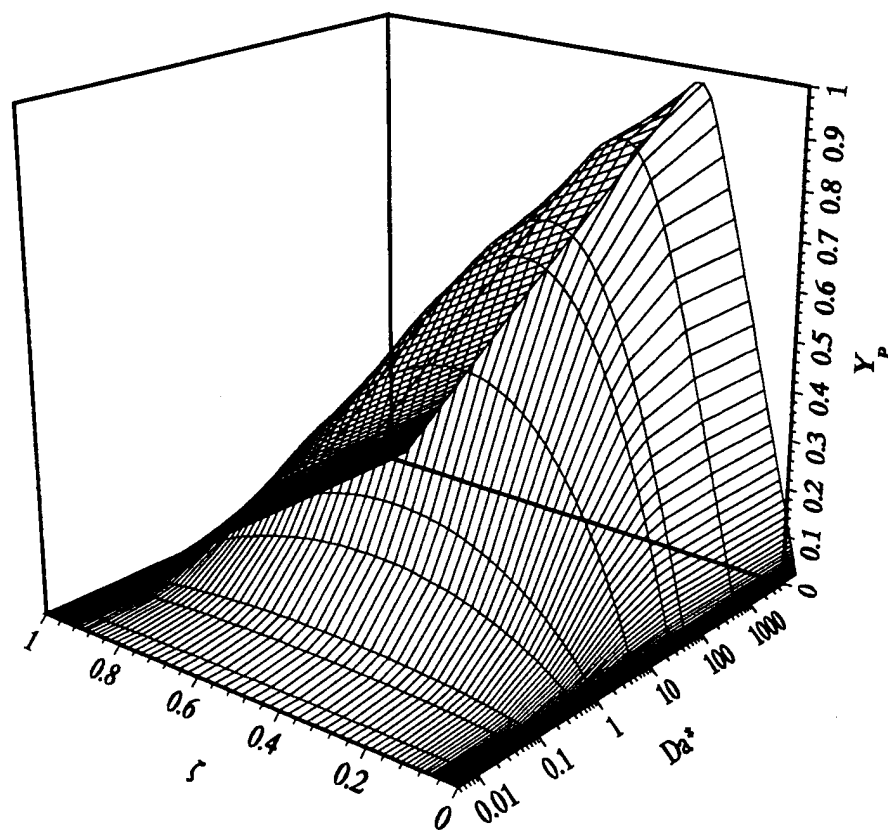


Figure 9. Product mass fraction solution,  $Y_p(\zeta, Da^*)$ , for the one-dimensional advection-diffusion-reaction equation with chemical kinetics as described in (3) and (4) and pure fuel/pure air boundary conditions.



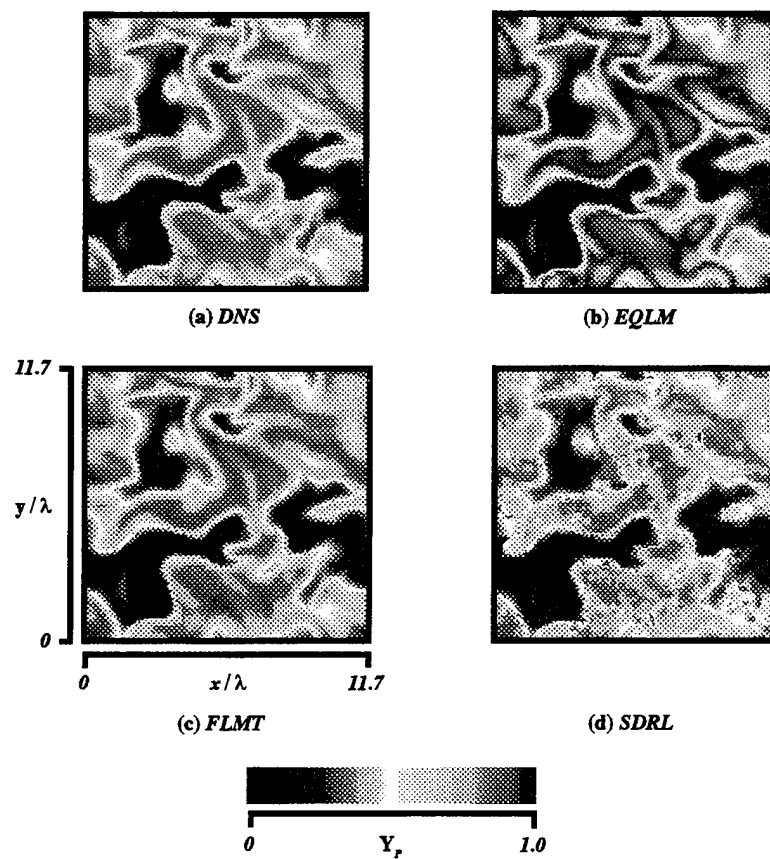


Figure 10. Product mass fraction field,  $Y_p(\mathbf{x}, t)$ , results for large Damköhler number (near equilibrium chemistry). (a) Direct numerical simulation of Mell *et al* (1994). (b) Flame sheet approximation. (c) Laminar flamelet model. (d) SDRL formulation.

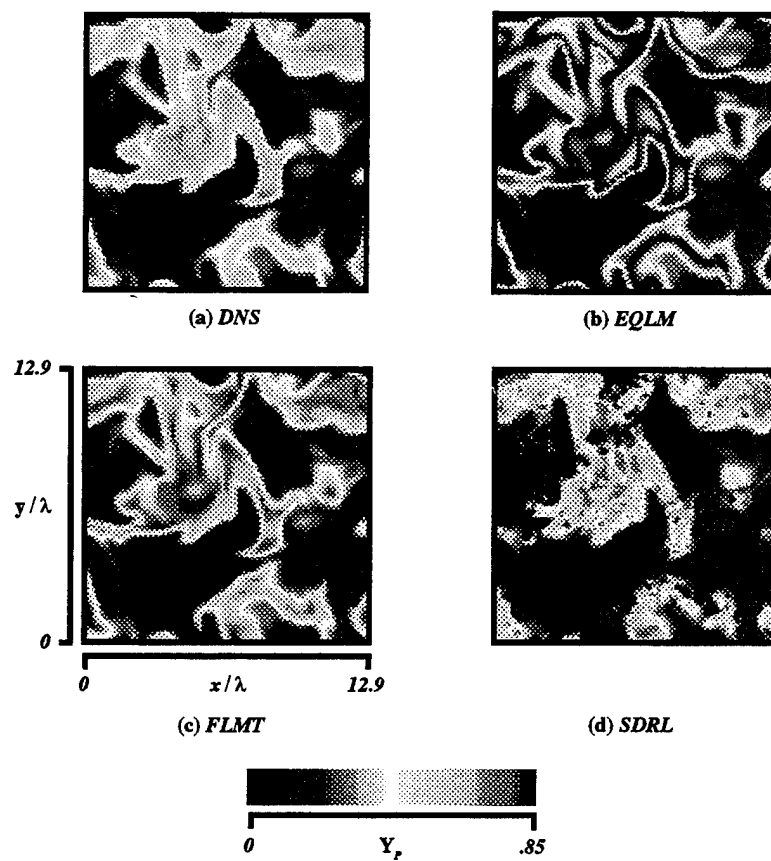


Figure 11. Product mass fraction field,  $Y_p(x, t)$ , results for moderate Damköhler number (substantial equilibrium chemistry departure). (a) Direct numerical simulation of Mell *et al* (1994). (b) Flame sheet approximation. (c) Laminar flamelet model. (d) SDRL formulation.

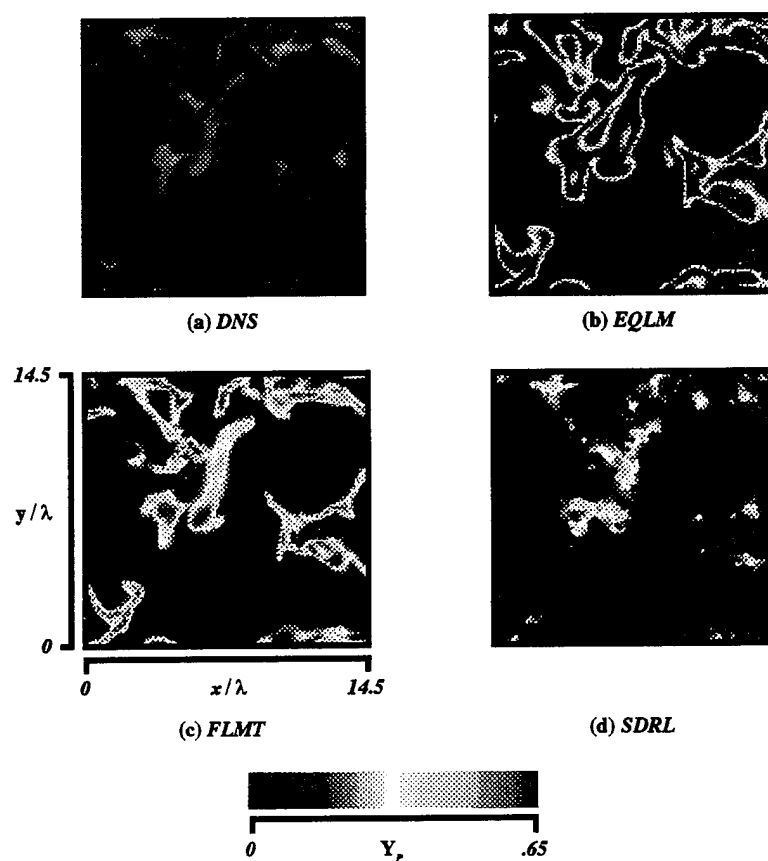


Figure 12. Product mass fraction field,  $Y_p(x,t)$ , results for small Damköhler number (deep nonequilibrium chemistry). (a) Direct numerical simulation of Mell *et al* (1994). (b) Flame sheet approximation. (c) Laminar flamelet model. (d) SDRL formulation.

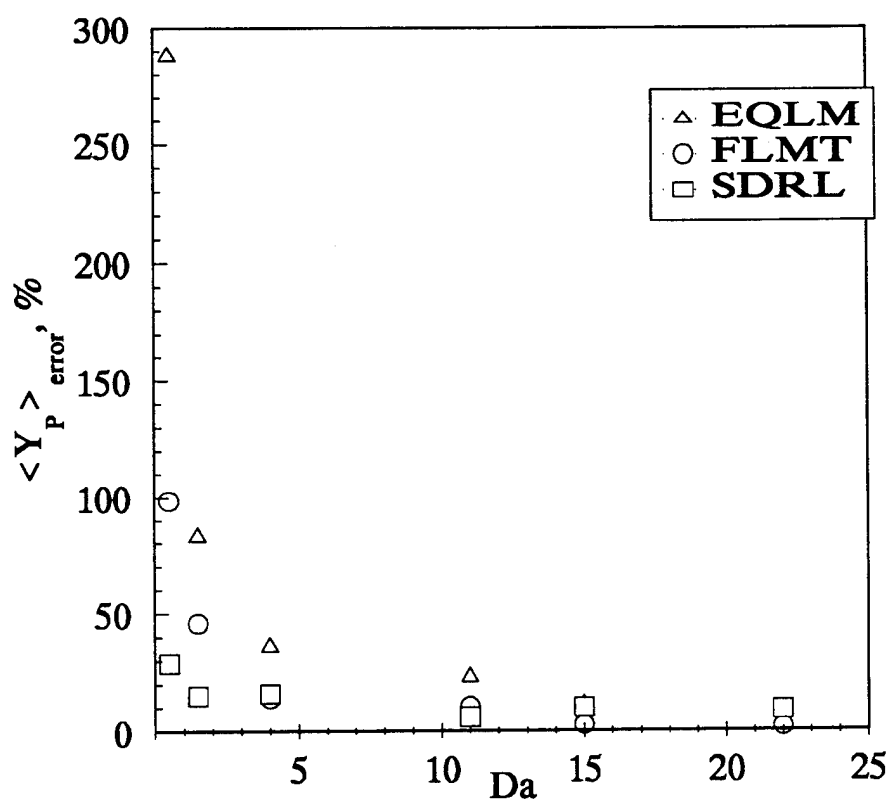


Figure 13. Mean product concentration error versus global Damköhler number for each of the three models examined.